DETERMINING THE PHYSICO-CHEMICAL CONDITIONS ON THE EARLY EARTH: BARBERTON SCIENTIFIC DRILLING PROJECT, SOUTH AFRICA.

Dissertation submitted to the Faculty of Science, University of Cape Town
for the degree of Doctor of Philosophy.

Eugene G. Grosch, *MSc*.

Department of Geological Sciences,
University of Cape Town,
December 2011

ACKNOWLEDGEMENTS

The author wishes to thank many friends and colleagues at the Department of Geological Sciences, University of Cape Town (UCT) and the Department of Earth Science & Centre for Geobiology, University of Bergen (UiB). At UCT, Prof. Chris Harris (former HOD) is thanked for efficiently facilitating the change of supervisor process during my PhD. Associate Professor Steve Richardson is sincerely thanked for standing in as my new principal supervisor, for providing administrative support as current HOD and for encouragement during the final year of my PhD research. Associated Professors Dave Reid and Hartwig Frimmel are remembered for interesting discussions on rocks and field geology adventures during my student years at UCT. I extend my appreciation and thanks to the technical staff at the Department of Geological Sciences: John Harrison, David Wilson, Ivan Wilson, Jonathan van Rooyen, Rene van der Merwe, Abiel Kidane and last but not least Ernest Stout are thanked for their friendship and valuable technical support. David Wilson and Rene van der Merwe are particularly thanked for thin-section preparation.

Prof. Rolf-Birger Pedersen is thanked for his remarkable leadership skills, inspiration as a geologist and for providing me with many analytical opportunities during my visits to Bergen, particularly during the 8 month Yggdrasil Scholarship stay that included both a Bergen rainy-snowy winter and a summer that apparently never seemed to arrive! Dr. Nicola McLoughlin is thanked for, skiing lessons, her wonderful sense of humor and for many interesting discussions on early Earth geobiology. Prof. Jan Kosler and the geochronology group (Dr. Jiri Slama, Dr. Kerstin Drost) from whom I have learnt much, is acknowledged for assistance with laser-ablation U-Pb zircon geochronology. Prof. Ulysses Ninnemann is acknowledged for his great help with carbon isotope analyses at the Bjerknes Climate Centre. Ingunn Thorseth is thanked for her interesting geobiology discussions. Siv Dundas, Ole Tumyr and Yuval Ronnen (UiB) is acknowledged for fantastic technical support in the TIMS, ICP-MS, EMPA and other analytical labs. To all my table tennis (ping pong!) friends, the administrative staff and colleagues on the second, third and fourth floor at the Centre for Geobiology (UiB), it has been really fun!

I wish to thank Prof. Olivier Vidal (University of Grenoble, France) for inspiration during dark days and for interesting and helpful discussions on thermodynamics of sheet silicates and metamorphic petrology. Martin Whitehouse is sincerely thanked for all his help during my analytical sessions on the Nordic Secondary Ion Microprobe (NORDSIMS) in Stockholm, Sweden.

Thanks to Annelize Steyn, Johan Eksteen, Shane Plumkel, and Property Mokoene from the Mpumalanga Tourism and Parks Agency (MTPA), Songimvelo Nature Reserve, South Africa for their support and valuable environmental advice prior to and during the Barberton Scientific Drilling Project in 2008. Drillers in Training (DiT) are thanked for all their on-site technical capabilities and assistance during the BSDP in 2008.

Cody, my South African Jack Russell buddy is thanked for always being available to fetch a bollie on the beach at times when I need to clear my scientific thoughts and have some fun! Finally I would like to thank my Mom and Dad (Patricia and Gerald Grosch) for their support and encouragement during my PhD, my brothers Warren and Garreth, my sister in-law Ramona and the two princesses, my nieces Allison (Big Princess) and new born Rachel.

This PhD project was funded by a National Research Foundation (NRF) Scarce Skills Scholarship, South Africa and Norwegian Research Council Yggdrasil Scholarship to E. G. Grosch.

Eugene G. Grosch

August, 2011

Declaration statement:

I, Eugene Gerald Grosch, declare that this PhD thesis is my own work.

_____

August, 2011

Abstract

Low-grade metabasites and hydrothermally altered ultramafic rocks comprise most of the ca. 3.5-3.2 Ga, Paleoarchean Barberton Greenstone Belt (BGB) of South Africa. However, *PT*-constraints and detailed petrological information on the variably altered mafic-ultramafic rocks are sparse and the nature of greenschist facies metamorphism is poorly characterized. In addition, alteration and silicification associated with distinct emerald green, fuchsite-(Cr-mica)-carbonate-quartz alteration zones is commonly found beneath chert horizons in the mafic-ultramafic rocks of the Onverwacht Group of the BGB. The origin of this silicification is highly debated and has important bearing on the nature of Paleoarchean geodynamic models, crustal geothermal gradients, hydrothermal oceanic regimes, as well as potential early life-sustaining environments. Over the past four decades, widely varying interpretations have been reported for the origin of these silica-rich fuchsitic alteration zones in the BGB, ranging from very low temperature (less than 60^{o}C) atmospheric weathering of komatiites (Lowe and Byerly, 1986; 1999); low-temperature (less than 125^{o}C) seafloor alteration (Hofmann and Harris, 2008); to bedding-parallel 'flaser-banded gneisses\schists' in oceanic 'extensional\overthrust glide planes' (de Wit, 1982a; 1986a,b; de Wit et al., 1982b; 1987b; 2011). Consequently, these fuchsitic-alteration zones have been at the centre of much debate surrounding stratigraphy models and the possible operation of early Paleoarchean plate-tectonic processes in the BGB.

This thesis presents detailed petrological and geochemical data on variably altered mafic-ultramafic surface samples, as well as continuous drill core material obtained during the Barberton Scientific Drilling Program (BSDP), across one of these fuchsite-carbonate-quartz alteration zones in the central Kromberg type-section, Onverwacht Group. The drill core spans variably silicified metabasalts and cherts that overlie a fuchsite-carbonate-quartz alteration zone, and intercepted metapyroxenitic rocks below. Application of a chlorite thermodynamic multiequilibrium calculation and pseudosection modelling in conjunction with petrographic observations indicate a wide range in metamorphic conditions from subgreenschist to the uppermost greenschist facies across the Kromberg type-section. The central fuchsite-bearing alteration zone containing strong mylonitic fabrics, referred to as the Kromberg Section Mylonites (KSM), records at least two metamorphic events: a high-*T*, low-*P* (420 ± 30^{o}C, < 3kbar) metamorphism, and a lower-*T* event (T = 240-350^{o}C, P = 2.9 ± 0.15 kbar) related to retrograde metamorphism associated with extensional quartz-carbonate veins.

Pillow lava metabasalts directly beneath the KSM record the same HT/LP-type metamorphic conditions, whereas metabasalts 90m and 125m above the KSM record temperatures of 250-340^{o}C. Lower in the Kromberg type-section, metamorphic conditions vary from 215-321^{o}C (at 2.9kbar, mid-lower parts) to very low-grade conditions of 140-209^{o}C in the lowermost Kromberg. Thus, an inverted metamorphic field gradient is documented beneath the KSM.

Cr-spinel compositions in the ultramafic protolith to the strongly banded KSM rocks indicate a supra-subduction setting. Geochemical constraints on the protoliths metabasalts and gabbroic intrusions also indicate formation in a supra-subduction zone setting. Major and trace element data across the KSM alteration zone shows enrichment in MgO, CaO, SiO_2 but depletion in LILE (e.g. Rb, Ba) and the LREE's. Oxygen stable isotope data from the mafic and ultramafic host rock display highly shifted $\delta^{18}O$ values that ranges from 9.3 up to 14.6 ‰ indicating extensive low-temperature alteration above and below the KSM. In-situ sulphur stable isotope data measured by SIMS points to (i) seafloor sulphides (positive MIF) that record an atmospheric sulphur reservoir preserved in a primary seafloor chert; (ii) intrusive chert veins with a mixed magmatic and seafloor sulphur signature (positive but smaller MIF); and (iii) purely magmatic sulphides ($d^{34}S$ and MIF near the origin) in the KSM zone. The extensive carbonate veins\bands record carbon isotope values of 0 ± 1.5‰ and highly radiogenic initial $^{87}Sr/^{86}Sr$ ratios of between 0.71048 to 0.71621.

The detailed petrological analysis of the fuchsite-bearing rocks of the KSM, indicates that they are listvenite, a hydrothermal alteration product typically found in mafic-ultramafic tectonic mélange zones of ophiolite terranes. Together with the new metamorphic *PT*-constraints this means that these rocks are not a product of Archean atmospheric weathering. Rather, in conjunction with field data, the inverted metamorphic field gradient in the Kromberg type-section suggests that the KSM represents a Paleoarchean thrust zone. A new geodynamic model is therefore proposed in, which the mafic-ultramafic oceanic rocks of the Kromberg-type section were obducted as a thrust nappe pile in a regional transpressional tectonic regime between 3227 and 3230 Ma. Thus, listvenitic alteration, including obduction-related silicification, must have post-dated earlier seafloor alteration and serpentinization of the rocks in the KSM. The new Paleoarchean hydrothermal alteration and tectonic model proposed here for the KSM, highlights the need to distinguish low temperature, subseafloor silicification environments that may have sustained early microbial life, from later (up to 100 myr) obduction-related silicification in shear zones, and also has important implications for currently proposed geodynamic and regional tectono-stratigraphy models for the BGB.

Geologic and geochronological evidence for the operation of even earlier plate-tectonic processes at ca. 3432 Ma, namely 200 million years earlier than the development of the fuchsite-carbonate-quartz zone in the central Kromberg type-section, is presented herein. Detrital zircon grains in coarse-grained sedimentary rocks of the Noisy formation, (traditionally considered as the H6 unit of the uppermost Hooggenoeg Formation) in the Paleoarchean Barberton Greenstone Belt (BGB) South Africa, are investigated by laser ablation (LA)-ICP-MS to determine their U-Pb and $^{207}Pb/^{206}Pb$ ages for depositional age and provenance determination. Drill core and field observations indicate that these rocks are clastic polymictitic diamictites and sandstones. A wide range in $^{207}Pb/^{206}Pb$ ages between ca. 3600 and 3430 Ma is reported. The youngest detrital zircon grain identified has an age of 3432 ± 10 Ma, constraining the maximum depositional age of the sedimentary sequence and formation of a major underlying erosional unconformity. Most of the zircon ages correspond in age to the underlying ca. 3460-3430 Ma tonalite trondjemite-granodiorite (TTG) gneisses of the Stoltzburg Terrane and felsic intrusions of the uppermost Hooggenoeg Formation that constitute most of the Songimvelo Block of the BGB on the Kaapvaal craton. The $^{207}Pb/^{206}Pb$ ages of the oldest grains identified corresponds to plutonic sources identified in older proto-continental blocks of the Kaapvaal craton, namely the ca. 3509 Ma Steynsdorp Block and ca. 3667-3223 Ma Ancient Gneiss Complex (AGC). These new $^{207}Pb/^{206}Pb$ zircon ages indicate provenancial linkage between the Songimvelo Block and older proto-continental blocks exposed on the Kaapvaal craton (e.g. AGC) at ca. 3432 Ma, argued here, to have occurred during major tectonic uplift that, in turn, lead to development of the erosional unconformity and a stable continental landmass as early as ca. 3432 Ma. Thus, the Noisy formation is a remnant of the earliest tectonic sedimentary basin in the BGB. In summary, new drill core and field observations, together with new geochronological and petrological constraints presented herein, support plate-tectonic processes operating in the proto-Kaapvaal craton in at least two major orogenic phases namely at ca. 3432 Ma and during a second phase at ca. 3230 Ma that resulted in obduction of the Kromberg oceanic sequences along the KSM.

Table of Contents

Chapter 1

Introduction

Drill site KD1, Barberton Scientific Drilling Project 2008.

1.1. Drilling in Africa's Oldest Greenstone Belt: Barberton Scientific Drilling Project

Earth's early evolution and the conditions under which life first emerged are highly controversial topics. Did Venus- type tectonics dominate the early Earth, with vast landscapes of hot spot volcanoes belching lava and gases into a tenuous carbon dioxide/methane-rich atmosphere, or was plate tectonics already in operation? Debates rage about when water first became dominant across Earth's surface, the temperatures and depths of early oceans, and when the first protocontinents began to form. These large uncertainties confound scientists' understanding of ecological niches available for the emergence of life, and a quantifiable image of the early Archean world is still missing.

Geoscientists seeking to learn more are restricted to the most ancient rock types partly preserved in sparse, complex crustal remnants known as greenstone belts. These rocks, located in southwestern Greenland, northern Canada, western Australia, and South Africa, have retained the hard facts that scientists can use to test theories and decipher geologic history of the early to middle Archean (3–4 billion years ago). The 3.5- to 3.2- billion- year-old Barberton Greenstone Belt (BGB) in South Africa's eastern Mpumalanga Province (Figure 1.1) has been widely used as a natural laboratory for early Earth analyses because of its extremely well preserved rock units. This location, considered a prime target for a scientific drilling project to further probe Earth's deep history and the origins of life, is the site of the Barberton Scientific Drilling Project (BSDP).

In July–August 2008, three boreholes were drilled into the BGB, that represented part of an ongoing early Earth research collaboration between the Department of Geological Sciences and the Africa Earth Observatory Network (AEON) at the University of Cape Town, South Africa, and the Centre for Geobiology (CGB) at the University of Bergen, Norway. Prior research in the BGB has been based on discontinuous outcrops that in parts have been exposed to long-term chemical weathering. Drilling during the BSDP used clean diamond core drilling, which helped to escape such adverse surface effects and provided continuous geologic information with depth, not previously achieved

Drilling focused on 3.47 to 3.33 billion year- old altered mafic-ultramafic and clastic sedimentary rocks in the middle to upper Onverwacht Group of the Swaziland Supergroup in the south westernmost BGB (Figure 1.1). The regional geological setting is discussed further in Chapter 2, which summarises the available stratigraphic models and interpretations. With 99% core recovery, oriented in situ, the cores provide abundant fresh rock materials to advance understanding of the geologic processes in the Archean. The BSDP has several goals,

including: to test whether or not plate tectonics was operating in the early Paleoarchean BGB; to understand metamorphic hydrothermal conditions in different Archean crustal settings; to investigate the temperature and compositional variations of the early Archean oceans; to potentially illuminate early Archean atmospheric composition and redox conditions; and to investigate the relationship between mantle dynamics and hydrothermal vents at the surface during the Archean. Scientists also found fossilized evidence for subseafloor microbes that are nearly 3.4 billion years old (Furnes et al., 2004; Furnes et al. 2008; Fliegel et al., 2010). These are the oldest known trace fossils on Earth and are perhaps ancient relics of its earliest ecosystems.

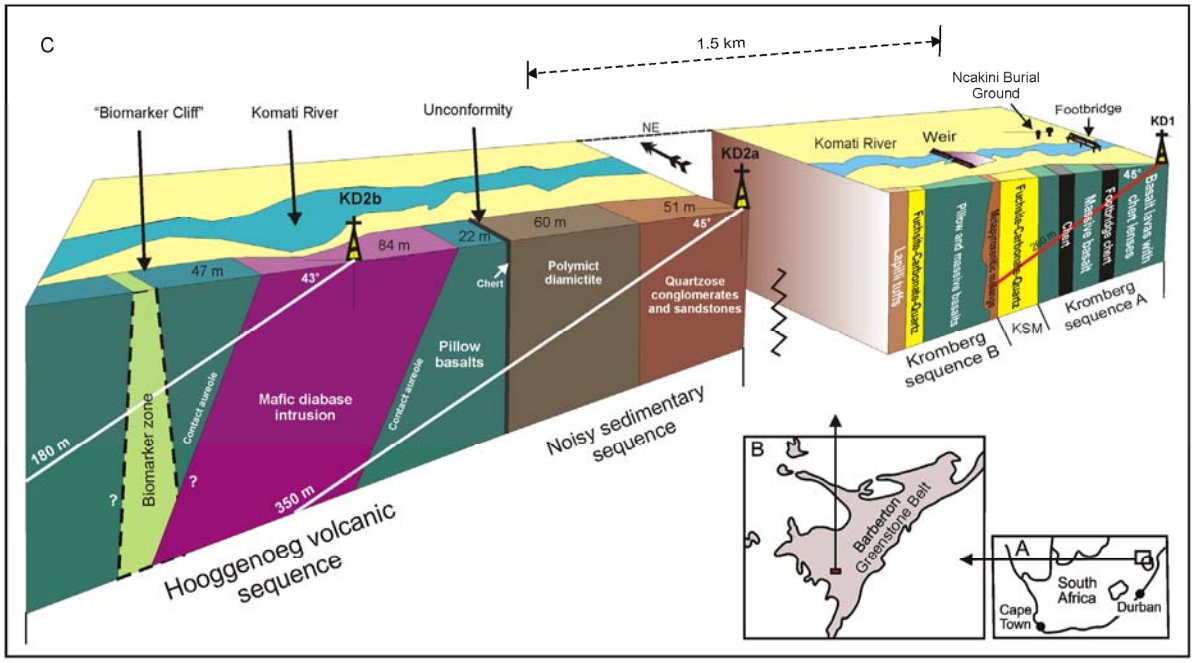

Figure 1.1. (a-b) Location of the study area in the Barberton Greenstone Belt, South Africa. **(c)** Three-dimensional block diagram with simplified geology along the Komati River depicting the positions and shallow drilling angles at drill sites KD1, KD2a and KD2b (GPS co-ordinates indicated in the text). Modified from Grosch et al., (2009a,b).

1.2. The First Hole: KD1

The primary objective of the first hole, KD1 (S26°02'15.3", E31°00'00.0", total depth of 261 m), involved drilling across the Kromberg type-section, which is representative of early

Paleoarchean oceanic sedimentary rocks, basaltic crust and ultramafic mantle (Figure 1.1). Drill hole KD1 includes seafloor cherts, basalt flows, coarse grained mafic intrusives, and pillow lavas that overlie a strongly banded, fuchsite (Cr-mica)-carbonate-quartz alteration zone within lower ultramafic rocks. This silicified zone, and similar such fuchsitic alteration zones beneath sedimentary chert horizons has been the subject of much debate in understanding the geologic evolution of the BGB (e.g. see Lowe and Byerly, 1999). The various interpretations of these silicified fuchsitic zones has bearing on the possible atmospheric conditions (Lowe and Byerly, 1986); oceanic seawater alteration regimes (e.g. Hanor and Duchac, 1990; Hoffman and Harris, 2008); geodynamic and stratigraphy models for the early evolution of the BGB (e.g. Lowe and Byerly, 1999; de Wit, 1982a; de Wit et al., 1982b, 1983; 2011); as well as ancient ecological niches that were once available for the emergence of early microbial life (e.g. de Wit, 1982a; de Wit et al., 1982b; Hofmann and Harris, 2008). However, there is currently only limited petrological data available on these silicified horizons in the BGB. The origin and petrogenetic history of these fuchsite-bearing zones are the focus of Chapters 4 and 5 as outlined in more detail below in Section 1.5. Geobiologists at the University of Bergen, aim to perform high resolution, in-situ laser- and ion- beam micro-spectroscopy of carbonaceous material and microtextures in the marine sedimentary cherts in search of geochemical and textural evidence for early microbial life. Detailed microscale to nanoscale analysis allows for a direct comparison of potential ecological niches in various Archean subseafloor environments; a test that has not been conducted previously. Sulphides (e.g. pyrite) are also present in various rock types throughout KD1 and will be studied by a high- resolution secondary ion microprobe (IMS 1280) to investigate mass- dependent and mass- independent sulphur isotope fractionation. Such multiple sulphur isotope data will help provide evidence of how microbial interactions evolved, particularly the early-mid Paleoarchean atmosphere-seawater sulphur cycle.

1.3. The Second Hole: KD2

The second drill hole, KD2, was completed in two parts in the Hooggenoeg volcano-sedimentary sequence, referred to as KD2a and KD2b (see Figure 1.1; KD2a, S26°01'50.0", E30°59'32.6" and KD2b, S26°01'25.3", E30°59'16.6"; total depths of 350 m and 180 m, respectively), to avoid a thick mafic intrusion. The main objective in drilling KD2a was to intercept at depth a basal unconformity between deep- water pillow lavas and an overlying

sequence of coarse to fine-grained clastic sedimentary rocks (diamictite, sandstones, and conglomerates). These rocks are the focus of Chapter 3 as outlined in Section 1.5 below. Field observations suggest that the top of the pillow lava pile was uplifted from deep- water conditions (possibly > 2 kilometres below sea level) and exposed to the early Archean atmosphere, possibly resulting in erosion of ~1500 meters of upper basalt during formation of the unconformity (see Figure 1.1). Geochronological constraints on the timing of this possible tectonic uplift, however, are not known. U-Pb analyses of detrital zircons from this sedimentary succession directly overlying the Hooggenoeg pillow lava sequence, is aimed at providing insight into the earliest sedimentary basin evolution of the BGB, as well as test for possible accretionary tectonic processes operating at that time. In addition, determining the depositional age of this sedimentary succession will constrain the age of the erosional unconformity as well as provide further reliable geochonological data to test current stratigraphy and geodynamic BGB models.

The underlying pillow lavas contain Archean biomarkers or trace fossils described by Furnes et al. (2004; 2008) from surface rocks in a location known as the “Biomarker Cliff” (Figure 1.1). Archean trace fossils have now also been found in drill core KD2b around 90 meters below surface in the continuation of the same pillow lava zone at depth. Thus, the rocks across the unconformity in KD2a and the bioalteration zone intercepted by KD2b will allow the application of several analytical techniques to determine the geochemical conditions of the early Archean hydrosphere-atmosphere and meteoric waters. The drill core will be used to investigate the possible responses of the ancient subseafloor microbial biosphere to possible exhumation of the pillow basalts. Rocks from KD2b are also the target of detailed petrological studies of bioalteration textures by Geobiologists in Bergen to evaluate spatial distribution and diversity of microbes in ancient subseafloor environments. Detailed geochemical investigations in KD2 not only serve to determine life-sustaining physiochemical conditions in early oceanic and continental crust, but they may also help scientists find textural and chemical evidence for early microbial life in extraterrestrial basalt, by far the most abundant rock type in the solar system. KD2b also penetrated metamorphosed pillow basalts in contact with a younger ~3.0- billion- year- old mafic intrusion (Figure 1.1). These thermally altered pillows metabasalts could potentially provide metamorphic geothermal information on mid-Paleoarchean contact aureoles along mafic intrusions, fluid-rock interactions along such contacts, the temperature of intrusive activity and availability of water in the Earth’s mantle at that time.

1.4. Drilling Methods

The drill rig was oriented perpendicular to the bedding or structural orientation of the lithological units, using the average strike and dip readings of rock outcrops at the site. Given the steep, generally vertical orientation of the geologic units, drilling for all three boreholes was carried out at the shallow angle of about 45° and a drilling direction towards 320° to 340° (Figure 1.1). Drilling at shallow angles raised a number of difficulties, including borehole wall collapses in the alluvial overburden. Due to frictional drag of the inner tube on the inside of the drill stem rods, the elapsed time between runs increased significantly as a consequence of the flat angle. The overshot instrument attached to the wireline for lowering the inner tube down the hole was modified with a heavy metal rod weight to overcome frictional energy downhole to shorten down time and to facilitate efficient latching of the inner tube onto the core barrel. The potentially delicate nature of bio-textures and chemical biosignatures (especially carbonaceous compounds) to be encountered made it vital not to alter the original Archean chemistry of the drilled rock. Furthermore, given that data on the redox state of the Archean atmosphere and seawater composition is one of the analytical goals, reducing oxidation was imperative. Therefore, a number of steps were taken during the drilling project to ensure that the original rock chemistry remained as intact as possible (see Figure 1.2a-d):

- Only clean water was used as drilling mud.
- A clean drill rig was used and repeatedly washed, and the site was kept clean of potential contaminants including smoke at all times.
- Only one person handled, washed, and dried all core immediately after retrieval.
- Cores were packed in wooden boxes with wood chips for support during shipping.

Core recovery for all three holes was typically above 98% providing up to 3-m rods of core (Figure 1.2). Only in the case of intercepting the first chert horizon in KD1, did core recovery temporarily drop to 92% due to partial fracturing of the chert. Initial stages of each hole involved emplacement of an HQ (63.5 mm diameter) size metal casing to stabilize the hole.

Water flow rate downhole generally varied at 30–33 L min-1. Optimum revolutions per minute were around 580, typical for basalts at a torque of around 3 kN. Given the flat 45° angle, the weight on the bit for the drill rig was adjusted to around 2–2.5 kN using a soft matrix NQ corebit (47.6-mm diameter). The very hard chert horizons were cored at 450 rpm. A core orientation tool was used to fix the drill core orientation in space.

Figure 1.2. (a) Plan layout of drill site KD2a illustrating the drilling angle of 45^{o}. **(b)** Image of the diamond coring drill bit used (47.6cm diameter) during clean drilling. Inner tube and core latch spring shown in the left of photo. **(c)** Typical 99% core recovery of intact rock achieved per 3 meter run during the drilling project. **(d)** Careful packing of drill core into boxes for temporary storage and transportation.

1.5. Thesis outline and objectives

The overall aim of this thesis is to determine the physical and chemical processes operating on the early Paleoarchean Earth as recorded in the Barberton Greenstone Belt of South Africa. The main objective is centred on critically testing geological evidence for Archean plate-tectonics in the BGB and the hydrothermal physico-chemical environments that were possibly available for sustaining early microbial life. In this regard, the thesis focuses on two of the BSDP drill core sections: (1) the lower part of KD1 across the fuchsite-carbonate-quartz alteration zone beneath two chert units in the upper Kromberg type-section (see Fig. 1.1 above) and (2) the basal unconformity and overlying coarse clastic sedimentary sequence

intercepted in KD2a. Novel questions are defined and new petrological data is provided from fresh, continuous drill core to address whether modern-day tectonic and oceanic hydrothermal processes were already in place at ca. 3.4 Ga in the BGB.

The thesis is a compilation of five first-author publications that have been, accepted for publication, under revision or currently being prepared for publication (please see Appendix A for publication list and status). The thesis includes three main data chapters, Chapters 3 to 5. Each of these chapters is based around a series of key scientific questions that are outlined below, the discussion and conclusions of each chapter are aimed at addressing each of these defined questions. A final synopsis chapter (Chapter 6) assimilates all of the new field and petrological drill core data and, in turn, discusses the implications for Earth's early geologic evolution, and tests current stratigraphic, geodynamic and Archean crustal hydrothermal models for the BGB.

Chapter 3: Paleoarchean U-Pb detrital zircon ages from drill hole KD2a

- Determine the depositional age of the earliest extensive succession of clastic sedimentary rocks in the Barberton Greenstone Belt by LA-ICP-MS analysis of detrital zircons.
- Does the range in U-Pb detrital zircon ages point to multiple sources on the Kaapvaal craton and if so, how can they be used to link various ancient gneissic terranes?
- Can the new U-Pb zircon ages provide stratigraphic constraints on specific geologic events (e.g. age of erosional unconformity, eruption time of pillow lava sequence, age of overlying fuchsite-carbonate-quartz horizons) and does the age data provide any evidence for tectonic accretion and proto-continent formation on the Kaapvaal craton at the time of deposition?
- Can the U-Pb age data provide insight into early Paleoarchean marine sedimentary basin evolution and possible microbial niches that may have been present at that time?

Chapter 4: *PT*-Constraints on the Metamorphic Evolution of the Paleoarchean Kromberg Type-section from drill hole KD1 and surface samples.

- Provide a detailed petrological analyses and characterization of the various altered mafic-ultramafic rocks, within stratigraphic context, across the Kromberg type-section, which is currently not available.

- Derive reliable estimates of metamorphic grade across the Kromberg type-section.
- Are any metamorphic field gradient(s) preserved and can a *PT*-time path be distinguished and reconstructed for the Kromberg? Is it possible to distinguish different low-grade to uppermost greenschist facies events in the Kromberg type-section?
- Determine the origin and reconstruct the petrogenetic history of the fuchsite-carbonate-quartz alteration zone in the central Kromberg type-section. What can these enigmatic and highly controversial rocks tell us about conditions on the early Earth?
- Do the fuchsite-carbonate-quartz alteration zones mark important structural and/or stratigraphic boundaries in the upper Onverwacht Group or do they simply represent very low temperature chemical weathering horizons in support of a continuous stratigraphy?
- Use the new metamorphic and petrological data to test current regional geodynamic models for the BGB. Does the new combined field and drill core data support the existence of horizontal plate tectonic-type processes in the early-mid Paleoarchean?

Chapter 5: Distinguishing Paleoarchean obduction- and seafloor- related silicification in the Barberton Greenstone Belt, South Africa: Implications for early life environments.

- Provide geochemical constraints on the protolith and geodynamic setting of the Kromberg mafic-ultramafic rocks.
- Determine the alteration extent and style of alteration within and surrounding the fuchsite-carbonate-quartz zone in the Kromberg type-section. How do they compare geochemically to other fuchsitic alteration zones beneath chert horizons in the BGB?
- To determine geochemically, the fluid origin of the carbonate-quartz veins/bands in the fuchsitic zone using stable and radiogenic isotope data.
- To better understand isotopic and geochemical fluxes between Archean oceanic crust, ancient seawater alteration and atmospheric reservoirs. Can the isotopic data help to further the understanding of fluid conditions and hydrothermal processes in this Archean environment?
- To test alteration and geodynamic models for silicification processes associated with the fuchsite-carbonate-quartz alteration zones regionally in the BGB. Can more than one type of silicification event be geochemically identified in the BGB?

- Is it possible to identify any biogeochemical fingerprints of early microbial life in the silicified fuchsitic alteration zones? Can the combined geochemical and metamorphic data from within these alteration zones help in identifying possible early life-sustaining environments that once existed in Paleoarchean BGB?

Chapter 2

Regional Geological Setting

Footbridge built by Paul Kruger (1910) and weir (further north) along the Komati River marking the approximate outcrop area of the Kromberg type-section, Barberton greenstone belt.

2.1. Regional geology and previous geochronology

The ca. 3.5-3.1 Ga Barberton Greenstone Belt forms part of the easternmost margin of the Kaapvaal Craton as a NE-SW trending tectono-metamorphic belt between northeasternmost Mpumalanga and Swaziland (Fig. 2.1). The overall structural geometry of the BGB comprises a NE-SW trending series of antiforms and synforms, with vertical to sub-vertical dipping bedding and cleavage surfaces (Fig. 2.1. e.g. Brandl et al., 2006). The BGB consists of a low-grade, supracrustal sequence of volcano-sedimentary rocks surrounded by tonalitic-trondhjemitic-granodioritic (TTG) gneisses and late potassic granites (Fig. 2.1 and 2.2). On a regional scale, it has generally been sub-divided into four, diachronous, fault-bounded proto-continental blocks that each record early magmatism and sedimentation, but are interpreted to have only been tectonically amalgamated between 3223 and 3227 Ma (see Fig. 2.2; and Lowe, 1994; 1999). These include: (1) the oldest Steyndorp Block including the ca. 3509 ± 8 Ma Steynsdorp trondhjemitic gneiss; (2) the Songimvelo Block, including the south-central Onverwacht greenstones and the 3460-3437 Ma Stolzburg TTG complex; (3) the Umuduha Block in the north-central parts of the BGB; and (4) the 3227 Ma Kaap Valley Block north of the Saddleback-Inyoka Fault System (see Fig. 2.2; also Lowe, 1994; 1999 and refs therein).

The oldest rocks in the vicinity of the BGB and on the Kaapvaal craton belong to the Ancient Gneiss Complex (AGC) of Swaziland (e.g. Compston and Kröner, 1988; Hunter, 1973a; Kröner et al., 1989). The only exposure where the Ancient Gneiss Complex can be seen in direct contact with the BGB is along a major shear zone known as the Phophonyane Shear Zone (PSZ) in northwestern Swaziland (see Fig. 2.1 and 2.2 inset B; Schoene et al., 2008). The ca. 3509 ± 8 Ma Steynsdorp trondhjemitic intrusion contains inherited zircon xenocrysts dated at 3553 ± 4 Ma (Kröner et al., 1992; 1996), indicating a possible early crustal connection between the Steynsdorp Block and the Ancient Gneiss Complex. The Ancient Gneiss Complex occurs as greenstone enclaves to the east and southeast of the BGB and consists of ca. 3667 - 3200 Ma TTG gneisses, metasedimentary rocks, intermediate-to-felsic intrusions and anorthosites (Hunter, 1968; Jackson et al., 1987; Kröner and Tegtmeyer, 1994; Schoene et al., 2008).

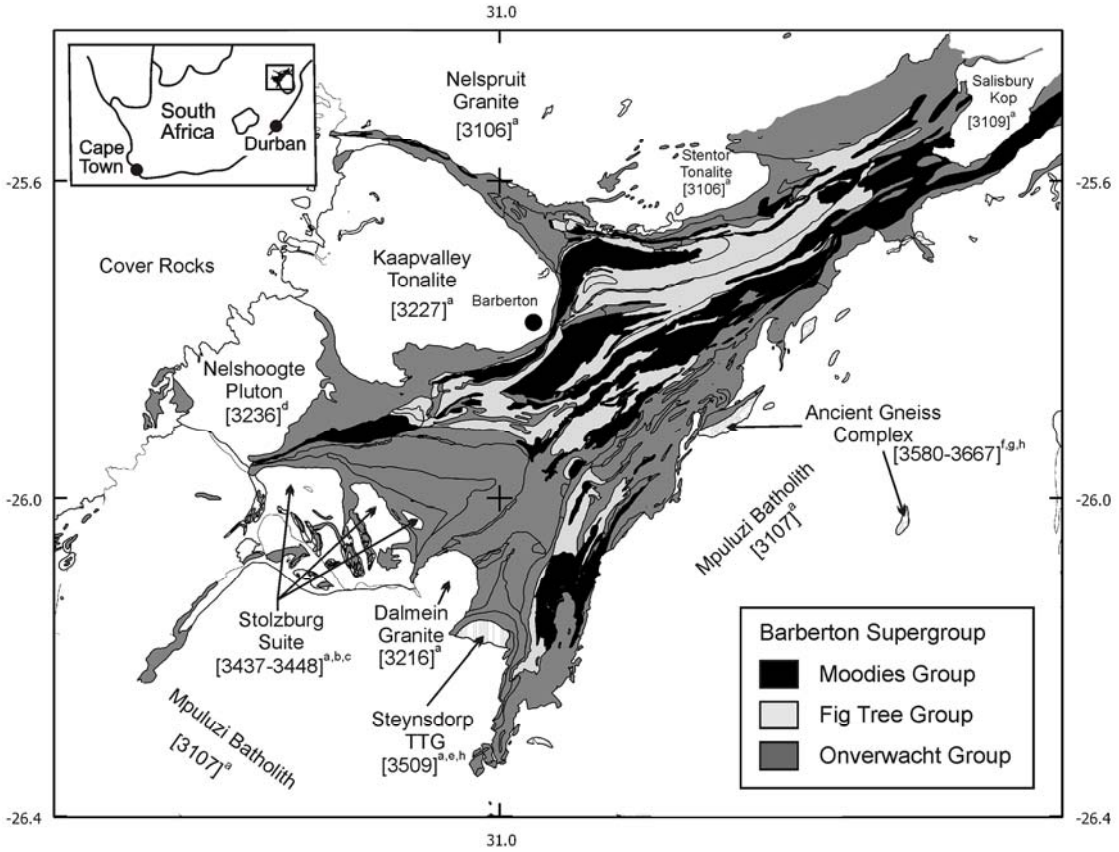

Figure 2.1. Regional geological map of the Barberton Greenstone Belt and the Ancient Gneiss Complex on the Kaapvaal Craton of South Africa (modified after Anhaeusser et al., 1983; Kamo and Davies, 1994). The 3 main groups of the Barberton Supergroup are indicated along with the surrounding granite-gneiss terranes and outcrops. Labelled U-Pb zircon ages for various surrounding TTG gneisses and plutons are referenced as follows: (a) Kamo and Davis (1994), (b) Armstrong et al. (1990), (c) Kroner et al. (1991), (d) De Ronde and Kamo (2000), (e) Kroner et al. (1996), (g) Compston and Kroner (1988), (f) Kroner et al. (1989) and (h) Schoene et al., (2008).

At least four major thermal-metamorphic-plutonic events have been recorded in the AGC by U-Pb zircon ages at > 3580, 3550-3504, 3433, and 3200 Ma (e.g. Compston and Kroner, 1988; Kröner et al., 1989; Schoene et al., 2008).

Contrasting stratigraphy models have been proposed for the dominant greenstone volcano-sedimentary sequences of the BGB. Some workers have argued for a continuous layer-cake, stratigraphy consisting of successive formations (Lowe and Byerly, 1999; 2007) whereas, others have argued for litho-tectonic 'complexes' bounded by major 3455 Ma shear zones (de Wit, 1982a; de Wit et al., 1982b; 1987a,b, 2011). These contrasting models are discussed and illustrated further below (see Section 2.2). Traditionally, in the continuous stratigraphy model, the low-grade supracrustal greenstone sequence is referred to as the Barberton Supergroup and consists of 3 groups shown in Fig. 2.1 - 2.2: the mafic-ultramafic (ca. 3530-3334 Ma) Onverwacht, the argillaceous (ca. 3258 - 3226 Ma) Fig Tree, and the arenaceous (ca. 3230 - 3110 Ma) Moodies Groups (e.g. Viljoen and Viljoen, 1969a; Brandl et al., 2006; Lowe and Byerly, 1999, 2007).

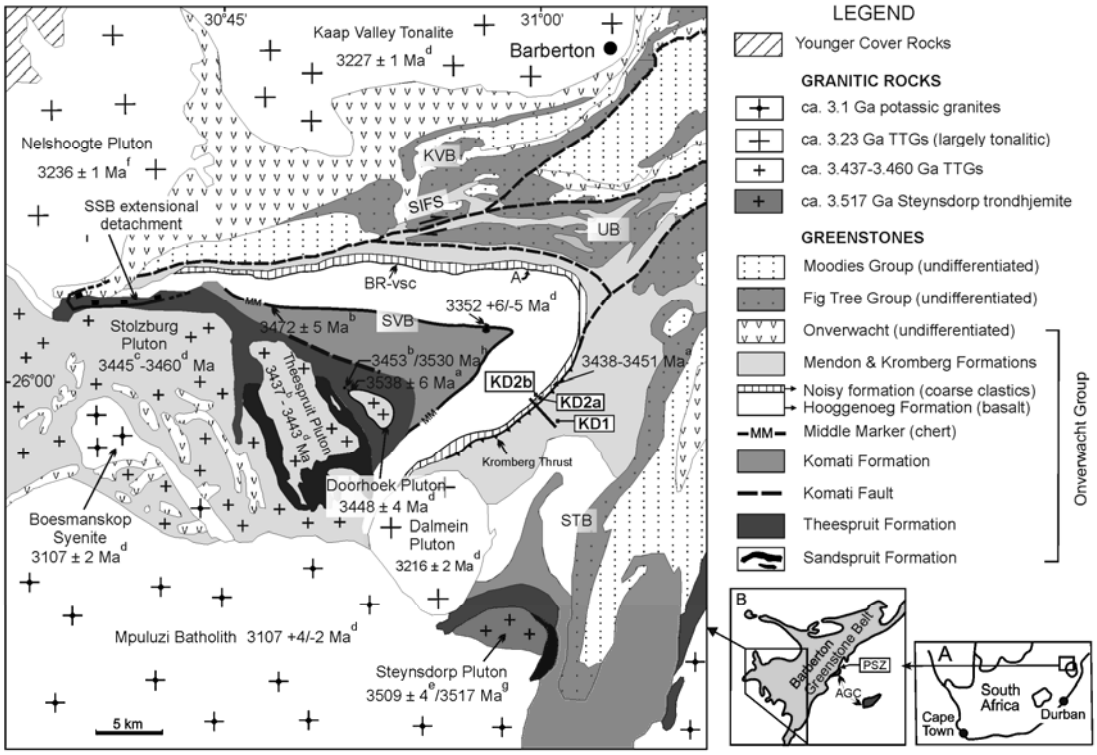

Figure 2.2. Regional geological map of the southwestern part of the Barberton Greenstone Belt (BGB) indicating the greenstone stratigraphy and granitoid rocks around the Onverwacht Antiformal Fold (modified after Anhaeusser et al., 1983). All of the BSDP drill sites are shown on the map. The four tectonostratigraphic domains of Lowe

(1994, 1999) for the BGB are indicated: STB = Steynsdorp Block, SVB = Songimvelo Block, UD = Umuduha Block and KVB = Kaap Valley Block. The location of the Phophonyane Shear Zone (PSZ) and the Ancient Gneiss Complex (AGC) on the Kaapvaal Craton relative to the BGB is shown in inset B. Labelled U-Pb zircon ages for various rock types are referenced as follows: (a) Kröner and Todt (1988), (b) Armstrong et al. (1990), (c) Kröner et al., (1991), (d) Kamo and Davies (1994), (e) Kröner et al., (1996), (f) de Ronde and Kamo (2000), (g) Schoene et al., (2008), (h) Van Kranendonk et al., (2009). SIFS = Saddle-Inyoka Fault System. BR-vsc = Buck Reef volcano-sedimentary complex.

The Onverwacht Group has been further subdivided into a lower dominantly komatiitic unit (Tjakastad Subgroup) and an upper mafic-to-felsic unit (Geluk Subgroup) that are separated by the Middle Marker Chert dated at 3472 Ma (Viljoen and Viljoen 1969a,b; Armstrong et al. 1990). Within each subgroup, three formations are recognized with a total estimated stratigraphic thickness of c.15 km. The lower part of the Geluk Subgroup is the focus of this thesis and consists traditionally of Hooggenoeg, Kromberg and Swartkoppie (or Mendon) Formations. The BSDP targeted some of the best exposures of this subgroup in the SW part of the BGB in the Onverwacht Antiformal Fold (OAF, Fig. 2.2).

The oldest formations in the Onverwacht Group are the variably deformed Sandspruit and Theespruit Formations of the Tjakastad Subgroup (Fig. 2.1; Viljoen and Viljoen, 1969a). The structurally oldest, undated Sandspruit Formation consists of metamorphosed komatiitic-basaltic rocks and minor metasedimentary units. The Theespruit Formation contains aluminous schists, felsic volcanics, volcaniclastics, komatiites and komatiitic basalts. A felsic volcaniclastic unit was initially reported to indicate a maximum depositional age of 3453 ± 6 Ma (Armstrong et al., 1990) however, subsequent mapping and geochronological work has argued for a much older depositional age of ca. 3530 Ma for the Theespruit Formation (Kröner et al., 1996; Van Kranendonk et al., 2009). In the oldest Steynsdorp Block of Lowe (1994; 1999), a felsic schist yielded an older age of 3547 ± 3 Ma for the Theespruit Formation surrounding the ca. 3509 Ma

Steyndorp trondhjemitic gneiss (Kröner et al., 1992; 1996). The Theespruit and Sandspruit are separated from the overlying Komati Formation by a major east-west trending, 1 km wide, fault-bounded structural discontinuity, known as the Komati Schist Zone (KSZ) or Komati Fault (Fig. 2.2). The Komati Formation comprises a continuous succession of peridotitic and basaltic komatiities and basalts (e.g. Dann, 2000; Viljoen and Viljoen, 1969a). A review on the petrogenetic origin of the komatiites is provided in Parman and Grove (2004). Ar-Ar dating of the komatiites and komatiitic basalts gives plateau ages between 3450 and 3490 Ma, believed to represent hydrothermal metamorphic ages of actinolite growth (López-Martinez et al., 1992). Zircons in volcaniclastic interflow sediments in the mid-lower Komati yielded an age of 3472 ± 5 Ma (Armstrong et al., 1990; also Kamo and Davis, 1994) and 3482 ± 2 Ma (unpublished data of S. Bowring, referred to in Dann, 2000).

The base of the Hooggenoeg is marked by the major 3472 ± 6 Ma Middle Marker Chert (e.g. Armstrong et al. 1990; see Fig. 2.2 and 2.3) which overlies the Komati Formation. The lower Hooggenoeg is dominated by tholeiitic and komatiitic basalts with numerous interlayers of cherts, whereas the upper part consists of thick felsic (dacitic to rhyodacitic) intrusions and volcaniclastic sediments (see Fig. 2.3; e.g. Viljoen and Viljoen, 1969a). These felsic intrusions, felsic volcaniclastic conglomerates, sandstones and tuffs have been termed the H6 upper unit of the Hooggenoeg Formation (Lowe and Knauth, 1977; Lowe and Byerly, 1999; see also Fig. 2.2) and have yielded U-Pb zircon ages of between 3416-3455 Ma (see Figs. 2.2 and 2.3; e.g. de Wit et al., 1987a; Byerly et al. 1996; Kröner et al., 1991; de Vries et al., 2006). The shallow level felsic intrusions intruding the Hooggenoeg Formation have been argued to be co-magmatic with the ca. 3460-3437 Ma Stolzburg TTG complex (Fig. 2.2 and 2.3; de Wit et al., 1987a,b; Armstrong et al., 1990) and occur in the Songimvelo Block of Lowe et al., (1994; 1999) in the southwesternmost part of the BGB (Fig. 2.2). This complex felsic unit has also recently been referred to as the Buck Ridge volcano-sedimentary complex (BR-vsc) of the upper Hooggenoeg Formation (see Fig. 2.2 and 2.3; de Vries et al., 2006; 2010). Together with age constraints from volcaniclastic interflow sediments, these felsic rocks mark a major phase of magmatism in the BGB generally referred to as the ca. 3480-3437 Ma Onverwacht magmatism (e.g. Kamo and Davis, 1994).

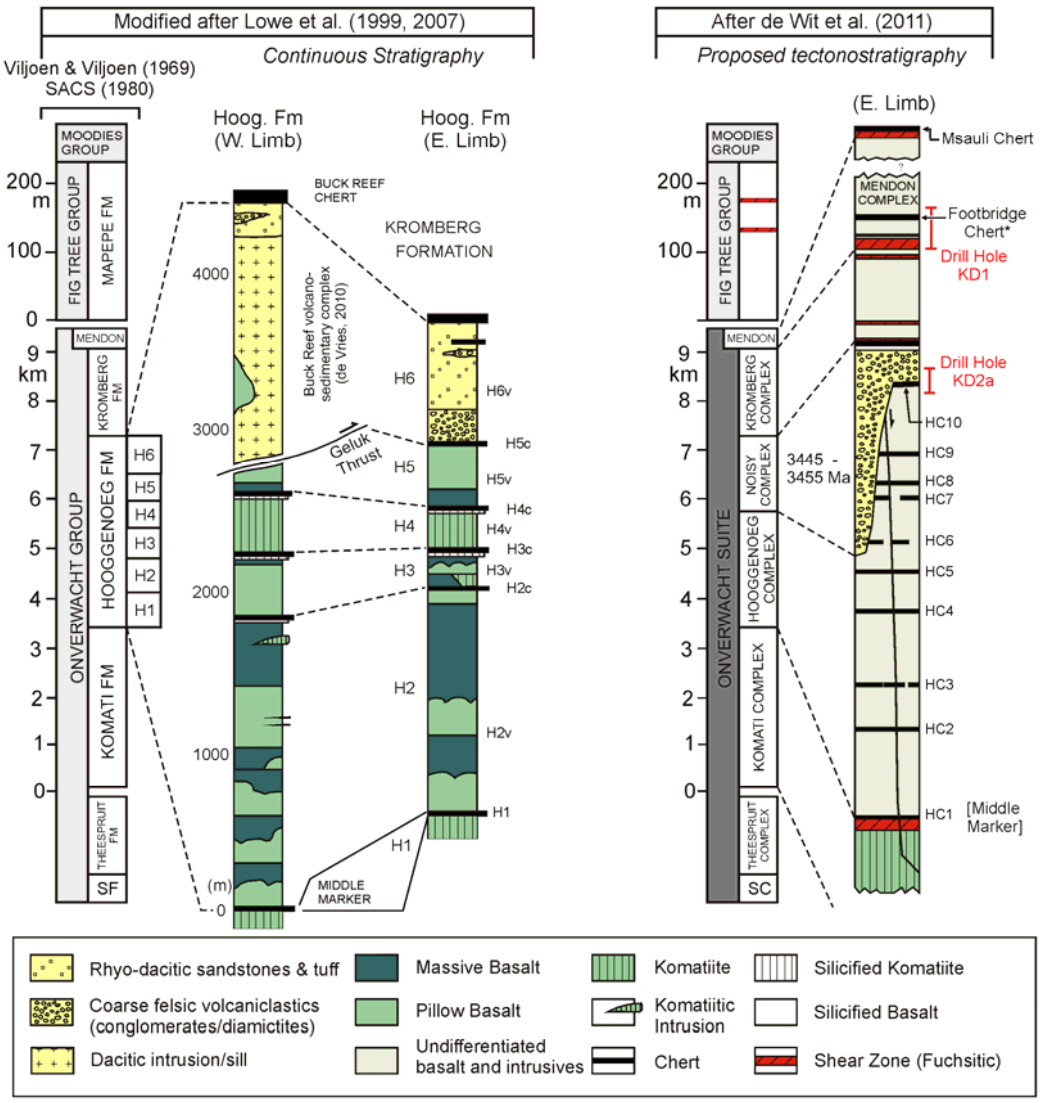

Figure 2.3. Stratigraphy models for the upper Onverwacht, Barberton Greenstone Belt, focussing on the uppermost Hooggenoeg Formation and the Noisy formation on the eastern and western limbs of the OAF (compiled and modified with data from Lowe and Byerly, 1999, 2007; de Wit et al., 2011, Furnes et al., 2011). Continuous stratigraphy for the Hooggenoeg Formation and uppermost sediments as mapped Lowe and Byerly (1999, 2007) also Viljoen and Viljoen (1969) for the SE and NW limbs of the Onverwacht Fold is shown on the left hand panel. This is contrasted with the 'complexes' in a tectonostratigraphy model as mapped on the SE limb by de Wit et al., (2011). Location of the drill holes KD1 and KD2a,b are indicated in the stratigraphy on the eastern limb of

the OAF. The unconformity between the Noisy formation and the underlying basalts is shown on the right hand panel with clast composition shown for major diamictite basal horizons. [SF] = Sandspruit Formation, [SC] = Sandspruit Complex, [Hv] = Hooggenoeg volcanic (mafic-ultramafic), [HC] = Hooggenoeg Complex.

Traditionally, the H6 unit on the NW limb has been correlated with coarse sedimentary rocks containing mostly rhyo-dacitic clasts on the SE limb of the OAF (Fig. 2.2 and 2.3; e.g. de Wit et al, 1987a,b; Kröner and Todt 1988; Compston and Kröner, 1988; Armstrong et al., 1990; Lowe and Byerly, 1999). On the SE limb, a recent study of a felsic tuff horizon contained within the sedimentary pile has yielded a U-Pb zircon age of 3455 ± 8 Ma and this was interpreted as the maximum depositional age for these sedimentary rocks and the underlying unconformity (Biggin et al., 2011). This tuff age has been used to correlate the sedimentary rocks on the SE limb (referred to as the Etimanbeni section by de Wit et al. 2011) with the felsic BR-vsc of de Vries et al. (2006) on the NW limb and furthermore, to argue that they form a single "conterminous litho-tectonic complex" referred to as the "Noisy Complex" (see Fig. 2.3; and de Wit et al., 2011). On the other hand, Biggin et al. (2011) has informally referred to the same sedimentary sequence as the Noisy *f*ormation. Chapter 3 of this PhD study focuses on these coarse-grained sedimentary rocks intercepted by drill hole KD2a on the SE limb of the OAF (see Figure 2.3), and for simplicity we will also informally refer to these rocks as the Noisy formation (see Fig. 2.3).

On the western limb of the OAF the Hooggenoeg Formation is overlain by the mostly mafic to ultramafic rocks of the Kromberg Formation (see Fig. 2.2 and 2.3). Whereas on the eastern limb de Wit et al., (1987a,b) has argued that a thrust zone separates the Hooggenoeg Formation from the Kromberg Formation (see Fig. 2.2). The type-section of the Kromberg Formation occurs on the eastern limb of the OAF along the Komati River and was originally described as consisting of mafic and felsic lavas, pillow breccias, volcanic debris, cherts and shales (Viljoen and Viljoen, 1969). Subsequently, Lowe and Byerly (1999) described the type-section of the Komati Formation along the Komati River as consisting of 1700m of volcanic and sedimentary rocks with three main

lithofacies characterized from bottom to top as: (1) massive and pillowed basalt, (2) mafic lapilli tuff and lapillistone, and (3) black and banded chert, known as the Footbridge Chert (3334 Ma, Byerly et al., 1996). Early workers identified a fuchsite-carbonate-quartz zone in the central Kromberg type-section that was interpreted as silicified tuffs (Viljoen and Viljoen, 1969), or low temperature weathered komatiities (Lowe and Byerly, 1986). A detailed stratigraphic outcrop and description of drill core KD1 across this type-section of the Kromberg, is presented in Chapter 4 and 5. The stratigraphic location of KD1, intercepting the Footbridge Chert and the fuchsite-carbonate-quartz alteration zone, is indicated in Figure 2.3. On the western limb of the Onverwacht Antiform, the Hooggenoeg Formation is overlain by the 350m thick Buck Reef Chert at the base of the Kromberg Formation with the lowermost unit reported to consist of shallow water sediments and evaporites (Lowe and Byerly, 1999).

In the more central parts of the BGB, Lowe and Byerly (1999) have assigned an approx. 1000m succession of massive komatiitic lavas and cherts that occur above the Footbridge Chert, and below the non-silicified clastic units of the younger Fig Tree Group, to the Mendon Formation. Five volcano-sedimentary successions have been described within the Mendon Formation, each consisting of a sequence of komatiitic lavas that is overlain by silicified komatiitic volcaniclastic rocks, with or without banded cherts (Lowe and Byerly, 1999). The uppermost unit of the Mendon Formation consists of the 20-35m thick Msauli Chert unit that is underlain by silicified ultramafics in a fuchsite-carbonate-quartz alteration zone (e.g. Lowe and Byerly, 1986; 1999; Ducaq and Hanor, 1987; Hanor and Ducaq, 1990; de Wit et al., 2011).

In their stratigraphic model, Lowe and Byerly (1999) suggested a new northern unit in the Onverwacht Group, north of the Inyoka Fault, namely the Weltevreden Formation, consisting predominantly of altered peridotitic and basaltic komatiite. Four principal lithologies have been characterized, including komatiitic rocks, layered ultramafic intrusive rocks, komatiitic tuffs and black and banded chert (Lowe and Byerly, 1999). These workers argued that the Weltevreden Formation can probably be correlated with the upper cyclic units of the Mendon Formation that occurs to the south of the Inyoka Fault.

2.2. Structural geology and geodynamic models

The geodynamic evolution of the Barberton Greenstone Belt remains a highly controversial and still largely unresolved subject (e.g. see de Wit et al., 1998 versus Hamilton, 1998; Lowe and Byerly, 1999; Van Kranendonk et al., 2009; Anhaeusser, 2010). Various crustal evolution models have been proposed for the BGB that have differing implications for the nature and style of geodynamic processes that were operating in the early Paleoarchean. Interpretations range from plume-type, vertical dominated crust-mantle processes, such as convective overturn (e.g. Anhaeusser, 1973; 2010; Van Kranendonk et al. 2009), to plate-tectonic type, 'hovercraft' crustal translations involving overthrust glide planes (de Wit et al., 1982b; 1983; 1987a,b, 2011). These early Paleoarchean geodynamic models are reflected in contrasting stratigraphy models for the BGB, which are summarized in Figure 2.4.

Three main deformation events (D_1 to D_3) are reported in the BGB (Brandl et al., 2006 and references therein). Although the geological evidence for a major phase of deformation recording thrusting and folding (D_2) during subduction and major felsic magmatism at around 3223 - 3229 Ga has been well characterized (e.g. Lowe and Byerly, 1999a,b; de Ronde and Kamo, 2000; Moyen et al., 2006; Schoene et al., 2008), evidence for an early D_1 deformation event at around 3455 Ma in the BGB has remained highly controversial (e.g. de Wit, 1998 versus Hamilton, 1998; Van Kranendonk et al., 2009). Workers challenging a continuous stratigraphy for the BGB have argued that banded fuchsite-carbonate-quartz rocks in the Kromberg type-section on the SE limb of the OAF (see Fig. 2.3 and 2.4) are early D_1 shear zones or "overthrust glide planes" and represent "quartz-carbonate-talc-fuchsite schists/gneisses" or "flaser-banded tectonites" (Fripp et al., 1980; de Wit, 1982a; de Wit et al., 1982b; 1983; 1986a,b, 1987a,b; Armstrong et al., 1990; de Ronde and de Wit, 1994; de Wit, et al., 1992, 2011). Moreover, these zones have been interpreted to mark duplication in the stratigraphy (e.g. de Wit and de Wit et al., 1982a,b; 1983, 1986a,b, 1992; 2011). De Wit et al., (2011) recently proposed a new tectonostratigraphy model for the BGB (see summary Figure 2.3) and have argued that all fuchsite-carbonate-quartz zones beneath chert horizons in the BGB represent shear zones, possibly oceanic 'glide planes' (e.g. de Wit, 1982a, de Wit et al., 1982b; 1987a,b; 2011).

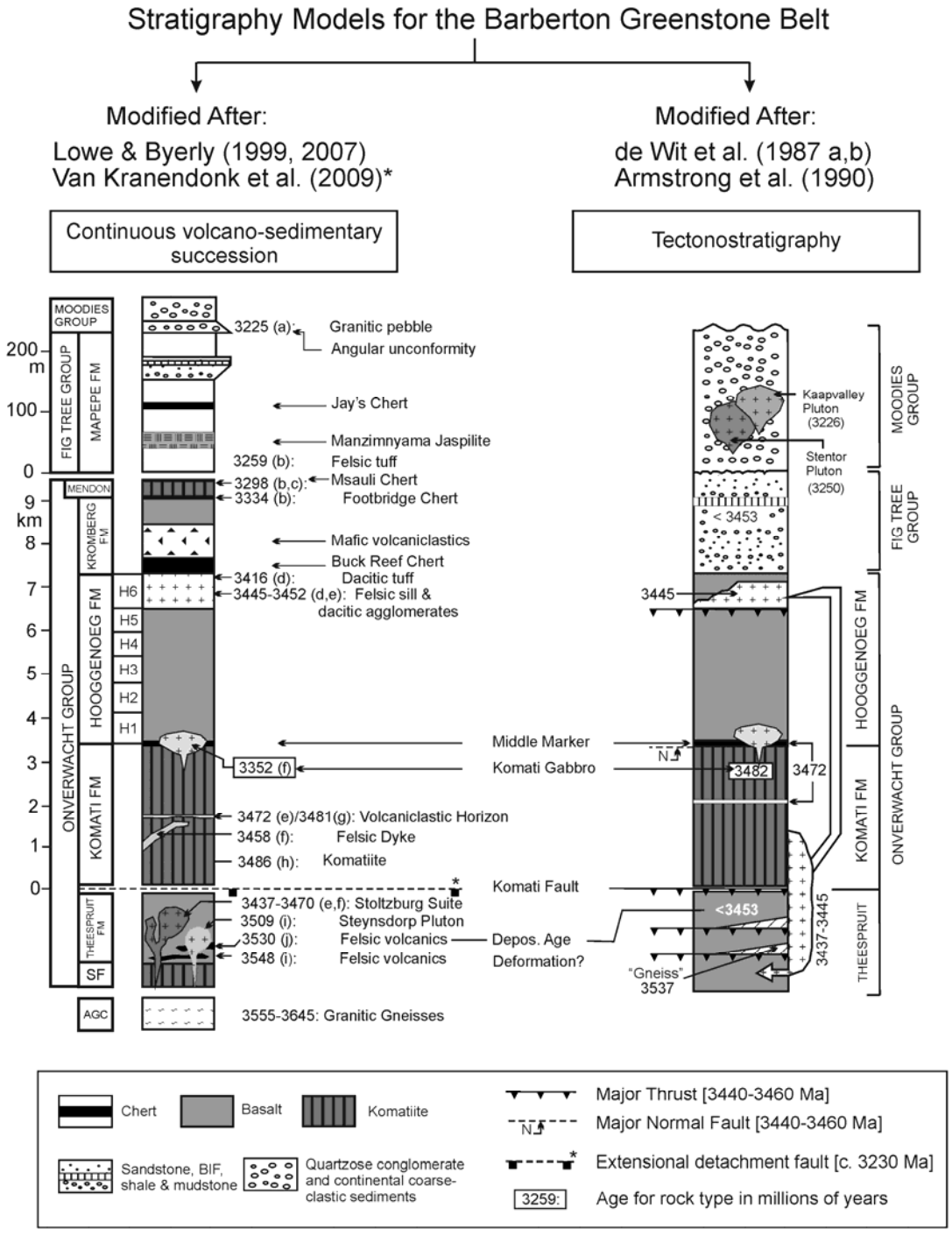

Figure. 2.4. Comparison between regional stratigraphy models for the BGB. A review of the tectonostratigraphy versus continuous stratigraphy models along with the geochronological age constraints is given in the text. References for the U-Pb age data

are labeled as follows: (a) Tegtmeyer and Kroner (1987), (b) Byerly et al., (1996), (c) Byerly et al., (1993), (d) Kroner et al.,(1991), (e) Armstrong et al., (1990), (f) Kamo and Davis (1994), (g) Dann (2000), (h) Lopez-Martinez et al., (1992), (i) Kröner et al. (1996) and (j) Van Kranendonk et al. (2009).

These include, for example, fuchsitic alteration zones beneath the Msauli Chert, the zone in the central Kromberg type-section, and an alteration zone beneath the Middle Marker Chert (see Figure 2.3 and 2.4). The timing of deformation within these proposed shear zones has not been directly dated, but some workers have argued on the basis of field relationships for early gravity-induced, overthrusting along silica-rich glide planes at 3455 Ma during intra-oceanic 'hovercraft-type' tectonics (de Wit, 1982a; de Wit et al 1982b; 1987a,b; 1992, 2011).

Early D_1 deformation has also been inferred in one model to have occurred along the east-west Komati Schist Zone (KSZ), involving thrusting of an older 3482 Ma Komati Formation over a younger 3453 Ma Theespruit Formation (see Fig. 2.2 -2.4, and also de Wit et al., 1983, 1987a,b; Armstrong et al., 1990; de Ronde and de Wit, 1994). The timing of the D_1 deformation is not well constrained but inferred to have been associated with intense TTG calc-alkaline plutonism dated at around 3445 Ma that intruded into the lower Theespruit and Sandspruit Formations (see Fig. 2.4**;** de Wit et al., 1987a; Armstrong et al., 1990). These workers have invoked an ophiolite-type geodynamic model, and referred to the rock units in the Onverwacht Group as belonging to a 'Jamestown Ophiolite Complex' (e.g. de Wit et al., 1987a,b; 2011). However, subsequent geochronological work by Kröner et al. (1996) has shown that, at least in the Steynsdorp area, the Theespruit is about 100 million years older than the equivalent rocks reported by Armstrong et al. (1990). In a more recent geochronological study, the complete Theespruit Formation and KSZ was re-examined and the depositional age of the Theespruit Formation was reported as ca. 3530 Ma, and the younger age of 3453 Ma reported by Armstrong et al. (1990) was reinterpreted to be of metamorphic origin (see Van Kranendonk et al., 2009). This new data argued against an older-over-younger thrust

relationship between the Komati and Theespruit Formations (Van Kranendonk et al., 2009).

In a separate study, Kamo and Davies (1994) argued on the basis of U-Pb age data of various rocks in the BGB, that although early oceanic rifting and extension may have been possible, their data did not support a model of early ~3.45 Ga oceanic 'glide plane overthrusting' as proposed by de Wit (1982a,b; 1986b). They indicated that major thrusting and compressional deformation occurred only much later between 3230 – 3215 Ga (Kamo and Davis, 1994). In addition, a gabbro intrusion that cross-cuts the Middle Marker Chert and intruded into the lower Hooggenoeg yielded an igneous baddeleyite crystallization age of 3352 ± 6 Ma (Kamo and Davies, 1994). This indicated that some of the intrusive rock units comprising the proposed 'Jamestown Ophiolite Complex' were 100 million years apart in age, arguing against an ophiolite-type model.

The D_2 phase of deformation and tectonic accretion is generally believed to have resulted in thrusting and folding of much older 3455 - 3530 Ma oceanic rocks during a protracted period of time of ~3 million years between 3223 and 3229 Ma (Kamo and Davis, 1994; de Ronde and Kamo, 2000; Lowe and Byerly, 1999, 2007). This phase of deformation occurred as NW-directed compression that coincided with deposition of the Fig Tree and Moodies Groups and the intrusion of another phase of TTG plutons, namely the Kaap valley and Nelshoogte tonalitic plutons at 3227 Ma (Kamo and Davis, 1994; de Ronde and Kamo, 2000). The D_2 resulted in vertical mostly isoclinal folding and NE-SW oriented thrust faulting and ultimately, final amalgamation of the northern and southern parts of the BGB along the Saddleback-Inyoka fault system (de Ronde and de Wit, 1994: Ronde and Kamo, 2000; Schoene et al., 2008).

A late-stage D_3 deformation event is argued to represent a transtensional to extensional event. Lower and upper limits of this phase are constrained by the deformation of porphyry dykes (3126 Ma) and the formation of hydrothermal rutile (3084 Ma); respectively. The hydrothermal rutile is associated with gold mineralization that occurs in shear-zone that truncates early D_2 shear structures (de Ronde et al., 1991). Final tectonic stabilization of the belt was associated with intrusion of large volumes of anorogenic sheet-like potassic granites at ca. 3100 Ma including the Nelspruit, Mpuluzi and Heerenveen batholiths (e.g. Anhaeusser and Robb, 1983; Robb et al., 1983; de Wit et

al., 1992; Kamo and Davis, 1994; Schoene et al., 2008). These granitic batholiths record a deformational fabric (Westraat et al., 2005; Belcher and Kisters, 2006) which probably coincides with the shear-zone and the gold mineralization of D_3 (de Ronde et al., 1991). Since that time, the BGB has been relatively little disturbed, thermally and tectonically (e.g. Schoene et al., 2008).

2.3. Previous metamorphic constraints in the BGB

High-grade metamorphic conditions have been reported from within and in the immediate vicinity of the Stolzburg TTG granitoid-gneiss terrane (see map Fig. 2.21 - 2.2) with T = 550-700^{o}C and P = 6-15kbar (e.g. Dziggel et al., 2002; Stevens et al., 2002; Diener et al., 2005; Moyen, 2006). These high-grade conditions are generally interpreted to be related to 3.23 Ga (D_2) major deformation phase in the BGB. These high-grade *PT*-constraints are contrasted with the observed low-grade conditions for the BGB greenstone sequence. At least four types of low-grade greenschist facies metamorphism have been proposed for the BGB: contact metamorphism related to early intrusive activity (Viljoen and Viljoen 1969a,b; Anhaeusser, 1969; Anhaeusser, 1973); regional low-grade metamorphism (Xie et al., 1997; Tice et al., 2004); seafloor hydrothermal alteration (de Wit, 1982a; de Wit et al., 1982b; 1983, 1987a,b; Ducaq and Hanor, 1987; Hanor and Ducaq, 1990; Lopez-Martinez, 1992; de Ronde and de Wit, 1994; Hofmann and Harris, 2008); and burial metamorphism (Cloete, 1991; Cloete, 1999). Some of these proposed metamorphic types are based largely on mineral assemblages observed in the field and constraints on the timing of these proposed low-grade events are lacking or very sparse (e.g. Lopez-Martinez, 1992). A regional metamorphic temperature estimate of ~320^{o}C has been derived by applying traditional empirical chlorite thermometry relations to a range of basalts, dacites and ultramafics from the upper Onverwacht Group (Xie et al., 1997; Cloete, 1991, 1999). Regional metamorphic conditions of ~315^{o}C have also been argued for by Tice et al. (2004) using Raman spectroscopy on organic carbon in various Onverwacht chert horizons.

Proponents of a continuous stratigraphy for the BGB, and only later D_2 deformation, have argued that banded fuchsite-carbonate-quartz rocks beneath chert horizons, such as that in the central Kromberg type-section, do not represent a major break in the Onverwacht Group stratigraphy but rather, very low temperature (60^{o}C) subaerial chemical weathering zones on the tops of komatiitic flows (Lowe and Byerly, 1986; Lowe and Byerly, 1999a,b, 2007), or low temperature silicification (75-150^{o}C) during Archean seawater alteration that record trace element enrichments in LREE's and LILE's (Ducaq and Hanor, 1987: Hanor and Ducaq, 1990, Hofmann and Harris, 2008). This interpretation is similar to that of early workers, who also argued for an intact stratigraphy and that the fuchsite-carbonate-quartz rocks represent altered silicified tuffs (Viljoen and Viljoen, 1969a,b; Anhaeusser, 1973). The fuchsite-carbonate-quartz alteration zone in the central Kromberg type-section is investigated petrologically in Chapter 4 and 5 of this thesis. The new petrological data from within this horizon is aimed at addressing a range of current debates surrounding these fuchsitic alteration zones in the BGB.

Chapter 3

Paleoarchean detrital zircon ages from the earliest tectonic basin in the Barberton Greenstone Belt, Kaapvaal craton, South Africa.

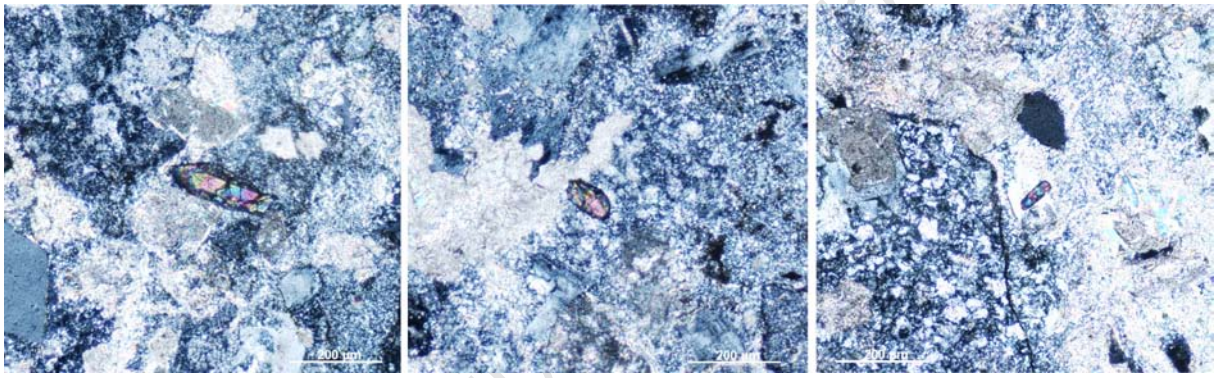

Spectrum of Paleoarchean detrital zircon sizes and morphologies (centre of each panel) ranging from angular to rounded, contained within diamictite matrix of the ca. 3432 Ma Noisy formation, Barberton Greenstone Belt.

3.1. Introduction

The ca. 3.2-3.5 Ga Barberton greenstone belt (BGB) of the Kaapvaal craton, South Africa consists of some of the world's best preserved Paleoarchean volcanic and sedimentary rocks (Viljoen and Viljoen, 1969a,b). The BGB has been argued to be a composite greenstone belt consisting of a number of fault-bounded terranes or 'blocks' that young towards the north, with each block recording diachronous phases of magmatic activity at 3550-3440 and 3223-3228 Ma (Lowe, 1994; 1999, Poujol et al., 2003). The Ancient Gneiss Complex (AGC), occurs in direct structural contact with the BGB in northwestern Swaziland (Fig. 2.1, Chapter 2) and contains the oldest rocks yet identified in the Kaapvaal craton (e.g. Compston and Kröner, 1988; Schoene et al., 2008). Together, the BGB and AGC constitute the oldest crustal nucleus of the Kaapvaal craton. Although tectonic accretion and clastic sedimentation on the Kaapvaal craton has been well characterized between the various terranes of the BGB and the Ancient Gneiss Complex at ca. 3227 Ma (e.g. Lamb, 1984; Jackson et al., 1987; de Ronde and de Wit, 1994; Heubeck and Lowe, 1994a,b; Lowe, 1994, 1999; Moyen et al., 2006; Poujol et al., 2003; Schoene et al., 2008, 2009) evidence for earlier crustal connections and plate-tectonic processes has remained obscure and highly controversial (e.g. Hunter, 1974; Condie and Hunter, 1976; Kröner and Todt, 1988; de Wit et al., 1992; 2011; Lowe, 1999; Van Kranendonk et al., 2009). Numerous studies have reported $^{207}Pb/^{206}Pb$ zircon ages from major shear zones and granitoids within and surrounding the BGB (e.g. Armstrong et al., 1990; Kamo and Davis, 1994; Diener et al., 2005; Schoene et al., 2008) but, in contrast, detrital geochronological constraints on the earliest Archean BGB sedimentary sequences are sparse (e.g. see Kröner and Todt, 1988, Van Kranendonk, 2009).

This study is located in the Kromberg area on the southeastern limb of the Onverwacht Antiformal Fold (OAF) in the BGB and focuses on sedimentary rocks that overlie pillow lavas of the Hooggenoeg Formation, the upper Onverwacht Group (Fig. 3.1 and map in Fig. 2.2). This is the stratigraphically lowest sequence of clastic sedimentary rocks in the greenstone belt and comprise diamictites, sandstones, siltstones and minor felsic tuff horizons that have traditionally been assigned to the H6 unit of the upper Hooggenoeg Formation (Lowe and Byerly, 1999, 2007; see Fig. 3.1), but will here be referred to as the Noisy formation (see explanation in Chapter 2 and further discussion below in Section 3.5). A detailed U-Pb detrital zircon analysis of this early BGB sedimentary sequence may thus, hold important insights into the geologic evolution of the BGB.

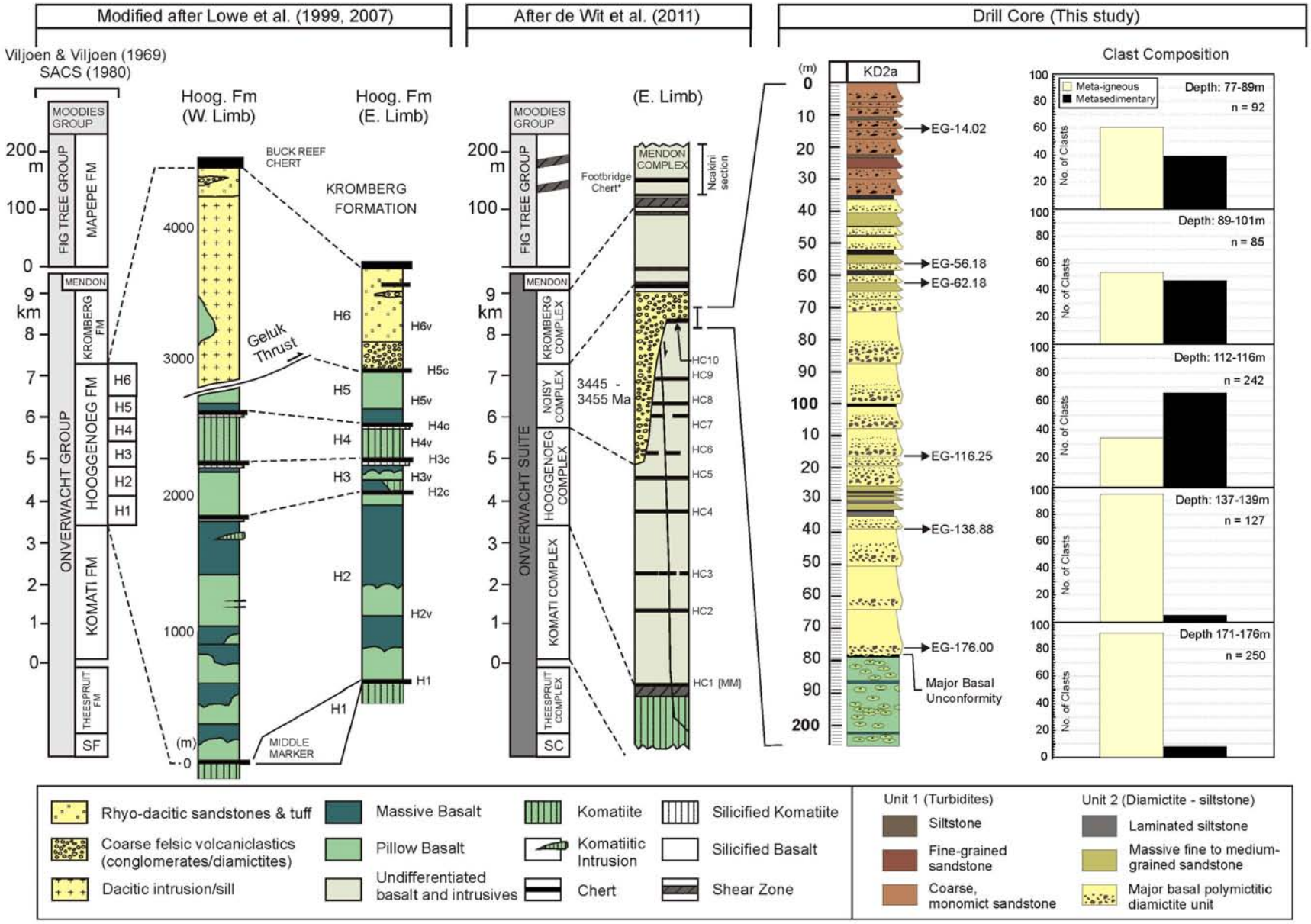
Modified after Lowe et al. (1999, 2007)
After de Wit et al. (2011)
Drill Core (This study)
Viljoen & Viljoen (1969)
SACS (1980)
Hoog. Fm
(W. Limb)
Hoog. Fm
(E. Limb)
(E. Limb)
MOODIES GROUP
FIG TREE GROUP
MAPEPE FM
ONVERWACHT GROUP
MENDON
KROMBERG FM
HOOGGENOEG FM
KOMATI FM
THEESPRUIT FM
SF
BUCK REEF CHERT
KROMBERG FORMATION
Geluk Thrust
MIDDLE MARKER
H1
H2
H3
H4
H5
H6
H1v
H2c
H2v
H3c
H3v
H4c
H4v
H5c
H5v
H6v
MENDON COMPLEX
Ncakini section
Footbridge Chert*
KROMBERG COMPLEX
NOISY COMPLEX
HOOGGENOEG COMPLEX
KOMATI COMPLEX
THEESPRUIT COMPLEX
SC
ONVERWACHT SUITE
3445 - 3455 Ma
HC1 [MM]
HC2
HC3
HC4
HC5
HC6
HC7
HC8
HC9
HC10
KD2a
EG-14.02
EG-56.18
EG-62.18
EG-116.25
EG-138.88
EG-176.00
Major Basal Unconformity
Clast Composition
Meta-igneous
Metasedimentary
No. of Clasts
Depth: 77-89m
n = 92
Depth: 89-101m
n = 85
Depth: 112-116m
n = 242
Depth: 137-139m
n = 127
Depth 171-176m
n = 250
Rhyo-dacitic sandstones & tuff
Coarse felsic volcaniclastics (conglomerates/diamictites)
Dacitic intrusion/sill
Massive Basalt
Pillow Basalt
Undifferentiated basalt and intrusives
Komatiite
Komatiitic Intrusion
Chert
Silicified Komatiite
Silicified Basalt
Shear Zone
Unit 1 (Turbidites)
Siltstone
Fine-grained sandstone
Coarse, monomict sandstone
Unit 2 (Diamictite - siltstone)
Laminated siltstone
Massive fine to medium-grained sandstone
Major basal polymictitic diamictite unit

Figure 3.1. Stratigraphy models for the Barberton Greenstone Belt, focusing on the Hooggenoeg Formation and uppermost sediments. Stratigraphy for the Hooggenoeg Formation and uppermost sediments as mapped Lowe and Byerly (1999, 2007) also Viljoen and Viljoen (1969) for the SE and NW limbs of the Onverwacht Fold is shown on the left hand panel. This is contrasted with the upper Onverwacht and Hooggenoeg stratigraphy model as mapped on the SE limb by de Wit et al., (2011) shown in the central panel, that proposes regional 'complexes'. Drill core log of the Noisy sedimentary rocks in KD2a indicating the unconformity with the underlying basalts is shown on the right hand panel with clast composition shown for major diamictite basal horizons. Sample positions for zircon U-Pb analyses are indicated on the drill core log. [MM] = Middle Marker Chert, [SF] = Sandspruit Formation, [SC] = Sandspruit Complex, [Hv] = Hooggenoeg volcanic (mafic-ultramafic), [HC] = Hooggenoeg Complex.

Several interpretations exist for the origin and depositional environment of this sedimentary sequence (Viljoen and Viljoen, 1969c; Lowe and Knauth, 1977; Wit et al., 1987a,b Armstrong et al., 1990; de Wit et al., 2011), ranging from reworked coarse- and fine-grained, felsic volcanics and tuffs deposited in a shallow marine environment as debris-flows and turbidites (Lowe and Knauth, 1977) to felsic volcaniclastics, coarse clastics and airborne tuff created by tectonic uplift and syntectonic intrusion of dacitic sills along active thrusts at ca. 3455 Ma in an inferred intra-oceanic setting (de Wit et al., 1987a,b, 2011).

A continuous drill core section across the sedimentary rocks and the basal unconformity was recently drilled in the Barberton Scientific Drilling Program (BSDP, see Grosch et al., (2009a,b). Detrital zircons were sampled systematically from basal horizons across the BSDP drill core, including one from directly above the unconformity in hole KD2a (Fig. 3.1; and Grosch et al., 2009a,b). Here U-Pb and Pb-Pb detrital zircon ages are presented for a relatively large number of Paleoarchean detrital zircon grains (60-80 grains per sample) determined by laser ablation ICP-MS (cf. Kosler et al., 2002). A reliable maximum depositional age for these sedimentary rocks and identification of possible detrital zircon sources will be presented. Considering principles of terrane analysis, and in conjunction with new drill core observations, new insights into the earliest geodynamic evolution of the BGB are gained that argue for plate tectonic-type processes operating at the time of sedimentation.

3.2. Outcrop geology and sedimentology: field and drill core observations

The Noisy formation sedimentary sequence is well-exposed along the Komati River on the SE-limb with ~200 m of well-bedded, upward-fining diamictites, conglomerates, sandstones, siltstones and laminated cherts (Fig. 3.2a-c). The sedimentary rocks unconformably overlie the pillow lavas of the Hooggenoeg Formation, and have an upper contact with the Kromberg Formation that is inferred to be a thrust (see Fig. 2.2; and de Wit et al., 1987b). Recent field observations indicate that the basal unconformity cuts down at least 1.5-2 km into the Hooggenoeg Formation pillow lavas (see Fig. 3.1; also Grosch et al., 2009a,b; de Wit et al., 2011; Furnes et al., 2011). A complete explanation of the regional and stratigraphic setting of this unit is presented in Chapter 2. On the SE-limb of the OAF there are two major components to the Noisy sedimentary succession: a lower coarse-grained, fining-upward, diamictite with prominent rhyo-dacitic clasts (Fig. 3.1 and 3.2); and an upper unit of monomictitic, well-bedded sandstone with an upper felsic tuff and chert (Fig. 3.1). In the lower ~120m thick diamictite unit clasts range from very angular to well-rounded and up to 60cm in size. In field outcrop, the diamictite is poorly sorted, matrix-supported and consists of mostly rhyo-dacitic and granitic clasts.

The upper ~80m thick finer-grained monomictitic unit consists of sandstones and a yellow felsic tuffaceous layer (~1.5m thick) with overlying laminated, black and grey cherts (Fig. 3.1 and Fig. 3.2a,b). Cross-bedding occurs in some of the sandstones, particularly in the basal erosional parts. Clasts in the sandy matrix are angular, with occasional sub-angular to angular grey-black laminated chert clasts in the lowermost parts of the beds. Soft sediment deformation features are common in this unit with convoluted bedding, flame structures, and slumping typical of sediments deposited by turbidity currents (Fig. 3.2b).

A continuous section across these sedimentary rocks was recently obtained in drill core KD2a of the BSDP (Fig. 3.1 and see Grosch et al., 2009a,b). The 350 m core intercepted the base of the upper turbiditic sandstones and it contains the entire lower diamictite unit and the basal unconformity between the Noisy formation sedimentary rocks and the pillow lavas of the Hooggenoeg Formation. In outcrop most of the diamictite clasts appear to be dacite, but in drill core a number of other meta-igneous and meta-sedimentary clasts are present. The compositions of the major clast-rich horizons at the base of fining upward units are presented in Figure 3.1. These include Cr-rich bright green metabasalts and meta-mafic clasts with a gabbroic, mottled texture; also felsic meta-igneous clasts including tonalitic to pink rhyolitic

clasts; plus meta-sedimentary clasts including fragments of conglomerates and black or grey massive and laminated cherts (Fig. 3.1 and 3.2). The proportions of meta-igneous versus meta-sedimentary clasts vary with depth, with the lowermost fining upward unit containing the largest proportion of meta-igneous clasts (Fig. 3.1). The mafic clasts comprise between 5 and 10% of the meta-igneous fraction. These together with the black chert clasts were most probably derived from the underlying silicified Hooggenoeg pillow lavas and interbedded cherts and possibly also the Komati Formation. In short, observations of the drill core clearly indicate that the diamictite is polymictitic and hence, derived from more than one source.

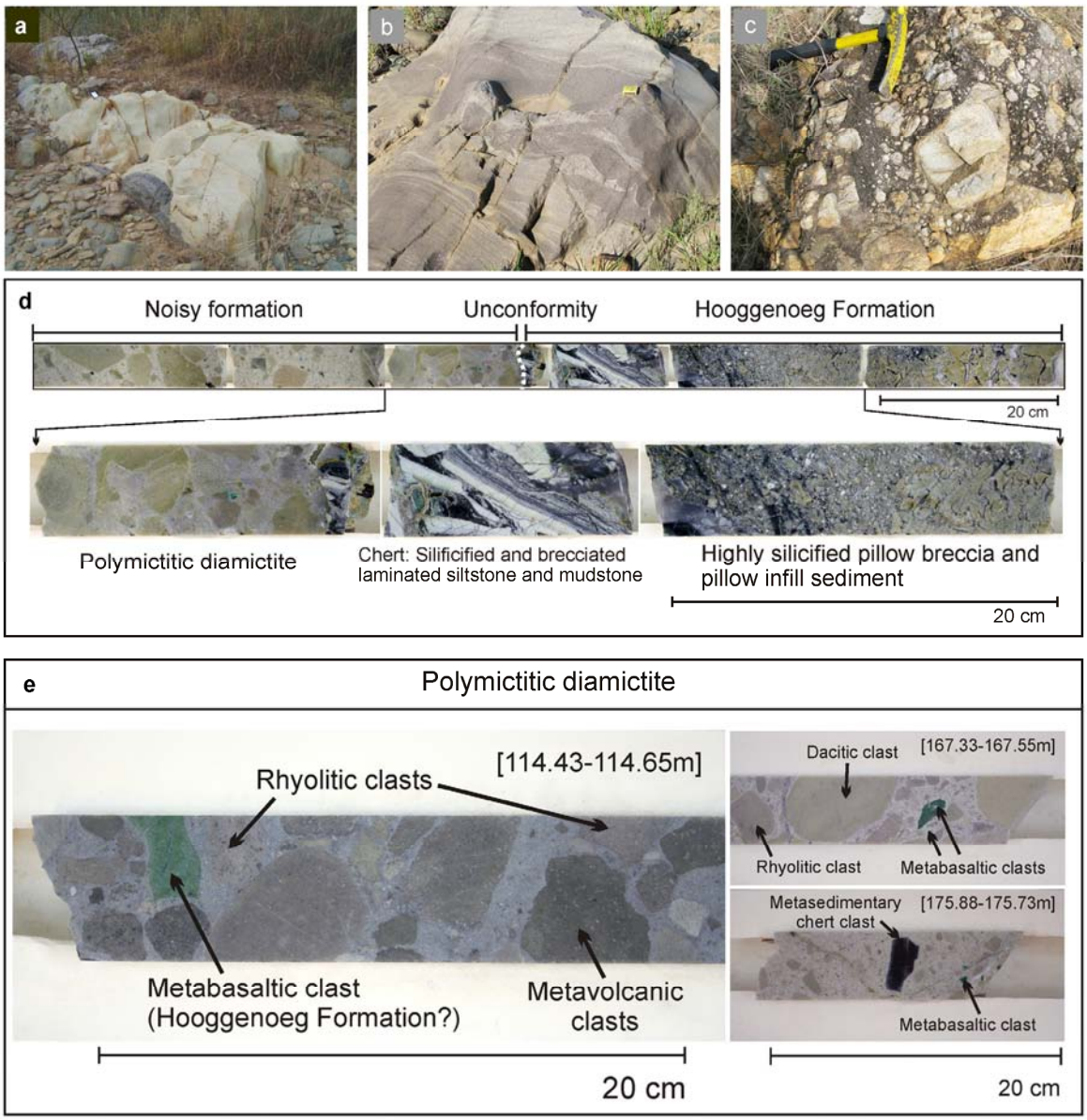

Figure 3.2. (a) Prominent, yellow tuff horizon in the uppermost turbidite unit that represents

reworked fine-grained felsic ash in the upper Noisy sedimentary rocks (clinometer = 6cm in width). **(b)** Soft sediment deformation and chaotic layering in turbiditic sandstones (matchbox = 5 cm). **(c)** Outcrop photo of poorly sorted, matrix supported diamictite in lower Noisy sedimentary rocks (geological hammer handle = 32 cm). **(d)** Drill core images showing a detailed section across the basal unconformity between the Noisy sedimentary rocks and the silicified pillow lavas. **(e)** Selected sections of drill core (corresponding depth interval indicated) illustrating the wide range of clast size, shape and lithology in the polymictitic Noisy formation diamictite. The images shown on the far right represent silicified diamictite above the basal unconformity

The basal unconformity as seen in drill core is marked by a sharp contact between the sedimentary rocks and an underlying laminated chert of the uppermost Hooggenoeg Formation (Fig. 3.1). This 17 cm of chert consist of siltstone and mudstone that has been silicified along with the underlying pillow lavas (Fig. 3.1 and Fig. 3.2d). The chert and underlying pillow lavas are brecciated by quartz veining most likely recording a second hydrothermal silicification and fluid brecciation event. The overlying sediments at the basal unconformity also record *in-situ* silicification, characterized by bleaching and white discolouration of the sedimentary clasts and matrix (Fig. 3.1).

3.3. Analytical methods and samples

A total of six representative samples were prepared from drill core KD2a, particularly from the base of coarse diamictite units (Fig. 3.1). These included 1 sample from the base of the upper turbidite unit (containing the yellow felsic 'tuff' horizon of Biggin et al. 2011) at 14.08 m, and 5 samples down to the lowermost silicified polymictitic diamictite at the basal unconformity (Fig. 3.1). The separated zircons were mounted in 1 inch epoxy-filled blocks and polished to obtain even surfaces for laser ablation ICP-MS analysis. Cathodoluminecence imaging was carried out on a Zeiss Supra 555VP scanning electron microscope at the Department of Earth Science, University of Bergen.

3.3.1 Laser ablation single-collector ICP-MS analysis

Prior to analysis the samples were cleaned in 2% HNO_3 to remove any surface contamination. Isotopic analysis of zircons by laser ablation ICP-MS followed the technique described in

Kosler et al. (2002). A Thermo-Finnigan Element 2 single collector sector field ICP-MS coupled to a 193 ArF excimer laser (Resonetics RESOlution M50-LR) at the Department of Earth Science, Bergen University was used to measure U/Pb and Pb isotopic ratios in zircons. The sample introduction system was modified to enable simultaneous nebulisation of a tracer solution and laser ablation of the solid sample (Horn et al., 2000). Natural Tl ($^{205}Tl/^{203}Tl$ = 2.3871 - Dunstan et al., 1980), ^{209}Bi and enriched ^{233}U and ^{237}Np (>99%) were used in the tracer solution, which was aspirated to the plasma in an argon - helium carrier gas mixture through an Apex desolvation nebuliser (Elemental Scientific) and a T-piece tube attached to the back end of the plasma torch. A helium gas line carrying the sample from the laser cell to the plasma was also attached to the T-piece tube.

The laser was set up to produce an energy density of ca 45 mJ at a repetition rate of 5 Hz. The laser beam was imaged on the surface of the sample placed in the two-volume ablation cell mounted on a computer-driven motorized stage of a microscope. During ablation the stage was moved beneath the stationary laser beam to produce a linear raster (ca 20 x 60 microns) in the sample. Typical acquisitions consisted of a 35 second measurement of analytes in the gas blank and aspirated solution, particularly ^{203}Tl - ^{205}Tl - ^{209}Bi -^{233}U - ^{237}Np, followed by measurement of U and Pb signals from zircon, along with the continuous signal from the aspirated solution, for another 120 seconds. The data were acquired in time resolved - peak jumping - pulse counting mode with 1 point measured per peak for masses 202 (flyback), 203 and 205 (Tl), 206 and 207 (Pb), 209 (Bi), 233 (U), 237 (Np), 238 (U), 249 (233U oxide), 253 (237Np oxide) and 254 (238U oxide). Raw data were corrected for dead time of the electron multiplier and processed off line in the spreadsheet-based program Lamdate (Kosler et al., 2002) and plotted on concordia diagrams using Isoplot (Ludwig, 1999). Data reduction included correction for gas blank, laser-induced elemental fractionation of Pb and U and instrument mass bias. Minor formation of oxides of U and Np was corrected for by adding signal intensities at masses 249, 253 and 254 to the intensities at masses 233, 237 and 238, respectively. No common Pb correction was applied to the data. Details of data reduction and corrections are described in Kosler et al. (2002) and Kosler and Sylvester (2003). Zircon reference material 91500 (1065 Ma - Wiedenbeck et al., 1995), GJ-1 (609 Ma – Jackson et al., 2004) and Plešovice (337 Ma - Slama et al., 2008) were periodically analyzed. Zircon standards GJ-1 and Plešovice yielded mean ages of 594 ± 3 Ma (n = 57) and 338 ± 2 Ma (n = 65), respectively.

3.3.2 Laser ablation multi-collector ICP-MS analysis

Additional analyses were done on three of the samples (KD2-116.08, KD2-138.88, KD2-176m) using a multi-collector ICP-MS (Thermo Finnigan Neptune) coupled to a Resonetics RESOlution M50 laser at the Department of Earth Science, Bergen University to measure U/Pb and Pb isotopic ratios in selected zircon grains. The laser was fired at 3.5 Hz repetition rate using energy of 45 mJ/pulse. Round mask was employed in the optical path of the laser to produce a circular beam (35x demagnified) with diameter of 7 micrometers on the sample surface. Helium (0.64 l/min) was used as ablation/carrier gas. During the ablation the stage was moved beneath the stationary laser beam at a speed of 10 μm/s that resulted in elongate laser craters (7 x 50 μm), which were not deeper than 5 μm. Data were acquired simultaneously for ^{202}Hg, ^{204}Hg+Pb, ^{206}Pb, ^{207}Pb and ^{238}U using the multiple ion counting system (channeltrons) of the Neptune MC ICP-MS. Typical signal intensities were 1600, 400, 80000, 23000 and 77000 cps for the above isotopes, respectively. The acquisition consisted of a 35 seconds measurement of all analytes in the gas blank, followed by measurement of U and Pb isotope signals produced by zircon ablation for another 35 seconds. The data were corrected for channeltron dead time and processed off line in a spreadsheet-based program. Data reduction included correction for channeltron yield, gas blank and mass discrimination and Pb/U fractionation using repeat analyses of an in-house zircon standard from the Kaap Valley Pluton (3227±1 Ma, Kamo and Davis, 1994). Reproducibility of the standards was better than 0.9% (1s) for ^{207}Pb/^{206}Pb and better than 1.7% (normally <1.1%) for ^{206}Pb/^{238}U during the individual runs. The application of a common Pb correction was not necessary due to negligible amounts of non-radiogenic Pb in combination with the old age of the zircon grains.

3.4. Results

All U-Pb and Pb-Pb age data measured on the single collector ICP-MS Thermo-Finnigan Element 2 for detrital zircons from the drill core samples are provided in Appendix C1 and ^{207}Pb/^{206}Pb ages are shown in Figure 3.3 (a-f). Between 100-120 zircons were analyzed per sample, however, some analyses showed large analytical uncertainties and deviated severely from concordia due to unresolved polyphase zircon composition and/or Pb-loss near cracks present in the grains. The data were therefore, screened for quality and only the remaining ^{207}Pb/^{206}Pb ages that were 100 ± 10% concordant were used.

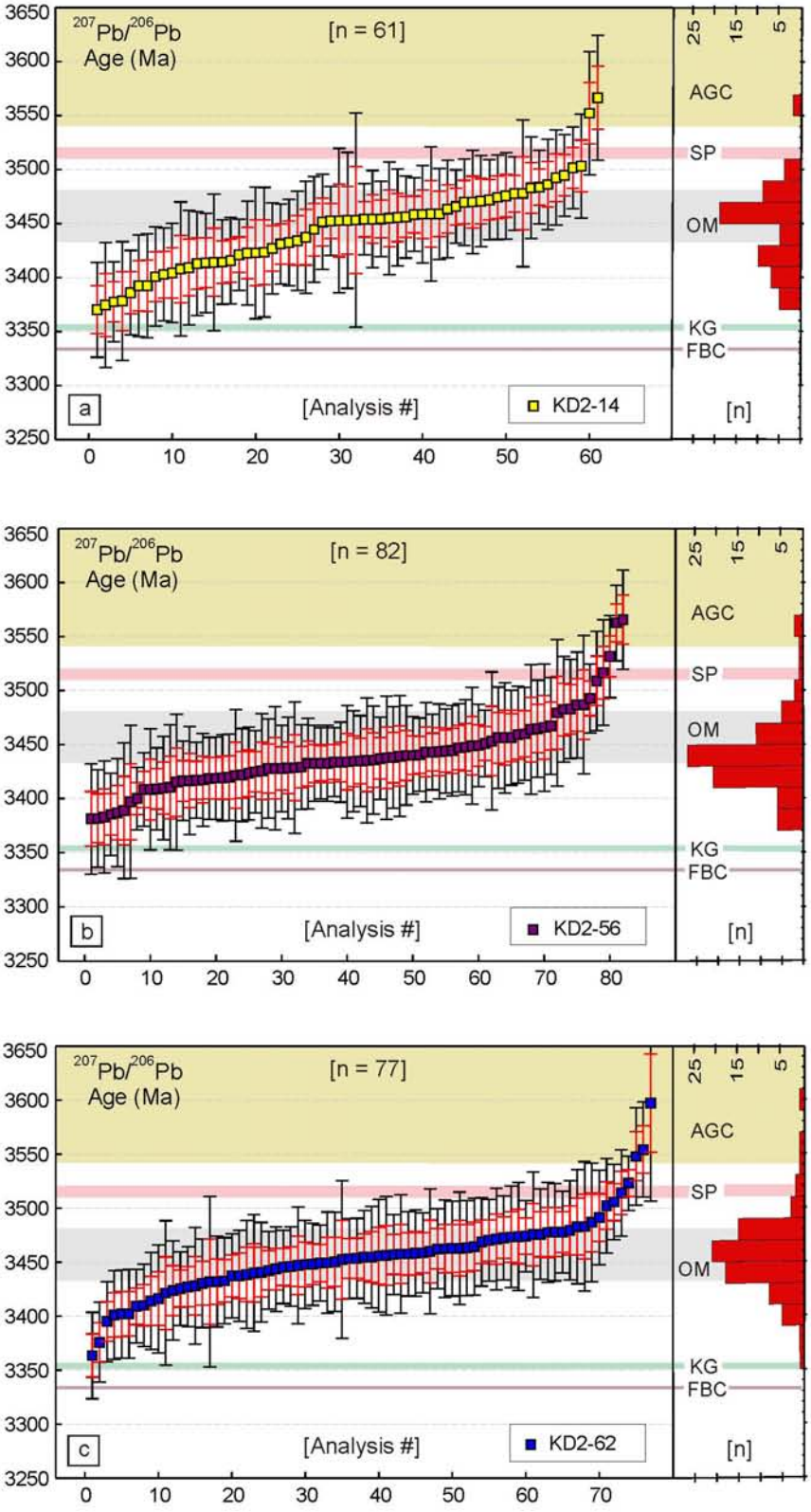

Figure 3.3. **(**continued over page)

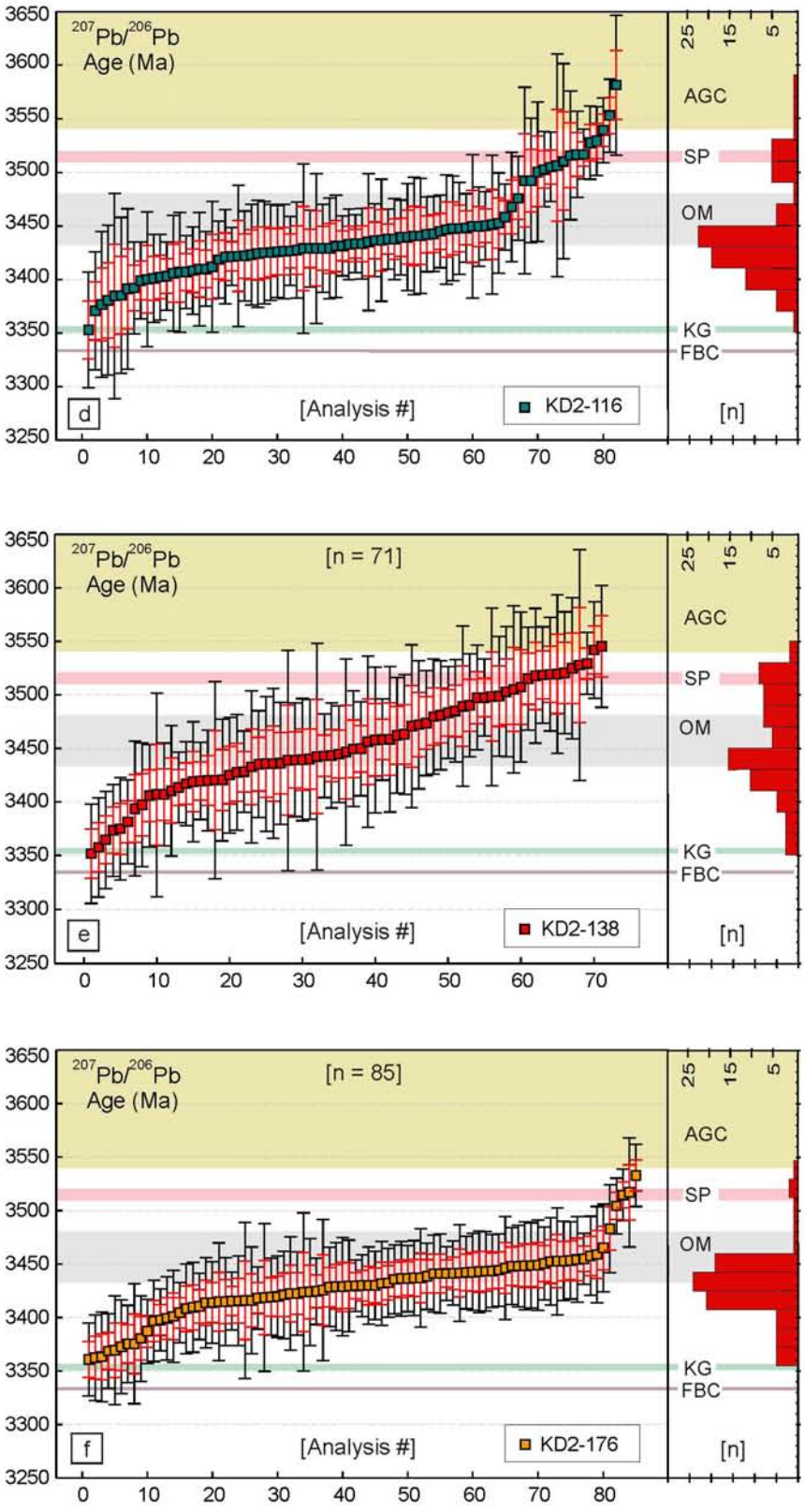

Figure 3.3. The distribution in $^{207}Pb/^{206}Pb$ ages for detrital zircon grains in the 6 selected drill core samples with ages arranged in ascending order (youngest to oldest) and plotted along

with their uncertainties at both 1- and 2-sigma level. The corresponding histograms for the $^{207}Pb/^{206}Pb$ zircon ages are plotted for each sample. Sample names correspond to the depth in the drill core. Example, KD2-176.18 = diamictite sample at a depth of 176m in the drill core, directly above the basal unconformity. Sample KD2-14 = turbiditic sandstone at the base of the turbidite sequence in the Noisy formation overlying the polymictitic sequence.

In general the $^{207}Pb/^{206}Pb$ ages are preferred for Archean zircons because they show the lowest uncertainty in comparison to the $^{206}Pb/^{238}U$ and $^{207}Pb/^{235}U$ ages (see all data in Appendix C1). In Figure 3.3 (e-f), the $^{207}Pb/^{206}Pb$ ages for zircon grains in the 6 selected drill core samples were arranged in ascending order (youngest to oldest) and plotted along with their uncertainties at both 1- and 2-sigma level uncertainty. The corresponding histograms for the $^{207}Pb/^{206}Pb$ zircon ages are plotted for each sample (Fig. 3.3e-f). Potential detrital sources and major magmatic events of well-known ages in the BGB are highlighted in the background. The data distributions for each sample indicate a wide range in $^{207}Pb/^{206}Pb$ ages between 3350 and 3600 Ma. The main peaks in $^{207}Pb/^{206}Pb$ ages indicated in the histograms are between 3430 and 3470 Ma. The two oldest grains shown in the histograms occur in samples KD2-62.08m and KD2-116.18m, with $^{207}Pb/^{206}Pb$ ages of ca. 3597 and 3582 Ma, respectively.

The $^{207}Pb/^{206}Pb$ zircon age distributions display asymmetry both within and between samples as indicated by the distribution about their mean values (Fig. 3.3). For example, the turbidite sandstone sample KD2-14.08, containing the yellow tuff horizon, displays a moderately well-developed plateau in $^{207}Pb/^{206}Pb$ ages near the central part of the distribution at around 3455 Ma. In contrast, the polymictitic diamictite samples KD2-116.18m and KD2-138.88m show a sharp change in gradient with many zircon ages older than 3500 Ma. The $^{207}Pb/^{206}Pb$ age distributions for samples, KD2-138.88m and KD2-176.08m include the youngest possible zircon ages in the dataset at around 3350 Ma. It is important to note that the narrow time interval that includes the potential BGB source rocks is relatively small compared to the uncertainties on the determined $^{207}Pb/^{206}Pb$ ages (see Fig. 3.3), and thus, it is difficult to distinguish specific detrital sources on the basis of these data alone.

To resolve individual detrital sources and to test the reliability, particularly of the young tails in the $^{207}Pb/^{206}Pb$ age distributions (Fig. 3.3a-f), further more precise zircon ages were determined using a Thermo Finnigan Neptune multi-collector ICP-MS. A total of 120

additional analyses were carried out on three selected samples (KD2-116.08m, KD2-138.08m KD2-176.08m).

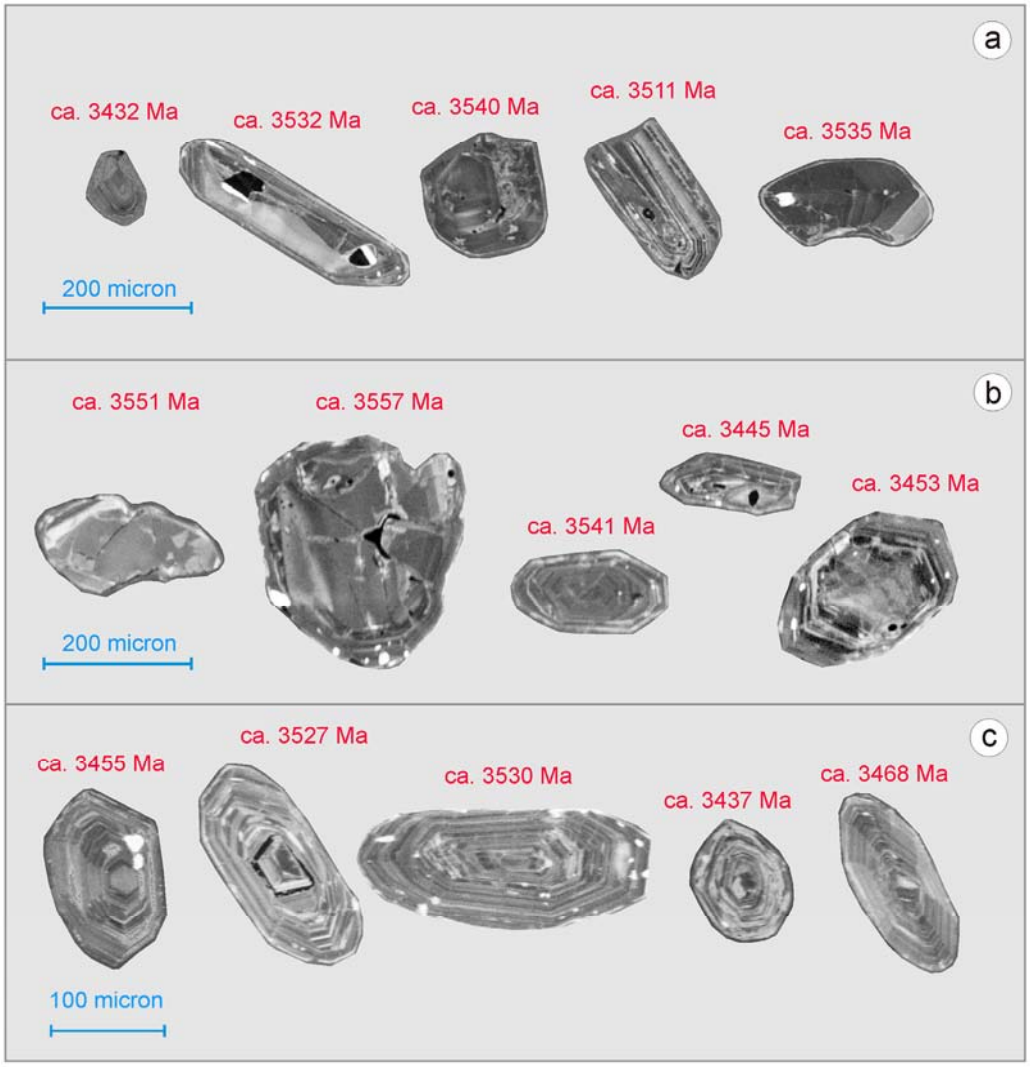

Figure 3.4. Cathodoluminescence (CL) images illustrating rounded, subrounded and angular zircon morphologies analysed by multicollector ICP-MS. Sample **(a)** = KD2-116.18m; **(b)** = KD2-138.88m; **(c)** KD2-176.08m. U-Pb zircon isotope data is provided in Table 3.1.

Only the $^{207}Pb/^{206}Pb$ ages for analyses that are 100 ± 10% concordant are presented in Appendix C2 and representative analyses are provided in Table 3.1. By comparison, even at 2-sigma level, the uncertainties on the $^{207}Pb/^{206}Pb$ ages as determined by multi-collector ICP-MS are much smaller than those determined by the single-collector ICP-MS method (compare data in Fig. 3.5a to Fig. 3.3a-f).

Table 3.1. U-Pb isotope data determined by laser abaltion multiple-collector ICP-MS analysis

	ISOTOPIC RATIOS						CALCULATED AGES Ma					
Analysis#	$^{207}Pb/^{206}Pb$	± 1 sigma	$^{207}Pb/^{235}U$	± 1 sigma	$^{206}Pb/^{238}U$	± 1 sigma	$^{207}Pb/^{235}U$	± 1 sigma	$^{206}Pb/^{238}U$	± 1 sigma	$^{207}Pb/^{206}Pb$	± 1 sigma
Sample KD-116.08m												
KD2-116-8	0.2930	0.0018	25.1597	0.3128	0.6263	0.0069	3314	12	3135	28	3433	5
KD2-116-11	0.3118	0.0019	28.3712	0.3247	0.6599	0.0069	3432	11	3267	27	3530	5
KD2-116-14	0.2928	0.0018	28.1562	0.3236	0.6952	0.0073	3425	11	3402	28	3432	5
KD2-116-21	0.3122	0.0028	30.4869	0.4219	0.7130	0.0076	3503	14	3470	29	3532	7
KD2-116-27	0.3079	0.0028	27.8073	0.3981	0.6586	0.0072	3412	14	3262	28	3511	7
KD2-116-28	0.3128	0.0028	27.9782	0.3957	0.6478	0.0070	3418	14	3220	28	3535	7
KD2-116-29	0.2973	0.0027	27.2236	0.3893	0.6693	0.0074	3392	14	3303	29	3456	7
KD2-116-30	0.3139	0.0028	30.1778	0.4215	0.6981	0.0075	3493	14	3413	28	3540	7
Sample KD-138.88m												
KD-138-5	0.3070	0.0015	30.4792	0.5613	0.7242	0.0115	3502	18	3512	43	3506	8
KD-138-8(1)	0.3145	0.0016	31.4958	0.5821	0.7229	0.0115	3535	19	3507	43	3543	8
KD-138-10	0.3173	0.0020	31.3793	0.3573	0.7259	0.0074	3531	11	3518	28	3557	5
KD-138-11	0.3141	0.0019	31.9365	0.3627	0.7404	0.0076	3548	11	3572	28	3541	5
KD-138-13	0.2967	0.0018	27.3368	0.3190	0.6707	0.0072	3396	11	3308	28	3453	5
KD-138-20	0.3161	0.0019	30.2323	0.3419	0.6953	0.0071	3494	11	3403	27	3551	5
KD-138-27	0.2951	0.0019	27.5530	0.3186	0.6830	0.0071	3403	11	3356	27	3445	5
KD-138-29	0.3001	0.0018	26.5849	0.3154	0.6449	0.0069	3368	12	3208	27	3471	5
Sample KD-176.08m												
KD2-176-1	0.3113	0.0028	30.2449	0.6160	0.6997	0.0077	3495	20	3419	29	3527	7
KD2-176-2(1)	0.2970	0.0027	28.9994	0.5875	0.7026	0.0076	3453	20	3430	29	3455	7
KD2-176-6	0.3097	0.0028	29.0090	0.5949	0.6771	0.0077	3454	20	3333	30	3519	7
KD2-176-12	0.2936	0.0026	26.6412	0.5499	0.6629	0.0077	3370	20	3278	30	3437	7
KD2-176-14	0.3118	0.0028	30.2462	0.6149	0.7091	0.0077	3495	20	3455	29	3530	7
KD2-176-15	0.2970	0.0027	28.6854	0.5790	0.7097	0.0076	3443	20	3457	29	3455	7
KD2-176-16	0.2999	0.0031	29.1685	0.5989	0.7046	0.0117	3459	20	3438	44	3470	8
KD2-176-30	0.2996	0.0018	27.7848	0.3141	0.6710	0.0069	3412	11	3310	27	3468	5

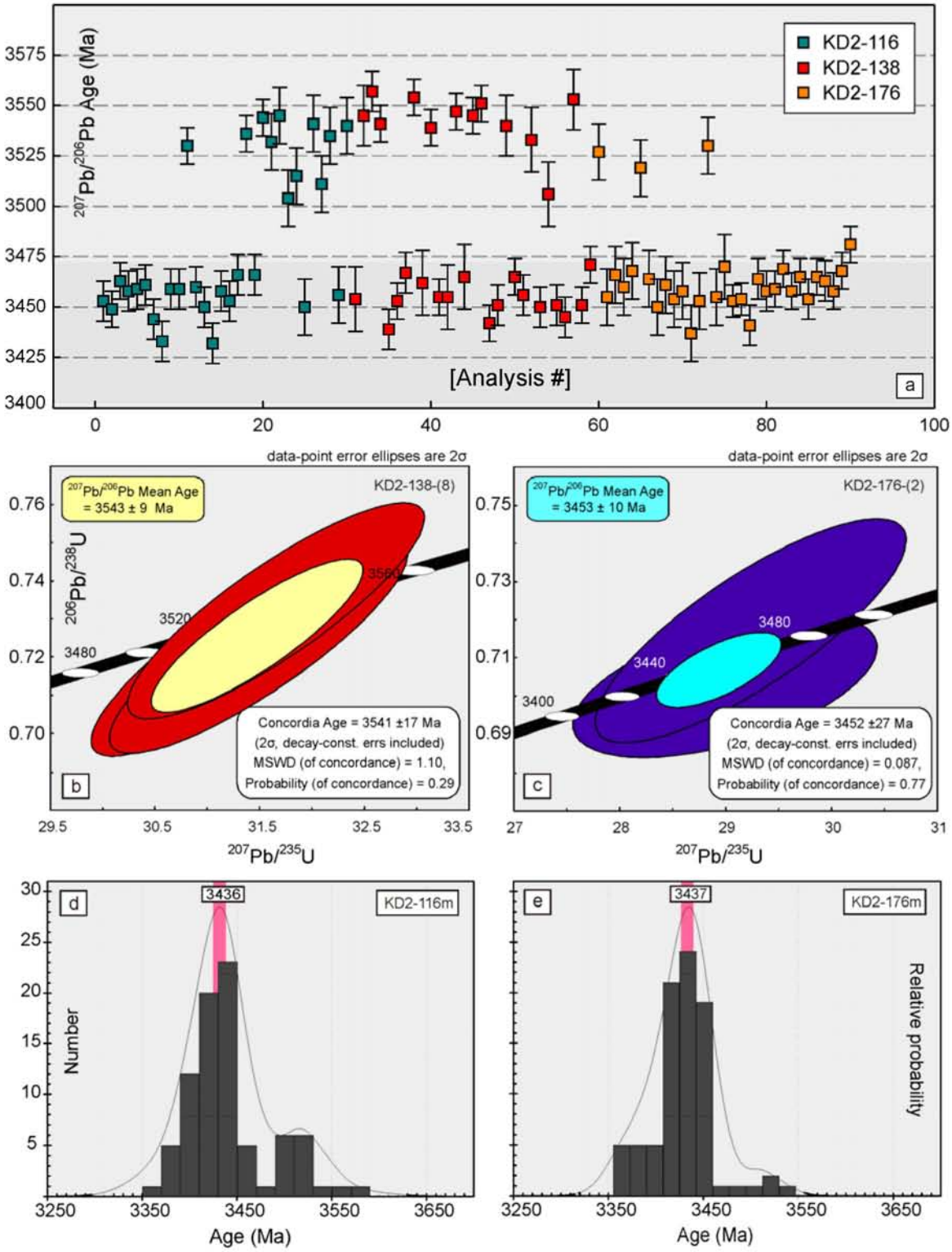

Figure 3.5. (a) Wide spread in $^{207}Pb/^{206}Pb$ ages indicated by more precise isotopic measurements determined by the multi-collector laser ablation ICP-MS method. The error bars are at 2- sigma level uncertainty. **(b-c)** Multiple analyses on single grains, (**b**) detrital zircon grain KD2-138.88-(8) and (**c**) zircon grain KD2-176.08-(2). The uncertainty on the

$^{207}Pb/^{206}Pb$ and concordia ages are reported at 2-sigma level. **(d-e)** Probability density distribution of $^{207}Pb/^{206}Pb$ ages for detrital zircons in drill core samples KD2-116.08m **(d)** and KD2-176.08m **(e)**. The youngest $^{207}Pb/^{206}Pb$ zircon ages confirmed by laser ablation multicollector ICP-MS is indicated in the background (pink band) and corresponds to the main peak in the relative probability distribution curves for each sample.

However, a comparably wide range in zircon ages is still observed between 3560 Ma and 3430 Ma (Fig. 3.5a). Although two broad data clusters are observed, namely one older than 3500 and another between 3480-3430, several different ages are observed within each cluster (Fig. 3.5a). To still further improve the precision in zircon ages, multiple laser-ablation analyses were performed on two randomly selected grains in two separate samples (KD2-138.88m and KD2-176.08m). Zircon grain KD2-138.88m-(8) yielded a weighted mean $^{207}Pb/^{206}Pb$ age of 3543 ± 8.8 Ma (n = 3), whereas zircon grain KD2-176.08m-(2) yielded a weighted mean $^{207}Pb/^{206}Pb$ age of 3453 ± 10 Ma (n = 2; see Fig. 3.5b,c).

The youngest $^{207}Pb/^{206}Pb$ ages (at 2-sigma uncertainty) for individual zircon grains that could be confirmed by multi-collector ICP-MS in each of the 3 samples, include 3432 ± 10 Ma (99% concordant, KD2-116.08m), 3439 ± 10 Ma (95% concordant, KD2-138.88m) and 3437 ± 14 Ma (95% concordant, KD2-176.08m; c.f. Table 3.1 and Appendix C2). These relatively precise $^{207}Pb/^{206}Pb$ ages for the youngest grain in each sample are compared to the main peak age as determined from the relative probability density curve calculated from the single collector ICP-MS data for the unconformity sample KD2-176.08m and KD2-116.08m (Fig. 3.5 d,e). Good agreement is indicated with the youngest grains overlapping within error with the main peak in the $^{207}Pb/^{206}Pb$ relative probability curves. The additional analyses confirm the youngest main peak in the $^{207}Pb/^{206}Pb$ probability curves at ca. 3432 Ma for the detrital zircons in the Noisy formation clastic sequence (Fig. 3.5d,e).

3.5. Discussion and interpretation

3.5.1 Depositional age

The depositional age of the Noisy formation has previously been inferred from U-Pb zircon ages from a fine-grained felsic horizon on the SE limb of the Onverwacht anticline (see Fig. 3.2a) dated at 3455 ± 8 Ma (11 zircon grains) that was used to argue that the underlying

sandstones, diamictites and the major unconformity are older than ca. 3455 ± 8 Ma (Biggins et al., 2011; de Wit et al., 2011). A mean $^{207}Pb/^{206}Pb$ age of 3438 ± 6 Ma from two samples in the same horizon (4 grains each) has also been reported (Kröner and Todt 1988). Significantly, in both cases, older zircon grains were also found at 3546 ± 12 Ma (Biggins et al. 2011) and 3451 ± 3 Ma (Kröner and Todt, 1988), respectively. These older grains were regarded as inherited igneous xenocrysts, because the fine-grained yellow horizon investigated was interpreted to be a volcanic airfall tuff (de Wit et al., 2011) or a dacitic felsic flow (Kröner and Todt, 1988). The zircon data reported here indicate that all of the previously reported zircon ages, as well as many others, are present in the underlying clastic sedimentary sequence of the Noisy formation (e.g. see Fig. 3.5a-e). Several sediment sources are indicated by the diverse lithologies, shapes and sizes of clasts observed in the drill core, indicating the polymictitic nature of the Noisy formation (see Fig. 3.2). On the basis of the new data presented here, it is concluded that the maximum depositional age of the clastic sedimentary rocks underlying the previously investigated tuff is ca. 3432 Ma (Fig. 3.5a, d, e). (Younger zircon ages could not be confirmed; c.f. Fig. 3.5 and Table 3.1). This indicates that the tuff is most likely not of airfall origin as proposed by de Wit et al., (2011), but rather a reworked felsic volcanic ash deposit. Moreover, the new data indicate a maximum depositional age of ca. 3432 Ma for the clastic polymictitic Noisy formation, indicating that sediment deposition and formation of the underlying major erosional unconformity is younger than ca. 3432 Ma - not older than ca. 3455 as currently proposed. It is noteworthy that reworking of the tuff is supported by previous detailed sedimentological studies that described the yellow felsic horizon on the SE limb as not of airfall origin, but rather reworked felsic material deposited as turbidites and debris flows in a shallow marine environment (Lowe and Knauth 1977). In short, the tuff horizon is reworked and is therefore an unreliable chronostratigraphic marker. In addition, the depositonal age for the clastic rocks of the Noisy formation, indicates that the overlying Kromberg type-section is younger than ca. 3432 Ma (**see Fig. 3.6**), but older than the Footbridge Chert dated at ca. 3334 Ma (Byerly et al., 1996).

3.5.2 Provenance and stratigraphic setting of the Nosiy formation sedimentary rocks

The Pb-Pb age distributions have main peaks between 3462–3430 Ma indicating that the dominant source of detritus to the Noisy formation was derived from gneissic and felsic volcanic rocks of the ca. 3460-3437 Ma Stoltzburg TTG terrain (e.g. Armstrong et al., 1990, Kamo and Davis, 1994, Van Kranendonk et al., 2009) and the felsic volcanic rocks of

equivalent age in the BR-vsc of de Vries (2006; 2010) in the uppermost Hooggenoeg Formation. This implies that the polymictitic diamictites and turbidites studied here cannot be geochronologically and stratigraphically correlated with the ca. 3445-3455 Ma BR-vsc of the upper Hooggenoeg Formation on the northwestern limb of the OAF as proposed by de Wit et al., (2011).

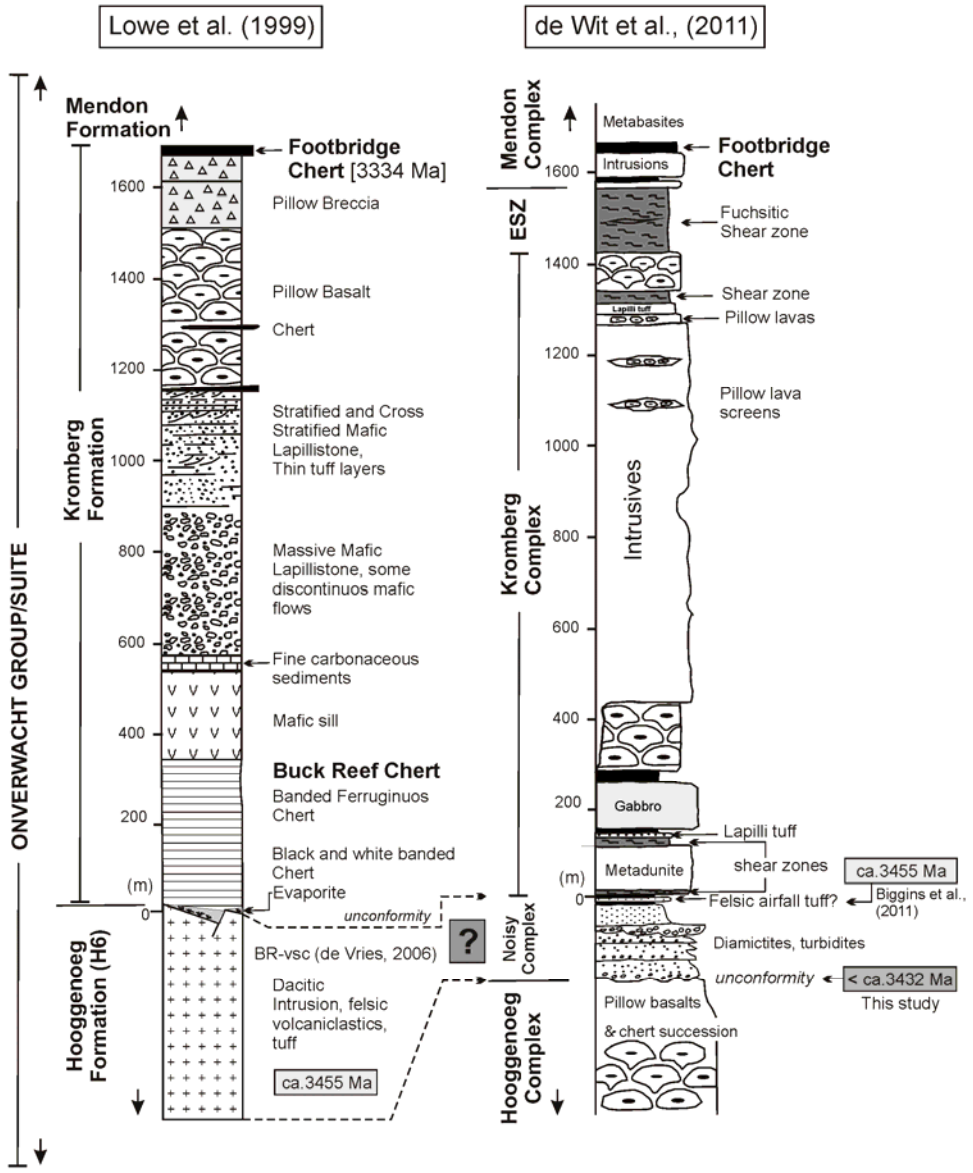

Figure 3.6. Contrasting stratigraphy models for part of the upper Onverwacht Group, as seen on the western (modified after Lowe et al., 1999) and eastern limb (modified after de Wit et al., 1987b; 2011) of the Onverwacht Antiformal Fold (OAF). The maximum depositional age of the Noisy sedimentary sequence at ca. 3432 Ma determined in this study is shown and contrasted with the depositional age of Biggin et al. (2011) and de Wit et al., (2011). The new

data presented herein, indicates that the major erosional unconformity is younger than ca.3432 Ma and is thus not compatible with a 'conterminous Noisy Complex' as proposed by de Wit et al., (2001) that argues for a simple stratigraphic correlation between the sedimentary rocks of interest on the eastern limb and the BR-vsc on the western limb. Age of the Footbridge Chert is after Byerly et al. (1993, 1996) from detrital zircon Pb-Pb ages. U-Pb age of the felsic intrusions in the uppermost Hooggenoeg Formation is after de Vries et al., (2006, 2010).

It is indicated here that the Noisy formation is younger than, and unconformably overlies the BR-vsc and basaltic lavas of the upper Hooggenoeg Formation and moreover, includes many clasts derived from within the BR-vsc and Stolzburg TTG terrane. Thus, the Noisy formation sedimentary rocks are distinct in age and lithology from the H6 unit of the uppermost Hooggenoeg Formation of the Onverwacht Group (see Fig. 3.6 and Fig. 3.1). Moreover, it is probable that deposition of the Noisy formation is diachronous and that there are marked facies differences between the limbs of the OAF. In this regard, the new data is not compatible with a the recently proposed 'tectonostratigraphy' for the BGB, which argues for a 'conterminous Noisy Complex' defined by a simple stratigraphic correlation between the sedimentary rocks of interest on the eastern limb and the BR-vsc on the western limb (see Fig. 3.6 and de Wit et al., 2001).

In general, two broad data clusters, each with a wide spread in $^{207}Pb/^{206}Pb$ ages, are recorded by the detrital zircons of the Noisy formation (Fig. 3.7a). The younger cluster displays a range in zircon ages of between 3480 and 3430 Ma and corresponds to the major phase of Onverwacht felsic magmatism (Stoltzburg TTG intrusions and felsic rocks of the BR-vsc) recorded in the Songimvelo Block of the BGB (e.g. Kamo and Davis, 1994; Lowe, 1999). Significantly, many older zircons are identified here to occur in the Noisy formation, corresponding in age to volcanic or plutonic sources from the southwestern parts of the BGB within the ca. 3550-3509 Ma Steynsdorp Block and the AGC of Swaziland. For example, detrital zircon ages overlap in age with the age of the Steynsdorp trondhjemitic gneiss and possibly the oldest component of the Theespruit Formation in the Steynsdorp Block (see Fig. 3.7a). Even older zircon ages overlap with ages of granitoid gneisses in the AGC recently dated at 3545.6 ± 0.5 Ma (Fig. 3.7b; Schoene et al., 2008), within and immediately SE of the Phophonyane Shear Zone (see Fig. 3.7a, b). This new data indicates that some older continental crustal components of the AGC were most likely in close proximity and/or directly beneath the mid-upper volcano-sedimentary Onverwacht Group at ca. 3432 Ma.

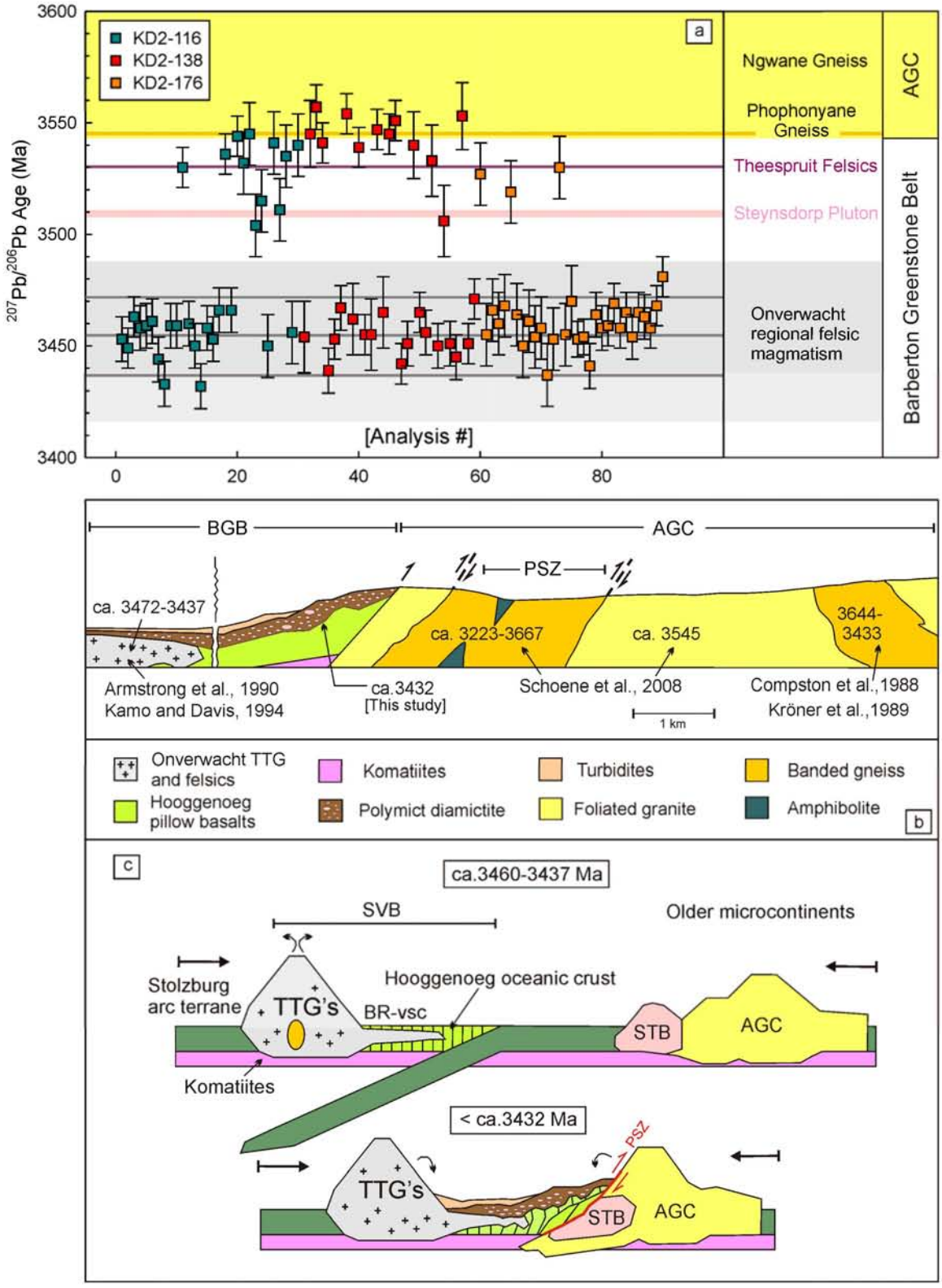

Figure 3.7. (a) Summary diagram showing the distribution of $^{207}Pb/^{206}Pb$ ages (at 2-sigma uncertainty) of various detrital zircon populations with likely detrital zircon sources of known age in the Songimvelo Block, the Steynsdorp Block and the Ancient Gneiss Complex shown

in the background. **(b)** Simplified cartoon cross-section across the Phophoyane Shear Zone between BGB and AGC. AGC geological profile simplified and modified after Schoene et al., (2008). The new detrital zircon data points to provenancial linking between the BGB and the AGC by ca. 3432 Ma. The Noisy formation detrital $^{207}Pb/^{206}Pb$ ages overlap in age with a fine-grained foliated granite within and immediately on the southeastern side of the PSZ in the AGC. Banded gneisses within the AGC with igneous protolith ages of 3644 Ma have been recrystallized at 3433 ± 8 Ma, consistent with tectonic accretion between the BGB and the AGC at ca. 3432 Ma as proposed in this study. The PSZ was subsequently reactivated at 3223 Ma (see Schoene et al., 2008). **(c)** Geodynamic plate tectonic model for accretion of proto-continental blocks of the Kaapvaal craton at ca. 3432 Ma, forming a stable crustal nucleus. In this model, the Songimvelo Block (SVB) is accreted onto older microcontinental terranes of the Steynsdorp Block (STB) and the Ancient Gneiss Complex, in an arc-continent collision zone setting similar to that of Phanerozoic ophiolite terranes.

3.5.3. Geodynamic Model and Provenancial Linkage between the BGB and Ancient Gneiss

The term provenancial linkage (*sensu* Jones et al., 1983) describes the sudden appearance of detritus in one terrane derived from its neighbour. The depositional age of the detritus is thus used to infer the chronology of tectonic accretion between the two (or more) terranes along a suture zone. The new detrital zircon ages reported here from the Noisy formation indicate that 30-35 million years were available for eruption of ~3 km of Hooggenoeg oceanic basalts (i.e. between ca. 3472 and 3437 Ma), followed by a major change in the geologic environment from deep marine pillow lava eruption to shallow marine conditions and then development of a major erosional unconformity that incises at least 1.5 to 2 km down into the basaltic Hooggenoeg Formation (see Fig. 3.1 and Grosch et al., 2009a,b; Furnes et al., 2010). This relatively rapid and dramatic change in depositional environment is comparable to arc-continent convergent margins and ophiolite obduction processes as observed in Phanerozoic ophiolites such as the Oman (e.g. Searle, 2007) or Caledonian ophiolite terranes (Pederson et al., 1991). In this context, it is argued that the 3460-3437 Ma Stolzburg TTG terrane and the Hooggenoeg oceanic crust of the Songimvelo Block most likely developed in a supra-subduction zone setting and were subsequently tectonically accreted onto the older Steynsdorp Block and Ancient Gneiss Complex (Fig. 3.7c). This resulted in major uplift and erosion of the Hooggenoeg oceanic crust including the BR-svc in the Songimvelo Block during terrane accretion and possible obduction onto older proto-continental blocks of the

Kaapvaal craton at or some time shortly after ca. 3432 Ma (Fig. 3.7c). In support of this tectonic accretion model, is the occurrence of both zircon overgrowths with Pb-Pb ages and new zircon growth ages of 3433 ± 8 Ma reported in ca. 3644 Ma banded gneisses in the northwestern AGC in close proximity to the Phophoyane Shear Zone (see Fig. 3.7a-c; Compston and Kröner, 1988; Kröner et al., 1989). The inherited zircon xenocrysts in the Steynsdorp trondhjemitic intrusion dated at ca. 3553 ± 4 Ma (Kröner et al., 1992; 1996) indicate a possible early intrusive connection between the Steynsdorp Block and the Ancient Gneiss Complex, prior to a major craton-scale tectonic accretion event with the Songimvelo Block of the BGB at ca. 3432 Ma. Hence, the detrital zircon ages in the Noisy formation present a new line of evidence for the operation of horizontal accretion and plate tectonic processes in the early Paleoarchean and evidence for the existence of a stable, amalgamated Kaapvaal proto-continent as far back as ca. 3432 Ma. The banded gneisses and foliated granitic rocks of the Phophonyane Shear Zone were most likely reactivated along this ancient suture more than 200 million years later, during the next major phase of tectonic activity as recorded by syn-tectonic felsic dykes dated at 3223.4 ± 2 Ma (see Schoene et al., 2008) that cross-cut the banded gneisses in the PSZ.

3.6. Conclusions

[1]. The maximum depositional age of the Noisy formation sedimentary rocks is ca. 3432 Ma. This also represents the maximum age for the development of the major underlying erosional unconformity. This new data in conjunction with field observations implies that the presumed tuff horizon underpinning the existing age constraints on the Noisy formation and regional correlations is, in fact, a reworked sedimentary deposit and not a primary volcanic airfall deposit (c.f. Biggins et al. 2011, de Wit et al. 2011). More generally it is cautioned that other fine-grained felsic horizons in the BGB may also be reworked tuffs, and are therefore unreliable chronostratigraphic markers.

[2]. A wide range in detrital zircon ages was determined for the Noisy formation and together with drill core observations reveals many potential detritus sources from older basement for the polymictitic clasts. These sources are found in the Songimvelo Block of the BGB that includes the BR-vsc of the uppermost Hooggenoeg formation; the Hooggenoeg pillow lavas and cherts; and the Stoltzburg and Theespruit TTG gneisses. Additional

sources include older rocks of the Steynsdorp Block and from within the Ancient Gneiss Complex (AGC) of Swaziland. This new U-Pb detrital zircon data indicates that some older continental crustal components of the AGC were most likely in close proximity and/or directly beneath the mid-upper volcano-sedimentary Onverwacht Group at ca. 3432 Ma.

[3]. The Noisy formation contains many detrital zircon grains that overlap in age with zircons from the Steynsdorp Block and granitic gneisses on the SE margin of the Phophonyane Shear Zone (PSZ) in the Ancient Gneiss Complex. This implies provenancial linkage between small proto-continental blocks in the BGB and the Ancient Gneiss Complex (structurally separated by the PSZ) that records tectonic accretion at ca. 3432 Ma. It is proposed here that major erosion and coarse clastic deposition of the Noisy formation occurred during tectonic accretion of the Songimvelo Block onto the older Steynsdorp and Ancient Gneiss microcontinental blocks of the Kaapvaal craton. In other words, this study presents new geologic evidence that is consistent with plate tectonic processes operating at ca. 3432 Ma in the BGB and the existence of a stable, amalgamated continent at that time.

[4]. The new depositional age constraint for the Noisy formation places a maximum age on the Kromberg type-section, indicating that the Kromberg mafic-ultramafic sequence must be younger than ca. 3432 Ma on the SE limb of the OAF (see Fig. 3.6).

[5]. The lower Noisy formation sedimentary rocks, were deposited as shallow marine polymictitic debris flows during tectonic uplift of a ca. 3472 Ma Hooggenoeg oceanic basin, with turbidite deposition occurring during or after tectonic activity at ca. 3432 Ma, most likely in a shallow, intra-continental epieric sea.

Chapter 4

PT-constraints on the Metamorphic Evolution of the Paleoarchean Kromberg Type-section, Barberton Greenstone Belt, South Africa

Strongly banded, fuchsite-carbonate-quartz alteration zone in the central Kromberg type-section, Barberton greenstone belt.

4.1. Introduction

The Paleoarchean Barberton Greenstone Belt (BGB) of South Africa (Fig. 4.1) comprises some of the world's best preserved ca. 3.2-3.5 Ga volcanic and sedimentary rocks. The central parts (Fig. 4.1) consist mostly of low-grade mafic-ultramafic rock units preserved as the Onverwacht Group of the Barberton Supergroup (Brandl et al., 2006; Lowe and Byerly, 2007). These low-grade rocks may provide an important window into understanding Paleoarchean hydrothermal and crustal processes. However, there are no metamorphic pressure constraints and very few temperature estimates available in the literature for the pervasive greenschist facies metamorphism in the BGB, particularly in stratigraphic context. Furthermore, a number of different low-grade metamorphic types, for example seafloor, regional contact and burial metamorphism have been proposed for the Onverwacht Group but distinguishing these has proven to be controversial (Viljoen and Viljoen, 1969a; Anhaeusser, 1973; de Wit et al., 1987a,b; Cloete, 1999; Hofmann and Harris, 2008). This is in large, partly due to the general challenge of deriving *PT*-constraints from low-grade metabasalts, in comparison to metapelitic rocks (e.g. Frey et al., 1991; Spear, 1993). For example, on the basis of empirical chlorite geothermometry and bulk rock considerations, Xie et al., (1997) proposed a regional metamorphic temperature estimate of ~320^{o}C for the greenstone supracrustal rocks of the BGB. However, various workers have cautioned against the use of empirical chlorite geothermometry and, for a number of crystal-chemical reasons, have questioned its reliability (e.g. de Caritat et al., 1993; Jiang et al., 1994).

This study focuses on deriving metamorphic PT-constraints for the mafic-ultramafic rocks of the Kromberg Formation (traditionally the Kromberg type-section), which occurs in the upper part of the Onverwacht Group, on the SE limb of the Onverwacht Antiformal Fold (OAF; see Fig. 4.1 and 4.2). The central part of the Kromberg type-section includes a 150m wide zone consisting of strongly banded Cr-mica(fuchsitic)-carbonate-chlorite-quartz rocks (Fig. 4.2). The petrogenetic origin of these banded fuchsitic rocks has historically been at the centre of much debate, with contrasting interpretations ranging from very low temperature Archean atmospheric weathering of komatiites, to formation in early `overthrust glide planes´ (Viljoen and Viljoen, 1969a, b; Anhaeusser, 1973; Lowe and Byerly, 1986b; de Wit et al., 1982a,b; 1983; 1986a,b; 1987a,b; 1992; 2011). A detailed petrological analysis of these rocks in terms of what they are, how they formed, and their geodynamic setting is therefore important for understanding the geologic evolution of the BGB.

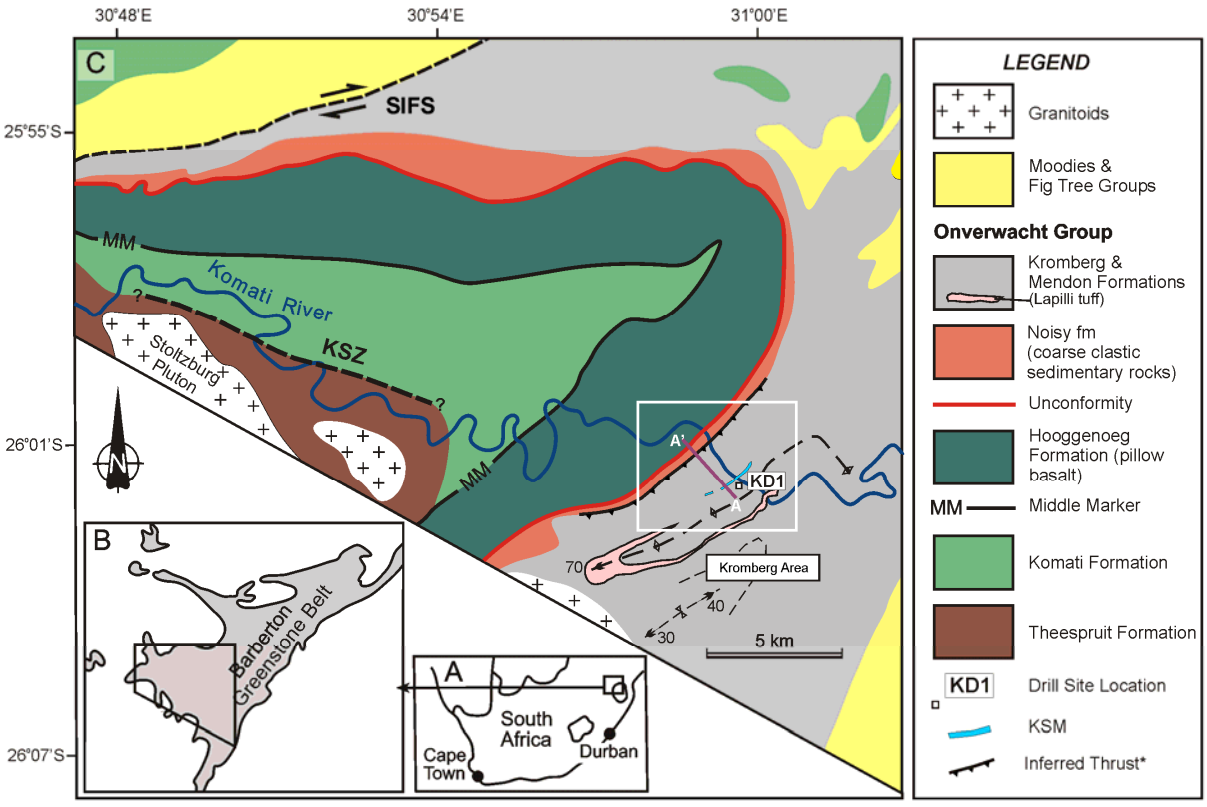

Figure 4.1. Location of the drill site KD1 in the Kromberg Area on the eastern limb of the Onverwacht Antiformal Fold, Barberton Greenstone Belt, South Africa. Drill hole KD1 (Kromdraai 1) is the focus of this study and intercepted at depth the Kromberg Section Mylonites (KSM) in a shear zone with outcrop indicated in light blue on the map along the southern bank of the Komati River (see legend). The red line on the map A-A' corresponds to the lithological profile of Furnes et al. (2011) which highlights the sheared mafic-ultramafic rocks in the KSM. SIFZ = Saddleback-Inyoka Fault Zone. KSZ = Komati Shear Zone. Inferred thrust zone in the Kromberg area between Hooggenoeg and Kromberg Formation after de Wit et al., (1987a,b).

In conjunction with petrographic analysis, chlorite, white mica and chromium-spinel data is presented systematically across the metabasaltic and banded fuchsitic rocks of the Kromberg-type section. The sample set includes both surface samples and new drill core collected during the Barberton Scientific Drilling Project (BSDP; Grosch et al., 2009a,b). *PT*-constraints are derived using a chlorite-quartz-H_2O thermodynamic modelling approach; a chlorite-mica-quartz-H_2O multi-equilibrium calculation; a new geothermobarometer that considers hydration in white mica; and pseudosection modelling in THERMOCALC v 3.31.

The metamorphic results are compared to traditional and recently developed empirical chlorite geothermometers. On the basis of new petrological and field data, the aim is to provide constraints on the geodynamic setting and metamorphic evolution of the rocks in the Kromberg type-section. In addition, a new model for the petrogenetic origin of these banded fuchsitic rocks is proposed.

4.2. Outcrop Geology

The study area is located in the Kromberg Area, on the southeastern limb of the OAF (Fig. 4.1) where the Kromberg Formation is exposed in its type-section along the Komati River in the Songimvelo Nature Reserve. Here, the Kromberg forms a synclinal structure, separated from the uppermost Hooggenoeg Formation by an inferred thrust fault (Fig. 4.1; de Wit, 1986a, 1987b). The most detailed lithological description for the Kromberg-type section is provided by Furnes et al., (2011) and shown in Figure 4.2 (see also corresponding line A-A` on map in Figure 4.1). A fuchsite-carbonate-quartz zone in the central Kromberg type-section, has been interpreted to represent chemically weathered komatiites (Lowe and Byerly, 1986) or a shear zone (Furnes et al., 2011; de Wit et al., 2011). In a recently proposed and controversial stratigraphy model, the former Kromberg Formation (type-section) has been subdivided into an upper Mendon Complex and a lower Kromberg Complex (de Wit et al. 2011; Furnes et al. 2011). However, it is not clear how the newly proposed Mendon Complex relates to the Mendon Formation of Lowe and Byerly (1999a,b, 2007) further north in the Onverwacht Group and in the general stratigraphy of the BGB.

A strong banded fabric is observed in the fuchsite zone and overlies proto-mylonitic to mylonitic fabrics in metapyroxenite in this central zone. For simplicity here, the Kromberg type-section will be referred to in two parts: an upper Kromberg sequence A, above the fuchsite-carbonate-quartz zone, and a lower Kromberg sequence B. The variably sheared mafic-ultramafic rocks including the banded fuchsitic zone will be referred to in this study as the Kromberg Section Mylonites (KSM, Fig. 4.2). The KSM is ~ 150m thick in outcrop and is here, further subdivided into two parts: a lower composite variably mylonitic, dominantly metapyroxenitic section ~85m thick (KS2); and an upper, 65m thick banded fuchsite-quartz-carbonate unit (KS1, see Fig. 4.2 and also Grosch et al., 2009a,b).

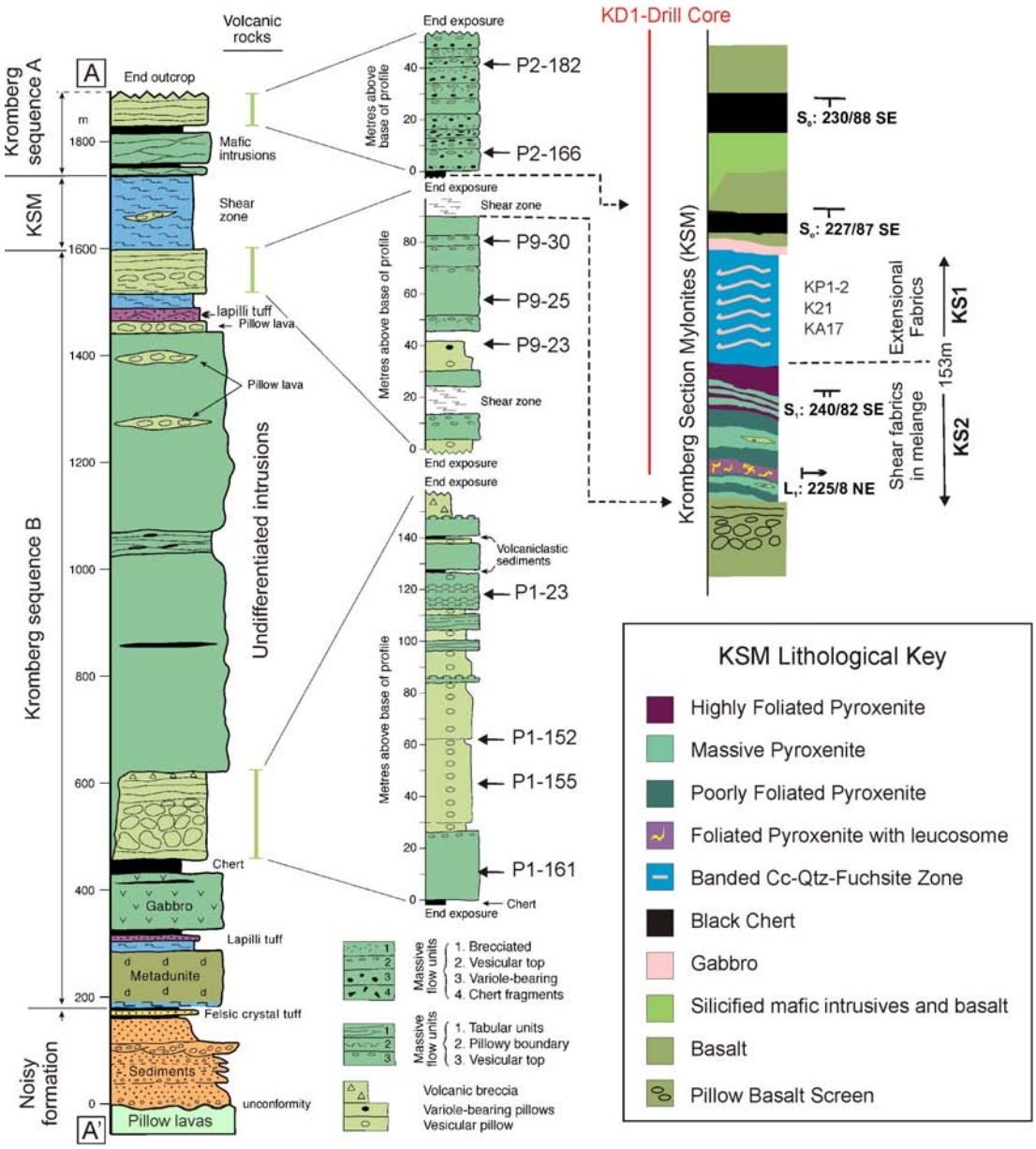

Figure 4.2. Detailed volcanic lithostratigraphy corresponding to the red line on the map in Fig. 4.1 modified after Furnes et al. (2011) and Grosch et al. (2009a,b) for the Kromberg-type section (terminating in the coarse clastic sediments of the Noisy formation that unconformably overlies the Hooggenoeg pillow basalts), showing the Kromberg Section Mylonites (KSM) separating the Kromberg Formation into Kromberg sequence A and the lower Kromberg sequence B. The shear zone in the Kromberg Section is shown in detail on the right. All surface samples (P-samples) including those in the Kromberg Section (K-samples) are indicated on the profile across the stratigraphy. The position and length of the Barberton Scientific Drilling Programme drill core KD1 is indicated.

The outer strongly banded KS1 zone consists of distinct bright emerald green, foliated mafic-ultramafic microlithon bands (Cr-mica, Cr-chlorite) and reddish-brown carbonate-quartz bands (Fig. 4.3a). In the central part of KS1, carbonate-quartz veins appear to represent tension gashes that developed during intense shearing.

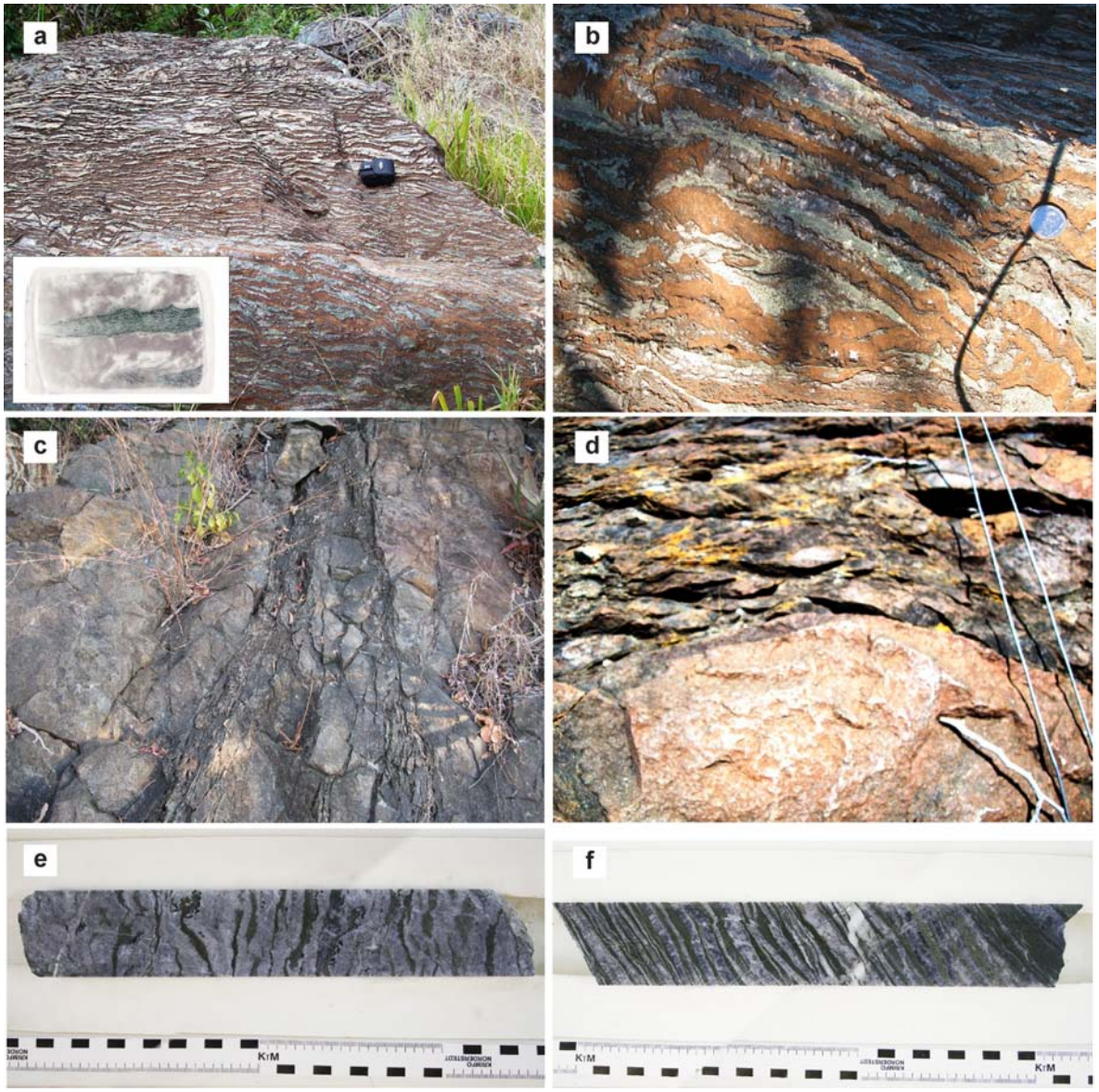

Figure 4.3. KSM mylonitic zone in the central Kromberg type-section. **(a)** Banded fuchsite-carbonate-quartz mylonite in the upper shear zone, KS1. A typical thin section sample (KP21) illustrating the fuchsitic ultramfic microlithon band is shown in the inset. **(b)** Cross-fibrous growth of carbonate-quartz veins in the banded mylonite zone. **(c)** Anastomizing shear splays in the lower metapyroxenite unit (KS2). **(d)** Crystal plastic deformation with foliation

deflected around more competent ultramafic block (boudin). **(e-f)** Banded mylonitic drill core sections from the upper and lower parts of KS1 (scale indicated in cm). The banded mylonite sample in (e) is 27cm long and corresponds to a depth interval of 215.75-216.02m in the drill core KD1. The banded mylonite sample in (f) is 30cm long and corresponds to a depth interval of 231.85-232.15m.

Although the strong banding in the rock records intense shearing related to compressional deformation, the widespread occurrence of extensional cross-fibrous carbonate-quartz veins at high angles to the ultramafic microlithon bands, indicates a major component of extensional deformation (Fig. 4.3b). This demonstrates a major extensional phase syn or post-dating a main phase of shearing. The lower part (KS2) consists of foliated, mylonitic to protomylonitic metapyroxenite with sections of deformed pillow lava screens and metagabbroic blocks (Fig. 4.3c). A number of anastomosing shear splays occurs in this composite metapyroxenitic zone (Fig. 4.3d) with foliation and shearing appearing to be moderately more intense, closer to the transition zone between KS1 and KS2. In the Barberton Scientific Drilling Project (BSDP; Grosch et al., 2009a,b), the lower part of the Kromberg sequence A and the KSM were intercepted in the drill core KD1 (Fig. 4.1 and 4.2).

4.3. Geology of the Drill Core

A summary of the lithological log data for KD1 (total length 261m, drill at 45^{o}) is shown in Figure 4.4. Towards the end of the KD1, the banded mylonitiic zone (KS1) occurs as a 20m thick zone of carbonate-quartz bands/veins in a matrix of dark green chlorite microlithon bands with sulphides (Fig. 4.4). Examples of drill core sections from the upper and lower parts of KS1 are shown in Figure 4.3e and 4.3f. The upper banded part of the KSM displays a central complex zone (Fig. 4.4) with evidence for both ductile and brittle deformation (Fig. 4.4 and see petrographic section below). The ductile deformation is recorded by stylolites and partly folded dynamically recrystallized carbonate-quartz veins and early mylonitic domains.

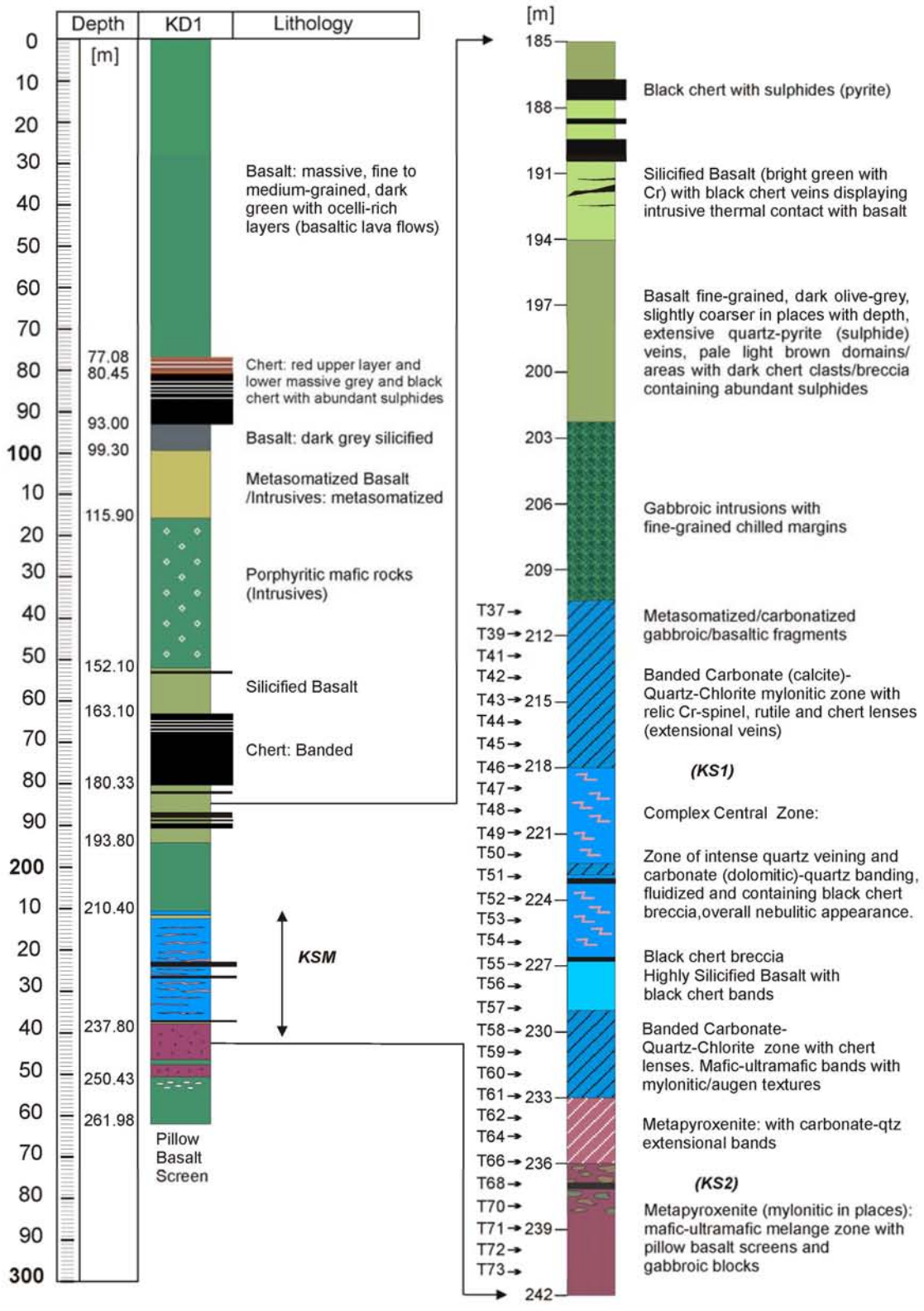

Figure 4.4. Drill core lithological data for KD1 indicating the two major chert horizons, i.e the Footbridge Chert (uppermost) and a lower laminated and massive black chert horizon. The banded mylonites in KSM occur at the end of KD1 and are shown at a higher resolution in the

sketch on the right over the depth interval 185m to 242m. The depth position of the drill core samples are indicated (T-samples) on the figure and in Appendix B.

Whereas the brittle deformation is recorded by 25cm thick extensively fractured composite quartz veins, angular black chert breccia, dolomite and calcite breccia fragments. The outer banded flanks of KS1 display dilation with extensive cross-fibrous extensional qtz-carbonate (calcite) veins between altered foliated mafic-ultramafic bands. Both the upper and lower banded parts of KS1 incorporate “xenoliths” or foreign angular blocks of highly altered gabbro (upper section) and silicified pillow lava screens (lower section). The upper and the lower parts have an overall appearance of previously previously deformed mylonitic rocks with in-situ brecciation fabrics and with subsequent retrograde fluid infiltration recorded by extensional veins. In the deeper parts of KS1 the mafic–ultramafic microlithon bands found between extensional carbonate-quartz bands preserve a foliation. In places, they record a mylonitic fabric that becomes more pronounced and is better preserved with depth.

4.4. Sampling

Fieldwork included mapping and sampling rocks from and directly on either side of the KSM and into the lower Kromberg sequence B. These surface samples include metabasalts (massive flows and pillow lavas) and the KS1 fuchsite-quartz-carbonate (listvenitic) mylonitic rocks. Mafic intrusives and gabbros were not sampled. The surface samples are combined with drill core samples for the banded mylonite zone in KS1. Sample positions in the stratigraphy are shown in Fig. 4.2 and drill core samples are shown in Fig. 4.4. Sample nomenclature (labels) is as follows: Banded mylonite surface samples from KS1 are K-samples; metabasalt surface samples from the Kromberg sequence A are P2-samples. Metabasalt pillow lavas and massive flows of the mid-lower Kromberg sequence B are P9-samples, whereas those of the lowermost Kromberg sequence B are P1 samples. Drill core samples from across the banded mylonite zone KS1 are T-samples.

4.5. Petrography

4.5.1. Banded mylonite (KS1 surface samples)

In thin section, the bright green mafic-ultramafic bands/microlithons in the banded mylonite consist of fine-grained fuchsite ± chlorite overprinting a previously formed ultramafic mylonitic fabric/foliation preserving an augen-type texture between carbonate-quartz bands/veins (Fig. 4.5a,b). The accessory minerals include epidote, rutile, Cr-spinel, magnetite and sulphides (pyrite). The assemblage fuchsite + carbonate + quartz ± sulphides (± Cr-spinel), corresponds to that of listvenite (Halls and Zhoa, 1995, and references therein). In some samples, altered asymmetric σ-style (winged) pyroxene and possibly olivine porphyroclasts are preserved as carbonatized pseudomorphs or replaced by fine-grained fuchsite and/or by chlorite (Fig. 4.5a,b). The textures preserved as σ-style porphyroclast pseudomorphs indicate a sinistral shear sense (Fig. 4.5a,b) and in places are carbonatized (Fig. 4.5a). Extensional cross-fibrous growth textures of carbonate is observed in carbonate-quartz bands that typically follow the orientation of the foliation and augen-texture, with fine-grained carbonate forming extensional fringes along the margins (Fig. 4.5c). The cross-fibrous carbonate-quartz veins are in turn cross-cut by second generation carbonate-quartz veins, indicating at least two vein generations (Fig. 4.5d). Chlorite occurs in rare microdomains in the matrix of mafic-ultramafic microlithon bands and is also preserved at the border of extensional carbonate-quartz veins where it displays anomalous brown birefringence (Fig. 4.5e). In the ultramafic microlithon bands fuchsitic mica is the dominant sheet silicate and chlorite occurs in sparse microdomains in textural contact with the mica (Fig. 4.5e).

4.5.2. Banded mylonite (KS1 drill core samples)

On the outer flanks of KS1, quartz-carbonate extensional veins occur parallel to mafic-ultramafic microlithon bands. An overall porphyroclastic texture is displayed in the ultramafic microlithon bands by brecciated Cr-spinel (see BSE images in Figure 4.11), silicified ferromagnesian grains, magnetite and pyrite with disseminated Ti-bearing phases, such as rutile. Chlorite together with disaggregated Cr-spinel and pyrite define a foliation adjacent to carbonate-quartz bands. Samples collected from the uppermost parts of the banded mylonite show completely altered (silicified) pyroxene and olivine crystals with a poikilitic appearance in a matrix of fine-grained colourless to pale green Cr-chlorite. In the central part of KS1 (central complex zone in Fig. 4.4), mylonitic microlithon bands are disrupted and in-situ brittle deformation appears to have overprinted early mylonitic banding and dynamically

recrystallized carbonate-quartz veins. In this complex central zone, the carbonate-quartz veins are in places folded and brecciated, pointing to possible brittle failure during shearing (Fig. 4.5f). Deformation and brecciation of formerly deformed quartz-carbonate veins resulted in angular quartz clasts with pronounced undulose extinction (Fig. 4.5f).

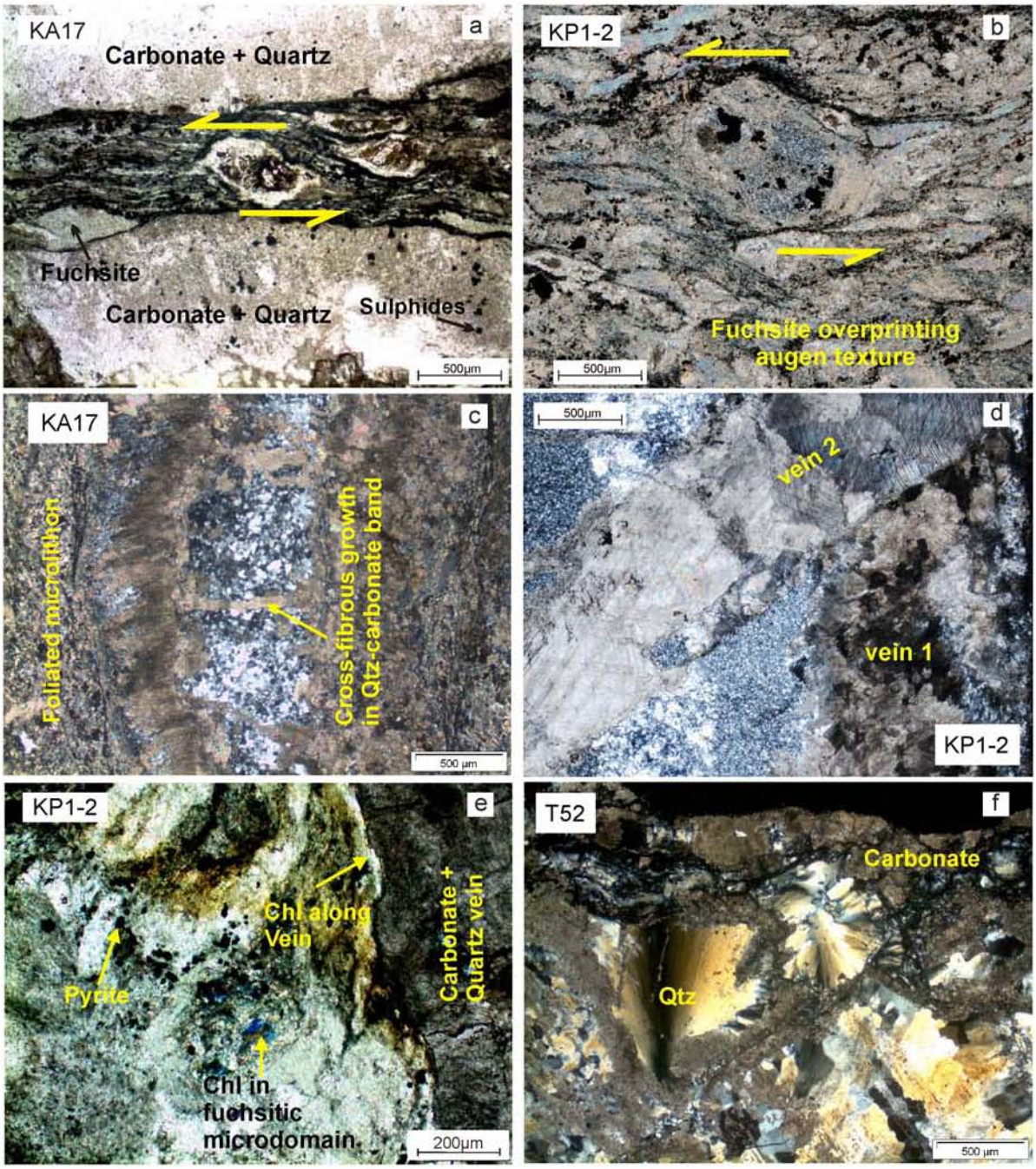

Figure 4.5 *(Continued on next page).*

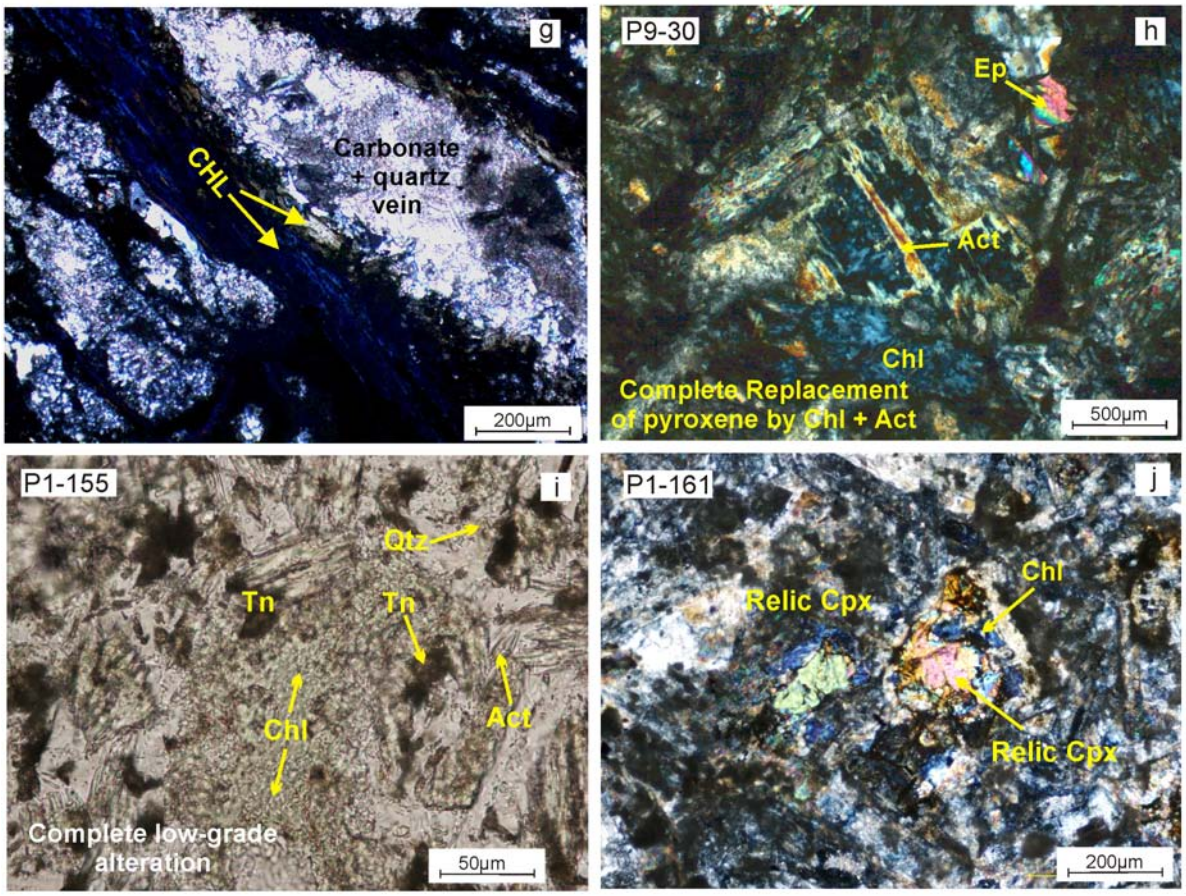

Figure 4.5. Photomicrographs of selected samples from across the Kromberg-type section **(a-b).** Variably developed mylonitic fabrics in listvenite surface samples. **(a)** Former ultramafic (olivine?) σ-style porphyroclast now carbonatized in a matrix of fuchsitic mica overprinting a previously ultramafic mylonitic fabric. **(b)** Former winged ultramafic (pyroxene?) porphyroclast indicating sinistral shear sense and completely silicified and altered to fine-grained mica with rare chlorite. The former mylonitic to protomylonitic ultramafic augen-type deformation fabric is completed overprinted by the fuchsitic mica. **(c)** Quartz-carbonate vein with extensional cross-fibrous growth texture and fibrous carbonate margins. **(d)** Two carbonate vein generations in KSM samples with cross-cutting relationship. **(e)** Occurrence of rare chlorite associated with abundant fuchsite and quartz in an ultramafic microlithon in listvenite sample KP1-2. **(f)** Brittle deformation superimposed on ductile deformation indicated by deformed, brecciated quartz-carbonate veins now cataclastic clasts with undulose extinction recording in-situ brecciation during deformation (in drillcore sample T52 in KS1). **(g)** Drill core sample, T37 in KS1, indicating chlorite observed along quartz-carbonate veins and in the central parts of ultramafic microlithon bands. **(h)** High degree of alteration observed in P9 metabasalt samples below KSM. **(i)** Complete alteration observed in sample

P1-155 from the mid-lower Kromberg type section (THERMOCALC sample). **(j)** Low degree of alteration observed in P1-161 metabasalt sample from the lowermost part of the Kromberg type-section in study area.

The occurrence of chlorite in microlithon bands is similar to that described in surface samples, except that chlorite is the dominant alteration phase in microlithons and fuchsitic mica is absent (Fig. 4.5g). Shear fabrics and foliation development appear to intensify with depth. Intense augen-type textures similar to that preserved in fuchsite-bearing surface samples (Fig. 4.5a and b) are observed near the base of the KS1 in banded mylonite zone that are now completely overprinted and chloritized. Immediately below KS1 in the sheared metapyroxenitic zone, radial growth of elongate pyroxene crystals is pseudomorphed by quartz. In the lower parts of KS2 more massive, variably deformed and intensely carbonated metapyroxenite occurs with a hydrothermally altered pillow lava metabasalt screen. Petrographic analysis of samples throughout the banded KSM zone found no serpentine minerals.

4.5.3. Metabasalts of the Kromberg above and below the KSM

Although completely altered, igneous textures are still preserved in the metabasalts, and range from equigranular, porphyritic, amygdoloidal and sub-ophitic. In almost all samples, the igneous phases are completely replaced by metamorphic minerals. The metamorphic minerals are typically chlorite, actinolite, epidote, albite, quartz, titanite, sericite and magnetite. Carbonate and sulphides are also present in some of the rocks. No hornblende has been observed in any of the samples.

Proportion and occurrence of these greenschist facies minerals vary considerably depending on metamorphic grade. Unlike the KSM samples, no deformation fabric or preferred orientation of phyllosillicate metamorphic minerals are observed. Rather metamorphic minerals occur in restricted microdomains or alteration veins. Chlorite and quartz is present in all samples typically in the groundmass and in alteration microdomains. Actinolite is texturally associated with groundmass chlorite in most samples and typically occurs as fine nematoblasts fringing the grain boundaries of relic pyroxene grains. In the most advance stages of alteration (uralitization) of pyroxene, actinolite completely replaces clinopyroxene with a higher proportion of chlorite + epidote + quartz present. Metamorphic titanite and/or rutile occur in mono-mineralic aggregates or as rim overgrowths replacing

minor ilmenite. Clinozoisite/epidote shows more Fe-rich rims and occurs as single, stubby, euhedral, prismatic crystals of variable size, or as granular aggregates in textural equilibrium with chlorite and quartz, or in places with actinolite, quartz and albite.

Intensity of greenschist facies metamorphic alteration in the Kromberg metabasalts varies with distance below the shear zone. Metabasalts (P9-samples) directly below the shear zone displaying very advance degrees of chloritization and alteration of pyroxene to actinolite (Fig. 4.5h). Pyroxene grains are completely pseudomorphed by actinolite and chlorite (Fig. 4.5h) and there is extensive development of large metamorphic microdomains consisting of chlorite, epidote, actinolite and quartz with the former igneous textures completely overprinted (Fig. 4.5h). No hornblende is present in these samples and these metabasalts lack deformation fabrics. Metamorphic epidote form clusters and display radial elongate growth morphology.

In metabasalts above the shear zone, hydrous alteration minerals are not as abundant as in the metabasalts directly beneath the shear zone (i.e. P9-30 and P9-25). Metabasalts of the mid-lower Kromberg also show chlorite + epidote + actinolite + albite present as alteration minerals but generally lower abundance of actinolite development in comparison to the P9-pillow basalts. Sample P1-155 displayed complete alteration with no igneous phases present (Fig. 4.5i) A metabasalt (P1-161) from the lowermost Kromberg displays a very low degree of alteration indicated by sericitization of plagioclase and a low proportion of chlorite and epidote in the groundmass. Uralitization of pyroxene is limited, with the relic pyroxene cores still being preserved (Fig. 4.5j).

4.6. Mineral Chemistry

Electron microprobe analysis of the metamorphic mineral phases, chlorite and fuchsite, was carried out to derive mineral compositions for calculation of *PT*-conditions. Relic Cr-spinel was also analyzed as it was the only unaltered mineral that could be used to derive protolith constraints. Cr-spinel analysis has a long history as a petrogenentic indicator tool and in the interpretation of tectonic setting of ophiolitic rocks (Irvine, 1965; Dick and Bullen, 1984; Matveev and Balhaus, 2002) as well as in Archean rock sequences (Cotterill, 1969; Chadwick and Crewe, 1986; Stowe, 1994; Byerly, 1999; Kusky and Jianghai, 2010). Chemical analyses of the minerals were obtained using a JEOLJXA-8600 electron microprobe, equipped with

four wavelength-dispersive spectrometers, at the Department of Geological Sciences, University of Cape Town and an ARL electron microprobe equipped with a WDS at the Department of Earth Science, University of Bergen. Running conditions were 20 nA and 15 nA beam current for each instrument respectively, and 15 kV accelerating voltage for both instruments. Counting time for the elements determined ranged from 10 to 60s at both peak and background. Mineral abbreviations are after Kretz (1983) and Bucher and Frey (1994).

4.6.1. Chlorite

Chlorite grains analyzed in this study have a sum of Ca + Na + K below 0.08 apfu (Table 4.1 and Appendix D1). Contamination with smectite or other clay minerals can thus be ruled out. Chemical formula was calculated based on 14 oxygen atoms (see Table 4.1 caption). Site occupancy is calculated according to Vidal et al., (2005; 2006). All chlorite in the Kromberg type section in surface and drill core samples are tri-octahedral in nature (Fig. 4.6a and b). Their composition can be expressed as a linear combination of clinochlore, daphnite, 14A amesite and sudoite and therefore, fulfill the compositional requirements for applying the thermodynamic model of Vidal et al. (2001, 2005, 2006) to estimate metamorphic temperature. In the banded mylonite KSM samples, the chlorite analyzed along carbonate-quartz veins has an intermediate Fe-Mg composition (Fig. 4.6a and b). Chlorite in the ultramafic microlithon bands away from the margins of these extensional veins is Cr-bearing, reflecting the protolith composition (Fig. 4.6c and d). The Cr-bearing chlorite has Cr contents in the range of 0.05 to 0.21 apfu (Fig. 4.6c). Chlorite composition of massive pillow lava metabasites of Kromberg sequence A and B displays generally intermediate XMg (Mg/Mg + Fe) values ranging between 0.38 and 0.58 (Fig. 4.6a). Chlorite composition in the banded mylonite zone (KS1) indicates generally higher XMg values ranging between 0.52-0.75 (Fig. 4.6b). Surface sample, KP1-2 from the banded mylonitic zone (KS1) displays Cr-bearing chlorite with higher 14A amesite content in comparison to the other chlorites (Fig. 4.6b).

4.6.2. White Mica

Mica structural formula is presented in Table 4.2 and Appendix D2 and has been calculated on the basis of 11 oxygen and assuming $Fe_{Total} = Fe^{2+}$. Mica composition corresponds to that of muscovite (Fig. 4.6e) with low celadonite and phengitic components (Fig. 4.6e). The micas are also chromium bearing (fuchsitic) with Cr^{3+} contents mostly ranging between 0.05 and 0.15 apfu (Fig. 4.6f). The low Si-content is also shown in Figure 4.6f indicating that the studied micas most likely formed under low pressure conditions (e.g. see Velde, 1965).

Table 4.1. Representative electron microprobe analysis of chlorite mineral compositions in Kromberg metabasalts and ultramafic KSM rocks

	Above the KSM							In the KSM						
	Surface							Drill core						
Sample	P2-183-52	P2-183-38	P2-166-29	P2-166-12	KP1-2-chlx2	KP1-2-chlx4	KP1-2-chlx5	T37chl33	T37chl36	T41chlb8	T41chl-a1	T59-chl9	T59-chl4	T44chl13
SiO_2	27.25	25.52	27.91	28.58	25.99	24.95	25.23	28.21	25.11	28.78	26.79	28.73	28.05	28.80
TiO_2	0.06	0.01	0.04	0.07	0.04	0.05	0.14	0.07	0.05	0.02	0.09	0.66	0.08	0.06
Al_2O_3	18.70	18.83	19.02	18.37	24.57	22.70	22.63	20.34	18.92	20.10	18.04	21.81	22.71	20.35
FeO*	28.64	28.74	25.06	24.12	25.08	25.79	25.14	24.37	24.36	24.12	24.37	16.64	17.48	20.34
MnO	b.d.l	b.d.l	b.d.l	b.d.l	0.11	0.17	0.20	0.19	0.18	0.13	0.18	0.12	0.17	0.15
MgO	13.98	14.15	16.78	17.45	12.71	12.16	13.83	16.79	15.85	17.93	18.36	21.98	22.27	19.46
Cr_2O_3	b.d.l	b.d.l	b.d.l	b.d.l	1.03	1.09	1.36	1.28	1.24	0.58	1.69	0.15	0.14	1.07
CaO	0.41	0.09	0.15	0.14	0.13	0.12	0.21	0.03	0.18	0.03	0.05	0.03	0.03	0.09
Na_2O	b.d.l	0.11	b.d.l	0.08	0.07	0.05	0.24	0.04	0.04	0.04	0.02	0.02	0.02	0.06
K_2O	0.03	0.02	b.d.l	0.05	0.33	0.06	0.82	0.01	b.d.l	0.01	0.02	0.02	0.01	0.06
F	b.d.l	b.d.l	b.d.l	b.d.l	b.d.l	b.d.l	b.d.l	b.d.l	b.d.l	b.d.l	b.d.l	b.d.l	b.d.l	b.d.l
Total	89.06	87.47	88.97	88.85	90.06	87.15	89.80	91.33	85.94	91.74	89.61	90.15	90.96	90.44
Structural formula calculated on the basis of 14 O														
Si	2.77	2.69	2.78	2.83	2.66	2.58	2.59	2.77	2.70	2.78	2.72	2.72	2.70	2.79
Al^{iv}	1.23	1.31	1.22	1.17	1.34	1.42	1.41	1.23	1.30	1.22	1.28	1.28	1.30	1.21
Al^{vi}	1.02	1.04	1.02	0.98	1.52	1.31	1.47	1.13	1.10	1.07	0.89	1.21	1.27	1.11
Mg	2.12	2.23	2.49	2.58	1.94	2.11	2.07	2.46	2.54	2.58	2.78	3.11	3.19	2.81
Fe^{2+}	1.46	1.91	1.13	1.00	2.10	1.44	1.98	1.13	1.76	1.03	1.22	0.59	1.16	0.74
Fe^{3+}	0.97	0.63	0.96	1.00	0.21	0.71	0.24	0.87	0.43	0.92	0.85	0.73	0.24	0.91
Sum other elmts	0.05	0.02	0.02	0.03	0.05	0.14	0.08	0.02	0.04	0.02	0.02	0.02	0.02	0.03
Oct Sum	5.62	5.82	5.62	5.59	5.88	5.78	5.88	5.61	5.88	5.62	5.77	5.65	5.89	5.60
XMg	0.59	0.54	0.69	0.72	0.51	0.48	0.59	0.68	0.59	0.71	0.69	0.84	0.73	0.79
$*XFe^{3+}$	40	25	46	50	12	8	32	44	20	47	41	55	17	55
T (^oC) Vidal (2006)	257	334	263	336	292	336	293	242	403	252	326	266	421	245
T(^oC) Inoue (2009)	244	368	248	228	307	351	308	238	391	244	337	250	400	230
T(°C) H&V (1992)	286	327	281	254	346	339	384	286	321	283	309	288	323	278

$*XFe^{3+}$ calculated at convergence of equilibria (after Vidal et al., 2001, 2006). b.d.l = below detection limit

Table 4.1. *(Continued)*

	Below the KSM						Mid-lowermost Kromberg						
	Surface						Surface						
Sample	P9-23-26	P9-23-5	P9-30-18	P9-30-23	P9-25-34	P9-25-43	P1-23-26	P1-23-39	P1-155-5	P1-155-36	P1-152-23	P1-152-39	P1-161-4
SiO_2	28.13	26.90	26.84	25.61	26.79	24.97	26.49	25.22	26.42	25.25	28.37	26.39	29.13
TiO_2	0.03	0.01	0.03	0.05	0.00	0.05	0.12	0.12	0.05	0.01	b.d.l	0.05	0.02
$Al2O_3$	20.89	21.47	19.26	18.49	18.48	19.81	18.67	19.82	19.10	19.60	20.18	20.72	17.88
*FeO	25.05	25.91	32.07	33.57	27.87	28.77	28.85	28.95	30.07	29.57	28.33	27.97	29.69
MnO	0.45	0.43	0.46	0.44	b.d.l	b.d.l	b.d.l	b.d.l	b.d.l	b.d.l	0.48	0.47	0.36
MgO	15.77	16.30	11.52	12.27	13.12	12.94	12.71	12.83	11.94	12.49	13.65	14.35	14.00
Cr_2O_3	b.d.l	b.d.l	b.d.l	b.d.l	b.d.l	b.d.l	b.d.l	b.d.l	b.d.l	b.d.l	b.d.l	b.d.l	b.d.l
CaO	0.36	0.02	0.43	0.03	0.76	0.09	0.15	0.07	0.09	0.11	0.11	0.15	0.05
Na_2O	0.01	0.01	0.21	0.01	0.06	b.d.l	0.04	b.d.l	0.02	0.05	b.d.l	0.03	0.01
K_2O	0.02	b.d.l.	0.06	0.01	0.01	0.01	0.03	0.01	0.01	b.d.l	0.03	0.01	0.05
F	b.d.l	b.d.l	b.d.l	b.d.l	b.d.l	b.d.l	b.d.l	b.d.l	b.d.l	b.d.l	b.d.l	b.d.l	b.d.l
Total	90.70	91.06	90.88	90.49	87.10	86.64	87.06	87.00	87.71	87.09	91.15	90.15	91.19
Structural formula calculated on the basis of 14 O													
Si	2.76	2.70	2.74	2.69	2.79	2.69	2.77	2.69	2.77	2.69	2.80	2.69	2.92
Al^{iv}	1.24	1.30	1.26	1.31	1.21	1.31	1.23	1.31	1.24	1.31	1.20	1.31	1.08
Al^{vi}	1.18	1.24	1.06	0.98	1.05	1.22	1.08	1.18	1.12	1.16	1.15	1.18	0.96
Mg	2.31	2.44	1.75	1.92	2.03	2.08	1.98	2.04	1.86	1.99	2.01	2.18	2.11
Fe^{2+}	1.27	1.92	1.89	2.40	1.45	2.32	1.59	2.07	1.79	2.08	1.40	1.88	1.47
Fe^{3+}	0.79	0.26	0.85	0.55	0.97	0.28	0.93	0.51	0.84	0.55	0.94	0.50	0.98
Sum other elmts	0.08	0.04	0.11	0.04	0.09	0.01	0.02	0.01	0.01	0.02	0.05	0.06	0.05
Oct Sum	5.63	5.90	5.67	5.89	5.60	5.90	5.60	5.81	5.63	5.80	5.56	5.81	5.57
XMg	0.65	0.56	0.48	0.44	0.58	0.47	0.55	0.50	0.51	0.49	0.59	0.54	0.59
*XFe^{3+}	39	12	31	19	40	11	37	20	32	21	40	21	40
T (^oC) Vidal (2006)	243	420	256	396	245	417	241	318	244	310	217	321	143
T(^oC) Inoue (2009)	228	397	246	426	224	457	241	346	248	338	210	317	202
T(°C) H&V (1992)	291	323	301	327	281	325	284	326	289	327	273	326	215

*XFe^{3+} calculated at convergence of equilibria (after Vidal et al., 2001, 2006). b.d.l = below detection limit

Table 4.2. Representative mica (fuchsite) analyses in listvenite surface samples of KS1, Kromberg type-section

	KP21-mica-1	KP21-mica-13	KP21-mica-12	KP21-mica-21	KP1-2mica-1	KP1-2mica-11	KP1-2mica-17	KP1-2mica-4	KA17-mica-6	KA17-mica-9	KA17-mica-13	KA17-mica-16
SiO_2	48.26	48.86	47.89	47.77	46.40	48.35	47.23	46.50	46.48	47.77	49.02	48.78
TiO_2	0.22	0.14	0.25	0.17	0.15	0.27	0.12	0.24	0.13	0.22	0.09	0.28
Al_2O_3	36.13	35.95	35.47	35.80	35.91	35.80	36.69	32.18	35.28	34.71	34.21	34.71
Cr_2O_3	1.31	1.58	1.42	1.37	1.12	1.61	1.26	0.62	1.16	1.87	0.93	2.01
FeO*	0.76	0.81	0.84	0.85	0.66	1.23	0.60	1.51	1.26	0.74	0.72	0.97
MnO	0.04	0.02	0.04	b.d.l	b.d.l	0.07	0.04	0.06	0.06	b.d.l	0.02	0.04
MgO	0.90	0.99	1.02	1.04	0.89	1.04	0.69	1.74	0.82	1.14	1.25	1.28
CaO	b.d.l	0.02	b.d.l	0.01	0.16	0.13	0.13	0.04	b.d.l	b.d.l	0.02	0.02
Na_2O	0.39	0.42	0.38	0.48	0.70	0.56	1.26	0.21	0.38	0.44	0.37	0.33
K_2O	10.48	10.49	10.64	10.54	10.28	10.11	9.33	10.75	10.32	10.37	9.77	9.87
F	0.02	0.14	0.22	0.19	0.11	0.11	0.00	0.12	0.09	0.27	0.26	0.20
Cl	0.04	0.03	0.08	0.07	0.13	0.11	0.14	0.05	0.06	0.08	0.28	0.08
Total	98.53	99.45	98.25	98.29	96.51	99.39	97.50	94.02	96.04	97.62	96.94	98.57
Si	3.10	3.11	3.10	3.09	3.05	3.09	3.06	3.16	3.08	3.11	3.19	3.14
Ti	0.01	0.01	0.01	0.01	0.01	0.01	0.01	0.01	0.01	0.01	0.00	0.01
Al^{iv}	0.90	0.89	0.90	0.91	0.95	0.91	0.94	0.84	0.92	0.89	0.81	0.86
Al^{vi}	1.83	1.81	1.81	1.82	1.84	1.79	1.86	1.73	1.83	1.78	1.82	1.77
Cr	0.07	0.08	0.07	0.07	0.06	0.08	0.06	0.03	0.06	0.10	0.05	0.10
$*Fe^{2+}$	0.04	0.04	0.05	0.05	0.04	0.07	0.03	0.09	0.07	0.04	0.04	0.05
Mn	0.00	0.00	0.00	0.00	0.00	0.00	0.00	0.00	0.00	0.00	0.00	0.00
Mg	0.09	0.09	0.10	0.10	0.09	0.10	0.07	0.18	0.08	0.11	0.12	0.12
Ca	0.00	0.00	0.00	0.00	0.01	0.01	0.01	0.00	0.00	0.00	0.00	0.00
Na	0.05	0.05	0.05	0.06	0.09	0.07	0.16	0.03	0.05	0.06	0.05	0.04
K	0.86	0.85	0.88	0.87	0.86	0.82	0.77	0.93	0.87	0.86	0.81	0.81
Xprl	0.09	0.09	0.07	0.07	0.04	0.10	0.06	0.04	0.08	0.08	0.14	0.15
Xms	0.86	0.85	0.88	0.87	0.86	0.82	0.77	0.93	0.87	0.86	0.81	0.81
Xpg	0.05	0.05	0.05	0.06	0.09	0.07	0.16	0.03	0.05	0.06	0.05	0.04
T0 (^oC)	295	288	296	304	342	295	331	281	312	290	261	268
T2kbar' (^oC)	334	325	335	346	392	334	374	323	354	325	292	302
T3kbar (^oC)	353	343	355	367	417	353	395	345	375	342	308	319

*All Fe reported as Fe^{2+}. n.d = not determined. b.d.l = below detection limit.

T (^oC) calculated after the method of Dubaq et al. (2009). Uncertainties on mica T estimates are 30^oC.

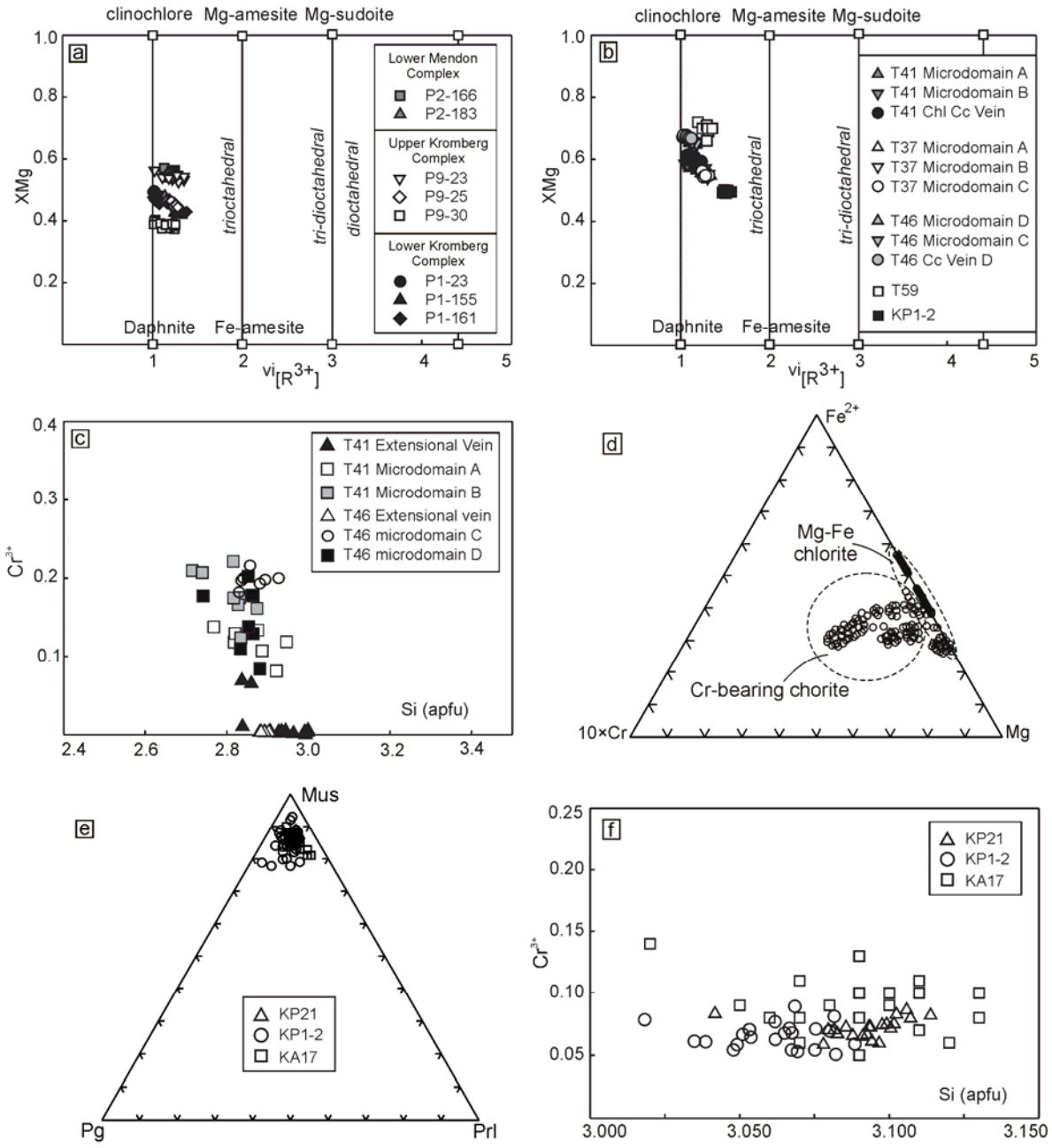

Figure 4.6. Mineral chemistry of chlorite and mica (all structural formulae calculated assuming $Fe^{2+} = Fe_{Total}$). (a-b) Classification of chlorites after Bailey, (1988) where XMg = ($Mg^{2+}/Mg + Fe^{2+}$) and $^{vi}[R^{3+}]$ = sum of trivalent cations in octahedral sites. **(a)** Composition of chlorites in various metabasaltic surface samples across the Kromberg sequence. **(b)** Composition of chlorites in a KS1 listvenite surface sample and drill core banded mylonitic samples. **(c-d)** Composition of chlorite (Cr-poor and Cr-rich) in ultramafic microlithon bands in selected drill core samples (T41, T46). **(e)** Mica composition plotted on a ternary diagram after Guidotti (1984), indicating muscovite composition for the 3 listvenite samples. Mus =

Muscovite, Pg = Paragonite, Prl = Pyrophyllite. **(f)** Fuchsitic mica composition with low Si-contents indicated in a Cr^{3+} vs Si binary diagram, with Cr-content for the micas ranging between 0.05 – 0.15 apfu.

4.6.3. Cr-Spinel

Spinels were analysed in the banded mylonites and the structural formula was calculated on the basis of 32 oxygens (Table 4.3). Compositions of the studied spinel are compared to a limited dataset available for spinel compositions in the BGB (Fig. 4.7a).

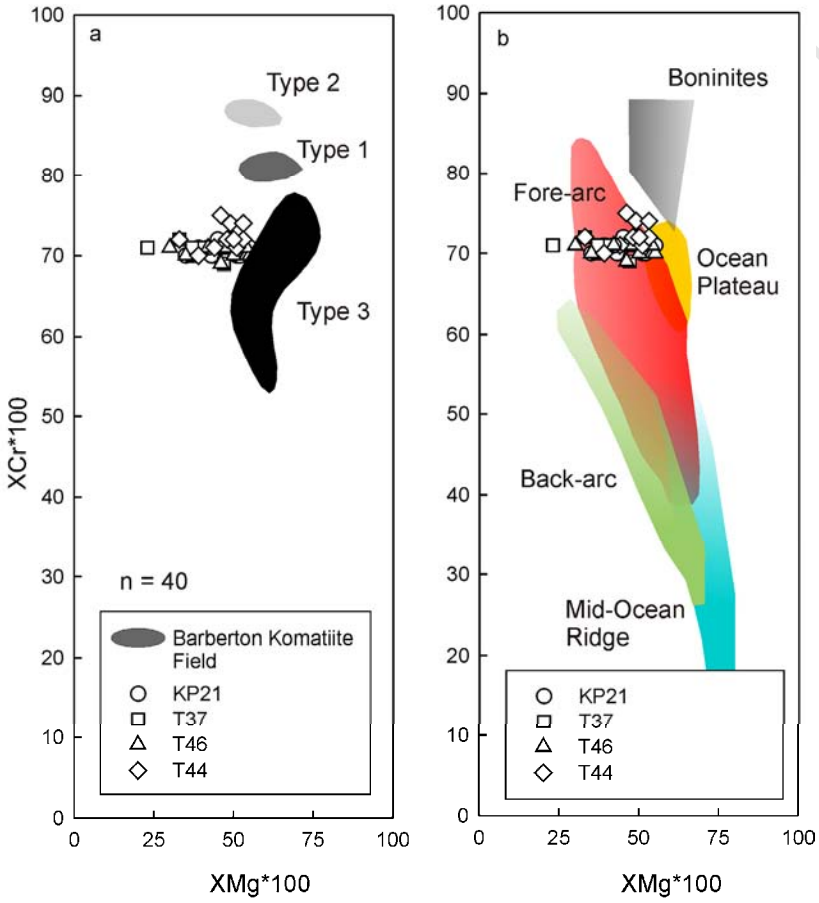

Figure 4.7. Cr-spinel composition and geodynamic classification. **(a)** Cr-number [XCr*100 = 100*(Cr/Cr+Al) vs Mg-number [XMg*100 = $100*Mg^{2+}/(Mg^{2+} + Fe^{2+})$] diagram for ultramafic banded mylonite drill core samples and listvenite surface samples in comparison to some Cr-spinel data available for basaltic komatiites in the BGB from the Onverwacht Group (data for komatiitc fields after Byerly et al., 1999). **(b)** Classification of Cr-spinel in banded mylonite samples in relation to tectonic setting (fields after Dick and Bullen, 1984; Barnes and Roeder, 2001) pointing to petrogenesis of the Kromberg spinels in a fore-arc setting.

Table 4.3. Representative Cr-spinel compositions from the KSM

Sample	KP21-8	KP21-12	KP21-1	T37-1	T37-7	T37-24	T46-4	T46-6	T46-15	T44-3	T44-9	T44-6
SiO_2	0.14	0.09	0.12	0.11	0.06	0.49	0.08	0.16	0.1	0.06	0.08	0.07
TiO_2	0.36	0.53	0.41	0.53	0.74	0.51	0.55	0.52	0.35	0.46	0.55	0.72
Al_2O_3	14.02	13.36	13.61	13.64	12.78	14.35	13.53	14.03	13.95	12.4	13.14	13.24
$Cr2O_3$	49.83	50.25	49.6	49.25	47.21	48.67	49.91	47.96	50.74	52.01	51.19	49.34
FeO	20.74	20.14	21.2	19.65	26.67	19.96	19.27	23.55	17.23	17.38	17.58	20.79
Fe_2O_3	5.33	5.74	5.92	6.72	6.34	5.95	6.5	5.79	6.07	6.25	6.13	7.43
MnO	0.31	0.38	0.32	0.4	0.68	0.25	0.24	0.38	0.31	0.32	0.28	0.27
MgO	8.93	9.28	8.64	9.71	4.36	9.97	10.07	7.13	11.29	11.02	11.1	8.26
CaO	b.d.l	0.02	b.d.l	0.01	0.01	0.1	0.01	0.03	0.01	0.04	0.01	0.03
ZnO	0.13	0.13	0.09	0.12	0.93	0.1	0.09	0.11	0.03	0.03	0.06	0.14
Total	99.79	99.92	99.91	100.14	99.77	100.35	100.28	99.67	100.08	99.98	100.12	100.3
Si	0.04	0.02	0.03	0.03	0.02	0.13	0.02	0.04	0.03	0.01	0.02	0.01
Ti	0.07	0.1	0.08	0.1	0.15	0.1	0.11	0.1	0.07	0.09	0.11	0.12
Al	4.32	4.11	4.2	4.17	4.09	4.36	4.13	4.38	4.22	3.79	3.99	4.15
Cr	10.3	10.38	10.28	10.1	10.14	9.91	10.21	10.04	10.29	10.65	10.43	10.2
Fe^{+2}	4.53	4.4	4.65	4.26	6.06	4.3	4.17	5.22	3.7	3.76	3.79	3.91
Fe^{+3}	1.17	1.25	1.3	1.46	1.44	1.28	1.41	1.28	1.3	1.35	1.32	1.4
Mn	0.07	0.08	0.07	0.09	0.16	0.05	0.05	0.09	0.07	0.07	0.06	0.05
Mg	3.48	3.61	3.38	3.76	1.77	3.83	3.88	2.82	4.32	4.26	4.27	4.15
Ca	-	0.01	-	-	-	0.03	-	0.01	-	0.01	-	0.01
Zn	0.02	0.03	0.02	0.02	0.19	0.02	0.02	0.02	0.01	0.01	0.01	0.01
Total	24	24	24	24	24	24	24	24	24	24	24	24
Fe#*100	57	55	58	53	77	53	52	65	46	47	47	49
Mg#*100	43	45	42	47	23	47	48	35	54	53	53	51
Cr#*100	70	72	71	71	71	69	71	70	71	74	72	71

b.d.l = below detection limit

The spinels have XCr [(Cr/(Cr + Al)] ratios between 0.69 and 0.75 apfu and XMg [Mg/(Mg + Fe^{2+}] ratios between 0.25 and 0.61. The Cr-numbers or Cr#'s (XCr*(100) = 100*Cr / Cr + Al) of the studied spinel (69-75) are different from that of spinel in basaltic komatiites and komatiites in the Onverwacht Suite (Byerly, 1999) with relatively low Mg-numbers (Fig. 4.7a). The low Mg# and high Cr#'s of the Kromberg spinels are very similar to those that formed in mantle peridotite of supra-subduction zone settings (e.g. Dick and Bullen, 1984; Barnes and Roeder, 2001; Kusky and Jiang, 2010). The Kromberg Cr-spinel compositions are contrasted to those in Barberton komatiites that show a boninitic and oceanic plateau association (Fig. 4.7a).

4.7. Metamorphic *P-T-aCO₂* conditions (THERMOCALC modeling)

As a first order attempt to estimate metamorphic *PT*-conditions for the Kromberg rocks, a general pseudosection was calculated for a typical pillow lava metabasite from the mid-lower Kromberg (sample P1-155) using THERMOCALC tc331 (Powell and Holland, 1988), the internally consistent dataset of Holland and Powell (1998) and the solution models that are cited in the figure caption of Fig. 4.8. Sample (P1-155) was used here since it shows a homogenous alteration texture (equilibrium texture) and is completely altered with the absence of igneous mineral relics (see Fig. 4.5i). The XRF whole rock analysis of sample P1-155 shows that the K_2O and the MnO constitute less than one percent of the bulk rock (see figure caption of Fig. 4.8). A *P-T* pseudosection was, therefore constructed in the chemical system NCFMASHTO+qz+H_2O (Fig. 4.8a).

The *P-T* pseudosection (Fig. 4.8a) is characterized by a series of mineral assemblage fields with steep boundaries. Three divariant fields (ep chl di lws pmp ab ttn), (act hbl ep chl pl ab ttn) and (act hbl ep pl ab ttn mag) appear at (250°C – 4.5 kbar and 280°C – 5.3 kbar), (450°C – 2.5 kbar and 485°C – 5 kbar) and (450°C – 2.7 kbar and 500°C – 4.5 kbar); respectively. The disappearance of pmp and lws occurs above (250°C – 3.7 kbar and 310°C – 7 kbar). Actinolite is stable over a wide range of pressure and temperature (> 270°C), indicating the greenschist facies conditions above this temperature. Hornblende becomes stable above ~450°C and 2.7 kbar. Magnetite-in reactions appear between 440°C – 2 kbar and 500°C – 4.5 kbar. Plagioclase stability field starts at (430°C – 2 kbar) and (485°C – 5 kbar). Diopside is a stable phase at low temperature condition over a wide pressure range. The

diopside stability region at these *P-T* conditions was defined by Banno (1998) as the pumpellyite-diopside region. No metamorphic or relic diopside is present in sample P1-155 (see Fig. 4.5i).

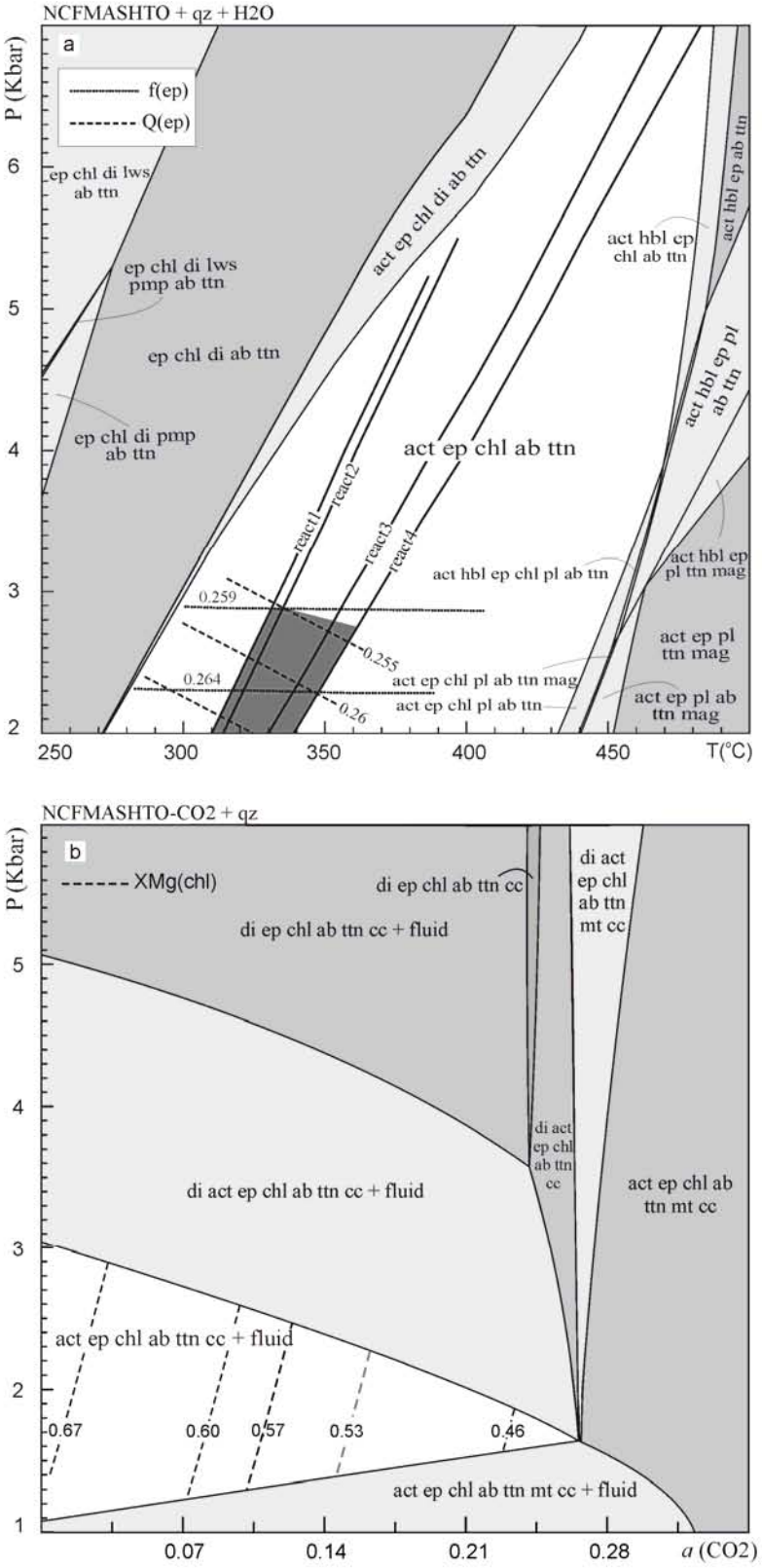

Figure 4.8. Pseudosections for sample P1-155. **(a)** *P-T p*seudosection in the system NCFMASHTO+qz+H_2O (H_2O in excess) for the metabasalt sample P1-155. The oxidation state was calculated using Le Maitre (1976) equation for the partitioning of FeO and Fe_2O_3 from $Fe_2O_3^{tot}$ and the program MBC1.7 (Abu-Alam and Stüwe, 2009). The bulk composition is XRF (mol. %): SiO_2:64.51, Al_2O_3:8.09, CaO:8.19, MgO:6.40, FeO:6.00, Na_2O:5.07, TiO_2:1.07, O (Fe_2O_3) :0.68 H_2O: (10-0), CO_2: (0-10). React. 1 is cz + parg + qz = an + ab + tr + H_2O. React. 2 is cz + ab + clin + qz = an + parg + H_2O. React. 3 is cz + daph + qz = an + fact +H_2O. React. 4 is cz + clin + qz = an + tr + H_2O. The white polygons indicate conditions constrained by epidote mineral isopleths and end-member reactions. Dashed lines in the legend indicate epidote composition isopleths, with the site distribution f(ep) = (Fe^{3+}(M_1 & M_3)/(Fe^{3+}(M_1 & M_3) + Al (M_1 & M_3)) and Q(ep) = (½ (Fe^{3+}(M_3) - Fe^{3+}(M_1)) (Holland and Powell, 1998; Patrier et al., 1991). Epidote composition isopleths plotted in the PT stability field intersect with the four end-member reactions and indicate metamorphic conditions of *T* = 310-360^{o}C and *P* < 2.9 kbar (dark grey area). The position of the modelled XMg chlorite composition isopleths using THERMOCALC are indicated by the dashed lines in the highlighted PT field (see text for discussion). Mineral abbreviations are after Kretz (1983). **(b)** *P-a*(CO_2) pseudosection for the same bulk composition as in Fig. 4.8a, the oxidation state was calculated using Le Maitre (1976) equation for the partitioning of FeO and Fe_2O_3 from $Fe_2O_3^{tot}$ and the program MBC1.7 (Abu-Alam and Stüwe, 2009). The following a-x models were used: amphibole (Diener et al., 2007); clinopyroxene (Green et al., 2007); plagioclase (Holland and Powell, 2003); chlorite (Holland et al., 1998; Mahar et al., 1997); epidote (Holland and Powell, 1998); magnetite (White et al., 2002) and Fluid (Holland and Powell, 1998).

The equilibrium assemblage of sample P1-155 (act ep chl ab ttn) appears in a quadrovariant field (see white *PT*-field in Fig. 4.8a) in the region between (270^{o}C – 432^{o}C at 2 kbar) and narrows to higher pressure where it terminates at (442 ^{o}C – 488 ^{o}C at 7 kbar). Within this field, the *P-T* conditions can be further constrained using the epidote mineral composition (see epidote composition given in Table 4.4) with the site distribution f(ep) = (Fe^{3+}(M_1 & M_3)/(Fe^{3+}(M_1 & M_3) + Al (M_1 & M_3)), Q(ep) = (½ (Fe^{3+}(M_3) - Fe^{3+}(M_1)) (Holland and Powell, 1998; Patrier et al., 1991) as well as four reactions between the end-members which are cited in the figure caption. Epidote composition isopleths plotted in the

PT stability field (dashed lines in Fig. 4.8a) for the equilibrium assemblage intersect with end-member reactions and indicate metamorphic conditions of T = 310-360^{o}C and P < 2.9 kbar (see dark grey area in Fig. 4.8a).

Table 4.4. Mineral compositions and end-member activities of sample P1-155

Point No.	Ab-738	Ep-735	Chl-751	Act-753
Mineral	Albite	Epidote	Chlorite	Actinolite
SiO_2	68.26	38.71	26.21	53.49
TiO_2	0.98	0.07	0.14	0.01
Al_2O_3	19.02	26.84	19.42	1.56
Fe_2O_3	0.98	8.11	b.d.l	0.92
FeO	b.d.l	b.d.l	29.82	16.98
MnO	b.d.l	b.d.l	b.d.l	0.01
MgO	0.31	0.04	12.4	12.7
CaO	1.37	23.88	0.14	12.48
Na_2O	9.55	0.01	0.03	0.17
K_2O	0.1	b.d.l	0.01	0.02
Total	100.47	97.65	88.17	98.34
O	8	12.5	14	23
Si	2.97	3.028	2.81	7.812
Ti	0.032	0.004	0.01	0.001
Al^{iv}	0.98	-	1.18	0.187
Al^{vi}	-	2.475	1.28	0.082
Fe^{+2}	-	-	2.67	2.075
Fe^{+3}	0.04	0.477	-	0.101
Mn	-	-	-	0.001
Mg	-	0.005	1.98	2.764
Ca	0.07	2.002	0.02	1.953
Na	0.92	0.002	0.01	0.048
K	0.01	-	-	0.004
Sum	5.01	7.992	9.95	15.061
End-member activities				
An	0.126			
Ab	0.92			
cz		0.53		
ep		0.47		
clin			0.00326	
daph			0.0086	
ames			0.0132	
tr				0.079
fact				0.013
parg				0.00106

b.d.l = below detection limit

From the petrographic investigations calcite was present in some of the pillow lava metabasalts above and below the KSM, indicating that the study area was affected by a hydrothermal fluid containing some degree of CO_2. Therefore as a second step, a *P-a* (CO_2) pseudosection was drawn at fixed temperature (330^oC) for metabasalt sample (P1-155) in the mid-lower Kromberg section using THERMOCALC tc331 (Powell and Holland, 1988) to further determine the pressure condition and the fluid activity of the CO_2. The *P-a* (CO_2) pseudosection was calculated in the system NCFMASHTO- CO_2 and using the bulk rock and mineral solution models that are cited in the caption of Figure 4.8. The *P-a*(CO_2) pseudosection (Fig. 4.8b) indicates that the magnetite is stable at lower pressure condition (<1.6 kbar) and a wide range of CO_2 activity, whereas it becomes a stable phase at higher pressure (1.6-6 kbar) only at a(CO_2) greater than 0.26. The observed equilibrium assemblage of sample P1-155 (act ep chl ab ttn cc H_2O) is stable at lower pressure conditions (1.1 – 3.1 kbar) and activity of CO_2 < 0.25. The XMg of chlorite involved in this assemblage is calculated to decrease with increasing temperature (dashed lines in white highlighted PT-field in Fig. 4.8b, Table 4.4). The observed XMg of chlorite (0.49-0.52, see grey dashed line and chlorite composition in Table 4.4) in sample P1-155 constrains the activity of CO_2 at a low value of less than 0.15. The pressure estimate in the P-a(CO_2) pseudosection is identical to that derived from the epidote isopleths in Fig. 4.8a.

In summary, the THERMOCALC pseudosections indicate low-grade PT-conditions of T = 310-360^oC at P < 3 kbar, with low a(CO_2) fluid conditions of less than 0.15 for the mid-lower Kromberg. The pseudosections indicate that the upper thermal stability limit of chlorite for the assemblage in P1-155 near the greenschist-amphibolite facies transition is around 440 ± 50^oC (Fig. 4.8b). Above this temperature, the hornblende stability field occurs at pressures above ~2.7 kbars, whereas the epidote amphibolite facies transition occurs below ~2.7 kbars. However, it is necessary to point out that the thermodynamic solid solution models for chlorite in THERMOCALC tc331 (Powell and Holland, 1988), cannot account for all natural chlorites, because it assumes no vacancies and full octahedral occupancy in the chlorite crystal structure, whereas low temperature natural chlorite show octahedral vacancies (see Cathelineau and Nieva, 1985; Vidal *et al.* 2001, 2005; 2006). For this reason, further thermodynamic modeling and analysis is required for the altered mafic-ultramafic rocks of the Kromberg.

4.8. Metamorphic PT-estimates based on the composition of chlorite and mica

4.8.1. Chl-Qtz-H_2O equilibrium

Cathelineau and Nieva (1985), showed that the amount of Al^{IV} increases and the amount of vacancies decreases in the chlorite structure with increasing temperature. Vidal *et al.* (2001, 2005; 2006) showed that these trends observed in chlorite can be explained and modelled thermodynamically. The substitutions in chlorite can be modelled with five end-members: clinochlore (Clin), Fe-, Mg- 14 Å end-members of amesite composition (Fe-ames and Mg-ames), daphnite (Daph) and Mg-sudoite (Sud). Using these end-members, four reactions (two independent) can be written for the chlorite-quartz-water assemblage:

$2Clin + 3Sud = 4Mg\text{-}Ames + 7Qtz + 4H_2O$ (1)

$4Clin + 5Fe\text{-}Ames = 4Daph + 5Mg\text{-}Ames$ (2)

$16Daph + 15Sud = 20Fe\text{-}Ames + 6Clin + 35Qtz + 20H_2O$ (3)

$4Daph + 6Sud = 5Fe\text{-}Ames + 3Mg\text{-}Ames + 14Qtz + 8H_2O$ (4).

The temperature locations of the equilibria (1) to (4) depend on the activity of the Clin, Daph, Sud and amesite end-members as well as the activity of water. At fixed water activity and pressure, an increase in sudoite component (increase in vacancies) and Clin + Daph components (increase in Si) leads to a shift in the equilibria towards lower temperatures, consistent with the numerous empirical thermometers based on the amount of Al^{IV} in chlorite (e.g. Cathelineau and Nieva (1985); Cathelineau, (1988); Hillier and Velde (1991); Inoue et al., (2009). In theory, the pressure could be estimated from the location of the point where equilibria (1) to (4) intersect in a *P-T* space. However, these equilibria are near vertical, so that pressure estimate is poor and not reliable. Vidal et al. (2005; 2006) suggested that a simultaneous estimation of Fe^{3+} in chlorite and equilibrium temperature for the Chl-Qtz-H_2O assemblage can be made using criterion based on the convergence of equilibria (1) to (4) at given pressure, which is achieved for a minimal $XFe^{3+} = (Fe^{3+}/Fe_{tot})$ of chlorite. Following this approach, XFe^{3+} is increased and the structural formula of chlorite is recalculated until convergence of (1) to (4) is achieved. Although this method has been validated quantitatively by comparing estimated values of XFe^{3+} with XANES measurements (Vidal et al., 2006; Munoz et al., 2006), and also Mossbauer measurements on natural chlorites (Tarantola et al., 2009) it provides minimum XFe^{3+} and maximum T estimates only. Depending on the chlorite

composition, a further increase of Fe^{3+} is sometimes possible without loosing convergence of (1) to (4), which are all shifted at LT.

In the present study, the whole range of possible Fe^{3+} content and temperature conditions for which convergence of (1) to (4) was achieved was determined for all chlorite compositions (Fig. 4.9a) from the Kromberg type-section. The calculation was made at a pressure of 2 kbar for all samples and with XFe^{3+} from 0.05 to 0.6 with 0.02 steps. The highest value possible for chlorite is XFe^{3+} = 0.6 (Munoz *et al.,* 2006; and references therein), and most estimated XFe^{3+} values in the present study are lower than this value. The presence of carbonate in the studied sample suggests that the activity of water can be less than 1, as a result of H_2O-CO_2 mixing. However, as discussed above, the activity of CO_2 in the fluid phase is likely to be less than 0.15 so that the activity of water should be close to unity. Moreover, given that equilibrium (2) above does not involve water, varying aH_2O has no influence on its temperature location at 2 kbar and for a given XFe^{3+}. For these reasons, all calculations were performed at aH_2O = 1. Except for sample P1-161 (see below), convergence was considered to be achieved when the temperature difference between all equilibria (1) to (4) was less than 30°C. This value was adopted in order to take into account the cumulative uncertainties stemming from errors and uncertainties in the thermodynamic data of the chlorite end-members, solid solution properties and the analytical uncertainties. No convergence was achieved with a temperature difference between equilibria (1) to (4) less than 30°C for the Si- and -vacancy richest chlorites of sample P1-161, a metabasalt in the lowermost parts of Kromberg. The activity of (Fe,Mg)-14A amesite is close to zero for these chlorites, and the error on the location of equilibrium (2) is very large. For this reason, the temperature reported for this sample were calculated using a criteria based on the convergence within 30°C of equilibria (1), (3) and (4) only.

The results of calculation indicate that the metamorphic temperature and XFe^{3+} conditions cover a wide range between 140 and 500°C and 0.1 to 0.55, respectively (Fig. 4.9a-f). Two groups of chlorite temperature can be identified, a low T group at T < 350°C, and a HT group at T > 350°C (Fig. 4.9a,b). The range of possible temperature for the chlorites of the HT group is wide, and can be as high as 450 to 500°C (Fig. 4.9a). This temperature estimate is clearly too high, given the absence of hornblende but observation of epidote in the samples. As seen in the THERMOCALC pseudosection analysis, the lower stability limit of hornblende is about 440 ± 50°C at *P* = 1 to 5 kbar for this bulk rock composition (Fig. 4.8b).

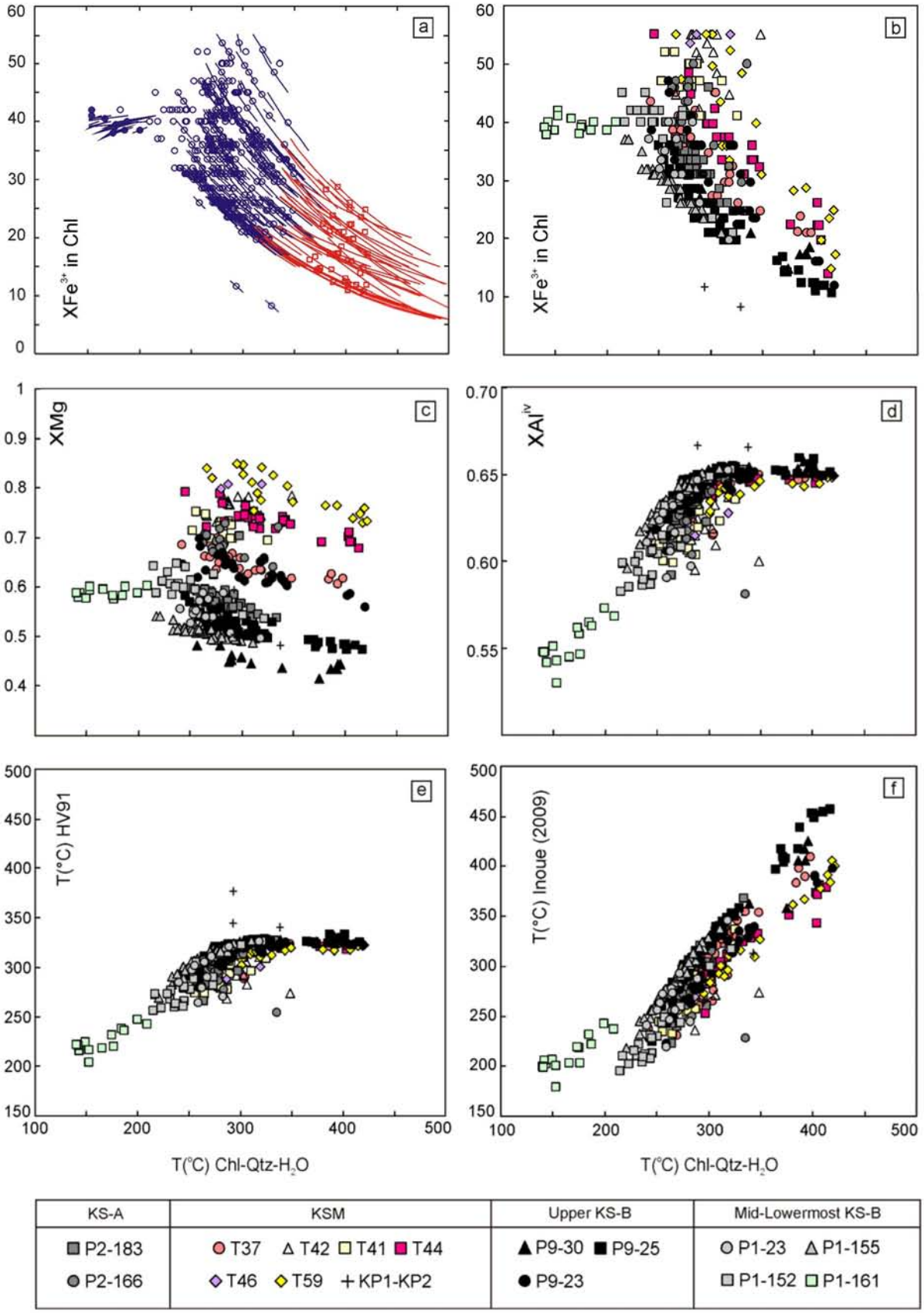

Figure 4.9. Results of Chl-Qtz-H_2O equilibrium temperatures (Vidal et al., 2006) calculated for a(H_2O) = 1. The temperatures are plotted as a function of calculated XFe^{3+} (= Fe^{3+}/Fe_{Total})

(a and b), XMg (= Fe^{2+}/Fe^{2+} + Mg) **(c),** XAl^{iv}_{T2}(= $Al^{iv}/2$) **(d),** the temperatures derived with the empirical thermometer of Hillier and Velde (1991) **(e)** and Inoue et al. (2009) **(f).** In (a), the lines show for each chlorite analysis the range of possible temperature and the symbols show the average temperatures reported in b-f and in Fig. 4.10 and 4.11.

A lower temperature is obtained for higher XFe^{3+} whilst maintaining the convergence criteria and the mean temperatures calculated for all chlorite of the HT group is 375 to 420°C (Fig. 4.9b). The range of possible temperatures obtained for the LT chlorite group is from about 200 to 350°C, with most mean temperatures at 300°C.

The mean chlorite temperatures for all samples at 2 kbar are shown in relation to modelled XFe^{3+} content, $XMg = Mg^{2+}/(Mg^{2+} + Fe^{2+})$ and XAl^{IV} in Fig. 4.9b-c. The *X*Mg values vary systematically with modelled XFe^{3+} values and temperature estimates, as higher Fe^{3+} values also corresponds to lower Fe^{2+} content and thus higher Mg-number (Fig. 4.9c). However, drill core T-samples in KS1 clearly show the highest XMg values, typically between 0.65-0.87, reflecting their ultramafic protolith in comparison to chlorite compositions in the metabasalts (Fig. 4.9c). The XAl^{IV} values of the low temperature group are also found to vary systematically and show positive trends between calculated temperature and the Al^{IV} as observed in empirical chlorite geothermometers (Fig. 4.9d,e). The temperatures derived using the multi-equilibrium approach and the empirical Al^{IV}-chlorite thermometer of Hillier and Velde (1991) are similar below 300°C. Above this temperature, the multi-equilibrium approach gives a temperature range higher than the empirical method. In particular, two sample groups (T37, T44, T59 and P9) show an upper temperature limit of about 420 ± 30°C by the thermodynamic method, compared to ~330°C by the empirical chlorite geothermometry method (Fig. 4.9e). The same observation is also made for when using the T versus Al^{IV} equations of Cathelineau and Nieva (1985) or Cathelineau (1988). In comparison, a much better agreement is observed with the temperatures derived using the empirical equation of Inoue et al. (2009), which also points out two groups of HT and LT chlorites (Fig. 4.9f).

The two chlorite temperature generations HT (375-420°C) and LT (240-350°C) occur in drill core samples (e.g. T59, T44, T37) from within the KSM (KS1) and in pillow lava samples directly below the KSM (P9-30, P9-25, P9-23). Chlorite temperature estimates are shown in relation to textural information in BSE images for drill core samples T41 and T44 (Fig. 4.10a,b). In sample T41, low temperature chlorite occurs along a quartz-carbonate vein

with metamorphic temperatures between 250-326°C (Fig. 4.10a), whereas in sample T44 the HT chlorite group is recorded along a similar extensional carbonate-quartz vein with temperatures as high as 414°C (Fig. 4.10b). This indicates multiple fluid infiltration events in the KSM recorded by the HT and LT chlorite groups along extensional carbonate-quartz veins.

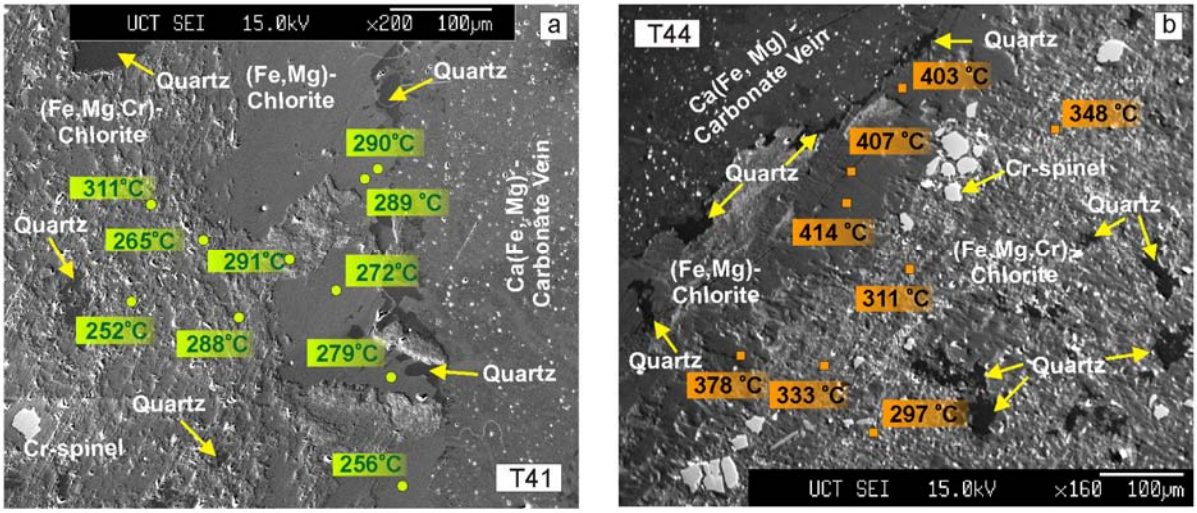

Figure 4.10. Backscatter electron images and indicated chl-qtz-H_2O temperatures calculated from point analyses of different chlorites grains coexisting in the same thin section (aH_2O = 1). **(a)** Scatter in calculated chl-quartz-H_2O temperature estimates of the LT group at about 300°C along quartz-carbonate vein in sample T41. **(b)** The scatter in temperature estimates of the HT group along a quartz-carbonate vein in sample T44.

An attempt was made to reconstruct a thermal profile in the drill core across KS1 from the outer banded zone into its central complex fluidized and veined zone (Sample T37 to T59 in Fig. 4.11). In general, the two chlorite groups HT and LT are recorded in the outer banded zones (samples T37-T44 in upper KS1) and closer to the central complex zone, only the lower temperatures are recorded of 280-350°C (e.g. T46). Metamorphic temperature estimates could not be calculated for samples T45, T47 and T48 further down in the central complex zone as chlorite compositions do not satisfy the compositional criteria of Vidal et al. (2005, 2006). The distribution of T estimates in the drill core suggests lower T fluid infiltration from the central complex zone overprinting earlier higher temperature fluid infiltration events in the outer banded zones. Electron microprobe analyses from listvenitic surface sample KP1-2

(KSM) indicates the presence of trace amounts of chlorite still preserved within mafic-ultramafic microdomains in a matrix consisting of fuchsite. Chlorite temperature estimates for sample KP1-2, for example, indicate T = 290 - 335°C (see Table 4.1, Table 4.5).

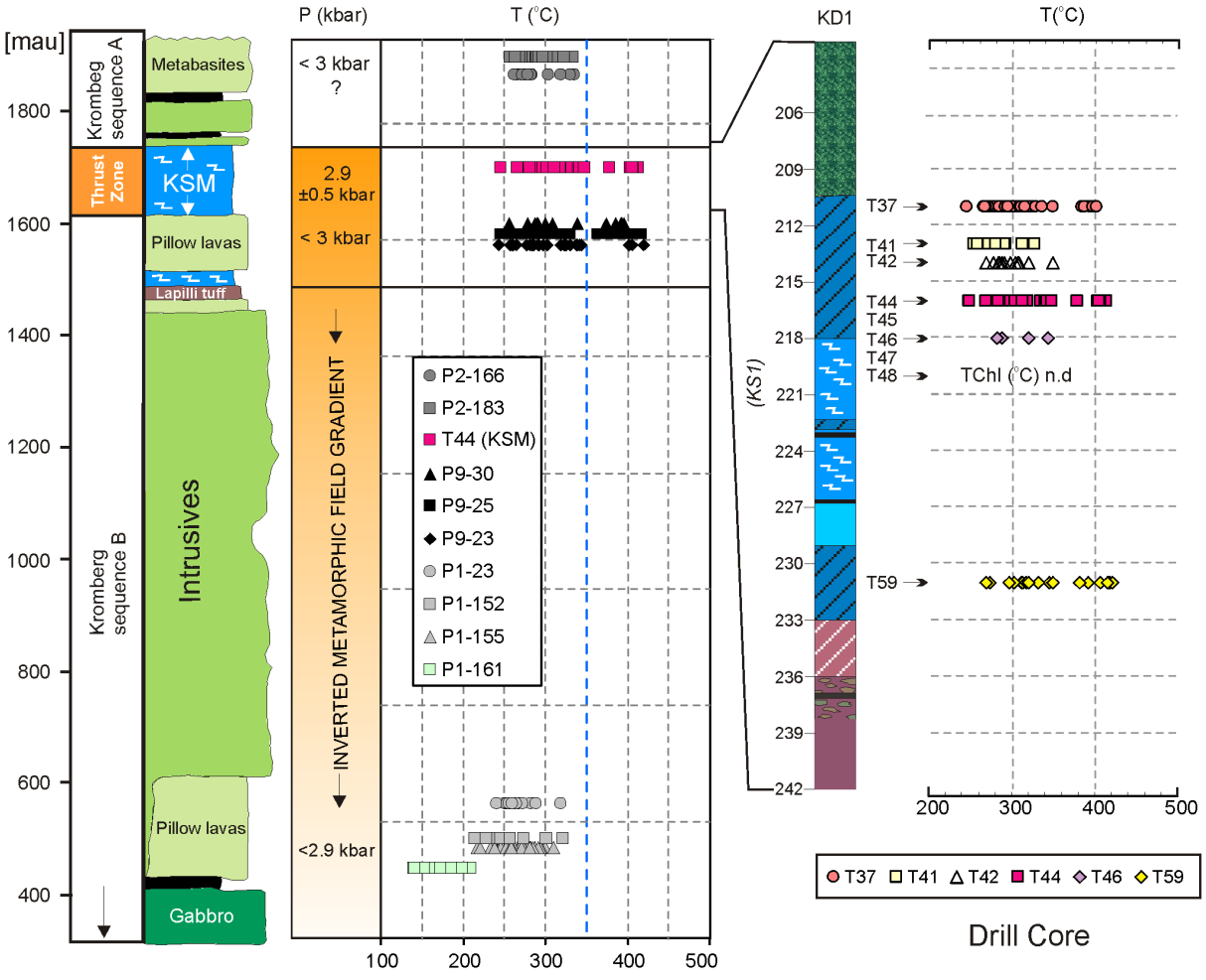

Figure 4.11. Summary of *PT*-constraints across the Kromberg-type section indicating the presence of an inverted metamorphic field gradient. The KSM and underlying pillow lava section records HT/LP-type metamorphism, whereas metamorphic conditions in the overlying Kromberg sequence A and the mid-lower Kromberg sequence B are much lower, typically less than 350°C (see dashed blue reference line). Average temperature variation determined from chl-quartz-H_2O equilibrium indicated with depth in the drill core. TChl(°C) n.d. = temperature estimate not determined because the chlorite compositions do not satisfy compositional criteria of Vidal et al (2001, 2006). [mau] = metres above unconformity between Hooggenoeg Formation pillow lavas and the Noisy formation clastic sedimentary rocks (see Fig 4.2.)

Table 4.5. Selected chlorite-mica pairs used in the multi-equlibrium PT-calculation for KSM

	KP1-2-chlx5 chlorite	KP1-2-m5 mica	KP1-2_chlx4 chlorite	KP1-2-m4 mica
SiO_2	25.23	46.2	24.95	46.5
TiO_2	b.d.l	0.2	b.d.l	0.24
Al_2O_3	22.63	33.4	22.70	32.18
FeO	25.14	1.1	25.79	1.51
MnO	0.20	0.1	0.17	0.06
MgO	13.83	1.2	12.16	1.74
CaO	0.21	b.d.l	0.12	0.04
Na_2O	0.24	0.3	0.05	0.21
K_2O	0.82	10.7	0.06	10.75
Cr_2O_3	1.36	2.01	1.09	0.62
F	b.d.l	0.05	b.d.l	0.12
Structural formula calculated on the basis of 14 O				
Si	2.59	3.14	2.58	3.17
Ti	b.d.l	0.01	b.d.l	0.01
Al(iv)	1.41	0.85	1.42	0.82
Al(vi)	1.47	1.83	1.31	1.77
Mg	2.07	0.12	2.11	0.18
Fe^{2+}	1.98	0.06	1.44	0.09
Fe^{3+}	0.24	0.00	0.71	0.00
Sum other elts	0.08	0.97	0.14	0.97
Oct Sum	5.88	6.99	5.78	7.00
XMg	0.59	-	0.48	-
XFe^{3+}	32	-	8	-
T(^{o}C) Vidal (2006)	293		336	
T(^{o}C) Inoue (2009)	308		351	
T(°C) H&V (1992)	384		339	
TChl (^{o}C)	*no equilibrium*		324 (+/- 30)	
P (bars)			2910 (+/-150)	

b.d.l = below detection limit

XFe^{3+} calculated after the method of Vidal et al., (2006)

In contrast to the drill core samples, metabasalts of Kromberg sequence A, namely P2-166 and P2-182, at distances of 90 and 125m above the KSM, respectively, record low metamorphic conditions of between 263 - 336^{o}C and 257 - 334^{o}C (Fig. 4.9 and 4.11). In the mid-lower parts of Kromberg sequence B, pillow lava metabasites generally record variable and much lower grade greenschist facies conditions. Sample P1-155, for example, records metamorphic conditions of T = 240 - 310^{o}C, and similarly sample P1-152 records chlorite temperature estimates as low as T = 215 - 321^{o}C (Fig. 4.9 and 4.11). A metabasalt sample in the lowermost parts of the Kromberg (P1-161) records the lowest metamorphic grade with chlorite temperature estimates ranging between 140 - 209°C (Fig. 4.9 and 4.11). Similar low temperature estimates (170-250^{o}C) were also obtained using the empirical thermometer of Inoue et al., (2009), typically applied to very low-grade, Si-rich chlorites as in the case of sample P1-161. These low temperatures estimated for the mid-lower parts of Kromberg sequence B are consistent with petrographic observations, namely the very low abundance of epidote (one or two grains) that typically forms well above ~200^{o}C (Cho *et al.*, 1986; Liou *et al.*, 1985), and very low proportion of chlorite (<2%) and the absence of actinolite in this sample. Given that no zeolite (or prehnite) could be identified in thin section, it is possible that this sample may have been affected by a low temperature, CO_2 containing fluid.

4.8.2. Metamorphic PT-conditions based on Chlorite-Mica-Quartz-H_2O equilibria

Chlorite-phengite-quartz-water equilibrium has been recently applied to various low-temperature metapelites (e.g. Trotet et al., 2001a,b; Le Hebel et al., 2002; Parra et al., 2002b; Augier et al., 2005; Rimmelé et al., 2005; Willner, 2005; Vidal et al., 2006; Yamato et al., 2007). With five chlorite and four dioctahedral mica end-members (Mg- and Fe-celadonite, muscovite, pyrophyllite), 64 reactions (4 independent) can be written in the system SiO_2-Al_2O_3-MgO-FeO-K_2O for an assemblage comprising mica, chlorite, quartz and water (Parra et al., 2002a, 2002b). As previously described, the temperature and $(Fe^{3+})_{chlorite}$ estimation is first constrained at fixed pressure using the chlorite-quartz-H_2O assemblage. The amount of $(Fe^{3+})_{mica}$ is then adjusted to locate the Fe-Mg exchange reaction between chlorite and mica at a similar temperature. Pressure is then calculated with the 64 reactions using the INTERSX software included in the TWEEQ package (Berman, 1991). In practice, the intersection between the 64 equilibria is not always perfect and gives scattered results due to the accumulated uncertainties in the calculation of the reactions position (e.g. uncertainties in the thermodynamic data, standard state properties, solid solution models).

The method described above was used to constrain average *P-T* conditions and to test for chemical equilibrium between chlorite and mica in the selected pairs for sample KP1-2 in the KSM (Table 4.5). The *P-T* estimates are shown by boxes with size that corresponds to the *P-T* scatter and uncertainty (Fig. 4.12a, b). Some chlorite-mica pairs in selected microdomains show a wide scatter in equilibria and a large PT-box due to a poor intersection between all equilibria (Fig. 4.12a). In this case, PT-boxes are large but low pressures of 3.5 to 1.3 kbar are still indicated. Other chlorite-mica pairs, particularly near the margins of carbonate-quartz veins, were found to indicate very good intersection between all 64 equilibria with *PT*-conditions estimated to be T = 325 ± 30°C and P = 2.9 ± 0.15 kbar (Fig. 4.12b).

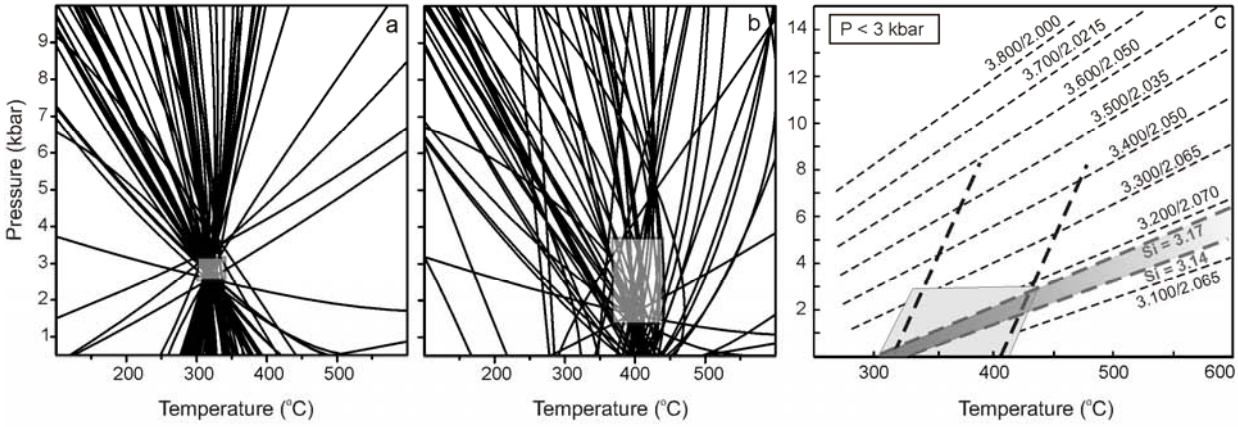

Figure 4.12. Chlorite-mica-quartz multi-equilibrium calculation for chlorite-mica pairs along quartz-carbonate vein in listvenite surface sample KP1-2 (a and b), and (c) P estimates based on the Si-in-mica geobarometer (y-axis) of (Velde, 1965; Massonne and Szpurka, 1997) for the range of chl-qtz-H_2O temperatures (x-axe) estimated in the same sample. The transparent boxes in a-b show the average P-T conditions + 2σ standard deviation calculated from the intersection of all equilibria. Dashed lines in (c) are the Si-isopleths from Massonne and Szpurka (1997).

4.8.3. Temperature estimates based on Dioctahedral mica-Qtz-H_2O equilibrium

Low-temperature (LT) dioctahedral micas show a decrease in their interlayer content (IC, excluding interlayer water) and an increase in their Si-content with decreasing T. This has been observed in LT and high pressure (HP) phengite (Agard et al., 2001; Bishop and Bird, 1987; Cathelineau, 1988; Battaglia, 2004; Vidal and Dubacq, 2009; Dubacq et al., 2010; 2011)), where the vacant sites of LT and LP pressure illite are partially hydrated (Loucks,

1991; Drits and McCarty, 2007, Dubacq et al., 2010; Vidal et al., 2009; 2010). These compositional variations can be modelled as a function of T and P using the recently proposed formalism of Dubacq et al. (2010) that involves dehydrated micas and hydrated pyrophyllite-like thermodynamic end-members. The equilibrium conditions of quartz + water + K-bearing mica of fixed 2:1 composition are represented by a divariant P-T line along which the interlayer water content varies. The P-T location of this line can be calculated from the condition of equilibrium of the following equilibria:

3 Celadonite + 2 Pyrophyllite ↔ 2 Muscovite + Biotite + 11 Quartz + 2 H_2O (5)

3 Celadonite + 2 Pyrophyllite.1H_2O ↔ 2 Muscovite + Biotite + 11 Quartz + 3 H_2O (6)

Pyrophyllite.1H_2O ↔ Pyrophyllite + H_2O (7)

where celadonite, pyrophyllite, pyrophyllite.1H_2O, muscovite and biotite are solid solution components of the mica phase. Dubacq et al. (2010) and Vidal et al. (2010) showed that the mica-quartz-water equilibrium curves could be used as a thermometer in low-pressure rocks. In the present study, the temperature, pressure and water content for the convergence of (5) to (7) was determined for the compositions of micas occuring in KSM surface samples KP1-2, KP21 and A17. The phengite hydration isopleths are shown in PT space in Figure 4.13 for these three samples. For pressure conditions of around 3 kbars or less (as determined from the chl-mica multi-equilibrium calculation above), metamorphic temperatures of between 250-425^oC are indicated by the steep isopleths for KSM listvenite surface samples KP21, KA17 and KP1-2, respectively (Fig. 4.13a-c). At a pressure of 3kbar (as determined by chl-mica-quartz-H_2O equilibrium calculation), mica compositions in microlithon bands in samples KP21 and KA17 record metamorphic temperatures of between 300-365^oC, whereas much higher metamorphic conditions are recorded by mica in sample KP1-2 up to about 420 ± 30^oC (Fig. 4.13d). The range and distribution in metamorphic temperature estimates derived from the Phg-Qtz-H_2O equilibria are in good agreement with the temperature estimates derived from Chl-Qtz-H_2O thermodynamic modelling in the drill core KSM samples.

Figure 4.13. Metamorphic temperature estimates using Phg-Qtz-H_2O equilibria in the thermodynamic method of Dubaq et al., (2009). **(a-c)** Metamorphic conditions from the position of hydrated mica phengite isopleths in *PT*-space for various listvenite surface samples in the KSM. *PT*-boxes correspond to likely PT conditions for each sample derived

from intersection between pressure estimates (from chl-mica multi-equilibrium calculation and Si-in mica geobarometry) and the calculated temperature range indicated by the mica isopleths. **(d)** Metamorphic temperature estimates from mica compositions at 3 kbar (pressure from good convergence of all 64 equilibria using chl-mica multi-equilibrium calculation) in two listvenite surface samples recording similar LT and HT conditions to that derived from Chl-Qtz-H_2O thermodynamic modelling, in altered ultramafic microlithons. The mica in a microlithon band in listvenite sample KA17 (blue) overlaps in temperature range with sample KP1-2 (red), but records lower metamorphic temperature conditions than in the KP1-2 microlithon.

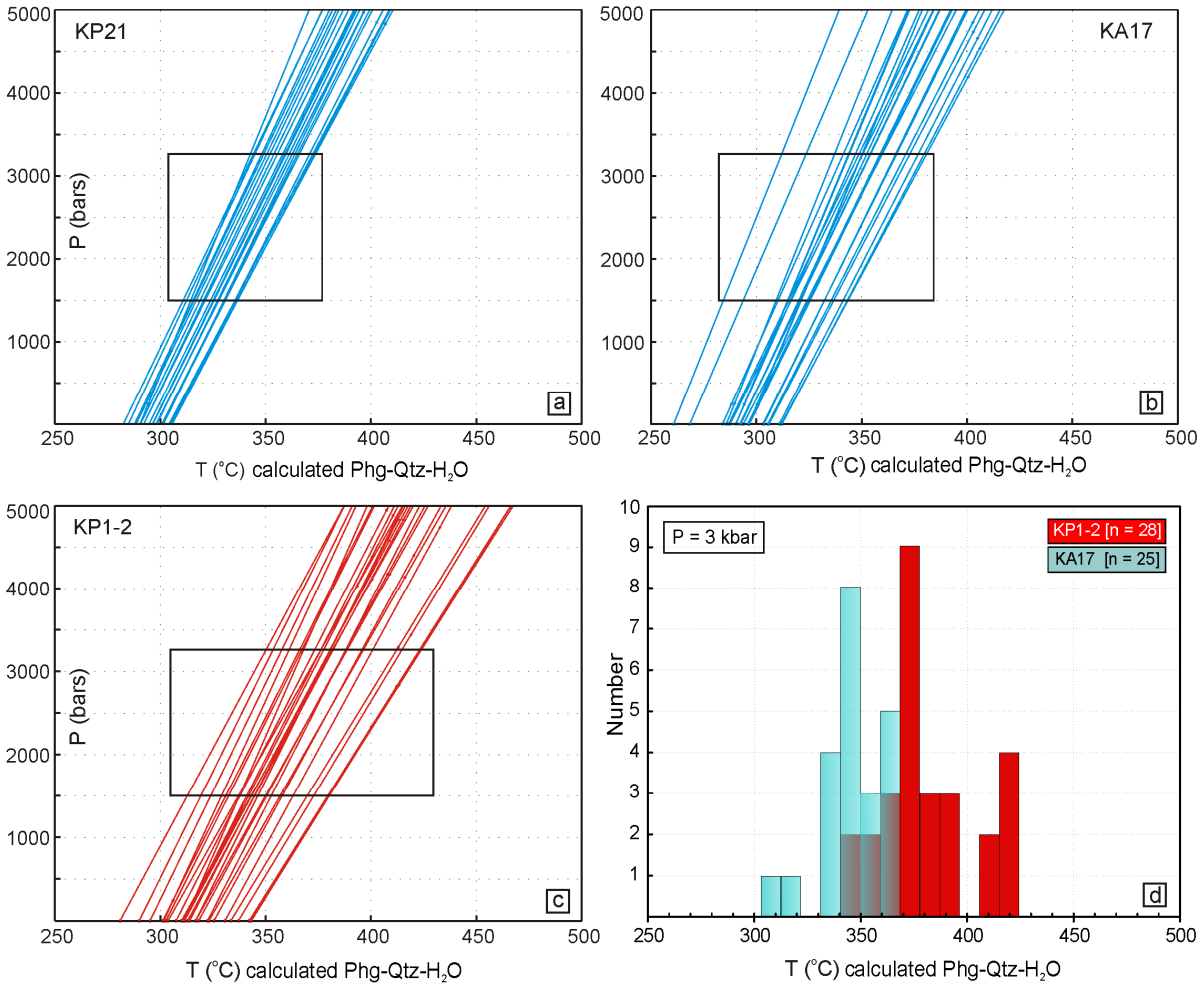

4.8.4. Pressure estimates based on Si- in mica geobarometry

The celadonite content of phengite is mainly dependent on pressure and has been proposed as a geobarometer (Velde, 1965, 1967; Massonne and Schreyer, 1987; Massonne and Szpurka, 1997; Parra et al., 2002a). Using the Si content in micas, applying the classic geobarometer of

Velde (1965) and temperature estimated from the Chl-Qtz-H_2O equilibrium, low pressures of less than 3 kbar are indicated for all mica compositions in the KSM banded fuchsite-bearing mylonites (see K-samples in Fig. 4.6f). The Si isopleths of the micas were also used to estimate the pressure according to the geobarometer of Massonne and Szpurka (1997). The intersection between the wide temperature range (up to 420 ± 30 ^{o}C) calculated from chlorite thermodynamic modelling, and Si-isopleths in mica using the geobarometer of Massonne and Szpurka (1997), indicate low pressure conditions P < 3 kbar (Fig 4.12c). Given that this Si-in mica geobarometer was calibrated for high pressure rocks, the uncertainty on this low pressure estimate is most likely large. However, this low pressure estimate is compatible with low pressure estimates derived from both the chlorite-mica multi-equilibrium calculation, and the THERMOCALC PT-grid (see Fig. 4.12 and Fig. 4.8).

4.9. Discussion and Interpretation

4.9.1. PT-constraints across the Kromberg type-section

The Kromberg type-section including the central KSM records a wide range in metamorphic conditions from subgreenschist to uppermost greenschist facies conditions (Fig. 4.11 and Fig. 4.14). The KSM records two chlorite temperature populations, with a *HT* group of *T* = 422-375^{o}C and a *LT* chlorite groups of *T* = 240-350^{o}C that are related to alteration along extensional quartz-carbonate veins. The pressure recorded in the KSM is 2.9 ± 0.15 kbar as calculated from chlorite-mica-quartz equilibria and is related to the *LT* event. Undeformed, extensively altered pillow lavas directly below the KSM also recorded these two metamorphic events. Although these metabasalts record high temperatures near the upper greenschist-amphibolite facies transition, no hornblende is found but rather actinolite + epidote. This indicates that the pressure conditions were most likely less than 3kbar (see PT-grid in Fig. 4.8a with facies transition at around T = 440 ± 50^{o}C and also Maruyama et al., 1983). Metamorphic temperatures recorded in undeformed metabasalts above the shear zone in Kromberg sequence A are T = 250-340^{o}C. These low-grade metabasalts show no deformation fabrics, and most likely also experienced pressures lower than ~ 3kbar. Pillow lava metabasalts in the mid-lower Kromberg sequence record metamorphic conditions of T = 215 - 321^{o}C. Sample P1-155 from this part of the Kromberg sequence B (about 1.1km beneath the

KSM) shows a pressure condition of less than 2.9 kbar and low fluid XCO_2 conditions of less than 0.15 (Fig. 4.8a, b). Much lower grade conditions of between 140 - 209^{o}C are estimated in the lowermost part of the Kromberg type-section for sample P1-161 (Fig. 4.11 and 4.14).

A first order observation is that the metamorphic field gradient is inverted, decreasing from conditions near the uppermost greenschist-amphibolite facies boundary to metamorphic conditions as low as 140 - 209^{o}C, near the base of the Kromberg type-section (see Fig. 4.11). The presence of an inverted metamorphic field gradient supports thrust repetition across the Kromberg type-section (see discussion on geodynamic model below). The chemistry of the chlorites, together with multi-equilibrium thermodynamic modelling approaches, as well as the petrographic descriptions, indicate a complex fluid infiltration and thermal history in the Kromberg Section Mylonites (in drill core and surface samples). The HT (T = 420 ± 30^{o}C, low P < 3kbar) and LT (240-350^{o}C, P = 2.9 ± 0.15 kbar) metamorphic events recorded in both the KSM and the underlying P9 pillow lava samples is interpreted as retrograde metamorphic events that post-dated mylonitic fabric development that occurred in an earlier higher pressure event related to thrusting. A summary of metamorphic conditions across the Kromberg-type section and a PT-path for the KSM and P9-metabasalst are provided in Fig. 4.14.

The metamorphic *P-T* estimations reported here show that much more complex and varied metamorphic conditions are recorded across the Kromberg-type section, compared to that of less than 150^{o}C (Hofmann and Harris, 2008) or ~320^{o}C (Xie et al., 1997; Tice et al., 2004) available in the published literature. The metamorphic grade is variable with increasing depth and decreases from relatively high metamorphic temperatures of T = 420 ± 30^{o}C (P < 3kbar) in the KSM and uppermost Kromberg to as low as 140 - 209^{o}C in the lower Kromberg, over a distance of about 1.2 km. Similarly, the new PT-data across the Kromberg type-section, is not compatible with current regional metamorphic profiles for the Onverwacht Group as a whole, which argue for either low temperature (less than 150^{o}C) seafloor metamorphism for the entire Onverwacht Group (Hofmann and Harris, 2008) or gradual increase in metamorphic grade with depth regionally in the Onverwacht Group (Cloete, 1991, 1999). The new inverted metamorphic field gradient reported here indicates much more internal variation in metamorphic grade for the Onverwacht Group and that more than one origin for the low-grade metamorphism can be distinguished.

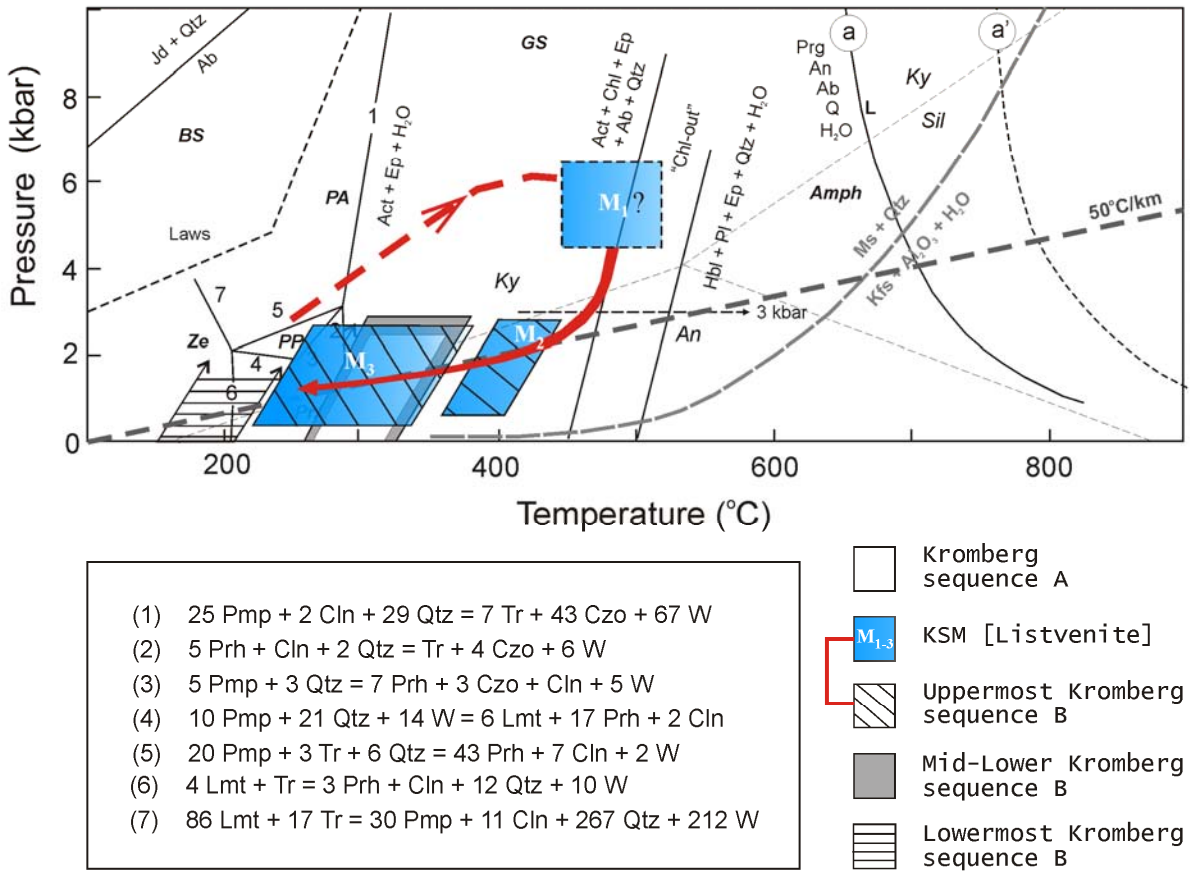

Figure 4.14. Summary diagram of *P-T* constraints and *PT*-path for the Kromberg-type section. M_1 indicates an early metamorphic event of unknown *PT*-condition that lead to mylonitic fabric development in the KSM during thrusting and obduction. M_2 (*HT*) and M_3 (*LT*) refer to the metamorphic conditions during the retrograde path that were constrained in this study in the KSM and in the underlying pillow lava sequence (P9). Aluminosilicate triple point is after Bohlen et al. (1991). Reactions (1) to (7) represent bands in *PT*-space that indicate the approximate positions of reactions generally defining the subgreenschist and greenschist facies in the NCMASH system (after Frey et al., 1991). Approximate location of lawsonite field from Chatterjee (1976) and phase relations of the greenschist–amphibolite transition in metabasite as related to the stabilities of albite-oligoclase, actinolite-hornblende, epidote and chlorite are from Maruyama et al. (1983). The subgreenschist-greenschist facies boundary indicated by reactions (1) and (2) generally accepted to be located around 280 ± 30°C (Frey et al., 1991). Reactions (a) and (a') are from Pattison (2003) calculated on the basis of a pargasite composition with *X*Mg = 0.5. Approximate position of the muscovite break-down reaction (wet solidus) is indicated (after Johannes, 1978; Piwinskii, 1968, Wyllie and Wolf, 1993).

4.9.2. Petrogenesis of the fuchsite-bearing rocks in KS1

The assemblage fuchsite-carbonate-quartz ± chlorite ± sulphide (with relic Cr-spinel) in rocks of the KSM corresponds to that of listvenite and rocks of the listvenite series (see Halls and Zhoa, 1995 for review). Listvenite is typically reported from shear zones in dismembered ophiolite terranes (e.g. Kishida and Kerrich, 1987; Ash, 2001; Johnson et al., 2004; Tsikouras et al., 2006; Nasir et al., 2007; Plissart et al., 2009) and occasionally also from greenstone belts, for example, in Burkina Faso (Béziat et al., 1998) and Archean greenstone belts of Ontario and Quebec in the Canadian Shield (e.g. Auclair et al., 1993; Kishida and Kerrich, 1987). The observation of mylonitic textures together with the PT-conditions recorded in the highly altered mafic-ultramafic rocks of KS1 do not support previous interpretations that they are low temperature (~60^{o}C) chemical weathering of komatiitic flow tops (Lowe and Byerly, 1986); or low-temperature alteration of volcanic tuffs (Viljoen and Viljoen, 1969a,b; Anhaeusser, 1973). The origin of the fuchsitic rocks as a weathering product is also highly unlikely because: (i) thermodynamic modelling indicates greenschist facies metamorphic temperatures, up to 420 ± 30^{o}C, that are not compatible with low-T atmospheric weathering; (ii) chlorite- mica pairs are in chemical equilibrium at conditions of T = 325 ± 30^{o}C and P = 2.9 ± 0.15 kbar, conditions that cannot be explained by weathering. In addition, atmospheric surface weathering of ultramafic rocks has been reported to result in Ni-Fe-Cr laterites in ophiolite terranes rather than listvenites (e.g. the Semail ophiolite, Oman, Nasir et al., 2007; Sharhan and Nasir; 1996, Stanger, 1985).

A petrogenetic model is proposed in which, the listvenitic rocks of KS1 formed as a result of deformation and multi-stage fluid infiltration along a basal thrust zone in the Kromberg-type section. The rocks of the listvenite series develop between the serpentinite and fuchsite–bearing (true) listvenite depending on the extent of fluid-rock interaction. For example, a typical serpentinite protolith may undergo the following alteration and mineralogical changes (after Halls and Zhoa, 1995): (1) serpentine → (2) serpentine-carbonate (breunnerite) → (3) serpentine-talc-carbonate rocks → (4) chlorite-quartz-carbonate → (5) chlorite-carbonate → (6) fuchsite listvenite (end product). As observed in the drill core and surface samples, mylonitc rocks of KS1 include a spectrum of hydrothermal alteration assemblages typical of the more advance stages (stages 4 to 6) of listvenitic alteration (see carbonate and/or silica pseudomorphs after pyroxene and petrographic descriptions in Fig. 4.5 a-f). It is also possible that the KSM rocks represent an early subseafloor hydrothermal alteration zone that was subsequently overprinted by tectono-thermal metamorphism (see Chapter 5 for further distinction between seafloor and tectonic metamorphism).

4.9.3. Geodynamic model and metamorphic evolution

The KSM contains mafic-ultramafic rocks with abundant carbonate veining that show some similarities to rocks formed in oceanic detachment faults in modern mid-ocean ridge settings, or off-axis extensional detachment faults along transform boundaries (c.f. Dick et al., 1991; Karson and Lawrence, 1997; Karson et al., 2006; Kelly et al., 2001). However, the PT-conditions of ~3 kbar recorded in and around the KSM are too high for a purely oceanic extensional setting (e.g. Alt and Honnorez 1984; Bach et al. 2001). In addition the listvenite rocks of the KSM most likely do not reflect typical oceanic MOR-type alteration (Miyashiro et al., 1971; Alt and Honnorez, 1984, Bach et al., 2001), and differ from the talc-bearing schists observed in modern-day detachment fault scarps in oceanic core complexes (e.g. Karson et al., 2006). For these reasons, a purely oceanic (core-complex detachment model or mid oceanic ridge) geodynamic setting for the Kromberg type-section is unlikely.

The presence of an inverted metamorphic field gradient in the Kromberg type-section is more compatible with development of the KSM as a basal thrust zone that formed during tectonic obduction of oceanic crust in which Kromberg sequence A was thrust over Kromberg sequence B (e.g. as observed in metamorphic 'soles' beneath obducted ophiolites such as the Newfoundland ophiolite; Williams and Smyth, 1973; Malpas, 1979; Jamieson, 1980; Jamieson, 1986). On the basis of field observations, these banded fuchsitic rocks were previously interpreted to represent complex extensional "glide planes" along which sub-horizontal overthrusting occurred during intra-oceanic obduction at 3455-3460 Ma (de Wit, 1982a,b, de Wit et al., 1986a,b, 1987a,b; 2011). This intriguing mid-Archean "hovercraft tectonics" model has remained highly controversial however, because of a lack of detailed petrological data on the fuchsite-bearing rocks, together with the absence of field and geochronological data to support intra-oceanic shear zone development and early ophiolite obduction at 3455 Ma in the BGB (e.g. see Lowe and Byerly, 1986; de Wit et al., 1992; Kamo and Davies, 1994; de Wit, 1998; Hamilton, 1998; Lowe and Byerly, 1999a,b, 2007; Van Kranendonk et al., 2009). In contrast, there is field data and numerous U-Pb age constraints for major deformation and crustal accretion in the BGB at a much later stage between 3227 and 3230 Ma, due to oblique subduction, thrusting and transpressional tectonics (e.g. Kamo and Davies, 1994; de Ronde and Kamo, 2000; Lowe and Byerly 1999a,b; Lowe et al., 1999, 2007; Moyen et al., 2006; Schoene et al., 2008).

Although the timing of shearing in the KSM is not directly constrained in the present study, detrital zircon ages of 3334 ± 3 Ma from the Footbridge Chert in the upper part of Kromberg sequence A (see black chert horizon in Fig. 4.2 and Byerly et al., 1996) provide a

maximum age constraint upon the underlying Kromberg shear zone. A more likely geodynamic origin for the Kromberg type-section is thus, a thrust nappe duplex that developed during the regional crustal accretion event at ca. 3230 Ma. In addition to the inverted metamorphic field gradient observed, the calculated pressure estimate of 2.9 ± 0.15 kbar also supports a thrust and obduction model. The occurrence of listvenite in the KSM is similar to that reported in basal tectonic mélange zones of dismembered Neoproterozoic ophiolite terranes of the Arabian Shield that were obducted during a transpressional tectonic regime (e.g. Johnson et al., 2004; Tsikouras et al., 2006; Nasir et al., 2007; Plissart et al., 2009). Furthermore, Cr-spinel compositions in KSM banded mylonites record high Cr#'s, that indicate that the Cr-spinels formed from high degrees of partial melting from a depleted mantle source, typical of fore-arc tectonic settings (e.g. Dick and Bullen; 1984; Kusky and Jianghai, 2010). The KSM Cr-spinel compositions are distinct from high temperature BGB komatiites, but are very similar to peridotite spinel compositions of late Archean oceanic rock sequences argued to be ophiolites (Kusky and Jianghai, 2010) as well as Neoproterozoic and Cenozoic ophiolites that are argued to have formed in a supra-subduction zone tectonic setting (Dick and Bullen, 1984; Stowe, 1994; Stern et al., 2004).

The Kromberg sequence B beneath the KSM is c. 1.4 km thick and is therefore interpreted to represent a relatively thin, dismembered sequence of oceanic, mafic-ultramafic rocks. In this context, a geodynamic model is preferred in which the Kromberg type-section represents sequential tectonic stacking of relatively thin, shear zone-bounded allochtonous slices of Paleoarchean oceanic crust and mantle obducted at c.3230 Ma over the underlying clastic sedimentary rocks of the Noisy formation (see Figure 4.2). Thin oceanic crust in the early-mid Archean as a result of elevated mantle geothermal gradients, has previously been proposed (e.g. see Arndt, 1983). The upper parts of KSM (KS1) display late extensional features in the form of quartz-carbonate veins, whereas KS2 deeper in the section only displays ultramafic mylonitic fabrics. This suggests that the major transpressional tectonic event at 3227-3230 Ma may have involved upper crustal level extension in the KSM with fluid infiltration, and simultaneous lower crustal shearing and compression, a tectonic mechanism that has been proposed in major transpressional settings (c.f. Carson et al., 1997). Alternatively, thrusting during obduction may have been followed by extensional detachment and or retrograde fluid infiltration, subsequent to obduction of the oceanic sequence. In summary, a tectonic model is preferred for the Kromberg type-section in, which multi-stage retrograde metamorphism occurred in a syn- and/or post-obduction regime that most likely involved tectonic burial of an ophiolitic-type thrust nappe pile. Extensive retrograde fluid

alteration appears to have been focused locally along the KSM shear zone. Although previously the low-grade upper Onverwacht Group has been thought to have escaped the major 3.2 Ga tectonothermal episode in the BGB, but this study argues to the contrary that the Kromberg type section records obduction and tectono-thermal metamorphism at that time.

4.10. Conclusions

[1]. Metamorphic constraints determined here indicate a more variable and complex metamorphic history for the Kromberg-type section rocks than previously indicated. A wide range in metamorphic conditions spanning sub-greenschist to uppermost greenschist facies conditions is reported. Two metamorphic events are recorded in the Kromberg Section Mylonites (KSM): (a) a high-*T* (420 ± 30^{o}C), *P* < 3 kbar event, and (b) a lower-*T* event (240-350^{o}C), *P* = 2.9 ± 0.15 kbar, related to late-stage fluid infiltration during extension and recorded by multiple carbonate-quartz veins. The earliest metamorphic event related to deformation and mylonite development in the KSM could not be constrained in this study due to subsequent retrograde overprinting by the *HT* and *LT* fluid infiltration events. Pillow lavas directly below the mylonite zone record the same metamorphic conditions. Metabasalts at a distance of 90m and 125m above the KSM record much lower conditions 250-340^{o}C. In the lower Kromberg sequence beneath the KSM, metamorphic conditions vary from 215-321^{o}C (at P < 2.9 kbar) to low-grade, subgreenschist facies conditions of between 140-209^{o}C in the lowermost Kromberg. Thermodynamic modelling of fluid conditions in the mid-lower Kromberg indicates low CO_2 activity of less than a(CO_2) = 0.15.

[2]. Petrographic observations and the high temperature upper greenschist facies conditions determined by thermodynamic modelling on chlorite and fuchsitic micas of the KSM, indicate that these rocks cannot be the result of low temperature (~60^{o}C) chemical weathering of komatiitic flow tops under Archean atmospheric conditions as previously proposed. Rather, the field observations, metamorphic conditions, relic protolith phases and alteration mineral assemblages of the KS1 mylonites indicate that they are listvenite and rocks of the listvenite series.

[3]. The presence of an inverted metamorphic field gradient (see Fig. 4.11) suggests thrust repetition in the Kromberg type-section. In this new geodynamic model, the KSM

represents a basal thrust zone along which Kromberg sequence A was thrust over sequence B. Cr-spinels bearing rocks in the KSM with high Cr#'s and are similar to ultramafic rocks formed in Archean, Neoproterozoic and Cenozoic supra-subduction zone settings. A tectonic model is therefore preferred, in which the oceanic rocks of the Kromberg type-section were obducted as a series of allochtonous thrust nappes over the underlying clastic sedimentary rocks of the upper Noisy formation. The occurrence of listvenite in the KSM further supports a thrust model given that listvenite formation in observed in basal thrust zones in dismembered ophiolite terranes (for example, the Cretaceous Semail ophiliote, Oman). Although no absolute ages are currently available, thrusting and emplacement of relatively thin oceanic crust most likely occurred during a major transpressional event in the BGB, during oblique subduction and ocean closure between 3227 and 3230 Ma.

[4]. Traditionally, the low-grade volcanic rocks of the Onverwacht Suite in the BGB are interpreted to be part of a continuous volcanic stratigraphy recording regional low-grade metamorphism with progressive increase in metamorphic grade with depth. Although Paleoarchean low temperature seafloor metamorphism may be preserved in some parts of the Onverwacht Group (e.g. Hofmann and Harris, 2008; Lopez-Martinez, 1992), the distribution of the metamorphic conditions with depth, preserved as an inverted metamorphic field gradient, in the Kromberg-type section does not support a simple regional greenschist facies metamorphic profile for Onverwacht Group of the BGB. Rather, the 150m wide KSM represents a basal thrust zone that marks an important tectono-thermal discontinuity in the stratigraphy of the upper Onverwacht Group along which there was extensive deformation, followed by high T, low P metamorphism and significant fluid infiltration.

Chapter 5

Distinguishing obduction- and seafloor- related silicification in the Barberton Greenstone Belt, South Africa: Implications for early life environments.

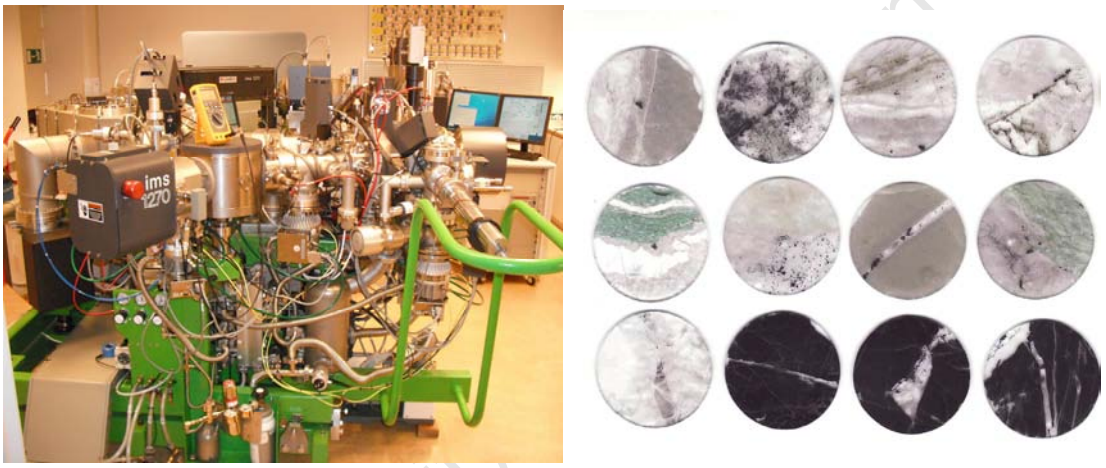

NORDSIM 1280 ion microprobe Stockholm, Sweden (left). Range of 1-inch SIMS samples from the Kromberg type-section prepared for in-situ sulphur stable isotope analyses (right).

5.1. Introduction

The origin of pervasive silica alteration associated with Cr-mica-carbonate-quartz zones observed in mafic-ultramafic Onverwacht Group rocks of the BGB is a highly debated topic (e.g. de Wit, 1982a; de Wit et al., 1982b; 1983; 1986a,b; 2011; Duchac and Hanor, 1987; Hanor and Duchac, 1990; Hoffman and Harris, 2008; Hoffman, 2011; Lowe and Byerly, 1986; Paris et al., 1985). Understanding hydrothermal and physical processes in these zones has important bearing on the nature and dynamics of shallow crustal alteration during the Archean, and the oceanic environments that were available to early microbial life (e.g. Hofmann and Harris, 2008). Many workers have argued that silicification of mafic-ultramafic rocks and the associated Cr-mica-carbonate-quartz alteration assemblage observed in these zones was the result of convecting, low-temperature (~50-150^{o}C), seafloor alteration beneath sedimentary chert units (e.g. Duchac and Hanor, 1987; Hanor and Duchac, 1990; Paris et al., 1985; Hoffman and Harris, 2008). On the other hand de Wit and de Wit et al., (1982a,b) have argued that extensive silicification of mafic and ultramafic rocks was the result of silica domes related to oceanic mafic intrusive activity that overlapped in time with development of fuchsite-carbonate-quartz along gravity-induced, tectonic glide planes. However, Paris et al., (1985) were the first to point out the possibility of more than one type of silicification event, and questioned penecontemporaneous silicification in the early Paleaoarchean tectonic model of de Wit and de Wit et al. (1982a,b). Whether more than one type of silica alteration event/style can be distinguished, and whether or not the timing of such silicification events can be resolved, remain open questions (e.g. Paris et al., 1985).

In this chapter the Cr-mica-carbonate-quartz rocks of the Kromberg mafic-ultramafic sequence are studied in detail from a geochemical perspective to further explore the ophiolite-type obduction model for the Kromberg sequence presented in Chapter 4. A geochemical profile across the KSM (Kromberg sequence mylonites) fuchsite-carbonate-quartz rocks is presented to provide insights into fluid-rock and hydrothermal-seawater-atmospheric interactions in the Paleoarchean. A range of bulk geochemical techniques are applied to the KSM protolith and vein assemblage, along with in-situ S isotopes on sulphides in mineralized chert veins and both the upper

silicified seafloor sediments and from within sheared rocks of the KSM. The overall aim is to further our understanding of the Paleoarchean atmospheric, seawater and possible microbial sulphur cycle. There is currently no published isotopic or other geochemical data on the carbonate veins within the KSM fuchsite-carbonate-quartz zone.

The specific objectives of this geochemical study therefore include: (i) to provide constraints on the protolith chemistry and geodynamic setting of the Kromberg mafic-ultramafic rocks; (ii) to determine the extent and style of alteration within and surrounding the KSM; (iii) to determine the origin of the carbonate-quartz veins/bands in the KSM; (iv) to better understand isotopic and geochemical fluxes between Archean oceanic crust (possible oceanic versus obducted geochemical signatures), ancient seawater alteration and atmospheric reservoirs; (v) to test alteration and geodynamic models for silicification processes in the BGB.

The pristine drill core KD1 allows for determination of a continuous alteration and geochemical profile across the KSM, not previously obtainable on surface. Routine X-Ray Diffraction (XRD) analysis was used to determine the presence or absence of major igneous and alteration minerals throughout the drill core section. Major and trace elements, including rare REE's were determined by X-Ray Fluorescence (XRF) Spectrometry and Inductively coupled plasma mass spectrometry (ICP-MS). Carbon, oxygen, strontium and sulphur isotopic analyses were conducted to determine the origin of the carbonate veins and distinguish possible fluid sources for the altered rocks observed in the KSM.

5.2. Geochemical sampling protocol and drill core descriptions

A brief description of the various lithologies of interest across the drill core KD1 (total length 261 m) is presented here to provide the context for the geochemical sampling. Drill core lithological log data at various scales along with representative images of selected rock types are presented in Figure 5.1 and 5.2, respectively. The drill core section KD1 includes two major laminated chert units of 12 m each in an 83-m-thick section of variably metasomatized and silicified, massive mafic intrusives and lava flows.

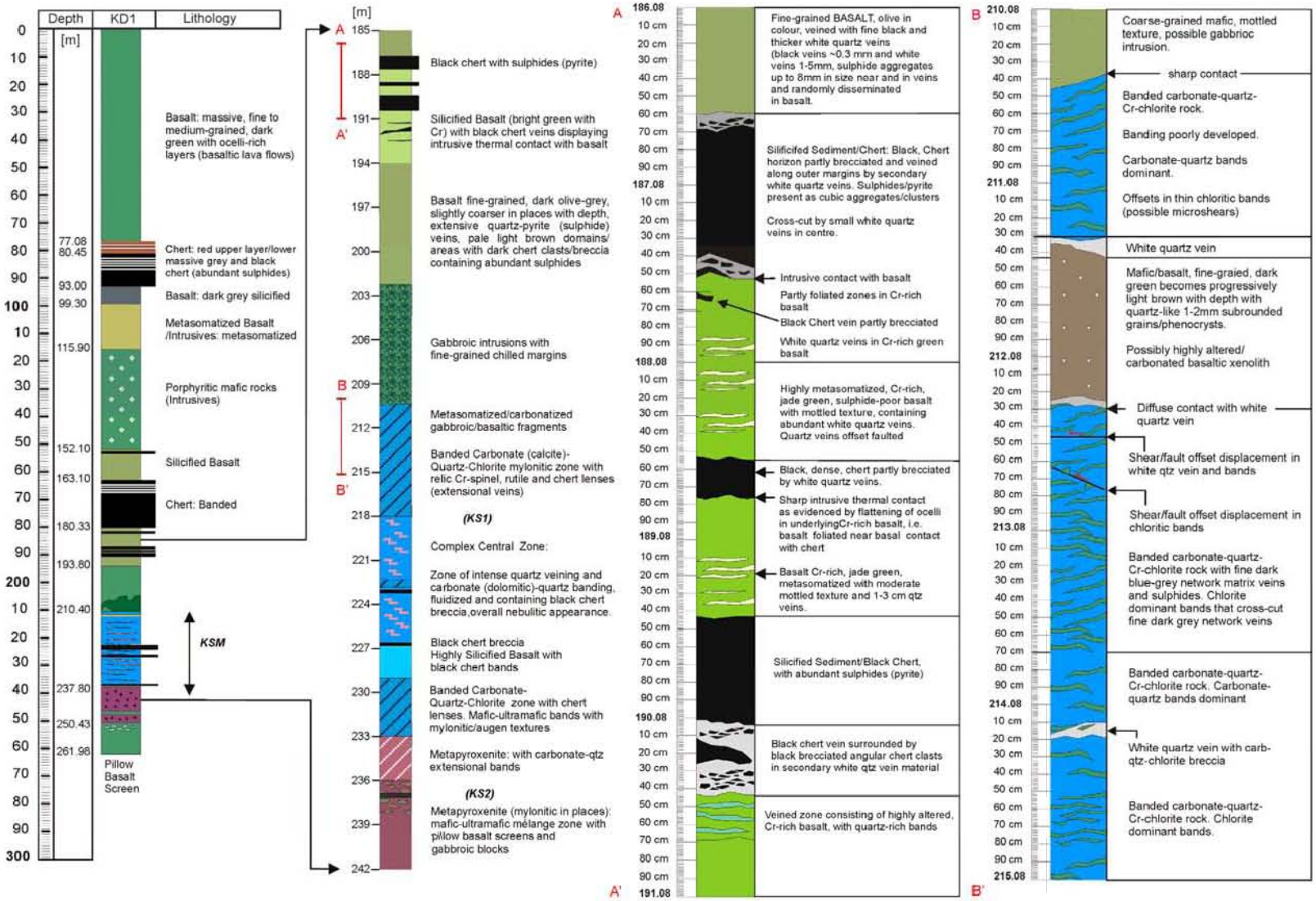
Depth
KD1
Lithology
[m]
Basalt: massive, fine to medium-grained, dark green with ocelli-rich layers (basaltic lava flows)
77.08
80.45
Chert: red upper layer/lower massive grey and black chert (abundant sulphides)
93.00
99.30
Basalt: dark grey silicified
Metasomatized Basalt /Intrusives: metasomatized
115.90
Porphyritic mafic rocks (Intrusives)
152.10
Silicified Basalt
163.10
Chert: Banded
180.33
193.60
210.40
KSM
237.80
250.43
261.98
Pillow Basalt Screen
A
A'
B
B'
Black chert with sulphides (pyrite)
Silicified Basalt (bright green with Cr) with black chert veins displaying intrusive thermal contact with basalt
Basalt fine-grained, dark olive-grey, slightly coarser in places with depth, extensive quartz-pyrite (sulphide) veins, pale light brown domains/ areas with dark chert clasts/breccia containing abundant sulphides
Gabbroic intrusions with fine-grained chilled margins
Metasomatized/carbonatized gabbroic/basaltic fragments
Banded Carbonate (calcite)-Quartz-Chlorite mylonitic zone with relic Cr-spinel, rutile and chert lenses (extensional veins)
(KS1)
Complex Central Zone:
Zone of intense quartz veining and carbonate (dolomitic)-quartz banding, fluidized and containing black chert breccia,overall nebulitic appearance.
Black chert breccia
Highly Silicified Basalt with black chert bands
Banded Carbonate-Quartz-Chlorite zone with chert lenses. Mafic-ultramafic bands with mylonitic/augen textures
Metapyroxenite: with carbonate-qtz extensional bands
(KS2)
Metapyroxenite (mylonitic in places): mafic-ultramafic mélange zone with pillow basalt screens and gabbroic blocks
Fine-grained BASALT, olive in colour, veined with fine black and thicker white quartz veins (black veins ~0.3 mm and white veins 1-5mm, sulphide aggregates up to 8mm in size near and in veins and randomly disseminated in basalt.
Silicifed Sediment/Chert: Black, Chert horizon partly brecciated and veined along outer margins by secondary white quartz veins. Sulphides/pyrite present as cubic aggregates/clusters
Cross-cut by small white quartz veins in centre.
Intrusive contact with basalt
Partly foliated zones in Cr-rich basalt
Black Chert vein partly brecciated
White quartz veins in Cr-rich green basalt
Highly metasomatiized, Cr-rich, jade green, sulphide-poor basalt with mottled texture, containing abundant white quartz veins. Quartz veins offset faulted
Black, dense, chert partly brecciated by white quartz veins.
Sharp intrusive thermal contact as evidenced by flattening of ocelli in underlyingCr-rich basalt, i.e. basalt foliated near basal contact with chert
Basalt Cr-rich, jade green, metasomatized with moderate mottled texture and 1-3 cm qtz veins.
Silicified Sediment/Black Chert, with abundant sulphides (pyrite)
Black chert vein surrounded by black brecciated angular chert clasts in secondary white qtz vein material
Veined zone consisting of highly altered, Cr-rich basalt, with quartz-rich bands
Coarse-grained mafic, mottled texture, possible gabbrioc intrusion.
sharp contact
Banded carbonate-quartz-Cr-chlorite rock.
Banding poorly developed.
Carbonate-quartz bands dominant.
Offsets in thin chloritic bands (possible microshears)
White quartz vein
Mafic/basalt, fine-graied, dark green becomes progressively light brown with depth with quartz-like 1-2mm subrounded grains/phenocrysts.
Possibly highly altered/ carbonated basaltic xenolith
Diffuse contact with white quartz vein
Shear/fault offset displacement in white qtz vein and bands
Shear/fault offset displacement in chloritic bands
Banded carbonate-quartz-Cr-chlorite rock with fine dark blue-grey network matrix veins and sulphides. Chlorite dominant bands that cross-cut fine dark grey network veins
Banded carbonate-quartz-Cr-chlorite rock. Carbonate-quartz bands dominant
White quartz vein with carb-qtz-chlorite breccia
Banded carbonate-quartz-Cr-chlorite rock. Chlorite dominant bands.

Figure 5.1. Lithological logs of KD1 drill core indicating the sections targeted for sampling and detailed lithological investigation. From left to right, full log of KD1, expanded log across the KSM, selected profiles A-A' and B-B'. The lithological symbols are consistent with those presented in Chapter 4. Textural observations in the drill core reveal at least 2 types of silicification and quartz veining. The profile A-A' highlights silicification, veining and brecciation of silicified basalt typical of seafloor-type alteration in the Barberton Greenstone Belt. The detailed profile B-B' illustrates the extensional carbonate-quartz bands, and textures associated with to listvenitic alteration in the KSM shear zone. Examples of the different rock types with depths are provided in Fig. 5.2.

The first of these chert units referred to as the Footbridge Chert includes an upper 2.5m-thick oxidized horizon, followed by an 8.5-m lower part consisting of black massive, occasional white-banded chert containing pyrite (Figure 5.1 and 5.2). The second laminated chert was intercepted at a depth of about 115 m below surface and occurs at the center of a 30-m-wide zone of variably silicified basalt (Figure 5.1 and 5.2). It is underlain by at least two minor sedimentary chert horizons that, in turn, are associated with a number of discontinuous black chert lenses and veins. In the drill core the carbonate mylonites of the KSM are approximately 20m thick (Figure 5.1 and 5.2). A mafic intrusion (gabbroic rock) with mottled texture and chilled margins occurs directly above the KSM (Figure 5.1 and 5.2). The drill core ends in a metapyroxenitic unit consisting of a mélange of ultramafic rocks, metagabbros and pillow basalt screens for about 17 m beneath the lower KSM.

Individual sample rock powders were made from a total of 93 rock slabs from the lower half of KD1 over the depth interval 179.58 to 261.08 m across the KSM (samples T1 to T93). The samples were taken at 1 meter intervals, but near major contacts with the shear zone the sampling density was increased to every 0.5 meters. The lithological log and sample descriptions over this depth interval are presented in Figs. 5.1 to 5.3 and depths for all 93 samples are given in Appendix B. Each sample included a quarter of the drill core with a total length of about 8 cm and weight of between 70-80 grams.

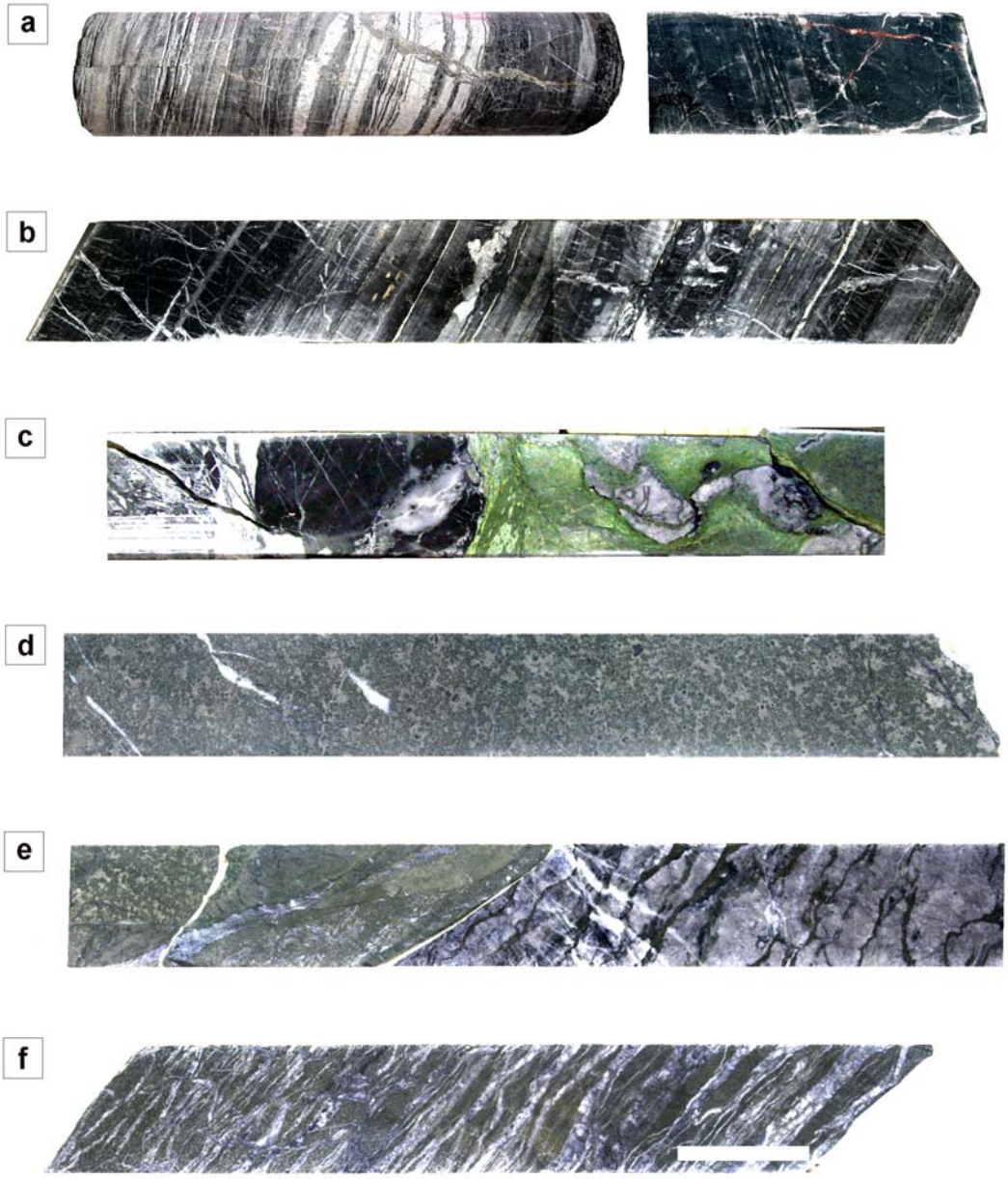

Figure 5.2. Representative drill core sections across KD1 related to geochemical sampling: **(a)** primary sedimentary laminations in the Footbridge Chert, outer surface of drill core left image, cut surface right image, depth interval 82.43 to 82.64 m; **(b)** second laminated chert horizon in the lower parts of KD1 with pyrite grains, depth interval 163.10 to 163.40 m; **(c)** contact between intrusive vein and highly silicified metabasalt, depth 188.78 – 189.05 m; **(d)** coarse-grain mottled texture in metagabbro/ mafic intrusion, depth 207.96 – 208.34 m; **(e)** structural contact between the KSM shear zone

and the metagabbro with carbonate-quartz bands present in the KSM, depth interval 210.32 to 210.65. **(f)** Carbonate-quartz extensional bands with metapyroxenitic bands in the lowermost KSM depth 221.06 – 221.34 m. White scale bar = 5 cms.

This sample size was chose in order to provide enough material for representative bulk rock mineral and chemical analysis for each sample depth in the drill core. The remaining quarter of the drill core material was kept for curation. Of the total 70-80 grams of powder, 6 grams were used for major and trace element analysis by XRF, less than 1 gram for ICP-MS analysis, 0.7 gram for XRD analysis, less than 1 gram for each stable and radiogenic isotope analyses. In addition, thin sections were prepared for in-situ SIMS sulphur isotope analyses from selected veins in the dill core (see section 5.7 below).

5.3. Major and trace elements by X-Ray Fluorescence (XRF) Spectrometry

Bulk rock major and some trace element concentrations, excluding the REE, were determined for all 93 samples by conventional x-ray fluorescence spectrometry (XRF) on a Philips X'Unique II PW1480 spectrometer in the Department of Geological Sciences at the University of Cape Town following the techniques described by le Roex et al., (2001). The lithium tetraborate fusion method of Norrish and Hutton (1969) was used to determine all major and some minor elements, whereas pressed powder briquettes were used for determination of the trace elements. A loss-on-ignition (LOI) value was obtained for each sample by heating in a furnace for at least 12 hours at ~950^{o}C. The disks were analyzed using XRF with a dual target Mo/Sc X-ray tube. Fe, Mn, Ni, Cr and Ti are measured with the tube at 50 kV, 50 mA. The other elements were determined with the tube at 40 kV, 65 mA. Peak only measurements were made on the elements Ni through Mg. Sodium was determined using powder briquettes at 40 kV, 65 mA, and with background measured at –2.00 and +2.00^{o}2 θ from the peak. Typical detection limits are below 0.01 wt% and 2 ppm for the major and trace elements, respectively.

Selected major and trace element ratios are plotted with depth and lithological log data in Figure 5.3 and representative sample data is presented in Table 5.1. All XRF sample data is presented in Appendix E1, and Fe_2O_3 is calculated at 15 wt% of total FeO. Drill core observations indicate extensive silicification associated with black chert veins, carbonate veining and hydrothermal alteration across the KSM.

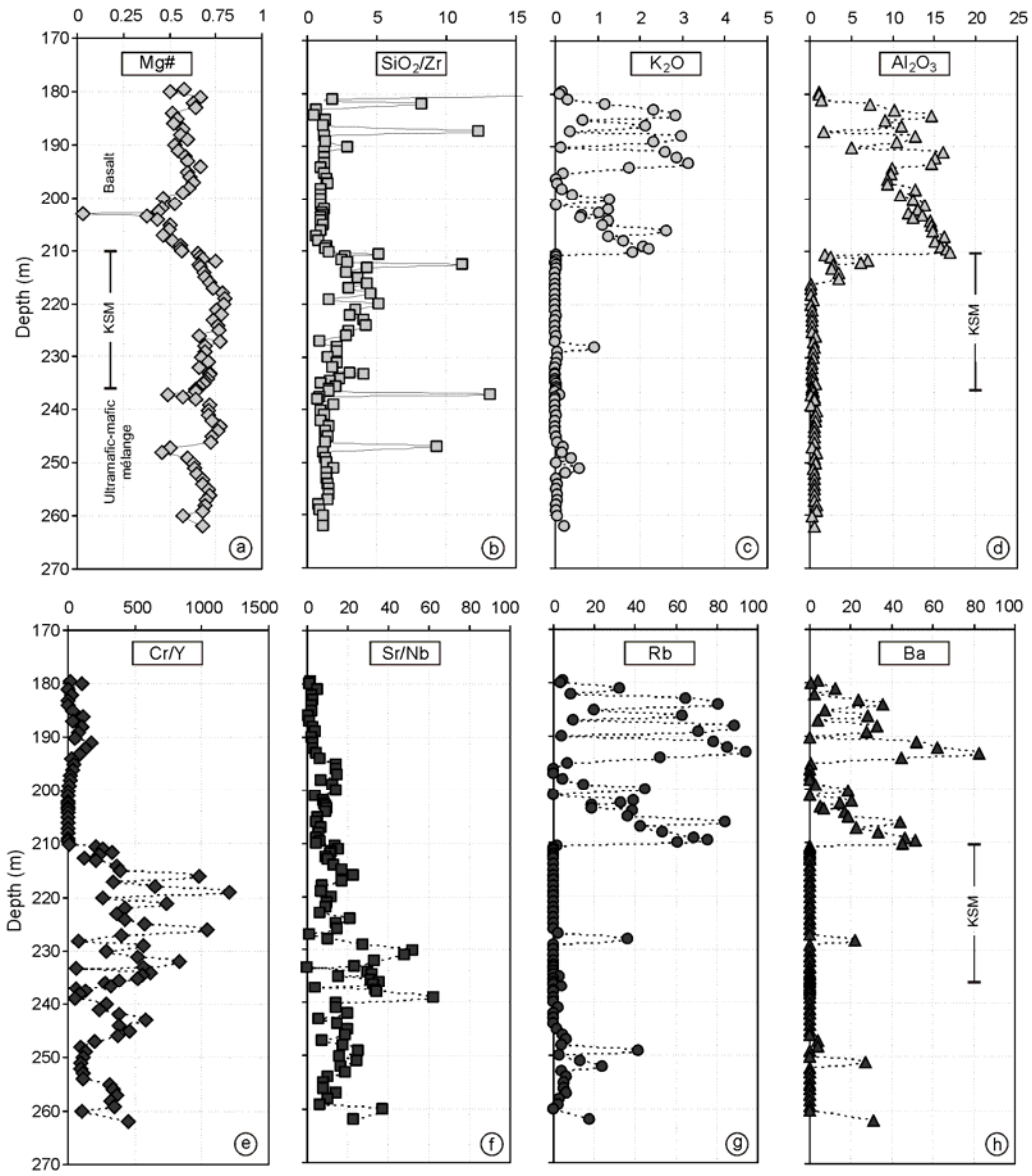

Figure 5.3. Major and trace element variation with depth across the KSM in drill core KD1.

Table 5.1. Major and trace element concentrations of representative rocks in drill core samples in KD1.

	KD1-T12 black chert	**KD1-T15** metabasalt	**KD1-T17** metabasalt	**KD1-T19** metabasalt	**KD1-T21** metabasalt	**KD1-T23** metabasalt	**KD1-T26** metagabbro Intrusion	**KD1-T29** metagabbro Intrusion	**KD1-T31** metagabbro Intrusion	**KD1-T33** metagabbro Intrusion	**KD1-T37** KSM mylonite	**KD1-T43** KSM mylonite	**KD1-T45** KSM mylonite	**KD1-T47** KSM mylonite
SiO_2	54.06	55.76	40.28	43.14	42.52	44.61	48.95	51.14	48.48	63.38	19.14	26.54	19.91	38.21
TiO_2	0.29	0.86	0.61	0.58	0.69	0.83	0.80	0.89	1.28	0.91	0.19	0.23	2.83	5.61
Al_2O_3	5.09	14.64	9.74	9.34	10.91	13.88	13.61	14.68	16.25	15.72	2.53	3.47	0.19	0.47
FeO	7.42	5.21	8.80	8.06	7.80	14.12	8.53	8.48	8.45	4.71	7.08	6.89	6.86	9.46
$Fe_2O_3^*$	0.82	0.57	0.97	0.89	0.86	1.55	0.94	0.93	0.93	0.52	0.78	0.76	0.76	1.04
MnO	0.31	0.16	0.20	0.24	0.22	0.19	0.29	0.20	0.19	0.08	0.97	0.83	0.75	0.15
MgO	4.66	4.38	7.40	7.60	5.93	8.96	0.15	4.84	4.16	3.34	7.98	8.70	10.63	21.41
CaO	5.43	4.89	14.06	15.86	13.83	4.81	10.61	6.26	5.99	1.39	27.62	23.13	24.15	6.50
Na_2O	0.09	1.05	0.66	0.29	1.28	0.64	3.71	2.64	3.85	3.29	0.18	0.18	0.06	0.16
K_2O	0.14	3.14	0.20	0.05	0.42	0.01	0.64	1.13	1.27	2.07	0.03	0.01	0.00	0.00
P_2O_5	0.02	0.10	0.05	0.05	0.06	0.07	0.06	0.07	0.13	0.10	0.06	0.06	0.03	0.05
SO_3	0.26	0.29	0.51	0.07	0.20	0.04	0.38	0.05	0.05	0.05	0.34	0.03	0.05	0.09
$C_{r2}O_3$	0.08	0.21	0.10	0.05	0.03	0.02	0.03	0.02	0.01	0.03	0.19	0.33	0.42	0.76
NiO	0.05	0.06	0.02	0.02	0.02	0.01	0.02	0.02	0.02	0.02	0.04	0.05	0.07	0.21
Mg#	0.53	0.60	0.60	0.63	0.58	0.53	0.03	0.50	0.47	0.56	0.67	0.69	0.73	0.80
H2O-	0.06	0.04	0.04	0.06	0.01	0.01	0.02	0.02	0.03	0.12	0.08	0.11	0.09	0.12
LOI	19.84	7.48	15.17	12.66	13.85	8.71	9.79	7.67	7.31	3.35	31.41	27.71	31.75	14.11
Total	99.44	99.44	99.80	99.84	99.49	100.05	99.46	99.97	99.33	99.60	99.38	99.81	99.30	99.44
Mo	10.3	b.d.l	b.d.l	b.d.l	b.d.l	b.d.l	b.d.l	b.d.l	b.d.l	b.d.l	b.d.l	b.d.l	b.d.l	b.d.l
Nb	4.1	4.4	4.3	3.9	4.9	4.5	5.0	5.1	5.2	4.3	3.7	3.2	3.2	4.3
Zr	18.6	46.0	31.8	28.4	41.9	46.3	43.0	45.0	74.8	45.9	7.0	7.3	6.6	23.9
Y	11.1	17.0	13.0	14.2	14.8	15.8	17.7	16.2	27.0	18.5	4.8	6.0	8.3	6.7
Sr	8.3	20.3	62.6	58.8	62.6	18.6	45.7	26.1	34.9	18.7	56.7	55.4	54.6	30.6
U	b.d.l	b.d.l	b.d.l	b.d.l	b.d.l	b.d.l	b.d.l	b.d.l	b.d.l	b.d.l	b.d.l	b.d.l	b.d.l	b.d.l
Th	b.d.l	b.d.l	b.d.l	b.d.l	b.d.l	b.d.l	b.d.l	b.d.l	b.d.l	b.d.l	b.d.l	b.d.l	b.d.l	b.d.l
Rb	3.8	94.1	6.6	b.d.l	15.0	b.d.l	18.5	36.3	42.9	68.8	b.d.l	b.d.l	b.d.l	b.d.l
Pb	b.d.l	b.d.l	b.d.l	b.d.l	b.d.l	b.d.l	b.d.l	b.d.l	b.d.l	b.d.l	b.d.l	b.d.l	b.d.l	b.d.l
Zn	112.5	75.4	130.5	106.7	113.9	182.2	97.9	166.2	180.1	92.5	82.4	82.6	101.2	210.7
Cu	49.4	78.8	74.7	43.6	51.0	43.3	27.2	64.6	49.0	87.6	16.4	14.8	8.0	64.2
Ni	431.1	387.4	130.8	86.2	81.3	67.3	56.6	85.5	112.7	112.2	275.2	418.3	543.4	1824.3
Co	59.1	56.2	46.4	35.8	41.2	63.2	24.8	75.5	73.4	41.8	42.1	68.7	73.7	161.3
Mn	2180.1	1818.5	1819.5	1819.9	1819.8	1819.4	1820.9	1819.5	1819.4	758.4	3003.3	3001.5	2999.7	2985.3
Cr	589.1	1511.0	541.6	219.1	125.8	24.2	58.3	25.3	b.d.l	21.2	1262.3	2331.2	2780.9	8113.9
V	152.3	363.7	242.2	199.4	232.7	350.0	291.9	347.5	402.9	377.0	70.8	101.5	83.8	230.3
Ba	b.d.l	82.4	0.4	b.d.l	3.0	b.d.l	4.8	18.9	22.7	46.1	b.d.l	b.d.l	b.d.l	b.d.l
Sc	31.5	56.7	37.0	30.1	33.2	46.5	39.8	47.0	51.2	49.5	10.9	16.3	15.2	29.8

Major element concentrations in wt% and trace element concentrations in ppm. b.d.l = below detection limit.

Table 5.1. (Cont.) Major and trace element concentrations of representative rocks in drill core samples in KD1.

	KD1-T49 KSM mylonite	**KD1-T51** chert vein	**KD1-T53** KSM mylonite	**KD1-T55** Silicified basalt	**KD1-T57** KSM mylonite	**KD1-T59** KSM mylonite	**KD1-T61A** KSM mylonite	**KD1-T64** KSM mylonite	**KD1-T68** chert vein	**KD1-T71** metapyrox. (mélange)	**KD1-T73** metapyrox. (mélange)	**KD1-T77** metapyrox. (mélange)	**KD1-T79** metapyrox. (mélange)	**KD1-T85** metapyrox. (mélange)
SiO_2	39.21	54.62	33.51	34.30	44.06	36.16	28.22	34.22	91.28	25.58	43.50	34.90	83.77	44.69
TiO_2	4.61	4.25	6.00	6.23	7.98	5.07	5.23	8.75	1.43	1.92	5.45	5.11	2.24	9.01
Al_2O_3	0.29	0.29	0.34	0.35	0.48	0.31	0.33	0.64	0.09	0.20	0.69	0.51	0.27	0.61
FeO	7.09	6.16	7.38	9.55	7.54	5.37	8.63	11.88	1.18	3.61	8.27	9.80	1.15	9.72
$Fe_2O_3^*$	0.78	0.68	0.81	1.05	0.83	0.59	0.95	1.31	0.13	0.40	0.91	1.08	0.13	1.07
MnO	0.29	0.26	0.36	0.47	0.51	0.56	0.24	0.18	0.05	0.32	0.25	0.23	0.11	0.22
MgO	12.40	9.48	13.51	18.14	9.57	7.37	12.11	14.45	0.63	5.17	11.44	14.86	0.65	11.67
CaO	12.28	8.64	11.26	19.80	12.34	21.70	17.74	11.83	2.52	42.40	15.94	15.71	6.09	10.23
Na_2O	0.13	0.09	0.06	0.11	0.12	0.04	0.08	0.09	0.01	0.02	0.12	0.08	0.42	0.05
K_2O	0.01	0.01	0.01	0.01	0.05	0.03	0.01	0.03	0.10	0.01	0.01	0.02	0.20	0.04
P_2O_5	0.03	0.02	0.03	0.03	0.08	0.03	0.03	0.05	0.02	0.01	0.05	0.03	0.06	0.05
SO_3	0.23	0.03	0.14	0.21	0.13	0.06	0.26	0.35	0.08	0.04	0.24	0.41	0.09	0.03
$C_{r2}O_3$	0.44	0.20	0.45	0.48	0.67	0.43	0.52	0.54	0.02	0.10	0.30	0.40	0.16	0.20
NiO	0.13	0.06	0.14	0.16	0.20	0.11	0.17	0.19	0.03	0.05	0.09	0.16	0.04	0.04
Mg#	0.76	0.73	0.77	0.77	0.69	0.71	0.71	0.68	0.49	0.72	0.71	0.73	0.50	0.68
H2O-	0.09	0.05	0.09	0.14	0.05	0.04	0.07	0.10	0.00	0.02	0.02	0.03	0.00	0.12
LOI	20.61	14.75	25.23	7.40	14.93	20.96	24.36	14.01	2.17	19.03	11.11	15.48	4.76	10.95
Total	99.42	100.27	100.16	99.49	100.38	99.41	99.89	99.93	99.87	99.29	99.33	99.91	100.26	99.78
Mo	b.d.l	b.d.l	b.d.l	b.d.l	b.d.l	b.d.l	3.2	b.d.l	2.0	b.d.l	b.d.l	b.d.l	b.d.l	b.d.l
Nb	3.8	3.8	3.7	4.2	2.7	3.4	14.0	4.5	3.8	3.7	5.1	3.7	3.4	4.2
Zr	11.3	13.3	11.3	36.7	20.0	16.9	6.9	33.2	7.0	13.6	35.7	23.2	9.0	31.9
Y	5.8	4.8	6.3	12.1	9.8	6.1	81.3	9.5	2.2	6.1	10.5	7.9	5.6	12.5
Sr	37.2	23.2	53.8	4.0	74.0	161.1	b.d.l	69.1	15.0	231.6	72.8	75.8	25.0	79.7
U	b.d.l	b.d.l	b.d.l	b.d.l	b.d.l	b.d.l	b.d.l	b.d.l	b.d.l	b.d.l	b.d.l	b.d.l	b.d.l	b.d.l
Th	b.d.l	b.d.l	b.d.l	b.d.l	b.d.l	b.d.l	b.d.l	b.d.l	b.d.l	b.d.l	b.d.l	b.d.l	b.d.l	b.d.l
Rb	b.d.l	b.d.l	b.d.l	2.1	b.d.l	b.d.l	b.d.l	2.7	3.9	b.d.l	2.2	1.9	6.4	3.8
Pb	b.d.l	b.d.l	b.d.l	b.d.l	b.d.l	b.d.l	b.d.l	b.d.l	b.d.l	b.d.l	b.d.l	b.d.l	b.d.l	b.d.l
Zn	126.3	100.2	166.3	366.5	211.8	80.9	141.7	191.1	21.0	57.8	141.3	148.7	43.3	151.7
Cu	55.1	22.1	33.1	2.1	38.8	30.9	24.8	31.7	28.6	17.9	65.1	43.0	30.2	31.6
Ni	967.3	494.4	935.2	625.5	1565.5	900.3	1254.9	1306.1	225.9	337.2	663.1	1171.2	239.8	278.7
Co	92.5	42.9	89.7	142.7	142.2	124.7	106.8	139.9	18.9	27.1	72.8	109.9	30.1	72.4
Mn	2989.2	2177.0	2991.6	2986.5	2182.5	2994.2	2987.1	2985.8	742.4	2987.4	2176.1	2986.8	743.7	2176.0
Cr	4297.1	1737.0	3593.2	4836.8	5526.5	3167.3	4785.5	4996.0	124.6	333.8	2439.9	3626.8	1106.1	1450.6
V	164.2	133.6	163.4	574.5	235.4	145.1	182.2	312.2	14.0	49.5	182.1	193.9	74.3	271.3
Ba	b.d.l	b.d.l	b.d.l	b.d.l	b.d.l	b.d.l	b.d.l	b.d.l	b.d.l	b.d.l	b.d.l	b.d.l	3.8	b.d.l
Sc	25.5	17.0	25.9	82.0	37.8	23.2	29.5	41.1	2.6	5.5	26.9	26.6	12.7	41.3

Major element concentrations in wt% and trace element concentrations in ppm. b.d.l = below detection limit.

As a first order attempt to assess bulk rock protolith variability in KD1, Mg-numbers were calculated for each sample. Mg-numbers for metabasaltic flows and altered mafic intrusives (over the interval 179-210m) generally range between 0.40 and 0.60, whereas rocks in the KSM and ultramafic mélange zone have typically higher ratios of between 0.65 – 0.77 (Fig. 5.3a). High SiO_2/Zr ratios correspond to silicified horizons and quartz veining (Fig. 5.3b). The high MgO, CaO and SiO_2 concentrations observed in the KSM are due to extensive carbonate (dolomite)-quartz veining in the KSM (see Figure 5.2). The Al_2O_3 concentration appears to indicate depletion in the KSM (Fig 5.3d). Calculated Cr/Y ratios were also plotted with depth as a monitor of the behaviour of relatively immobile elements across KD1. The Cr/Y ratios are the highest in the KSM due to the Cr-spinel in the pyroxenitic mantle protolith (Fig. 5.3e). Strontium concentration is variable but generally increases with depth across the KSM with the highest values near the basal contact between the KSM and the lower ultramafic mélange zone (Fig. 5.3f). The large-ion lithophile element (LILE) concentrations of Ba, Rb, and to a lesser extent Sc are relatively depleted in the KSM (Fig. 5.3g,h, Table 5.1 and Appendix E1).

A wide scatter in basalt compositions are observed in a total alkali versus silica diagram (Le Matré, 2002) for basalt compositions (Figure 5.4a) indicating that major elements cannot be used for basalt classification due to LILE mobility as a result of the extensive alteration. The highly altered carbonate mylonites in the KSM are plotted in a SiO_2-CaO-MgO listvenite diagram (after Nasir et al., 2007). The KSM banded carbonate mylonites have compositions which range between Type 1B and Type 2 (silica-rich) listvenite similar to the fuchsite-bearing listvenite types from basal thrust zones of the Semail Ophiolite in Oman (Fig. 5.4b; Nasir et al., 2007). In an attempt to constrain the least altered metabasalt and mafic intrusive protolith chemistry (over the depth interval 179 to 210m) bulk rock trace element compositions were plotted in discriminant diagrams of Pearce (2003) using the relatively immobile elements Cr, Zr and Y (Figure 5.4c,d). In a Zr/Y versus Zr diagram the basalts and mafic intrusives are tightly cluster in the island-arc thoelite field (IAT; Fig. 5.4c). A similar trend is seen in a Cr versus Y diagram where the least altered metabasalts and mafic intrusives above the KSM have island-arc to possible boninitic affinities (Fig. 5.4d).

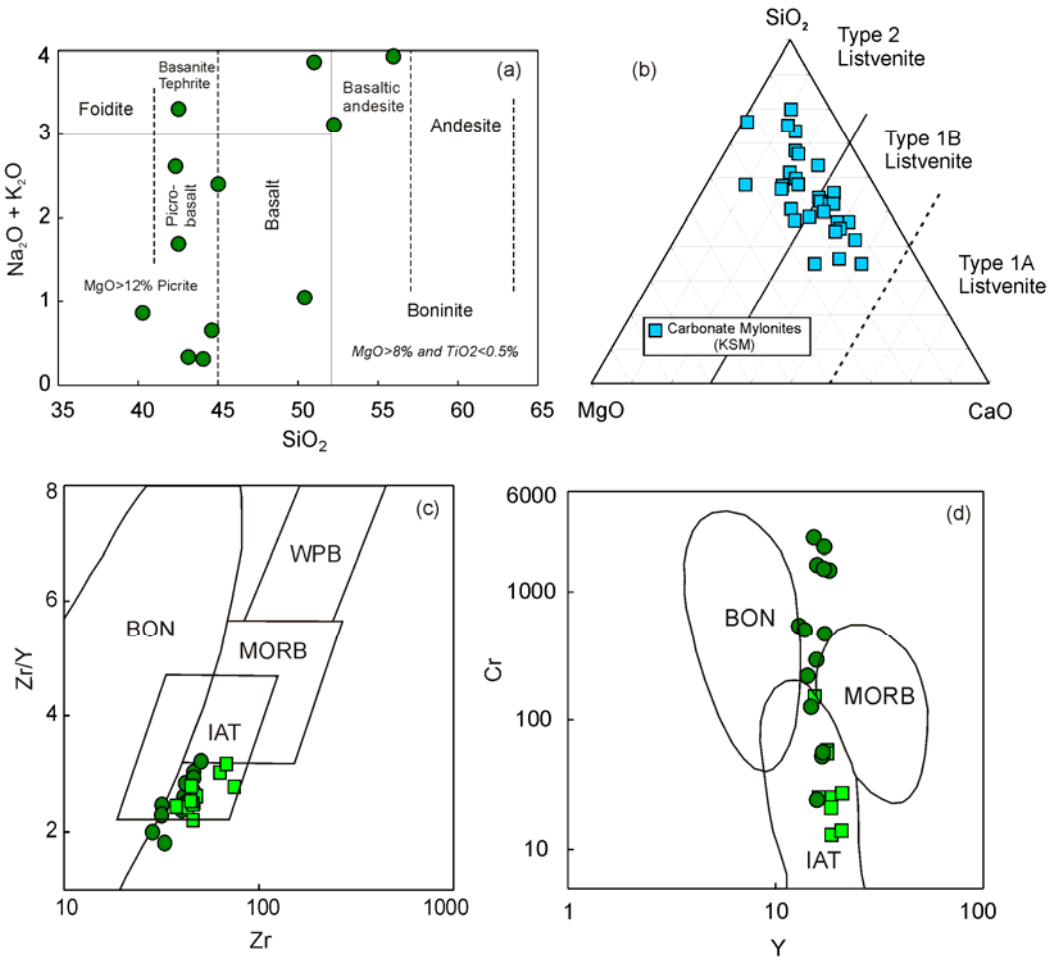

Figure 5.4. Major and trace element characterization of metabasalts (circles), mafic intrusives (green squares) and sheared rocks of the KSM (blue squares). **(a)** Attempt to classify metabasalts using major elements (after Le Matré, 2002). Extensive alteration and silicification, however, precludes the classification of the basalts on the basis of major elements. **(b)** Plotting the carbonate mylonites on the ternary diagram of Nasir et al. (2007) indicates that the extensively altered and silicified KSM samples plot in the Type 1B and Type 2 listvenite alteration fields. **(c-d)** Characterization of the metabasalts using relatively immobile elements. Metamorphic data across the Kromberg type-section in Chapter 4 supports the concept that plate-tectonics was likely operating during the Paleoarchean. The trace element data of the Kromberg metabasalts is compatible with their formation in a supra-subduction zone setting, i.e. IAT geodynamic environment (after Pearce, 2003).

5.4. Rare Earth Elements by Inductively coupled plasma mass spectrometry

A total of 28 samples were selected at 2m intervals across the KSM for Inductively-coupled plasma source mass spectrometry (ICP-MS) for the analysis of REEs. The ICP-MS analyses were performed on a Thermo Fisher Scientific ELEMENT2 HR-ICP-MS at the Department of Earth Science, University of Bergen. 100 mg of dry sample powders were digested in a microwave sample container using concentrated HNO_3 (4 ml), HF (1 ml) and HCL (5Ml). After digestion, the samples were transferred to 30 ml Savillex beakers and evaporated to dryness at 90ºC overnight. The residue was dissolved in 2N HNO_3, transferred to 50 ml volumetric flasks and diluted to volume with water. Before analysis the samples were diluted further and In was used as an internal standard. All REE data is presented in Appendix E2 and representative chondrite normalized data is presented in Table 5.2. The REE patterns for two silicified basalts and a metagabbro above the KSM (and beneath the second major chert horizon) is shown in Figure 5.5a, along with unsilicified rocks (open symbols) from above the KSM.

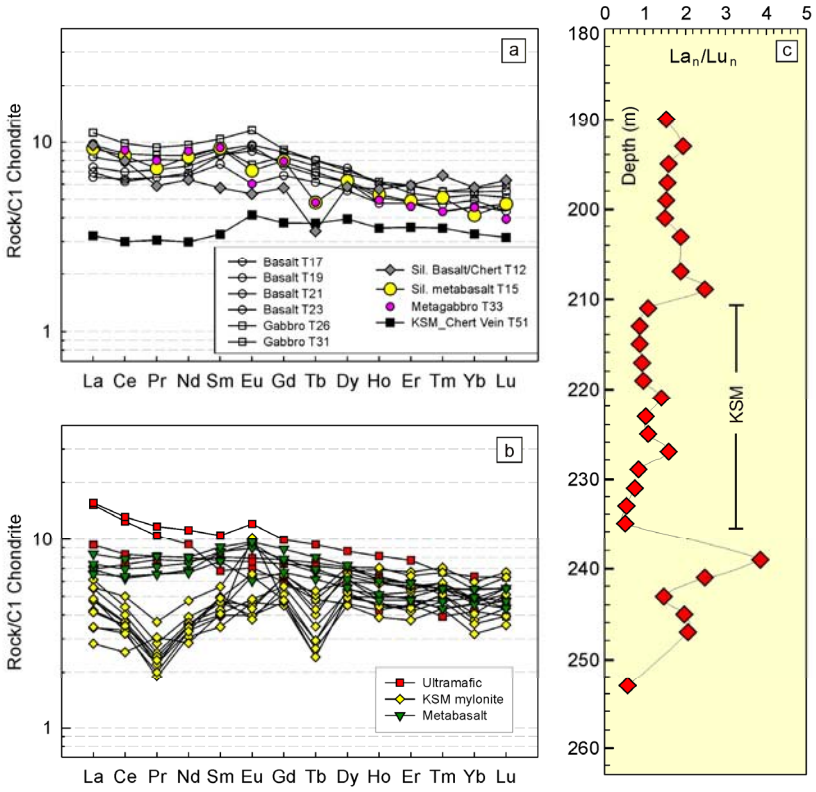

Table. 5.2 Chondrite Normalized REE data for selected KD1 drill core lithologies

Sample #	T12	T15	T17	T19	T21	T23	T26	T31	T33	T37	T41	T43	T45	T47
Descrp.	black chert	metabasalt	basalt	basalt	basalt	basalt	metagabbro	metagabbro	metagabbro	upp. KSM	upp. KSM	upp. KSM	upp. KSM	centr. KSM
Depth (m)	190.08	193.08	195.08	197.08	199.08	201.08	203.08	207.08	209.08	211.08	213.08	215.08	217.08	219.08
La	9.62	9.24	6.92	7.38	8.35	6.54	11.22	9.66	9.79	4.73	4.85	4.85	6.12	3.42
Ce	7.97	8.48	6.21	6.96	7.83	6.37	9.85	8.69	9.08	3.63	3.28	3.68	4.40	3.33
Pr	5.89	7.26	6.53	7.16	8.11	6.53	9.37	8.53	8.00	2.21	1.89	2.42	2.84	2.21
Nd	6.34	8.35	6.85	7.47	8.01	6.66	9.68	8.48	8.97	3.30	3.08	3.53	3.90	3.58
Sm	5.75	9.28	8.50	8.56	9.08	7.65	10.39	9.35	9.35	3.92	3.46	3.99	4.71	4.64
Eu	5.34	7.07	9.48	8.97	9.66	6.03	11.55	7.59	6.03	10.17	4.66	3.97	4.48	3.97
Gd	5.74	7.98	7.54	7.83	8.86	6.67	9.15	8.37	7.93	4.72	4.48	5.11	6.28	4.67
Tb	3.40	4.81	6.68	6.95	8.02	6.15	8.02	7.49	4.81	2.41	2.41	2.94	4.01	2.67
Dy	5.83	6.26	6.14	6.14	7.28	5.55	7.05	6.77	5.79	5.00	4.96	5.43	6.77	4.49
Ho	5.65	5.30	4.77	5.12	6.01	4.77	6.18	6.18	4.95	4.59	4.95	5.12	6.89	3.89
Er	5.92	4.89	4.77	4.83	5.86	4.77	5.92	5.38	4.59	4.41	4.95	5.26	6.71	3.75
Tm	6.67	5.10	4.31	4.31	5.49	4.71	5.49	5.10	4.31	5.10	5.49	5.49	7.06	4.31
Yb	5.76	4.12	4.59	4.53	5.47	4.94	5.71	5.29	4.53	3.76	4.88	4.59	5.94	3.18
Lu	6.30	4.72	4.33	4.72	5.51	4.33	5.91	5.12	3.94	4.33	5.51	5.51	6.69	3.54
La_n/Lu_n	1.53	1.96	1.60	1.56	1.52	1.51	1.90	1.89	2.49	1.09	0.88	0.88	0.91	0.96

Table. 5.2 (cont.)

Sample #	T49	T51	T53	T55	T57	T59	T61-A	T64	T68	T71	T73	T75	T77	T79
Descrp.	centr. KSM	chert vein	centr. KSM	silc.basalt	low KSM	low KSM	low KSM	low KSM	chert vein	metapyrox	metapyrox	metapyrox	metapyrox	metapyrox
Depth (m)	221.08	223.08	225.08	227.08	229.08	231.08	233.08	235.08	237.08	239.08	241.08	243.08	245.08	247.08
La	5.49	3.21	5.57	5.65	4.22	4.14	3.46	2.83	5.70	15.23	15.61	6.96	9.32	4.85
Ce	4.00	2.99	5.00	5.11	3.53	3.50	3.19	2.55	5.11	12.45	13.15	7.35	8.32	4.33
Pr	2.53	3.05	3.68	3.79	2.42	2.32	2.00	3.05	3.47	10.42	11.68	7.79	8.11	3.05
Nd	3.64	2.98	4.75	4.75	3.51	3.45	3.28	2.85	3.83	9.38	11.18	7.67	7.97	4.41
Sm	4.25	3.27	5.62	5.82	4.90	4.97	4.90	4.05	3.14	6.80	10.46	8.04	7.71	4.90
Eu	6.38	4.14	9.48	2.93	3.79	4.31	6.55	4.83	1.55	7.07	12.07	7.93	7.59	5.69
Gd	4.77	3.75	6.57	4.82	5.64	6.33	6.47	5.64	2.14	5.94	9.93	7.79	7.40	5.11
Tb	2.94	3.74	4.81	2.14	3.48	4.28	5.08	5.35	b.d.l	4.81	9.36	7.49	7.22	2.73
Dy	4.92	3.94	6.61	3.82	5.24	6.34	7.13	5.98	1.85	4.57	8.62	7.13	6.97	4.57
Ho	4.59	3.53	6.01	3.18	4.42	5.83	7.07	5.83	1.59	4.24	8.13	6.36	6.18	3.89
Er	4.17	3.56	5.44	2.90	4.35	5.62	6.40	5.68	1.51	4.53	7.73	5.80	5.86	3.14
Tm	4.71	3.53	5.88	3.53	5.10	5.88	6.67	5.49	1.96	3.92	6.67	5.49	5.10	3.14
Yb	3.59	3.29	4.65	2.76	4.06	4.88	5.41	5.41	1.12	4.18	6.35	4.94	4.94	2.24
Lu	3.94	3.15	5.12	3.54	5.12	5.51	6.30	5.51	1.57	3.94	6.30	4.72	4.72	2.36
La_n/Lu_n	1.39	1.02	1.09	1.60	0.82	0.75	0.55	0.51	3.62	3.87	2.48	1.47	1.97	2.05

upp. KSM = upper KSM., low. KSM = lower KSM, centr. KSM = central complex zone, silc. basalt = silicified basalt, metapyrox. = ultramafic mélange zone.

Figure 5.5. Correlation between LREE depletion and silicification. **(a)** Similarity of REE profiles between various silicified rock types in KD1 (filled symbols), including a chert vein within the KSM. Relatively unsilicified metabasalts and gabbroic samples (open symbols) are shown for comparison. **(b)** Marked LREE depletion observed in the highly altered and sheared KSM samples, as a result of high fluid rock ratios, shearing and silicification. **(c)** A plot of La_n/Lu_n ratio with depth as a measure of LREE depletion observed in the KSM. High degrees of silicification and alteration has resulted in severe depletion in LREE in the KSM.

The metabasalts display relatively flat REE patterns whereas the more silicified metabasalt samples show some loss of Sm and to a lesser extent Nd. A metagabbroic sample immediately above the KSM displays a similar pattern (Fig 5.5a). On the other hand, a carbonate-quartz vein bearing sample (T51) in the KSM displays similar Sm and Nd normalized values but with much lower overall LREE concentration. Relative to the less altered and unsilicified samples the KSM samples display much lower La_n/Lu_n ratios indicating likely LREE loss during extensive alteration (Fig. 5.5b). A plot of La_n/Lu_n ratios with depth clearly points to a much lower LREE concentration in the KSM zone, which can be attributed to LREE loss during extensive fluid alteration in the carbonate-quartz veined KSM zone (Fig. 5.5c)

5.5. X-Ray Diffraction

All 93 samples were analyzed using powder X-ray diffraction (XRD) to characterize the major mineral phases present across the drill core section between 179.58 to 261.08 m. The XRD data was also required to determine the presence of carbonate throughout the drill core section in preparation for carbon stable isotope analyses. Back-packed powder mounts were used to produce a high degree of randomness in crystallite orientation. X-ray diffraction data were collected from 2° to 82° 2θ using the Rigaku Rotaflex diffractometer in the Department of Earth Sciences, University of Western Ontario, with

Co Kα radiation (λ=1.79021 Å), step size 0.02°/step, 8 min total counting time, at 45 kV accelerating voltage and 160 mA beam current. X-ray diffraction patterns were analyzed using the Bruker-AXS EVA software package, using the International Center for Diffraction Data database (BrukerAXS, 2005). X-ray diffractograms for two representative samples, namely a metabasalt (T18 at 196.08m) and carbonate mylonite sample in the KSM (T37 at 211.08m) are shown in Figure 5.6 (b,c).

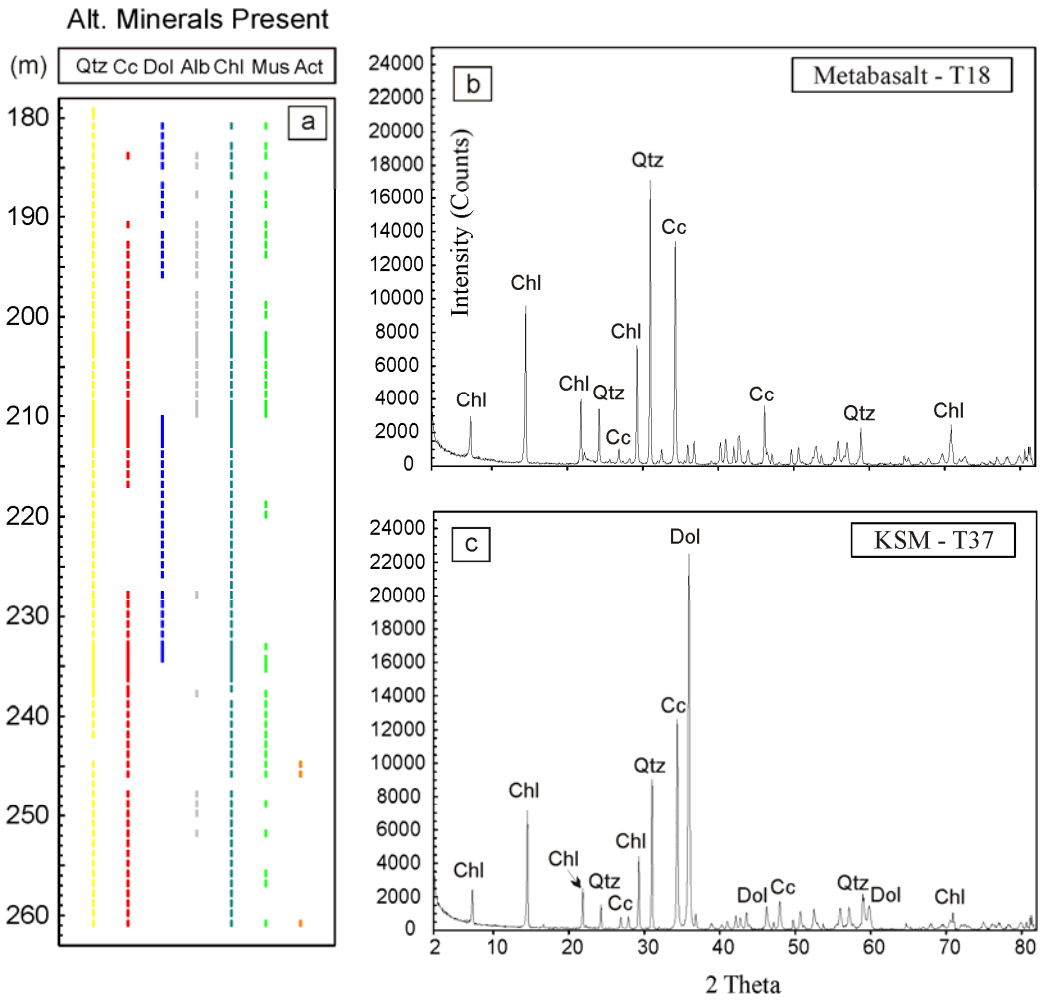

Figure 5.6. (a) Alteration minerals identified by XRD spectra plotted with depth in the drill core. The KSM occurs over the depth interval 210.18–236.08m. **(b-c)** Representative X-ray diffractogram patterns indicating the dominant alteration phases present in selected samples, **(b)** T18 (metabasalt) and **(c)** T37 (carbonate mylonite).

In the metabasalt sample quartz, calcite and chlorite are the main mineral phases, whereas in the banded mylonitic KSM sample, dolomite is an additional carbonate phase. X-ray diffractogram patterns for all samples indicate that greenschist facies alteration minerals are the dominant phase present. The main mineral phases found in each sample across the KSM are presented in Figure 5.6. The relative bulk rock proportions of carbonate phases (calcite versus dolomite) were estimated using the background subtracted peak heights of the Kα-peaks (main peaks) of each phase present. The estimated relative bulk rock proportions of calcite versus dolomite is plotted with depth in Fig. 5.7 (see carbon stable isotope Section 5.6.2 below) indicating that dolomite is the dominant carbonate phase in the KSM shear zone. Dolomite also occurs as the main carbonate phase associated with the black chert veins over the depth interval 180 to 195 m. Although the calculated carbonate bulk rock proportions are only relative and not absolute estimates, the data are generally in good agreement with drill core and field observations for the KSM, which indicate that the dolomite bands typically account for between 30 to 60 volume percent of the total rock volume in the KSM banded mylonites.

5.6. Stable isotope analyses

5.6.1. Whole rock oxygen stable isotopes

Oxygen-isotope results for whole-rock samples were obtained using the method of Clayton and Mayeda (1963), as modified by Borthwick and Harmon (1982) for use with ClF_3. Due to the high carbonate content in most of the KD1 samples and potential problems related to CO_2 gas over-pressuring in reaction vessels, only a limited number of samples with very low carbonate content could be analysed. A total of 10 bulk rock powders were selected from KD1 with the lowest carbonate content as determined by XRD. Whole-rock powders and mineral standards (~10 mg each) were weighed out and dried overnight at 200 °C while being evacuated. The dried samples and standards were then loaded into Ni-reaction vessels under dry nitrogen gas, and heated at 300 °C for 2 h while being evacuated. Appropriate quantities of ClF_3 were then added to each vessel, the

vessels were sealed, and the samples were reacted at 550 °C overnight to release O_2. The oxygen gas was then converted to CO_2 over red-hot graphite, and CO_2 yields were checked to ensure complete conversion and/or absence of contamination. The oxygen-isotope composition of the CO_2 gas was analyzed using an Optima dual inlet-mass spectrometer at the Department of Earth Science, University of Western Ontario, Canada. NBS-28, NBS-30, and KGa-1 (kaolinite) had averages values of +9.6 ± 0.1‰, +5.0 ± 0.2‰, and +21.1 ± 0.4‰ during the course of this study, which compares well with their accepted values of +9.6, +5.1, and +21.5‰, respectively. Reproducibility of the $\delta^{18}O$ values for samples was generally better than ± 0.2‰.

All bulk rock oxygen isotope results are reported in the usual δ-notation relative to VSMOW (Vienna Standard Mean Ocean Water; Coplen, 1994; Coplen et al., 2006) and are presented in Table 5.3a. Although the oxygen isotope dataset is limited to 10 samples (that may introduce sampling bias), they cover a wide range of rock types across the drill core KSM section. Black chert veins have bulk rock $\delta^{18}O$ values ranging between 14.6 to 15.3‰. Silicified basalts within and above the KSM have $\delta^{18}O$ values of 10.1 ‰ and 13.9 ‰, respectively. Relatively unsilicified metabasites and mafic intrusions above the KSM display a narrow range in $\delta^{18}O$ values of between 11.7 to 12.0 ‰.

Table. 5 3. Calculated δ18O* values for selected KD1 drill core samples.

Sample	Depth (m)	Yield (Umol/mg)	$\delta^{18}O$* (‰)	Lithology
ORX		16.91	11.90	Standard
T2	180.08	16.52	**14.65**	Black Chert
T8	186.08	15.74	**13.90**	Silicified Basalt
T9	187.08	16.67	**15.27**	Black Chert Vein
T13	191.08	15.04	**11.94**	Metabasite
T33	209.08	15.92	**11.99**	Altered mafic intrusive
T35	210.08	15.52	**11.65**	Altered mafic intrusive
T55	227.08	15.53	**10.12**	Silicified Basalt
T68	237.08	16.19	**14.95**	Black Chert Vein
T75	243.08	14.93	**9.23**	Metapyroxenite/ultramafic
T79	247.08	15.65	**14.57**	Metapyroxenite/ultramafic
NBS30		13.34	5.65	Standard

*Formula Used: 18O(VSMOW) = 46O(Craig)*1.0364 + 19.297

Table 5.3 (cont.) Literature $\delta^{18}O$ values for various mafic-ultramafic rocks types

Rock/mineral	$\delta^{18}O$ (‰)	Reference
Barberton (Archean)		
Cherts	11.2 - 21.3	de Wit et al. (1987)
Pillow and flow basalts	6.0 - 15.2	de Wit et al. (1987)
Intrusives/gabbros	5.2-7.2	de Wit et al. (1987)
Serpentinites/ultramafics	3.2-6.5	de Wit et al. (1987)
Komatiites (fresh)	4.8-6.4	Smith et al. (1984)
Archean ultramafic orthopyroxene	5.2 - 6.2	Smith et al. (1984)
Modern basalts	**Mean $\delta^{18}O$ (±1σ)**	
Oceanic basalts (all)	5.40 ± 0.75	Harmon and Hoefs (1995)
MORB	5.73 ± 0.21	Harmon and Hoefs (1995)
Ocean arc basalt	6.10 ± 1.10	Harmon and Hoefs (1995)
Continental basalt (all)	6.36 ± 1.06	Harmon and Hoefs (1995)
Lithospheric mantle		
Olivines/peridotite	aprox. 5.5	Mattey et al. (1994)
Range for ultramafic rocks	5.6 -6.7	Faure et al., (1986)

These Kromberg metabasites have $\delta^{18}O$ values that are similar to the most ^{18}O-enriched pillow metabasalts reported in the Barberton Greenstone Belt (de Wit et al., 1987b). On the other hand, the two metapyroxenitic samples in the ultramafic mélange zone display a wider range in oxygen isotope values (9.23 to 14.6‰). Unaltered Archean basalts probably had primary igneous $\delta^{18}O$ values similar to that of modern day oceanic basalts of +5.7 ‰ (de Wit et al., 1987b; Gregory and Taylor, 1981; Kyser et al., 1981; Taylor 1968, Muehlenbachs and Clayton 1972a,b, 1976). Compared to modern and fresh Archean basalts, the $\delta^{18}O$ values of the Kromberg metabasalts of KD1 are shifted to much higher values by up to 6 ‰ (see Table. 5.3b). Similarly, in comparison to modern and Archean ultramafic (e.g. peridotitic komatiites) mantle rocks, the Kromberg ultramafic metapyroxenite sample T79 shows an extreme shift away (by up to 6.5 ‰) from a typical fresh ultramafic value of around 5.5 ‰ (see Smith et al., 1984; Kyser et

al., 1981 in Table 5.2b). Altered intrusive rocks in KD1 are also strongly enriched in ^{18}O in comparison to other metagabbros in the Barberton Greenstone Belt (e.g. see de Wit et al., 1987b in Table 5.3b).

5.6.2. Carbon stable isotope analyses of carbonate

Whole rock carbonate was analyzed for carbon isotopes to determine the source(s) of carbonate in the altered mafic-ultramafic rocks across the KSM. The stable-isotope composition was analyzed using a Finnigan MAT 253 mass spectrometer, at the Department of Earth Science, University of Bergen, Norway. A total of 58 samples were analyzed over the depth interval of between 179.58 to 261.08 m and sample depths are indicated in Table 5.4. The sampling protocol for carbonate analysis was originally set to 2 meter spaced sampling intervals with an increased 1 meter sampling density across the KSM banded mylonite zone in KD1. However, due to very low to absent carbonate in some sample volumes is was not possible to analyze all these samples. For the 58 samples presented in Table 5.4, gas for isotope measurements was produced by a reaction with orthophosphoric acid at 70°C in an automated online system, the Kiel carbonate device, with the acid added to the sample in individual reaction vials. The long-term reproducibilities of the MAT 253 were ± 0.04‰ for $\delta^{13}C$ (standard deviation) for sample masses of 200-500 μg based on replicate measurements of an internal carbonate standard over a period of months. Precisions of the measurements performed on the MAT 252 were ± 0.09‰ for $\delta^{13}C$ (standard deviation) for the all samples. The mass spectrometer was tuned to handle small samples after calibration with a series of standards of different weights and after tests to find the optimal reaction temperature. The carbon isotope ratio of sample T50 was measured at different reaction times, namely at 30, 40 and 60 min. The measured ratios were found to be identical and independent of reaction time (Table 5.4). All isotope values are reported according to standards of the International Atomic Energy Agency, Vienna. The $\delta^{13}C$ values for all samples are reported in standard δ notation relative to Vienna Pee Dee belemnite (VPDB) through calibration against the NBS19 and NBS18 standards: $\delta = \left(\frac{R_{sample} - R_{s\tan dard}}{R_{s\tan dard}} - 1 \right) \times 1000(‰)$ where, R is the ^{13}C:^{12}C ratio in the sample or standard.

Table 5.4. Calculated $\delta^{13}C$ carbon stable isotope values with corresponding sampling depth in drill core KD1.

Sample	Depth (m)	Lithology	$\delta^{13}C$	Sample	Depth (m)	Lithology	$\delta^{13}C$	Sample	Depth (m)	Lithology
T3	181.08	Silicified basalt	-0.27	T40	212.58	KSM mylonite	1.44	T61	233.34	KSM mylonite
T5	183.08	Silicified basalt	0.06	T41	213.08	KSM mylonite	1.90	T62	234.08	KSM mylonite
T7	185.08	Silicified basalt	-0.92	T42	214.08	KSM mylonite	1.43	T63	234.58	KSM mylonite
T10	188.08	Metabasalt	-0.28	T43	215.08	KSM mylonite	1.42	T64	235.08	KSM mylonite
T12	190.08	Chert vein	0.57	T44	216.08	KSM mylonite	0.66	T65	235.58	KSM mylonite
T14	192.08	Metabasalt	-0.37	T45	217.08	KSM mylonite	1.34	T66	236.08	KSM mylonite
T16	194.08	Metabasalt	-0.39	T46	218.08	KSM mylonite	0.86	T67	236.58	metapyroxenite
T18	196.08	Metabasalt	-1.63	T48	220.08	KSM mylonite	-1.50	T69	237.58	metapyroxenite
T20	198.08	Metabasalt	-1.20	T49	221.08	KSM mylonite	-0.57	T70	238.08	metapyroxenite
T22	200.08	Metabasalt	-1.01	T50-30min	222.08	KSM mylonite	-0.41	T71	239.08	metapyroxenite
T24	202.08	Metabasalt	0.55	T50-30min	222.08	KSM mylonite	-0.41	T73	241.08	metapyroxenite
T26	203.08	Metagabbro	-0.82	T50-40 min	222.08	KSM mylonite	-0.44	T75	243.08	metapyroxenite
T28	204.08	Metagabbro	-0.63	T50-60min	222.08	KSM mylonite	-0.42	T81	249.08	metapyroxenite
T30	206.08	Metagabbro	-0.39	T50-60min	222.08	KSM mylonite	-0.39	T83	251.08	metapyroxenite
T32	208.08	Metagabbro	-0.10	T52	224.08	KSM mylonite	-0.47	T85	253.08	metapyroxenite
T33	209.08	Metagabbro	-0.21	T54	226.08	KSM mylonite	-0.63	T87	255.08	metapyroxenite
T34	209.58	Metagabbro	0.53	T56	228.08	Silicified basalt	0.54	T89	257.08	metapyroxenite
T36	210.58	KSM mylonite	1.48	T57	229.08	KSM mylonite	-0.21	T91	259.08	metapyroxenite
T37	211.08	KSM mylonite	1.52	T58	230.08	KSM mylonite	0.03	T92	260.08	metapyroxenite
T38	211.58	KSM mylonite	-0.59	T59	231.08	KSM mylonite	0.11	T93	261.08	metapyroxenite
T39	212.08	KSM mylonite	-0.50	T60	232.08	KSM mylonite	-1.07			

The $\delta^{13}C$ values of carbonate in drill core KD1 are plotted with depth across the KSM over the interval 179.58 to 261.08 m, along with lithological log data and carbonate mineralogy in Figure 5.7a. The $\delta^{13}C$ values of the samples are compared to the known range in $\delta^{13}C$ values for Archean seawater and sedimentary carbonate (limestone) as well as Archean mantle carbonate or CO_2 (see Fig. 5.7a caption for literature on the $\delta^{13}C$ of each reservoirs). The $\delta^{13}C$ carbonate values across the drill core section display a narrow range of 0 ± 2‰, with most carbon isotope values falling within the range of -1.5 to +1.5‰. Although carbonate mineralogy changes with depth from calcite to mainly dolomite in the KSM, the $\delta^{13}C$ values remain relatively constant with depth.

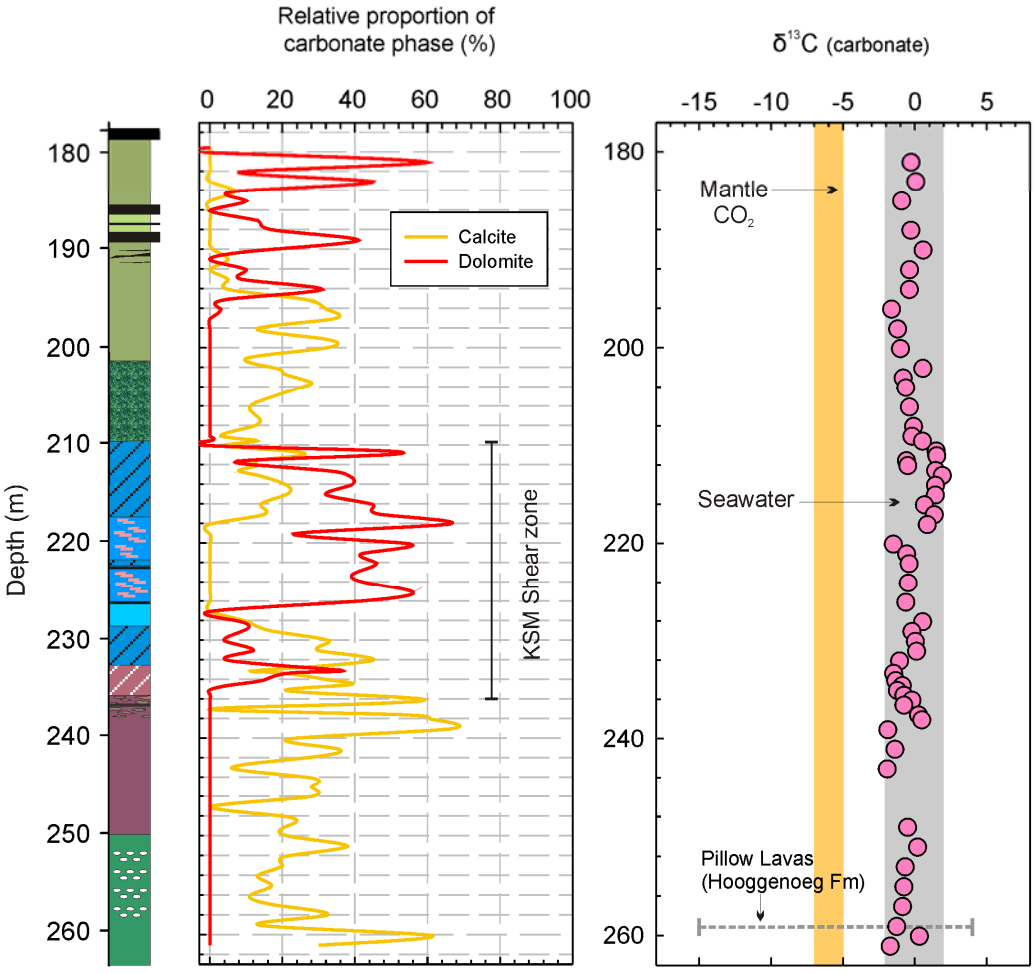

Figure 5.7. $\delta^{13}C$ carbon stable isotope variation and estimated relative proportion of carbonate phases as determined by XRD in the KSM. Hooggenoeg pillow lava carbonate

stable isotope data after Furnes et al. (2004). Mantle carbonate $\delta^{13}C$ range after e.g. Kyser, (1986), Taylor, (1986); Ohmoto, (1986), Hoefs, (1987). Seawater and limestone $\delta^{13}C$ range since 3.5 Ga after Veizer and Hoefs (1976) and Schidlowski et al., (1983).

The $\delta^{13}C$ values of carbonate from glassy pillow lava rims and ocelli-bearing pillow cores from the underlying Hooggenoeg Formation of the BGB (Furnes et al., 2004) are compared to the carbonate veins and alteration in KD1 (Fig. 5.5a). Furnes et al., (2004) pointed out that carbonate in Archean pillow lava cores have mantle-like values, whereas the pillow rims record much more negative values (up to -16 ‰) attributed to microbial metabolisms. In contrast to the carbonate in the structurally underlying Hooggenoeg pillow lava metabasites, the carbonate in the Kromberg KSM shear zone displays a much more limited range in $\delta^{13}C$ values that overlaps with that of Archean and modern-day seawater (i.e. 0 ± 2‰).

5.6.3. Multiple Sulphur isotopes by Secondary Ion Microprobe (IMS 1280)

Five pyrite-bearing samples were selected from KD1 for in-situ, micron-scale, multiple sulfur isotope (^{32}S, ^{33}S and ^{34}S) analysis using the Cameca IMS1280 at the NordSIMS facility at the Swedish Natural History Museum, utilizing a multi-collection method similar to that described by Whitehouse et al. (2005). An extended description of the SIMS analytical method, reproducibility and precision is described in Appendix E3 and all SIMS sulphur isotope data on pyrite in KD1 is provided in Appendix E4. Representative isotope analyses of various pyrite are provided in Table 5.5. The $\delta^{34}S_{CDT}$ values for all samples are reported in standard δ notation, where $\delta^{34}S_{CDT}$ = [1000 x ($^{34}S/^{32}S$sample)/($^{34}S/^{32}S_{CDT}$) – 1] relative to the accepted Canyon Diablo Troilite sulphide standard. Instrument parameters were broadly similar to those described by Whitehouse et al. (2005), and Kamber and Whitehouse (2007). Analyses were conducted on 30 μm and 100 μm thick polished, gold coated, thin-sections cut into ~25 mm diameter discs, from which a sector was cut to enable mounting with 3 sulfide standards (Isua monitor, Ruttan and Balmat) embedded in epoxy resin.

The five pyrite-bearing samples were selected for sulphur isotope analyses to further determine the physico-chemical environment, especially the redox conditions and extent of hydrothermal and/or diagenetic fluids from which the pyrite formed across different rock types in KD1. The pyrite in the five samples (KD1-83.0m - Footbridge Chert; KD1-178.48m - black laminated chert; KD1-187.30m - black chert vein; KD1-195.58m - metabasalt vein and KD1-212.58m - KSM carbonate mylonite) were first mapped in reflected light and these images were used to locate the pyrite grains when the sample was placed in the IMS 1280. Lithological context and petrographic description of the pyrite in these samples from KD1 are provided in Figure 5.8 (a-d).

Multiple sulphur isotope analysis of the pyrite indicates that magmatic values are dominant in the KSM shear zone (Figure 5.9). Pyrite in carbonate-quartz veins in the KSM mylonite sample, KD1-212.58m, displays typical magmatic values (0 ± 3 ‰) and plots near the origin on a $\Delta^{33}S$ versus $\delta^{34}S_{CDT}$ binary diagram (Figure 5.9), where $\Delta^{33}S$ is calculated deviation from the mass-dependent fractionation (MDF) line between $\delta^{33}S_{CDT}$ and $\delta^{34}S_{CDT}$ and defined by $\Delta^{33}S = \delta^{33}S - 1000 \times [(1 + \delta^{34}S/1000)\ 0.515 - 1])$.

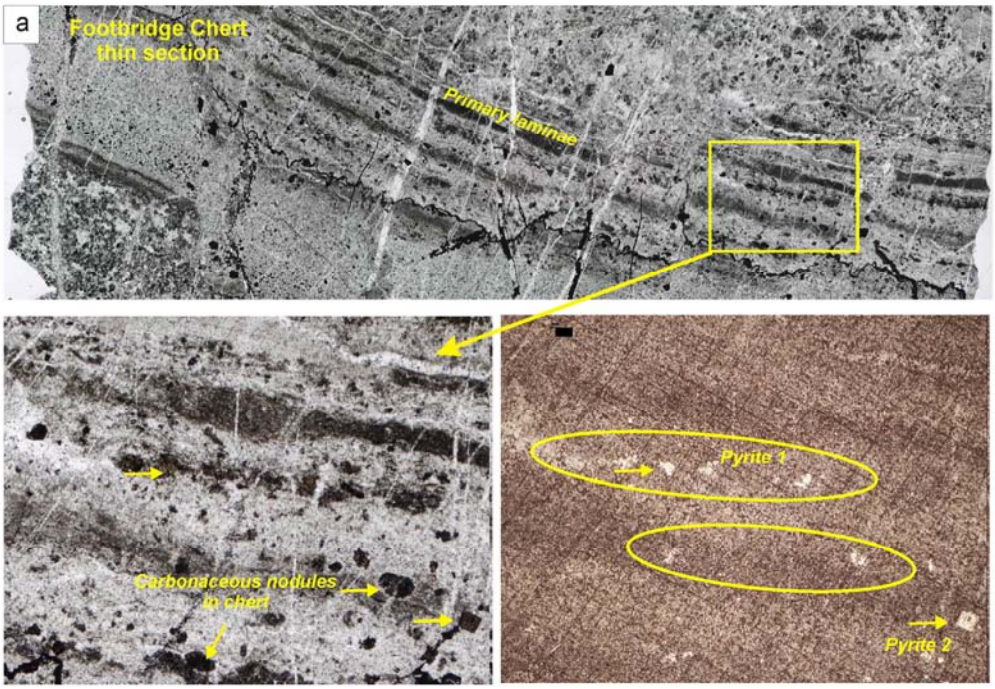

Figure 5.8. *(continued over page)*

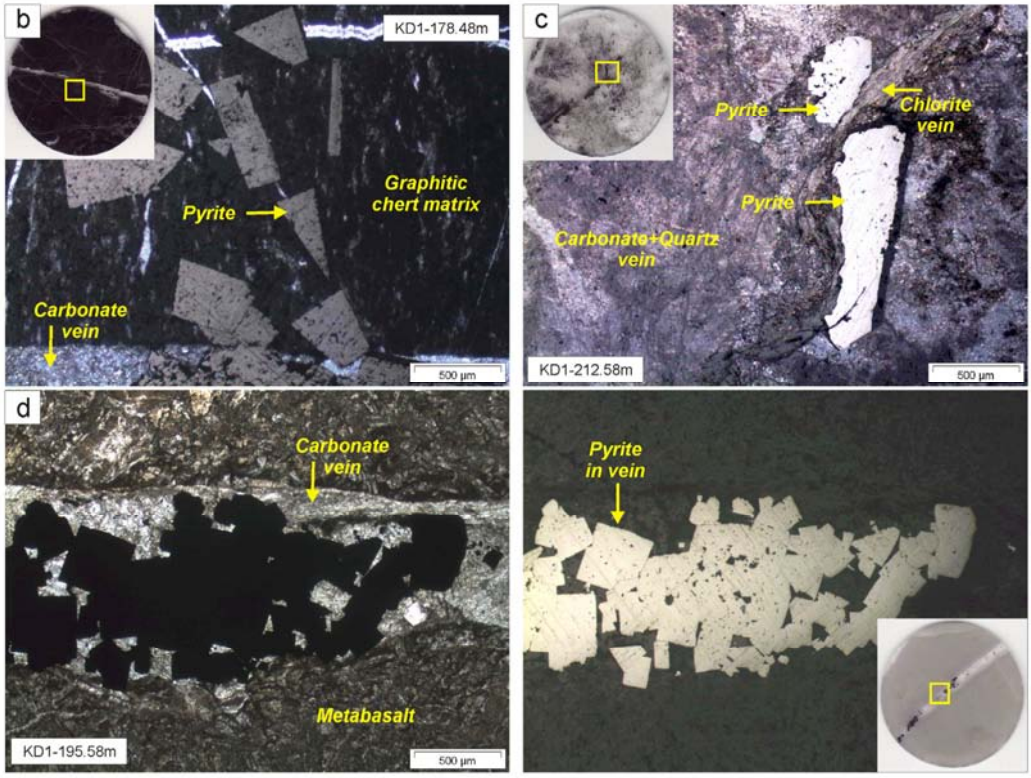

Figure 5.8. Textural context of pyrite in selected KD1 drill core samples. **(a)** Pyrite observed along primary sedimentary laminae (pyrite 1) compared to hydrothermal pyrite (pyrite 2) in Footbridge Chert. Scale bar = 50µm. **(b)** Hydrothermal pyrite along carbonate vein in second major laminated chert unit, sample KD1-178.48m. **(c)** Hydrothermal pyrite along chlorite vein in KSM carbonate mylonite sample KD1-212.58m. **(d)** Hydrothermal pyrite in carbonate vein in metabasalt sample KD1-195.58m.

Similarly the pyrite in a carbonate vein in metabasalt sample directly overlying the mafic intrusives in KD1 also displays a magmatic signature. Chert horizons and veins higher up in the drill core, on the other hand, display strong mass-independent fractionation (MIF) signatures indicated by positive $\Delta^{33}S$ values. Various analyses of pyrite in 3 micro-domains from a sample in the Footbridge Chert (KD1-83.0m) displays the most pronounced $\Delta^{33}S$ values up to +2.5 ‰ and the widest range in $\delta^{34}S_{CDT}$ values of between 0 and -6‰ (Figure 5.9).

Table 5.5. Representative in-situe sulphur isotope analyses of pyrite in various KD1 drill core samples

Sample ID	^{32}S cps (x1 e6)	$^{34}S/^{32}S$	±1σ (%)	$^{33}S/^{32}S$	±1σ (%)	$\delta^{34}S$	±1σ	±2σ	$\delta^{33}S$	±1σ	$\Delta^{33}S$	±1σ	±2σ
Rut_5A_091213@6	856	0.044440	0.01	0.0079072	0.01	1.09	0.17	0.34	0.57	0.17	0.01	0.17	0.33
Bal_5A_091213@9	866	0.045103	0.01	0.0079678	0.01	16.03	0.16	0.32	8.27	0.13	0.02	0.13	0.25
KD1-83.11-C3	807	0.044361	0.01	0.0079189	0.01	-0.69	0.17	0.34	2.06	0.16	2.41	0.16	0.32
KD1-83.11-C4	865	0.044311	0.00	0.0079007	0.01	-1.82	0.16	0.31	-0.26	0.11	0.68	0.11	0.22
KD1-83.11-C5	795	0.044175	0.01	0.0078893	0.01	-4.87	0.20	0.40	-1.71	0.13	0.80	0.13	0.25
KD1-83.11-C7	864	0.044322	0.00	0.0079027	0.01	-1.56	0.16	0.32	-0.01	0.12	0.79	0.12	0.25
KD1-83.11-C8	858	0.044281	0.01	0.0079043	0.01	-2.49	0.17	0.34	0.20	0.12	1.48	0.12	0.24
KD1-83.11-C9	792	0.044280	0.01	0.0079018	0.01	-2.51	0.17	0.33	-0.12	0.14	1.17	0.14	0.27
KD1-83.11-C10	614	0.044273	0.01	0.0079031	0.01	-2.67	0.16	0.32	0.05	0.15	1.43	0.15	0.29
KD1-83.11-C11	810	0.044347	0.00	0.0079048	0.01	-0.99	0.15	0.31	0.26	0.13	0.77	0.13	0.27
Is_5A_091213@6	837	0.044490	0.00	0.0079371	0.01	2.21	0.16	0.31	4.36	0.13	3.22	0.13	0.27

Sample ID	^{32}S cps (x1 e6)	$^{34}S/^{32}S$	±1σ (%)	$^{33}S/^{32}S$	±1σ (%)	$\delta^{34}S$	±1σ	±2σ	$\delta^{33}S$	±1σ	$\Delta^{33}S$	±1σ	±2σ
Rut_5A_110525@10	837	0.044183	0.03	0.0078815	0.02	1.48	0.34	0.68	0.70	0.18	-0.06	0.18	0.37
Bal_5A_110525@10	906	0.044846	0.03	0.0079429	0.02	16.50	0.35	0.69	8.56	0.18	0.06	0.18	0.37
KD1-178.48-1	854	0.044089	0.02	0.0078781	0.01	-0.66	0.30	0.61	0.25	0.16	0.59	0.16	0.33
KD1-178.48-2	833	0.044125	0.02	0.0078797	0.01	0.16	0.32	0.64	0.46	0.15	0.38	0.15	0.31
KD1-178.48-3	817	0.044076	0.03	0.0078742	0.02	-0.94	0.35	0.71	-0.24	0.19	0.24	0.19	0.38
KD1-178.48-4	836	0.044116	0.02	0.0078795	0.01	-0.04	0.31	0.62	0.44	0.14	0.46	0.14	0.28
KD1-178.48-5	896	0.044128	0.02	0.0078820	0.01	0.23	0.33	0.66	0.75	0.17	0.64	0.17	0.34
KD1-178.48-6	908	0.044104	0.03	0.0078780	0.02	-0.32	0.34	0.68	0.24	0.19	0.41	0.19	0.37
KD1-178.48-7	927	0.044099	0.02	0.0078775	0.01	-0.43	0.30	0.59	0.18	0.16	0.40	0.16	0.33
KD1-178.48-8	860	0.044076	0.02	0.0078756	0.01	-0.95	0.30	0.60	-0.06	0.17	0.43	0.17	0.34
Is_5A_110525@6	914	0.044228	0.02	0.0079118	0.01	2.49	0.33	0.66	4.55	0.15	3.27	0.15	0.30

Table 5.5 (cont.). Representative in-situe sulphur isotope analyses of pyrite in various KD1 drill core samples

Sample ID	^{32}S cps (x1 e6)	$^{34}S/^{32}S$	±1σ (%)	$^{33}S/^{32}S$	±1σ (%)	$\delta^{34}S$	±1σ	±2σ	$\delta^{33}S$	±1σ	$\Delta^{33}S$	±1σ	±2σ
Rut_5A_110525@5	1020	0.044160	0.03	0.0078804	0.02	0.97	0.35	0.71	0.58	0.22	0.08	0.22	0.44
Bal_5A_110525@7	950	0.044839	0.03	0.0079417	0.02	16.35	0.32	0.64	8.47	0.23	0.05	0.23	0.45
KD1-195.58-1	941	0.044143	0.03	0.0078785	0.02	0.58	0.34	0.67	0.34	0.24	0.04	0.24	0.48
KD1-195.58-2	923	0.044132	0.03	0.0078764	0.02	0.33	0.33	0.65	0.07	0.22	-0.11	0.22	0.45
KD1-195.58-3	1010	0.043778	0.04	0.0078436	0.02	-7.69	0.40	0.80	-4.14	0.27	-0.18	0.27	0.54
KD1-195.58-4	938	0.044156	0.03	0.0078790	0.02	0.87	0.31	0.63	0.41	0.22	-0.04	0.22	0.43
KD1-195.58-5	942	0.044138	0.03	0.0078788	0.02	0.47	0.31	0.62	0.37	0.21	0.13	0.21	0.42
Is_5A_110525@3	977	0.044225	0.03	0.0079092	0.02	2.45	0.33	0.66	4.24	0.22	2.98	0.22	0.44

Sample ID	^{32}S cps (x1 e6)	$^{34}S/^{32}S$	±1σ (%)	$^{33}S/^{32}S$	±1σ (%)	$\delta^{34}S$	±1σ	±2σ	$\delta^{33}S$	±1σ	$\Delta^{33}S$	±1σ	±2σ
Rut_5B_110525@5	962	0.044177	0.02	0.0078811	0.02	1.20	0.25	0.50	0.60	0.19	-0.01	0.19	0.38
Bal_5B_110525@7	893	0.044846	0.03	0.0079436	0.02	16.35	0.26	0.52	8.57	0.18	0.15	0.18	0.36
KD1-212.58-1	827	0.044153	0.02	0.0078781	0.01	0.64	0.23	0.46	0.23	0.17	-0.10	0.17	0.34
KD1-212.58-2	808	0.044116	0.02	0.0078753	0.02	-0.18	0.23	0.45	-0.13	0.19	-0.04	0.19	0.38
KD1-212.58-4	860	0.044180	0.03	0.0078826	0.01	1.27	0.25	0.51	0.80	0.15	0.14	0.15	0.29
KD1-212.58-6	880	0.044122	0.02	0.0078772	0.01	-0.05	0.25	0.50	0.10	0.16	0.13	0.16	0.31
KD1-212.58-8	877	0.044115	0.02	0.0078752	0.02	-0.22	0.24	0.48	-0.15	0.19	-0.03	0.19	0.37
Is_5A_091213@4	844	0.044487	0.01	0.0079368	0.01	2.14	0.17	0.34	4.33	0.12	3.22	0.12	0.24

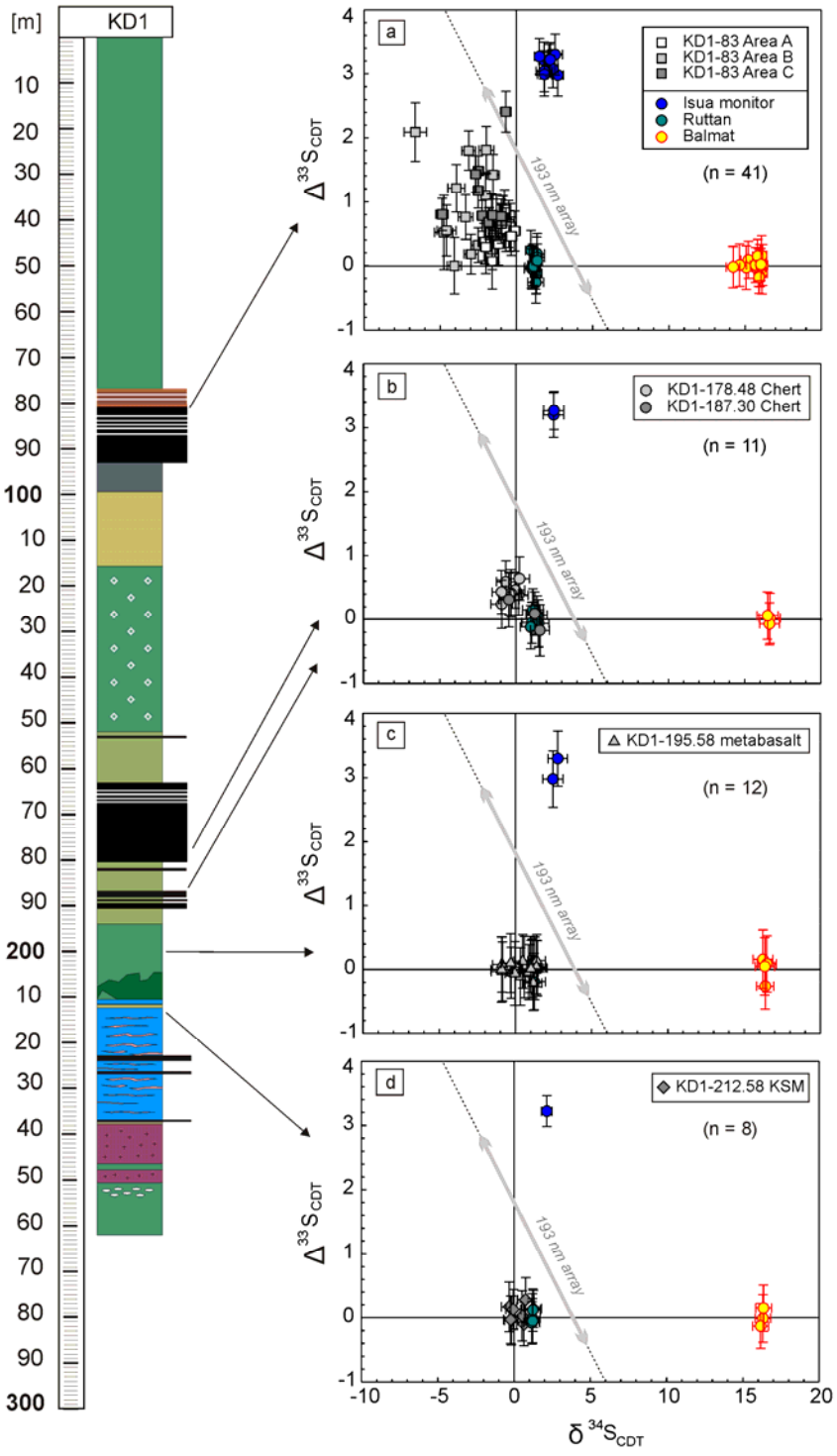

Figure 5.9. Multiple sulphur isotope chemical variation determined by SIMS (IMS 1280) for selected samples across KD1. Sample descriptions and petrography are provided in Figures 5.1, 5.2 and 5.8. Archean magmatic δ34S = 0 ± 3 ‰ (after Mojzsis et al., 2003).

5.7. Radiogenic isotopes: Rb-Sr isotope analyses of carbonate

The samples were prepared for Rb–Sr isotope analysis in a clean room environment using standard chemical separation techniques at the Department of Earth Science, University of Bergen, Norway. Whole-rock sample powders were spiked with a ^{84}Sr–^{86}Sr tracer and dissolved in HCl in Teflon beakers. Separation of Rb and Sr from the rock matrix was carried out using cation exchange columns, followed by a cleaning step using columns filled with Eichrom Sr-spec resin. For Rb isotope analysis the sample separates were then dissolved in 2% HNO_3 and measured using a Neptune multi-collector inductively coupled plasma mass spectrometer operating in static mode. The samples were doped with a 100ppb Zr solution to enable calculation of the instrumental mass fractionation. The mean value of 60 single measurements (3 blocks of 20 scans) was used. For Sr isotope analysis the sample separates were dissolved in 2.5N HCl acid and loaded onto double filaments then analysed on a Finnegan MAT 262 multicollector mass spectrometer operating in dynamic mode. The mean value of 100 single measurements (10 blocks of 10 scans) was used. The NBS987 Sr standard yielded $^{87}/^{86}Sr$ = 0.710234 (n=13, 2 standard deviation= 0.000054) across the analytical sessions. The contribution from the procedural blank was less than 0.01% for Sr. All $^{87}Sr/^{86}Sr$ data were normalized to a value of 0.71024 for the NBS987 standard. The 2sd% on calculated 87Rb/86Sr is 0.5 or less.

All Rb and Sr data is presented in Table 5.6, along with measured $^{87}Sr/^{86}Sr$ ratios. The initial $^{87}Sr/^{86}Sr$ ratios reported Table 5.6 are calculated at various Archean ages, ranging from 3.500 Ga to 3.223 Ga and the calculated initial ratios are all very similar at the different ages. The chosen ages of 3432 Ma corresponds to the depositional age of the structurally underlying Noisy formation (see Chapter 4) and the 3334 Ma age corresponds to that of the Footbridge Chert (Byerly et al., 1993; 1996) in the uppermost part of the drill core section. Calculated initial Sr values as well as the measured $^{87}Sr/^{86}Sr$ ratios indicate that carbonate in the upper part of KD1 especially is highly radiogenic (Table 5.6). Measured $^{87}Sr/^{86}Sr$ values for the purely dolomitic veins in the central KSM samples relatively high radiogenic values with a narrow range of between 0.71135 to 0.71324.

Table. 5.6. Rb-Sr isotope data for carbonate across the KSM

Depth (m)	Sample	Rb ppm	Sr ppm	$^{87}Sr/^{86}Sr$	2-sigma	$^{87}Rb/^{86}Sr$	Initial $^{87}Sr/^{86}Sr$ ratio calculated at different ages			
							3.500 Ga	3.432 Ga	3.334 Ga	3.223 Ga
190.08	T12	0.58	7.91	0.73770	0.0015	0.21116	0.72694	0.72716	0.72746	0.72781
196.08	T18	0.21	62.84	0.71990	0.0015	0.00947	0.71942	0.71943	0.71944	0.71946
198.08	T20	0.49	27.80	0.72517	0.0015	0.05158	0.72254	0.72259	0.72267	0.72275
200.08	T22	2.40	35.89	0.73010	0.0011	0.19382	0.72023	0.72043	0.72071	0.72103
202.08	T24	2.77	29.81	0.73252	0.0012	0.26965	0.71878	0.71905	0.71945	0.71989
203.08	T26	1.42	38.33	0.72784	0.0013	0.10726	0.72238	0.72249	0.72264	0.72282
204.08	T28	2.17	36.06	0.72874	0.0016	0.17451	0.71984	0.72002	0.72028	0.72056
210.58	T36	0.04	51.70	0.71633	0.0022	0.00245	0.71621	0.71621	0.71621	0.71622
211.58	T38	0.10	51.42	0.71425	0.0023	0.00555	0.71397	0.71397	0.71398	0.71399
212.58	T40	0.05	30.35	0.71620	0.0027	0.00463	0.71596	0.71597	0.71597	0.71598
214.08	T42	0.07	48.07	0.71416	0.0014	0.00396	0.71396	0.71396	0.71397	0.71397
216.08	T44	0.08	76.38	0.71262	0.0024	0.00297	0.71246	0.71247	0.71247	0.71248
218.08	T46	0.14	24.12	0.71135	0.0029	0.01721	0.71048	0.71050	0.71052	0.71055
220.08	T48	0.08	51.03	0.71288	0.0008	0.00478	0.71264	0.71265	0.71265	0.71266
222.08	T50	0.07	29.25	0.71311	0.0009	0.00695	0.71275	0.71276	0.71277	0.71278
224.08	T52	0.10	60.09	0.71149	0.0016	0.00500	0.71123	0.71124	0.71125	0.71125
226.08	T54	0.16	49.19	0.71324	0.0018	0.00916	0.71278	0.71279	0.71280	0.71282

Table. 5.6. (cont.) Rb-Sr isotope data for carbonate across the KSM

Depth (m)	Sample	Rb ppm	Sr ppm	$^{87}Sr/^{86}Sr$	2-sigma	$^{87}Rb/^{86}Sr$	Initial $^{87}Sr/^{86}Sr$ ratio calculated at different ages			
							3.500 Ga	3.432 Ga	3.334 Ga	3.223 Ga
230.08	T58	0.35	164.57	0.71325	0.0010	0.00624	0.71293	0.71293	0.71294	0.71295
232.08	T60	0.25	120.63	0.71118	0.0010	0.00599	0.71087	0.71088	0.71089	0.71090
233.34	T61	0.40	88.92	0.71111	0.0013	0.01297	0.71045	0.71047	0.71048	0.71051
234.58	T63	0.61	116.12	0.71189	0.0012	0.01513	0.71112	0.71113	0.71115	0.71118
235.58	T65	1.22	120.15	0.71115	0.0016	0.02939	0.70965	0.70968	0.70972	0.70977
237.58	T69	0.36	154.16	0.70864	0.0019	0.00669	0.70830	0.70831	0.70832	0.70833
238.08	T70	0.81	169.94	0.70735	0.0016	0.01382	0.70664	0.70666	0.70668	0.70670
239.08	T71	0.15	247.58	0.70745	0.0008	0.00180	0.70736	0.70736	0.70736	0.70736
241.08	T73	0.68	76.09	0.70868	0.0011	0.02599	0.70736	0.70738	0.70742	0.70747
243.08	T75	0.34	26.02	0.70789	0.0019	0.03782	0.70596	0.70600	0.70606	0.70612
245.08	T77	1.50	78.83	0.70818	0.0014	0.05524	0.70537	0.70542	0.70551	0.70560
251.08	T83	1.52	79.22	0.70988	0.0013	0.05546	0.70705	0.70711	0.70719	0.70728
253.08	T85	2.90	82.31	0.71087	0.0012	0.10206	0.70567	0.70577	0.70592	0.70609
255.08	T87	3.56	34.58	0.71678	0.0018	0.29851	0.70156	0.70187	0.70230	0.70280
257.08	T89	4.01	52.97	0.71280	0.0012	0.21937	0.70163	0.70185	0.70217	0.70253
259.08	T91	2.05	41.59	0.71240	0.0009	0.14294	0.70511	0.70526	0.70547	0.70570
260.08	T92	0.47	179.15	0.70878	0.0011	0.00763	0.70839	0.70840	0.70841	0.70842

Measured $^{87}Sr/^{86}Sr$ values of calcite in metabasalts overlying the KSM have the highest ratios, whereas calcite in the ultramafic mélange zone beneath the KSM have values that are closer to the Archean mantle and seawater value. Calculated initial Sr ratios at 3334 and 3223 Ma for the calcite in the ultramafic samples T87 and T89 with that the lowest radiogenic ratios (Table 5.6), are in good agreement with that of Archean mantle (~0.7025 – 0.7030; Veizer et al., 1989b). This possibly indicates that the carbonate alteration occurred at around (or more likely sometime after) 3334 Ma, namely the depositional age of the Footbridge Chert. A plot of initial $^{87}Sr/^{86}Sr$ ratio at 3334 Ma with depth is shown in Figure 5.10.

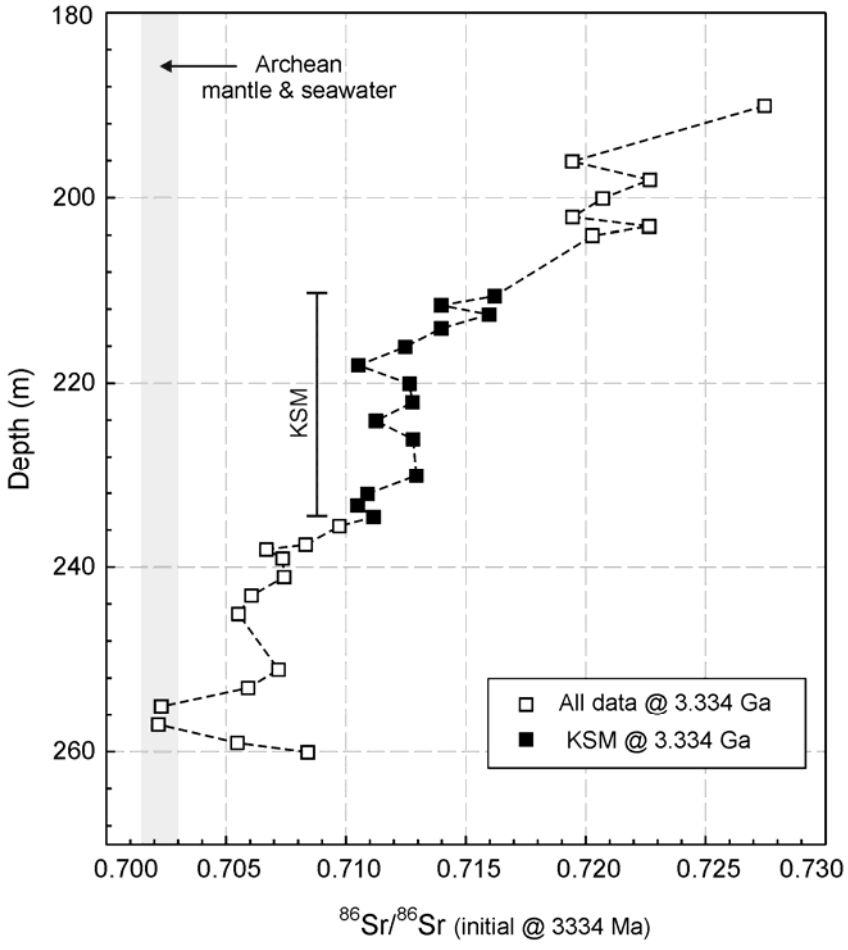

Figure 5.10. Strontium isotope profile of carbonate across KSM and surrounding rocks. Carbonate across the KSM is highly radiogenic relative to Archean mantle.

An increase towards highly radiogenic values is observed across the KSM, with decreasing depth the ratio shifts away from the Archean mantle and seawater values. This strong shift in Sr-isotope ratios indicates that the carbonate across the KSM was derived from a crustal continental fluid component, rather than an Archean oceanic mantle/seawater hydrothermal environment.

5.8. Discussion

5.8.1. Protolith geochemistry and geodynamic setting of the Kromberg rocks

Major element and XRF data indicate extensive alteration across the KSM in KD1 with LILE mobility in the altered mafic and ultramafic rocks (Figure 5.3), making geochemical protolith characterization difficult in the absence of field and drill core observations. In contrast, trace element data from only moderately altered and undeformed metabasalts and from a mafic intrusion above the KSM point to an island arc association (Figure 5.4). A forearc geodynamic setting is also suggested by the mineral chemistry of relic Cr-spinel within the ultramafic metapyroxenites of the KSM (see Fig 4.7 in Chapter 4). Taken together, the protolith geochemistry of both the Kromberg metabasalt flows and ultramafic metapyroxenite points to early formation of the Kromberg type-section in a supra-subduction zone oceanic setting, possibly similar to those of modern oceanic island arc environments and/or ophiolite-type settings.

5.8.2. Multiple sulphur isotopes across the Kromberg oceanic sequence

Over the past decade, sulphur isotope systematics have been applied to investigate atmospheric and biological processes on the early Earth and will be reviewed briefly here (e.g. Farquhar, et al. 2000; Farquhar, and Wing, 2003; Kamber, et al., 2007; Ono et al., 2006; Phillipot et al., 2007). Many workers studying sulphur-bearing minerals have independently discovered a distinctive mass-independent sulphur isotope ratio (anomalous $\Delta^{33}S = 1000* [(1 + \delta^{33}S/1000) - (1 + \delta^{34}S/1000)^{0.515}]$; e.g. Farquhar, et al. 2000; Farquhar, and Wing, 2003; Kamber, et al., 2007; Ono et al., 2006; Phillipot et al.,

2007). These $\Delta^{33}S$ or MIF- (Mass-independent Fractionation) anomalies have only been found in rocks older than 2400 Ma and are interpreted to have been produced by UV-induced photochemical reactions involving volcanic gases (SO_2 and H_2S) in a reduced Archean atmosphere (Farquhar, et al. 2000). A general model for the Archean S-cycle has been proposed which involves atmospheric photochemical reactions between UV rays and sulphur gasses, which in turn results in a mass-independent fractionation of dominant sulphur gases such as SO_2 and H_2S. This fractionation results in elemental sulphur aerosols with positive MIF-anomalies (S^0, $+\Delta^{33}S$) ultimately preserved as sulphides in marines sediments and sulphuric acid aerosols incorporated in seawater as dissolved sulphate with negative MIF-anomalies (SO_4, $-\Delta^{33}S$) eventually preserved as salts (gypsum, barite). It follows that sulphides formed from the biologic or abiologic reduction of sulphate should preserve a $-\Delta^{33}S$ anomaly, whereas sulphides formed from elemental sulphur by either inorganic reduction or microbial disproportionation should retain a $+\Delta^{33}S$ anomaly. Recent SIMS work on sulphides from a chert-barite unit of the 3490 Ma Dresser Formation in the Pilbara, Western Australia reported strong ^{34}S-depletion, but $+\Delta^{33}S$ anomalies that was used to argue for elemental sulphur disproportion rather than sulphate reducing microbial pathways (Phillipot et al., 2007). In contrast, subsequent nano-SIMS work on micron-sized pyrite associated with organic material in the 3400 Ma Strelley Pool Formation of Western Australia points to the co-existence of both metabolic pathways, namely microbial sulphate reduction of aqueous sulphate ($-\Delta^{33}S$) and microbial disproportionation of elemental sulphur ($+\Delta^{33}S$) in the early-mid Archean (Wacey, et al., 2010).

A first order observation in the sulphur isotope data in Figure 5.9, is that sulphides in carbonate veins in the lowest parts in KD1 retain a magmatic signature whereas the overlying cherts preserve a progressively positive $\Delta^{33}S$ or MIF anomaly. The early diagenetic pyrite in the uppermost Footbridge Chert records the largest $+\Delta^{33}S$ signal up to 2.4 ‰, indicating that the pyrites sourced particulate elemental atmospheric sulphur (S^0) as an Archean reservoir, rather than dissolved seawater sulphate. The sulphur isotope data is compatible with the Footbridge Chert representing a fine-grained submarine sediment that formed in a relatively reduced ocean-atmospheric environment, possibly in a shallow marine environment. The marine sediment was most likely formed in a moderately

isolated marine environment relative to the global Archean seawater composition as the MIF signal has not been completed diluted. The $\delta^{34}S$ values extend down to about -6 ‰, which could possibly indicate microbial disproportionation. Possible filamentous microfossils have been reported from the Footbridge Chert, in the Kromberg Formation (Walsh, 1992). However, to convincingly demonstrate a biogenic origin for some of the organic material, pyrites and microfossils in this unit demands further work (e.g. van Zuilen et al., 2007). In the lowermost part of KD1, pyrite within a metabasalt carbonate vein and pyrite in the KSM record a magmatic signature. Whilst, pyrite in carbonate veins in black chert horizons (see Figs. 5.1, 5.2 and 5.9) record only a small MIF-signal (average = +0.5‰) with likely mixing of magmatic and elemental atmospheric sulphur sources. The pyrite sulphur isotope systematics across KD1 therefore, most likely records different primary oceanic environments across a mid-Paleoarchean oceanic crustal section. An Archean seawater sulphate reservoir ($-\Delta^{33}S$) is not recorded in the five samples we analyzed and is most likely the result of a sulphate/sulphur-poor global Archean ocean (c.f. Bekker et al., 2009).

5.8.3. Geochemical variation across the KSM

Although the banded carbonate rocks of the KSM have carbonate veins in an ultramafic protolith and are structurally associated with underlying metapyroxenite, their $\delta^{13}C$ values are surprisingly not mantle-like. Instead, the $\delta^{13}C$ values are indistinguishable from that of Archean and modern day seawater (Figure 5.7). All bulk carbonate $\delta^{13}C$ values across the section fall largely within a homogeneous range of 0 ± 1.5 ‰, arguing against a mantle origin for the carbonate veining. On the other hand, Sr- isotope analyses of the carbonate veins in the KSM have initial $^{87}Sr/^{86}Sr$ ratios (at 3334 Ma) that are highly radiogenic ranging between 0.71048 to 0.71621. The $^{87}Sr/^{86}Sr$ isotope composition of Archean seawater is generally accepted to be mantle-like with a value of ~0.7025-0.7030 due to a strong hydrothermal mantle flux at that time (e.g. Veizer et al., 1989a,b). The $^{87}Sr/^{86}Sr$ ratios of the KSM carbonate veins are therefore far too radiogenic for a purely oceanic, seawater origin, but rather must represent some influence of continental (granitoid) crustal fluid sources (see Figure 5.10). The limited whole-rock oxygen isotope

data indicate that the $\delta^{18}O$ composition for the Kromberg mafic-ultramafic rocks across the KSM are highly shifted to positive values of between 9 and 15 ‰ (Table 5.3). An ultramafic rock sample beneath the lower contact of the KSM records a strongly shifted $\delta^{18}O$ value of nearly 15 ‰, indicating the possible influence of metamorphic waters. The oxygen isotope data points to high fluid/rock ratios during alteration and a late, low-temperature alteration event in rocks above and below the KSM. The XRD analyses shows that the drill core section is dominated by greenschist facies alteration minerals, and that serpentine minerals are absent throughout, even in the lower ultramafic metapyroxenitic unit (Figure 5.3). This suggests the possible breakdown of serpentine to release free metamorphic waters and silica in a fluid phase available as a possible source for extensive retrograde alteration including possible devolatilisation of lighter fluids.

The style of fluid-rock alteration in the KSM involves enrichment of MgO, CaO and SiO_2, along with depletion in Al_2O_3, most of the LILE elements such as Ba, Rb, and also the LREEs (Figure 5.3 and 5.5). The severe loss of LREE's, relative to surrounding rocks can be explained by a complex fluid alteration history and high fluid rock ratios in the KSM during alteration with pervasive fluids containing significant amounts of CO_2 and SiO_2 that interacted with the protolith (e.g. Nasir et al., 2007). Although it is difficult to distinguish, it is possible that more that one type of silicification event is present across KD1. For example, pyrite in a black chert vein intruding basalts beneath the lowermost laminated sedimentary chert unit, but overlying the KSM (see Figs. 5.1, 5.2 and 5.6), indicates mixing between oceanic, magmatic, and hydrothermal fluids with input from a possible atmospheric elemental sulphur reservoir. This is not observed in the KSM, where silicification is also extensive. Thus, silicification in the KSM may have been related to a separate and subsequent metamorphic fluid alteration event.

5.8.4. Tectonic and fluid alteration model

Multiple sulphur isotope data across the Kromberg type-section indicates that primary pyrite in fine laminae most likely formed in shallow marine sediments on the ocean floor and vein pyrites in sub-seafloor alteration settings. Similarly, the protolith trace element geochemistry of the KSM mafic-ultramafic rocks (see section 5.8.1 above) suggests an

oceanic supra-subduction zone setting, yet the prominent carbonate veins in KSM rocks, have a highly radiogenic Sr isotopic signature, which argues for both shear zone and mylonite development in a continental crustal setting. The combined geochemical dataset presented here, therefore, supports initial formation of a the Kromberg sequence of mafic and ultramafic mantle rocks in an oceanic subduction zone followed by mylonitic shearing and tectonic emplacement on top of continental crust, involving crustal fluids. In this regard, the KSM can be interpreted as a basal thrust zone to an ophiolite-type sequence of dismembered oceanic mafic-ultramafic rocks. Thus, the geochemical data reported here further supports the thrust model presented earlier in Chapter 4 on the basis of field, petrological and metamorphic data. Furthermore, the geochemical data is used to further elucidate the fluid-rock alteration processes that occurred across the range of environments recorded by the KSM from the early seafloor, obduction and post-obduction.

The style of fluid-rock interaction within the KSM involved enrichment in MgO, CaO, SiO_2 and CO_2, along with depletion in most of the LILE's and the LREE's. This style of mafic-ultramafic hydrothermal alteration is typical of listvenitic alteration (listvenitization) in basal thrust zones as seen for example in Neoproterozoic ophiolite terranes and the Semail ophiolite of the Oman (e.g. Nasir et al., 2007). Many studies in ophiolite terranes have demonstrated that listvenitic alteration typically overprints earlier seafloor serpentinization of ultramafic rocks (e.g. Spridonow, 1991; Schandal and Naldrett, 1992; Ucurum, 2000). Similarly, it can be argued for the Kromberg sequence that extensive listvenitic alteration occurred along the KSM post-dating both early serpentinization and obduction of the dismembered Kromberg oceanic crustal sequences, given both the absence of serpentine minerals across the section and the oxygen isotope data presented above. Thus, the variable extent of silificification and carbonitization (i.e. listvenitization) of the protolith rocks probably occurred during focused fluid flow and retrograde alteration along the KSM as a result of obduction followed by possible tectonic burial of the thrust nappe pile in a post-obduction regime (see also section 4.9.3).

Retrograde listvenitic alteration typically derives fluid from a range of sources including meteoric fluids, groundwater crustal fluids, metamorphic fluids from dehydration reactions of the serpentinized ultramafics and also seawater (e.g. Nasir et al.,

2007). For example, a typical serpentinite protolith may undergo the following alteration and mineralogical changes (after Halls and Zhoa, 1995): (1) serpentine → (2) serpentine-carbonate (breunnerite) → (3) serpentine-talc-carbonate rocks → (4) chlorite-quartz-carbonate → (5) chlorite carbonate → (6) fuchsite listvenite (end product). This process of listvenitization generally involves the breakdown of silicate minerals such as serpentine and, in places, direct replacement of olivine or pyroxene forming carbonate pseudomorphs as observed in the KSM samples (see Section 4.5.2 in Chapter 4). The serpentine-rich protolith has to undergo a multi-stage hydrothermal alteration process:

(1) Carbonitization of the serpentinite or mafic protolith (Halls and Zhoa, 1995)

Serpentine + CO_2 = Breunnerite + quartz + H_2O

(2) Silicification from an external silica source or from free silica produced from reaction (1) above (e.g. Kishida and Kerrich, 1987).

(3) Mica (Cr-muscovite) formation (Kishida and Kerrich, 1987)

e.g. $3Ab + K^+ + 2H^+ = Ms + 6Qtz + 3Na^+$

The hydrothermal fluid interacting with the protolith is believed to be reducing and transporting sulphur as HS- complexes resulting in the formation of pyrite like that found in KD1, or other Ni-bearing sulphides such as pentlandite or millerite (Henderson, 1969). Chromite remains as a relic ultramafic refractory phase that is most robust in terms of escaping the alteration processes; if chromite is not available in a particular microdomain, then yellowish brown sericite mica forms instead of fuchsite (Halls and Zhoa, 1995).

The fabrics of the banded fuchsite-carbonate-quartz rocks of the KSM (Fig. 5.1 and 5.2), display features typical of brittle failure during thrusting. Possible analogues for fluid flow processes in the KSM shear zone, may include the basal thrust zones described in the Phanerozoic Central Pyrenees by McCaig et al., (1995) and the Pan-African Naukluft Thrust in central Namibia (Miller et al. 2008). In these much younger thrust zones, workers have argued for highly focused fluid flow along the basal thrust zone, and that the source of radiogenic Sr enrichment in the carbonate mylonites of the thrust zone was fluids derived from the underlying crustal rocks. In the case of the KSM, the elevated Sr concentrations near the basal contact of the KSM with the underlying metapyroxenites

supports extensive fluid flow within the shear zone, and the Sr ratios suggest a crustally derived fluid source. A possible source of this highly radiogenic fluid, could have been the polymictitic (rhyo-dacitic to rhyolitic) diamictites of the Noisy formation (depositional age of 3432 Ma; Chapter 4) that structurally underlie the KSM. The distribution in initial $^{87}Sr/^{86}Sr$ isotope ratios with depth across the KSM, is very similar to than presented across the thrust zone of McCaig et al., (1995), where the $^{87}Sr/^{86}Sr$ ratios become progressively higher into the thrust zone or plane of focused fluid flow. A fault-valve model of fluid flow has been proposed by McCaig et al., (1995) as originally described by Sibson (1990), with fluid flow along the basal thrust involving dilatancy pumping and episodic brittle failure. A sudden increase in deviatoric stress due to over pressuring within the KSM mylonite zone would have resulted in extensive fracturing and veins systems as observed in KSM mylonites. If seismic/dilatancy pumping did occur it would have involved a suctioning effect of crustal fluids during episodic brittle failure. This may have occurred during obduction and/or post-obduction drawing in seawater as suggested by the $\delta^{13}C$ ratios of the carbonate veins, with related retrograde alteration and likely burial metamorphism of the thrust nappe pile. This would have included fluid from various sources, involving meteoric, crustal (e.g. TTG, rhyolitic conglomerates), seawater, metamorphic dewatering fluids from the dehydration of serpentinites and silica from early breakdown of serpentine during obduction.

5.8.5. Implications for Archean silicification and geodynamic models in the BGB

Some workers have argued that the BGB represents an oceanic plateau setting and that extensive silicification of komatiites and basalts associated with the alteration assemblage fuchsite-carbonate-quartz beneath sedimentary chert horizons in the BGB was the result of low temperature, seafloor alteration (less than 150^{o}C) in the Archean (Duchac and Hanor, J.S., 1987; Hanor and Duchac, 1990; Hofmann and Harris, 2008; Hoffman, 2011). These workers have reported that increasing SiO_2 contents of altered mafic-ultramafic rocks closer to the extensive fuchsitic alteration zones beneath sedimentary cherts is coupled to increases in LREE concentration, depletion in MgO, CaO and Sr and enrichments in LREE, Rb, Ba and Cs, whilst Al_2O_3 remains constant. For instance,

Hoffman and Harris (2008) and Hoffman (2011) argued that silicification is a result of low temperature seawater alteration driven by shallow sub-seafloor hydrothermal convection cells that was favorable for the emergence and sustainability of early microbial life. In contrast, the detailed geochemical profile reported here from across the KSM indicates the opposite major and trace element patterns to that reported by Hanor and Ducaq (1990) and Hofmann and Harris et al, (2008). Thus it is questioned whether the seafloor alteration model previously proposed for silicification and carbonatization of mafic-ultramafic rocks beneath sedimentary chert horizons in the BGB, is applicable to *all* such alteration zones throughout the BGB stratigraphy.

The geochemical profile reported here from across the KSM is attributed to silicification and carbonatization associated with thrust-related listventitic alteration of the Kromberg oceanic rocks (see Section 5.8.4 above). Moreover, the highly radiogenic Sr ratios for dolomitic veins in the KSM indicate a continental crustal signature for the alteration, rather than an Archean seawater-hydrothermal origin. In addition, metamorphic *PT*-data presented in Chapter 4 (and Grosch et al., 2011) indicate upper to mid-greenschist facies conditions that are at variance with the low temperature estimates of 75-150^{o}C seawater alteration previously reported beneath chert horizons in the BGB (Duchac and Hanor 1987; Hanor and Duchac 1990; Hofmann and Harris 2008, 2011). Thus, a low temperature (less than 150^{o}C) seawater alteration model cannot explain the geochemical alteration profile or *PT*-conditions for the fuchsitic alteration zone recorded in the KSM, neither the oceanic plateau like setting that has been proposed by the above mentioned authors.

An alternative hypothesis for the origin of the carbonate-quartz-fuchsite zones of the BGB has been argued for in a series of papers by de Wit and de Wit et al., (1982a,b; 1983, 1986a,b; 1992; 2011). These authors proposed that all ‘flaser-banded’ fuchsite-carbonate-quartz alteration zones and the associated silicification represent major structural breaks in the BGB stratigraphy, produced by oceanic ‘overthrust glide planes’ involving gravity-induced ‘hovercraft’ tectonics, silica domes related to oceanic mafic intrusive activity and flat subseafloor hydrothermal convection cells. In a recent paper, de Wit et al., (2011) proposed to redefine the stratigraphy of the upper Onverwacht group using 7 of these fuchsite-carbonate-quartz alteration zones beneath several chert horizons

as major structural breaks in the stratigraphy. These include, for example, the alteration zone presented in this study (KSM); a fuchsitic alteration zone beneath the Middle Marker at the base of the Hooggenoeg Formation; and a zone beneath the Msauli Chert in the uppermost Mendon Formation that are all interpreted to be oceanic extensional/ overthrust glide planes (see Fig. 14 in de Wit et al., 2011). It is important to point out that this contrasts with Hanor and Duchac (1990) who argued for low temperature seafloor alteration conditions (~100^{o}C) in the fuchsitic alteration zone beneath Msauli Chert. The intra-oceanic geodynamic and silicification model of de Wit and de Wit et al., (1982a,b) involving overthrust glide planes is not compatible with the new data presented here. Strontium isotope ratios are highly radiogenic and do not support an oceanic origin for the carbonate veins in the KSM. Moreover, the combined evidence in support of a much later silicification in the KSM due to listvenitization in a obduction/post-obduction crustal regime as explained above, is not compatible with the penecontemporaneous geodynamic silicification model of de Wit and de Wit et al., (1982a,b).

Multiple sulphur isotope analyses and textural evidence allows the different sources of sulphides associated with different silicification events in KD1 to be distinguished. Pyrite in black chert veins in silicified basalt and in a laminated chert horizon above the KSM record dilution of the atmospheric elemental sulphur reservoir (S^0, $+\Delta^{33}S$) by a magmatic reservoir (Figure 5.9). The black chert veins silicifying the metabasalt displaying a sharp intrusive contact as well as intense brecciation of black chert fragments (Figure 5.1, 5.2). These textural characteristics are very different from the carbonate-quartz bands observed in the KSM (see detailed drill core logs in Figure 5.1 and drill core images in Figure 5.2). This combined geochemical, lithological and textural data therefore points to another type of silicification related to magmatic silica-rich fluids most likely derived from mafic intrusive activity associated with for example, the gabbroic intrusive above the KSM (see Figure 5.1 and 5.2). This contrasts with sulphides of the Footbridge Chert that show a strong atmospheric S isotope signature (Fig. 5.9) and primary laminations in the chert (Figs. 5.2 and 5.8), suggesting an origin as early diagenetic pyrites on the seafloor in fine marine sediments.

Bringing together the drill core observations, metamorphic *PT*-constraints and geochemical (including isotopic) data across the KSM, this study distinguishes

silicification and alteration due to obduction-related listvenitization from lower temperature seafloor alteration reported beneath other sedimentary chert units in the BGB. Here a new alteration mechanism for silicification is proposed and should be tested for other alteration horizons in the BGB. This model is able to address a number of the outstanding questions previously raised by Paris et al., (1995) and paraphrased below, regarding silicification events in the BGB:

(i) *Styles and geological setting of silicification* – silicification in the fuschite bearing KSM is related to obduction of the Archean oceanic crust and post-obduction retrograde listvenitic alteration, it is distintict from altered, low-temperature (< 150^{o}C) silicified metabasalts beneath other sedimentary chert units in the BGB (e.g. those reported in Hoffman and Harris, 2008, de Wit et al., 1987a), as well as multiple silica generations within individual chert horizons (e.g. reported by Paris et al., 1985).

(ii) *Origin, timing and possibility of more than one silicification event* – this study identifies at least three different environments for silicification: (a) multiple silica veining events related to early low-temperature (100-150^{o}C) seafloor alteration of the oceanic crust beneath seafloor sedimentary horizons (e.g. beneath the Msauli Chert); (b) possible silica-rich fluids from oceanic mafic intrusive activity; (c) silicification related to listvenitic alteration in Paleoarchean thrust zones such as the alteration style identified in the KSM of the Kromberg type-section.

The new data presented therefore indicates a complex history of oceanic and tectonic alteration in the BGB, involving more than one type of temporally distinct silicification event. In the case of the KSM, the available zircon age constraints from the Footbridge Chert dated at 3334 Ma (Byerly et al., 1996), means that obduction-related silicification in the KSM shear zone most likely postdated seafloor silicification by more than 100 myr, given that obduction of the Kromberg oceanic sequences most probably occurred at 3223-3227 Ma. In summary, it is important that Archean geodynamic (de Wit et al., 1982b; 1983, 1986a,b; 1992), stratigraphic (e.g. de Wit et al., 2011) and fluid-rock

alteration models (e.g. Duchac and Hanor, 1987; Hanor and Ducaq, 1990; Hoffman and Harris, 2008) for the BGB distinguish these silicification and alteration types.

5.9. Conclusions

[1]. Trace element geochemistry of the least altered mafic rocks overlying the KSM suggests formation in a Paleoarchean supra-subduction zone setting. This is compatible with the tectonic setting of the protolith to the KSM banded mylonites, as recorded by relic chromian spinels.

[2]. In-situ sulphur isotope data from pyrites in the Footbridge Chert in upper KD1 preserve a primary sedimentary seafloor setting that records an Archean atmospheric signature.

[3]. X-ray diffraction across the KSM indicates a dominant alteration assemblage: chlorite, carbonate and quartz, and the absence of serpentine minerals. Limited bulk-rock oxygen stable isotope data above and below the KSM also points to extensive low temperature alteration of the mafic-ultramafic Kromberg sequence.

[4]. The carbonate-quartz veins in the KSM carbonate mylonites do not record a mantle $\delta^{13}C$ or $^{87}Sr/^{86}Sr$ isotope signature, despite the ultramafic metapyroxenite protolith. Rather, the combined $\delta^{13}C$ and $^{87}Sr/^{86}Sr$ isotope signature indicates that the carbonate veins in the KSM shear zone most likely formed in a continental setting. The distribution in the initial $^{87}Sr/^{86}Sr$ isotope ratios display a profile comparable to that found in modern-day continental thrust zones.

[5]. The style of fluid-rock interaction within the KSM involving enrichment in MgO, CaO, SiO_2 and CO_2, depletion in most of the LILE's and the LREE's, is characteristic of listvenitic alteration in basal thrust zones.. The mineral assemblage along with highly radiogenic Sr isotope signatures supports formation of a listvenite in an obduction setting with retrograde alteration involving a mixed fluid source (seawater, continental crustal fluids, and or meteoric waters) in a syn- to post-tectonic setting.

[6]. The style of alteration recorded in the KSM fuchsite-carbonate mylonite is distinguished geochemically from the silicified basalts and fuchsite-bearing alteration zones beneath other sedimentary chert horizons in the BGB. The KSM record silicification related to obduction at greenschist facies metamorphic grades, whereas other fuchsite-bearing alteration zones record silicification due to earlier, low-temperature seafloor alteration.

[7]. In-situ multiple sulphur isotopes measured on pyrite in carbonate-silica veins intruding metabasalts in KD1 record mixing between magmatic fluids and atmospheric elemental sulphur reservoirs, thus indicating a third style of silicification that postdates seafloor silicification and is distinct from listvenitization.

[8]. The combined geochemical data is not compatible with previous tectonic models for the BGB involving penecontemporaneous silicification in oceanic "overthrust/glide planes" (e.g. de Wit 1982a; de Wit et al., 1982b). Rather, this study identifies temporal decoupling between alteration and silicification event(s) in the Paleoarchean subseafloor (as described by Duchac and Hanor, 1987; Hanor and Duchac, 1990; Hoffman and Harris, 2008; Paris et al., 1985) from much later silicification related to thrusting and obduction of oceanic slices in the KSM. Moreover, this new data is not compatible with *all* the major fuchsite bearing silicification zones in the BGB being used to create a tectono-stratigraphic model involving early oceanic 'low-angle overthrust zones' (de Wit et al. 2011). Each of these fuchsitic alteration zones in the BGB needs to be investigated, to distinguish those resulting from early seafloor versus, later obduction related processes.

[9]. Sulphur and carbon isotope data in listvenitic zones such as the KSM does not preserve potential microbial fractionation processes. In order to search for potential early life sustaining environments containing traces of life, it is necessary to distinguish the different silica alteration processes characterized here. Listvenitic alteration horizons resulting from tectonic obduction are the least promising horizons for textural and biogeochemical fingerprints of early life.

Chapter 6

Synopsis

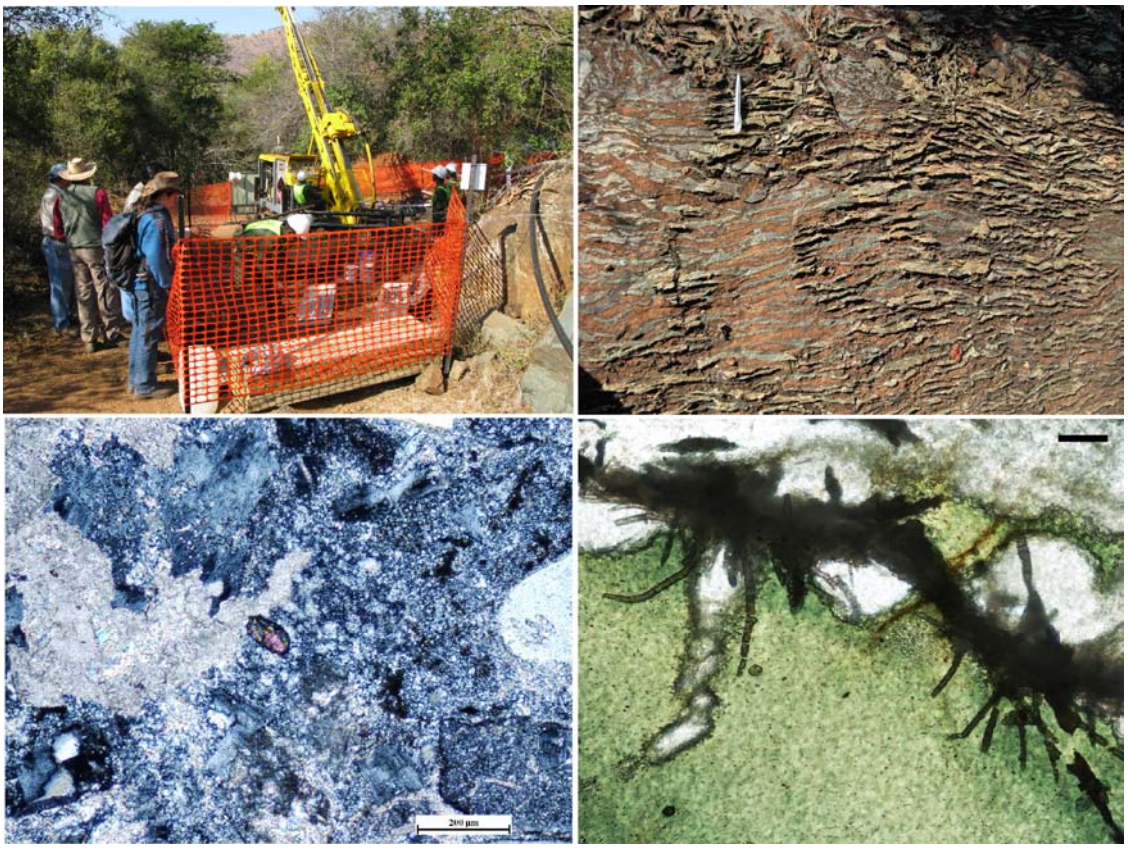

Bottom right: Photomicrograph of Archean subseafloor microbial biotextures in pillow lava breccia from the Hooggenoeg Formation, Barberton Greenstone Belt (from Grosch et al., 2009b).

6.1. Synopsis

A central theme of this thesis was to critically test available models for the geodynamic evolution of the Paleoarchean Barberton greenstone belt (BGB) of South Africa and the resulting physio-chemical environments available for early life. This was accomplished through the Barberton Scientific Drilling Project (BSDP) and combined petrographic, geochemical and geochronological investigations of field and drill core samples presented in Chapters 3-5. In brief, there are generally three main end-member geodynamic models, with associated fluid-rock hydrothermal processes, proposed in the literature for the BGB geologic evolution. These three geodynamic models are summarized below then discussed in light of the new data presented herein.

(i) Early, 3455 Ma, intra-oceanic subduction and 'extensional\overthrust glide planes' involving gravity-induced 'hovercraft' tectonics of oceanic crust with silica domes related to mafic intrusive activity providing the heat source for flat subseafloor hydrothermal convection cells. This in turn, is proposed to have resulted in bedding parallel subseafloor fuchsitic-silica alteration zones beneath chert horizons (de Wit and de Wit et al., 1982a,b; 1983, 1986a,b; 1987a,b; 1992; 2011). This early horizontal tectonics in the Onverwacht Group is reported to have been overprinted by compressional deformation involving folding and thrusting at ca. 3230 Ma (e.g. de Ronde and de Wit 2000; de Wit et al., 2011).

(ii) Early 3460 – 3430 Ma oceanic volcanism in an oceanic plateau setting with basin subsidence for eruption and deposition of the Onverwacht Group, followed by only later transpressional subduction tectonics and orogeny at ca. 3230 Ma (Cloete, 1991; 1999; Kamo and Davies, 1994; Lowe, 1994; 1999; Lowe and Byerly, 1999; Poujol et al., 2003; Chavagnac, 2004; Moyen et al., 2006; Hofmann and Harris, 2008; Schoene et al., 2008;), including multiple phases of tectonic folding and deformation (Lowe, 1994; 1999; Lowe and Byerly, 1999).

(iii) A multi-stage model of Van Kranendonk et al., (2009) and Van Kranendonk (2011) involving extrusion and deposition of a thick, continuous Onverwacht mafic-ultramafic-volcanosedimentary sequence between 3530 and 3416 (including deposition of the Theespruit and Hooggenoeg Formations) onto an older substrate of continental crust, possibly the 3644 Ma AGC (Ancient Gneiss Complex), that was followed by intrusion of 3470-3437 TTG felsic sheets. Eruption of mafic-ultramafic rocks of the Upper Onverwatch (the Kromberg and Mendon Formations) is argued to have resulted in overthickening of the volcanic pile between 3334 and 3298 Ma, partial melting of the TTG in the middle crust. This in turn resulted in partial convective overturn at ca. 3230 Ma, involving rising granite domes and sinking of dense, cool greenstone sequences as lobes/septae (e.g. Van Kranendonk, 2011). This model is similar to the vertical, plume-type tectonics proposed by Viljoen and Viljoen (1969) and Anhaeusser (1973; 2010).

These various geodynamic models are accommodated in two end-member stratigraphy models for the Onverwacht Group of the BGB, namely a thick, continuous volcanic-sedimentary pile (Viljoen and Viljoen, 1969; Lowe and Byerly, 1999; Van Kranendonk et al., 2009; 2011; Anhaeusser, 1973; 2010) versus a tectono-stratigraphic model with stacking and repetition of oceanic crust along intra-oceanic structural breaks in the form of 'extensional/overthrust glide planes' (e.g. de Wit, 1982a; de Wit et al., 1982b; 1983; 1986a,b, 1987a,b; de Ronde and de Wit, 1994; de Wit, et al., 1992, 2011). Summary figures contrasting these two stratigraphy models are illustrated in Figures 2.3 and 2.4 of Chapter 2. At the centre of these stratigraphy and geodynamic evolution models are fuchsite-carbonate-quartz alterations zones, which have been variously interpreted as: in situ sea-floor alteration of mafic-ultramafic rocks (Ducaq and Hanor, 1987; Hanor and Ducaq, 1990; Hofmann and Harris, 2008); very low temperature (60^{o}C) atmospheric weathering of komatiitic flow tops (Lowe and Byerly, 1999); or "quartz-carbonate-talc-fuchsite schists/gneisses" or "flaser-banded tectonites" that mark the proposed bedding-parallel oceanic silica-rich, extensional\overthrust glides planes (de

Wit, 1982a; de Wit et al., 1982b; 1983; 1986a,b, 1987a,b; de Ronde and de Wit, 1994; de Wit, et al., 1992, 2011).

In Chapters 4 and 5 of this thesis, one of these fuchsitic alteration zones in the Kromberg type-section of the Onverwacht Group, was studied in detail in order to test and resolve the significance of this zone for BGB stratigraphic debates and geologic evolution models. The detailed petrological analysis of the fuchsitic alteration zone beneath a chert horizon in drill core KD1 from the central Kromberg type-section, has revealed that these rocks are banded carbonate mylonites with petrological characteristics indicative of altered, mafic–ultramafic, mylonitic to protomylonitic rocks that have undergone listvenitic alteration. Metamorphic *PT*-contraints across the Kromberg type-section, indicates the presence of an inverted metamorphic field gradient (Fig. 4.11). The combined field and drill core observations strongly supports a model of tectonic thrust repetition across the Kromberg type-section, similar to that found beneath basal thrust zones in dismembered ophiolite terranes at ocean-continent collision zones. The mid- to upper greenschist facies conditions that span a high-*T* (420 ± 30^{o}C), *P* < 3 kbar event and a lower-*T* (240-350^{o}C), *P* = 2.9 ± 0.15 kbar event, is at variance with petrogenetic models for the central Kromberg fuchsitic alteration zone due to atmospheric weathering of komatiites at temperature conditions of less than 60^{o}C (Lowe and Byerly, 1999); or formation under a low temperature (75-125^{o}C) sea-floor hydrothermal regime (e.g. Ducaq and Hanor, 1987: Hanor and Ducaq, 1990, Hofmann and Harris, 2008).

Bulk rock trace element analyses of the metabasalts and mafic intrusives of the Kromberg type-section, together with relic Cr-spinel composition in the fuchsite-carbonate-quartz rocks of the KSM (Kromberg section mylonites) suggest a Paleoarchean supra-subduction zone setting for the Kromberg sequence on the eastern limb of the Onverwacht Antiform. Given the uncertainties associated with the application of tectonic discrimination diagrams in the Archean, it is the combination of the geochemical evidence and the inverted metamorphic field gradient that argues for a supra-subduction zone setting. This however, has to be reconciled with the highly radiogenic Sr isotope ratios recorded by the carbonate veins across the KSM that exclude a purely Archean oceanic setting for the KSM rocks. Thus, although the protolith mafic-ultramafic rocks

are argued to have formed in an oceanic supra-subduction zone setting, the highly radiogenic carbonate mylonites most likely formed in a continental setting during thrust related deformation. In addition, the geochemical alteration style preserved across the KSM, involving enrichment in MgO, CaO, SiO_2 and CO_2, depletion in most of the LILE's and the LREE's, also supports a fluid-rock alteration style characteristic of listvenitic alteration in basal thrust zones found in syn- to post-tectonic settings (e.g. Nasir et al., 2007; Halls and Zhoa, 1995). These findings contrast with that reported in low temperature oceanic hydrothermal settings (e.g. Hanor and Ducaq, 1990; Hofmann and Harris, 2008). The fuchsite-carbonate-quartz zone of the KSM, therefore marks an important tectono-thermal break in the Kromberg type-section of the upper Onverwacht Group.

The combined drill core observations, metamorphic and geochemical data allow at least three silica-alteration events in the BGB to be identified. The new data presented in this thesis indicates that an important distinction needs to be made between these different types of silica-fuchsite alteration zones with major implications for current stratigraphy and geodynamic models for the BGB. This includes a distinction between listvenitic alteration related to ophiolite obduction in some parts of the upper Onverwacht Group, from earlier silicification related to low temperature (75-125^{o}C) seafloor alteration in other fuchsitic alteration zones (e.g. Duchac and Hanor, (1987); Hanor and Duchac, (1990); Hofmann and Harris, (2008) and Paris et al., (1985)). Moreover, this new data is not compatible with *all* of the major fuchsite bearing silicification zones occurring beneath chert horizons in the BGB being used as shear zone or 'low-angle oceanic extensional/overthrust zones' proposed to subdivide the tectono-stratigraphic model of de Wit, (1982a) and de Wit et al., (1982b; 1983; 1986a,b; 1987a,b; 2011). In addition, the new data presented herein, is not compatible with previous tectonic models for the BGB involving penecontemporaneous silicification in oceanic "overthrust/glide planes" with formation of 'flaser-banded tectonites' due to hydrothermal silicification related to oceanic mafic intrusive activity (e.g. de Wit 1982a; de Wit et al., 1982b). Neither can *all* of the BGB fuchsite-carbonate-quartz alteration zones, have been formed solely in low temperature seafloor hydrothermal systems in a Paleoarchean oceanic plateau setting as proposed by Hofmann and Harris (2008). Rather, a new geodynamic

and alteration model is proposed in, which at least parts of the upper Onverwacht Group, as observed in the Kromberg type-section on the eastern limb of the Onverwacht Antiformal Fold (AOF), represent thin slices of allochtonous, obducted Paleoarchean oceanic crust that resulted in formation of some of the fuchsite-quartz-carbonate zones. The maximum depositional age of the Noisy formation sedimentary sequence constrained in Chapter 3 at ca. 3432 Ma, places a maximum age on the timing of thrusting in the overlying KSM fuchsitic shear zone (see Fig. 3.6). Although no absolute ages are currently available for the Kromberg sequence, thrusting and emplacement of relatively thin Kromberg oceanic crust along the KSM most likely occurred during a major transpressional event in the BGB, during oblique subduction and ocean closure at around ca. 3230 Ma. Silicification related to listvenitic alteration during and post-dating thrusting, most likely overprinted earlier low-temperature, sea-floor silica alteration that can be identified by sulphur MIF (mass independent fractionation) anomalies in sulphides still preserved in parts of the upper Onverwacht Group.

New detrital zircon age data together with field and drill core observations, provides new evidence for even earlier plate tectonic processes operating in the BGB at ca. 3432 Ma and the existence of a tectonically amalgamated continental landmass at that time. The depositional age of the Noisy formation constrained at ca. 3432 Ma, indicates that the major underlying unconformity in the Hooggenoeg Formation developed during tectonic uplift of the deep marine pillow lava pile and was accompanied by erosion and coarse clastic deposition at that time. A wide range in detrital zircon ages has been determined for the Noisy formation indicating many potential detritus sources from older continental rocks and terranes. These sources are found in the Songimvelo Block of the BGB that includes the BR-vsc of the uppermost Hooggenoeg formation; the Hooggenoeg pillow lavas and cherts; and the Stoltzburg TTG gneisses. Additional sources include older rocks of the Steynsdorp Block and from within the ca. 3667-3230 Ma Ancient Gneiss Complex (AGC). An early ca. 3432 Ma plate tectonic model is proposed in this thesis that involved tectonic accretion of the Songimvelo Block onto the older Steynsdorp and Ancient Gneiss microcontinental blocks of the Kaapvaal craton (Fig. 3.7c).

In summary, the combined data presented in this thesis proposes a new geologic evolution model for the BGB, which argues for at least two cycles of plate tectonic

activity similar to that of modern-day style ophiolite obduction processes at ca. 3432 Ma and subsequently at ca. 3230 Ma. The early intra-oceanic tectono-stratigraphic and hydrothermal silicification models of de Wit (1982a) and de Wit et al., (1982b; 1987a,b, 2011) are not supported by the new petrological data. Neither is the geologic evolution model presented herein compatible with an early oceanic plateau setting, with tectonic accretion and sedimentation occurring only 200 myr later at ca. 3230 Ma as proposed by Kamo and Davies (1994) Lowe (1994) and (1999). The new model is also contrasted with the extensional convective overturn model of Van Kranendonk et al., (2009) and Van Kranendonk (2011), which requires progressive eruption of a thick, autochtonous mafic-ultramafic sequence on older crust and subsequent burial metamorphism of the Onverwacht Group at mid-crustal level during partial convective overturn. Some of the fuchsite-carbonate-quartz horizons mark major structural breaks in the stratigraphy of the upper Onverwacht Group that indicate ca. 3230 Ma basal thrust zones such as that recorded in the KSM. Simple burial metamorphism of the entire Onverwacht Group as proposed by Van Kranendonk et al. (2009), Van Kranendonk (2011), and Cloete et al., (1991; 1999) is not supported by the *PT*-path derived for the Kromberg type-section in the upper Onverwacht Group. In addition, trace element geochemical data suggests an initial supra-subduction zone setting for the mafic and ultramafic rocks of the Kromberg type-section, rather than an autochtonous eruptive setting on older continental crust of the AGC related to plume magmatism. The mafic and felsic rocks of the ca. 3530 Ma Theespruit Formation, in the lowermost Onverwacht group is reported to record isotopic mixing between juvenile and older continental crustal sources (Van Kranendonk, 2009) and has thus been taken as evidence for older basement beneath the Komati-Hooggenoeg-Kromberg volcanic sequences. However, a juvenile oceanic source is generally accepted for the upper komatiitic-mafic sequences of the Onverwacht Group (e.g. Chavagnac, 2004; Parman and Grove, 2004), supporting formation of the younger overlying formations, namely the Komati, Hooggenoeg and Kromberg sequences in a oceanic juvenile settings, prior to ophiolite-type obduction onto older basement rocks (i.e. Steynsdorp and AGC rocks) as proposed herein. In addition, field observations (e.g. Grosch et al., 2009a,b; Furnes et al., 2011) and the geochronological constraints presented in Chapter 3 indicate development of a major erosional unconformity beneath

the Noisy formation that requires major tectonic uplift at ca. 3432 Ma and this cannot be explained by a regional BGB model involving only extensional tectonics and vertical doming of TTG melts in the partial convective overturn model of Van Kranendonk (2011) that is proposed to have occurred 200 million years after the depositional age of the Noisy formation as constrained in this thesis.

On this basis, it is proposed that the new data, field and drill core observation is consistent with plate tectonic-type crustal processes dominating over vertical, plume-type crustal processes throughout the early-mid Paleoarchean geologic evolution of the Barberton greenstone belt. It is therefore, very likely that a number of oceanic hydrothermal spreading centres and sub-seafloor environments were available for the origin and support of early microbial extremophile communities, as found in modern-day oceanic settings (e.g. Pedersen et al., 2010). In addition, evidence presented in the thesis for a shallow, intra-continental sea during deposition of the Noisy formation may also have provided ecological niches for early microbial life to thrive. Textural and biogeochemical fingerprints of early microbial communities have been identified in the ca. 3472 - 3432 Ma Hooggenoeg pillow lavas (e.g. Furnes et al., 2004; Fliegel et al., 2010; McLoughlin et al., 2009) and numerous chert horizons in the BGB (Walsh, 1992; Van Zuilen, 2007). However, further detailed work is on-going to confirm the biogenicity of these textures (McLoughlin, 2010). It is emphasized here that future searches for early oceanic life-sustaining environments in the Paleoarchean rock sequences of the BGB, should carefully distinguish between early low-temperature sub-seafloor hydrothermal settings and ophiolite obduction-related alteration settings.

Appendix A.

PhD publications in international peer-reviewed journals (Chapters 1- 5):

Grosch, E.G., McLoughlin, N., de Wit, M. and Furnes, H., (2009a). Deciphering Earth's Deep History: Drilling in Africa's Oldest Greenstone Belt. *Eos Trans. AGU*, 90(40), doi:10.1029/2009EO400002.

Grosch, E.G., McLoughlin, N., de Wit, M. and Furnes, H., (2009b). Drilling for the Archean Roots of Life and Tectonic Earth in the Barberton Mountains. *Scientific Drilling*, 8, 24-28.

Grosch, E.G., Kosler, J., McLoughlin, N., Drost, K., Slama, J., Pedersen, R. B., (2011). Paleoarchean detrital zircon ages from the earliest tectonic basin in the Barberton Greenstone Belt, Kaapvaal craton, South Africa. *Precambrian Research*, 191, 85-99.

Grosch, E.G., Vidal, O., Abu-Alam, T., Furnes, H., McLoughlin, N., (2012a). *PT*-Constraints on the metamorphic evolution of the Paleoarchean Kromberg type-section, Barberton Greenstone Belt, South Africa. *Journal of Petrology*, in press.

Grosch, E. G., McLoughlin, J., Ulyssess, N., Pedersen, R.B., (2012b). Obduction- and seafloor- related silicification in the Barberton Greenstone Belt, South Africa: Implications for early life environments. *Geochimica Cosmochimica Acta*, (in prep.)

Co-authored PhD publications in international peer-reviewed journals:

Philippot, P., Kranendonk, M.V., Van Zuilen, M., Lepot, K., Rividi, N., Teitler, Y., Thomazo, C., Blanc-Valleron, M-M., Rouchy, J-M., **Grosch, E.G.**, de Wit, M.J., (2009). Early traces of life investigations in drilling Archean hydrothermal and sedimentary rocks of the Pilbara Craton, Western Australia and Barberton Greenstone Belt, South Africa. *Comptes Rendus Palevol*, **8(7),** 649-663.

Abstracts at international conferences:

Grosch, E.G., de Wit, M.J, Furnes, H., McLoughlin, N. (2009c). Metamorphic Constraints Across a Mafic-Ultramafic Tectonite Zone Between the Mendon And Kromberg Complexes, Barberton Greenstone Belt, South Africa, Geological Society of America Abstracts with Programs, vol. 41, No. 7, p. 529, Paper No. 206-9.

Abu-Alam T.S. & **Grosch E.G.**, 2010. A thermodynamic activity-composition model for the Epidote group minerals and its petrological application. *Journal of Alpine Geology* 52, page 79. ISSN 1563-0846.

McLoughlin, N., Furnes, H., Staudigel, H., Muehlenbachs, K., Fliegel, D., **Grosch, E.G**., and de Wit, M. (2009). Microbial Bioalteration Textures in Greenstone Belt Pillow Lavas. Geological Society of America, Abstracts with Programmes, Vol. 41, No. 7, p. 529.

Appendix B. Sample depths across the KSM in KD1

Sample No.	Depth (m)	Description*	Sample No.	Depth (m)	Description*
KD1-T1	179.58	black chert	**KD1-T48**	220.08	KSM mylonite
KD1-T2	180.08	black chert	**KD1-T49**	221.08	KSM mylonite
KD1-T4	181.08	black chert	**KD1-T50**	222.08	KSM mylonite
KD1-T3	182.08	silicified basalt	**KD1-T51**	223.08	chert vein
KD1-T5	183.08	silicified basalt	**KD1-T52**	224.08	KSM mylonite
KD1-T6	184.08	silicified basalt	**KD1-T53**	225.08	KSM mylonite
KD1-T7	185.08	silicified basalt	**KD1-T54**	226.08	KSM mylonite
KD1-T8	186.08	silicified basalt	**KD1-T55**	227.08	KSM mylonite
KD1-T9	187.08	black chert	**KD1-T56**	228.08	KSM mylonite
KD1-T10	188.08	metabasalt	**KD1-T57**	229.08	KSM mylonite
KD1-T11	189.08	metabasalt	**KD1-T58**	230.08	KSM mylonite
KD1-T12	190.08	black chert	**KD1-T59**	231.08	KSM mylonite
KD1-T13	191.08	metabasalt	**KD1-T60**	232.08	KSM mylonite
KD1-T14	192.08	metabasalt	**KD1-T61**	233.08	KSM mylonite
KD1-T15	193.08	metabasalt	**KD1-T61A**	233.34	KSM mylonite
KD1-T16	194.08	metabasalt	**KD1-T62**	234.08	KSM mylonite
KD1-T17	195.08	metabasalt	**KD1-T63**	234.58	KSM mylonite
KD1-T18	196.08	metabasalt	**KD1-T64**	235.08	KSM mylonite
KD1-T19	197.08	metabasalt	**KD1-T65**	235.58	KSM mylonite
KD1-T20	198.08	metabasalt	**KD1-T66**	236.08	ultramafic mélange
KD1-T21	199.08	metabasalt	**KD1-T67**	236.58	ultramafic mélange
KD1-T22	200.08	metabasalt	**KD1-T68**	237.08	chert vein
KD1-T23	201.08	metabasalt	**KD1-T69**	237.58	ultramafic mélange
KD1-T24	202.08	metabasalt	**KD1-T70**	238.08	ultramafic mélange
KD1-T25	202.58	metagabbro	**KD1-T71**	239.08	ultramafic mélange
KD1-T26	203.08	metagabbro	**KD1-T72**	240.08	ultramafic mélange
KD1-T27	203.58	metagabbro	**KD1-T73**	241.08	ultramafic mélange
KD1-T28	204.08	metagabbro	**KD1-T74**	242.08	ultramafic mélange
KD1-T29	205.08	metagabbro	**KD1-T75**	243.08	ultramafic mélange
KD1-T30	206.08	metagabbro	**KD1-T76**	244.08	ultramafic mélange
KD1-T31	207.08	metagabbro	**KD1-T77**	245.08	ultramafic mélange
KD1-T32	208.08	metagabbro	**KD1-T78**	246.08	ultramafic mélange
KD1-T33	209.08	metagabbro	**KD1-T79**	247.08	chert vein
KD1-T34	209.58	metagabbro	**KD1-T80**	248.08	ultramafic mélange
KD1-T35	210.08	metagabbro	**KD1-T81**	249.08	ultramafic mélange
KD1-T36	210.58	KSM mylonite	**KD1-T82**	250.08	ultramafic mélange
KD1-T37	211.08	KSM mylonite	**KD1-T83**	251.08	ultramafic mélange
KD1-T38	211.58	KSM mylonite	**KD1-T84**	252.08	ultramafic mélange
KD1-T39	212.08	KSM mylonite	**KD1-T85**	253.08	ultramafic mélange
KD1-T40	212.58	KSM mylonite	**KD1-T86**	254.08	ultramafic mélange
KD1-T41	213.08	KSM mylonite	**KD1-T87**	255.08	ultramafic mélange
KD1-T42	214.08	KSM mylonite	**KD1-T88**	256.08	ultramafic mélange
KD1-T43	215.08	KSM mylonite	**KD1-T89**	257.08	ultramafic mélange
KD1-T44	216.08	KSM mylonite	**KD1-T90**	258.08	ultramafic mélange
KD1-T45	217.08	KSM mylonite	**KD1-T91**	259.08	ultramafic mélange
KD1-T46	218.08	KSM mylonite	**KD1-T92**	260.08	ultramafic mélange
KD1-T47	219.08	KSM mylonite	**KD1-T93**	261.98	ultramafic mélange

*Detailed lithological descriptions across the interval 179-262m is provided in the thesis chapters.

Appendix C1. U-Pb isotope data for detrital zircons in KD2a determined by single-collector ICP-MS

ISOTOPIC RATIOS						CALCULATED AGES Ma					
$^{207}Pb/^{235}U$	± 1 sigma	$^{206}Pb/^{238}U$	± 1 sigma	$^{207}Pb/^{206}Pb$	± 1 sigma	$^{207}Pb/^{235}U$	± 1 sigma	$^{206}Pb/^{238}U$	± 1 sigma	$^{207}Pb/^{206}Pb$	± 1 sigma
Sample: KD2-14m											
30.5427	1.6817	0.7474	0.0398	0.2964	0.0042	3504	54	3598	147	3451	22
26.1041	2.8207	0.6368	0.0684	0.2973	0.0036	3350	106	3177	269	3456	19
29.4158	2.6831	0.7086	0.0640	0.3011	0.0039	3467	90	3453	241	3476	20
26.5962	2.1372	0.6588	0.0523	0.2928	0.0038	3369	79	3263	203	3432	20
27.9018	1.8251	0.6824	0.0441	0.2965	0.0031	3416	64	3354	169	3452	16
30.7624	1.3160	0.7321	0.0300	0.3048	0.0038	3511	42	3541	112	3495	19
26.6557	2.3341	0.6308	0.0544	0.3065	0.0048	3371	86	3153	215	3503	24
26.9160	1.2025	0.6575	0.0284	0.2969	0.0034	3380	44	3257	110	3454	18
27.2501	1.5982	0.6618	0.0376	0.2987	0.0043	3392	57	3274	146	3463	23
30.0587	0.8490	0.7204	0.0188	0.3026	0.0033	3489	28	3498	70	3484	17
30.3336	1.6670	0.7229	0.0384	0.3043	0.0043	3498	54	3507	144	3492	22
30.1006	1.3641	0.7280	0.0316	0.2999	0.0039	3490	45	3526	118	3470	20
26.4163	0.8050	0.6549	0.0184	0.2925	0.0035	3362	30	3247	72	3431	19
29.6523	1.2092	0.7161	0.0279	0.3003	0.0036	3475	40	3481	105	3472	19
28.3886	1.4165	0.6883	0.0335	0.2991	0.0033	3433	49	3376	128	3466	17
30.2076	2.0780	0.7157	0.0485	0.3061	0.0037	3494	68	3480	182	3501	19
28.7275	1.1832	0.6910	0.0241	0.3015	0.0066	3444	40	3386	92	3478	34
28.5035	1.3850	0.6889	0.0322	0.3001	0.0040	3437	48	3378	123	3471	21
31.5668	1.7748	0.7170	0.0379	0.3193	0.0061	3537	55	3485	142	3567	29
29.8549	1.3016	0.6845	0.0270	0.3163	0.0058	3482	43	3362	104	3552	28
29.5857	1.8536	0.7233	0.0429	0.2967	0.0060	3473	62	3508	160	3453	31
26.0482	1.8563	0.6555	0.0448	0.2882	0.0057	3348	70	3250	175	3408	31
26.6930	2.3994	0.6501	0.0578	0.2978	0.0040	3372	88	3228	226	3459	21
29.1061	2.1392	0.7117	0.0500	0.2966	0.0064	3457	72	3465	188	3453	34
30.6237	1.6213	0.7327	0.0375	0.3031	0.0041	3507	52	3544	139	3486	21
27.0945	1.5591	0.6533	0.0367	0.3008	0.0038	3387	56	3241	143	3474	20
28.2830	1.1907	0.6890	0.0280	0.2977	0.0033	3429	41	3379	107	3458	17
28.8670	1.0590	0.6921	0.0231	0.3025	0.0046	3449	36	3391	88	3483	23
27.1003	1.1522	0.6621	0.0273	0.2969	0.0031	3387	42	3275	106	3454	16
26.7391	1.9071	0.6529	0.0452	0.2971	0.0050	3374	70	3239	176	3455	26

Appendix C1. *(continued)*

ISOTOPIC RATIOS						CALCULATED AGES Ma					
$^{207}Pb/^{235}U$	± 1 sigma	$^{206}Pb/^{238}U$	± 1 sigma	$^{207}Pb/^{206}Pb$	± 1 sigma	$^{207}Pb/^{235}U$	± 1 sigma	$^{206}Pb/^{238}U$	± 1 sigma	$^{207}Pb/^{206}Pb$	± 1 sigma
Sample: KD2-14m											
26.8303	1.9826	0.6536	0.0474	0.2977	0.0043	3377	72	3242	185	3458	22
26.6339	2.7621	0.6577	0.0673	0.2937	0.0049	3370	101	3258	262	3437	26
25.8663	2.5936	0.6255	0.0620	0.2999	0.0046	3341	98	3132	246	3470	24
28.4340	1.1154	0.6946	0.0254	0.2969	0.0043	3434	38	3400	96	3454	22
26.3456	1.2500	0.6574	0.0304	0.2907	0.0030	3359	46	3257	118	3421	16
25.7554	1.7329	0.6458	0.0424	0.2893	0.0043	3337	66	3212	166	3414	23
26.6616	2.8776	0.6643	0.0705	0.2911	0.0057	3371	106	3284	273	3423	30
30.2286	1.3580	0.7362	0.0296	0.2978	0.0059	3494	44	3556	110	3459	31
27.3559	1.1963	0.6582	0.0279	0.3014	0.0033	3396	43	3260	108	3478	17
28.0275	1.6130	0.6841	0.0381	0.2972	0.0043	3420	56	3360	146	3455	22
24.8048	2.2276	0.6257	0.0554	0.2875	0.0043	3301	88	3132	220	3404	23
28.0588	1.8017	0.6994	0.0428	0.2910	0.0057	3421	63	3418	162	3423	31
25.5608	1.3467	0.6590	0.0334	0.2813	0.0040	3330	51	3263	130	3370	22
28.1297	1.5796	0.6993	0.0381	0.2918	0.0039	3424	55	3418	145	3427	21
27.1719	2.0011	0.6642	0.0441	0.2967	0.0094	3390	72	3283	171	3453	49
28.3004	1.6734	0.6957	0.0397	0.2950	0.0046	3430	58	3404	151	3444	24
26.7257	1.4889	0.6756	0.0363	0.2869	0.0042	3373	55	3328	140	3401	23
29.3914	0.7282	0.7326	0.0142	0.2910	0.0045	3467	24	3543	53	3423	24
27.8793	1.6555	0.7087	0.0407	0.2853	0.0043	3415	58	3454	154	3392	23
26.5507	2.0934	0.6570	0.0509	0.2931	0.0043	3367	77	3255	198	3434	23
28.0791	2.1479	0.7137	0.0535	0.2854	0.0044	3422	75	3472	201	3392	24
25.1508	1.5253	0.6298	0.0373	0.2896	0.0037	3314	59	3149	148	3416	20
28.7829	1.8835	0.7215	0.0449	0.2893	0.0059	3446	64	3502	168	3414	32
24.3204	1.7636	0.6241	0.0446	0.2826	0.0034	3281	71	3126	177	3378	19
29.0791	1.6294	0.7477	0.0395	0.2821	0.0053	3456	55	3599	146	3374	29
27.3962	2.5549	0.6866	0.0634	0.2894	0.0036	3398	91	3370	243	3414	20
27.4159	1.5499	0.6893	0.0372	0.2885	0.0049	3398	55	3380	142	3409	26
24.7525	1.4871	0.6210	0.0361	0.2891	0.0044	3299	59	3114	143	3413	24
24.8012	1.5990	0.6262	0.0394	0.2873	0.0040	3300	63	3135	156	3403	22
23.3600	2.0929	0.5992	0.0526	0.2828	0.0050	3242	87	3027	212	3378	27
23.5504	2.2858	0.6011	0.0579	0.2842	0.0036	3250	95	3034	233	3386	20

Appendix C1. *(continued)*

ISOTOPIC RATIOS						CALCULATED AGES Ma					
$^{207}Pb/^{235}U$	± 1 sigma	$^{206}Pb/^{238}U$	± 1 sigma	$^{207}Pb/^{206}Pb$	± 1 sigma	$^{207}Pb/^{235}U$	± 1 sigma	$^{206}Pb/^{238}U$	± 1 sigma	$^{207}Pb/^{206}Pb$	± 1 sigma
Sample: KD2-56m											
28.0763	1.1250	0.7004	0.0244	0.2907	0.0057	3422	39	3422	93	3422	31
26.2684	2.0338	0.6463	0.0495	0.2948	0.0033	3357	76	3214	194	3443	17
25.3939	1.4651	0.6321	0.0357	0.2914	0.0035	3323	56	3158	141	3425	19
29.3980	1.0283	0.7250	0.0217	0.2941	0.0053	3467	34	3515	81	3439	28
26.2689	1.5072	0.6658	0.0351	0.2862	0.0065	3357	56	3290	136	3397	35
29.3958	1.2103	0.7303	0.0286	0.2919	0.0038	3467	40	3535	106	3428	20
26.9243	1.0100	0.6774	0.0223	0.2883	0.0052	3381	37	3334	86	3408	28
24.7515	1.7716	0.6336	0.0444	0.2833	0.0041	3298	70	3164	175	3381	23
26.5113	1.7327	0.6544	0.0411	0.2938	0.0054	3366	64	3246	160	3438	28
29.7662	0.8763	0.7261	0.0177	0.2973	0.0049	3479	29	3519	66	3456	25
28.4047	0.6327	0.6697	0.0111	0.3076	0.0046	3433	22	3305	43	3509	23
27.8325	1.0816	0.6813	0.0256	0.2963	0.0030	3413	38	3349	98	3451	15
29.2867	1.5969	0.6978	0.0374	0.3044	0.0031	3463	54	3412	142	3493	16
27.9973	0.8690	0.6886	0.0190	0.2949	0.0042	3419	30	3377	72	3444	22
26.8812	1.5671	0.6653	0.0382	0.2930	0.0030	3379	57	3288	148	3434	16
27.3166	1.5577	0.6734	0.0376	0.2942	0.0034	3395	56	3319	145	3440	18
25.9245	1.1662	0.6519	0.0283	0.2884	0.0035	3344	44	3236	110	3409	19
26.1821	1.3599	0.6551	0.0332	0.2899	0.0033	3353	51	3248	129	3417	18
26.1114	1.0053	0.6570	0.0243	0.2883	0.0032	3351	38	3255	94	3408	17
26.7693	1.4396	0.6727	0.0340	0.2886	0.0053	3375	53	3316	131	3410	29
26.3764	1.4196	0.6579	0.0342	0.2908	0.0040	3361	53	3259	133	3422	21
27.1102	1.2149	0.6695	0.0289	0.2937	0.0036	3387	44	3304	111	3437	19
30.0040	1.1733	0.6972	0.0259	0.3121	0.0038	3487	38	3410	98	3532	19
25.4902	1.3746	0.6448	0.0342	0.2867	0.0027	3327	53	3208	134	3400	15
27.8633	0.7190	0.6760	0.0144	0.2989	0.0043	3414	25	3329	56	3465	22
28.8834	1.1754	0.7080	0.0260	0.2959	0.0052	3450	40	3451	98	3449	27
27.3349	0.9091	0.6841	0.0199	0.2898	0.0047	3396	33	3360	76	3417	25
27.7447	0.9753	0.6822	0.0224	0.2950	0.0037	3410	34	3353	86	3444	19
25.7983	1.4544	0.6404	0.0352	0.2922	0.0036	3339	55	3191	138	3429	19
30.4160	2.1557	0.6926	0.0484	0.3185	0.0037	3500	70	3393	184	3563	18

Appendix C1. *(continued)*

ISOTOPIC RATIOS						CALCULATED AGES Ma					
$^{207}Pb/^{235}U$	± 1 sigma	$^{206}Pb/^{238}U$	± 1 sigma	$^{207}Pb/^{206}Pb$	± 1 sigma	$^{207}Pb/^{235}U$	± 1 sigma	$^{206}Pb/^{238}U$	± 1 sigma	$^{207}Pb/^{206}Pb$	± 1 sigma
Sample: KD2-56m											
26.0609	1.1777	0.6395	0.0276	0.2955	0.0039	3349	44	3187	109	3447	21
27.6846	1.4261	0.6639	0.0328	0.3025	0.0045	3408	50	3282	127	3483	23
28.2738	1.1374	0.6855	0.0243	0.2991	0.0057	3429	39	3365	93	3466	29
25.2964	1.3382	0.6236	0.0316	0.2942	0.0044	3320	52	3124	126	3440	23
30.2342	1.5650	0.6871	0.0341	0.3191	0.0047	3494	51	3372	130	3566	23
25.4273	1.7727	0.6237	0.0426	0.2957	0.0042	3325	68	3125	169	3448	22
26.7720	1.4001	0.6434	0.0305	0.3018	0.0066	3375	51	3202	120	3479	34
31.3269	1.4585	0.7350	0.0322	0.3091	0.0049	3529	46	3552	120	3516	24
26.0569	1.4784	0.6441	0.0350	0.2934	0.0048	3349	55	3205	137	3436	25
28.0157	1.7180	0.6700	0.0387	0.3032	0.0063	3420	60	3306	149	3487	32
26.8696	1.8737	0.6643	0.0446	0.2933	0.0055	3379	68	3284	173	3435	29
26.9953	1.0409	0.6636	0.0240	0.2950	0.0040	3383	38	3281	93	3444	21
26.5221	1.7113	0.6344	0.0397	0.3032	0.0048	3366	63	3167	157	3487	24
27.2202	1.4908	0.6671	0.0356	0.2960	0.0037	3391	54	3295	138	3449	19
26.5449	1.6092	0.6464	0.0380	0.2979	0.0044	3367	59	3214	149	3459	23
25.9294	1.0654	0.6417	0.0241	0.2931	0.0049	3344	40	3196	95	3434	26
26.0381	1.2007	0.6307	0.0276	0.2994	0.0043	3348	45	3152	109	3467	22
28.8795	1.5001	0.7045	0.0352	0.2973	0.0042	3449	51	3438	133	3456	22
27.7298	1.4744	0.6765	0.0345	0.2973	0.0045	3410	52	3331	133	3456	23
26.7772	1.9773	0.6422	0.0463	0.3024	0.0047	3375	72	3198	182	3483	24
27.5115	1.8653	0.6832	0.0443	0.2921	0.0057	3402	66	3357	170	3429	31
25.0206	1.5239	0.6267	0.0360	0.2895	0.0059	3309	59	3137	143	3415	32
28.9060	1.8148	0.7065	0.0419	0.2967	0.0061	3450	62	3445	158	3453	32
26.2173	1.1943	0.6451	0.0278	0.2948	0.0044	3355	45	3209	109	3443	23
28.5104	1.0321	0.7093	0.0227	0.2915	0.0050	3437	36	3456	85	3426	26
24.6679	1.9423	0.6129	0.0474	0.2919	0.0043	3295	77	3082	190	3428	23
27.5144	1.2652	0.6887	0.0306	0.2898	0.0035	3402	45	3378	117	3416	19
27.8056	1.3589	0.6864	0.0319	0.2938	0.0044	3412	48	3369	122	3438	23
26.1693	1.8617	0.6500	0.0452	0.2920	0.0044	3353	70	3228	176	3428	24
26.5875	1.6813	0.6651	0.0410	0.2899	0.0040	3368	62	3287	159	3417	22

Appendix C1. *(continued)*

ISOTOPIC RATIOS						CALCULATED AGES Ma					
$^{207}Pb/^{235}U$	± 1 sigma	$^{206}Pb/^{238}U$	± 1 sigma	$^{207}Pb/^{206}Pb$	± 1 sigma	$^{207}Pb/^{235}U$	± 1 sigma	$^{206}Pb/^{238}U$	± 1 sigma	$^{207}Pb/^{206}Pb$	± 1 sigma
Sample: KD2-56m											
26.0624	1.2975	0.6456	0.0313	0.2928	0.0033	3349	49	3211	123	3432	18
24.5075	1.4006	0.6274	0.0344	0.2833	0.0046	3289	56	3139	136	3381	25
26.4333	0.8860	0.6734	0.0179	0.2847	0.0058	3363	33	3319	69	3389	32
28.2203	0.9272	0.6981	0.0204	0.2932	0.0044	3427	32	3414	77	3434	23
26.3491	1.4010	0.6566	0.0337	0.2911	0.0040	3360	52	3254	131	3423	22
27.0518	1.9623	0.6567	0.0459	0.2988	0.0058	3385	71	3254	179	3464	30
27.9011	0.6616	0.6911	0.0147	0.2928	0.0031	3416	23	3387	56	3433	16
26.5436	1.4016	0.6629	0.0339	0.2904	0.0038	3367	52	3278	132	3420	20
27.6064	0.8339	0.6838	0.0191	0.2928	0.0033	3405	30	3359	73	3433	18
26.0745	1.2459	0.6555	0.0296	0.2885	0.0044	3349	47	3249	115	3410	24
25.9410	1.4608	0.6482	0.0355	0.2903	0.0037	3344	55	3221	139	3419	20
27.0436	1.2836	0.6664	0.0308	0.2943	0.0033	3385	46	3292	119	3441	17
24.1962	1.4420	0.6178	0.0360	0.2840	0.0035	3276	58	3101	144	3385	19
27.4296	1.8825	0.6795	0.0457	0.2928	0.0040	3399	67	3342	175	3432	21
26.7460	1.6568	0.6620	0.0402	0.2930	0.0035	3374	61	3275	156	3434	18
24.5107	1.8620	0.6268	0.0465	0.2836	0.0047	3289	74	3137	184	3383	26
25.5082	2.0190	0.6337	0.0488	0.2919	0.0053	3328	77	3164	193	3428	28
25.6665	1.2264	0.6349	0.0291	0.2932	0.0040	3334	47	3169	115	3435	21
26.3560	1.5718	0.6586	0.0384	0.2902	0.0036	3360	58	3262	149	3419	19
26.7081	1.1015	0.6675	0.0263	0.2902	0.0036	3373	40	3296	102	3419	19
25.4896	1.3642	0.6502	0.0332	0.2843	0.0046	3327	52	3229	130	3387	25
25.5963	2.1310	0.6229	0.0512	0.2980	0.0041	3331	81	3122	203	3460	21

Appendix C1. *(continued)*

ISOTOPIC RATIOS						CALCULATED AGES Ma					
$^{207}Pb/^{235}U$	± 1 sigma	$^{206}Pb/^{238}U$	± 1 sigma	$^{207}Pb/^{206}Pb$	± 1 sigma	$^{207}Pb/^{235}U$	± 1 sigma	$^{206}Pb/^{238}U$	± 1 sigma	$^{207}Pb/^{206}Pb$	± 1 sigma
Sample: KD2-62m											
29.6847	0.7062	0.7171	0.0132	0.3002	0.0045	3476	23	3485	50	3471	23
29.9301	0.7565	0.7295	0.0132	0.2975	0.0053	3485	25	3532	49	3457	27
28.7325	1.0596	0.7011	0.0230	0.2972	0.0050	3444	36	3425	87	3456	26
27.8738	0.9808	0.6773	0.0217	0.2985	0.0044	3415	34	3334	83	3462	23
31.9893	1.1716	0.7324	0.0247	0.3168	0.0045	3550	36	3543	92	3554	22
27.3809	0.8138	0.6691	0.0182	0.2968	0.0036	3397	29	3302	70	3454	19
29.1884	0.7319	0.7042	0.0141	0.3006	0.0046	3460	25	3437	53	3473	24
26.3213	0.4832	0.6649	0.0086	0.2871	0.0038	3359	18	3286	33	3402	20
26.4461	0.9391	0.6685	0.0220	0.2869	0.0038	3363	35	3300	85	3401	21
27.5436	0.7506	0.6755	0.0165	0.2957	0.0036	3403	27	3327	63	3448	19
29.1753	0.5768	0.7226	0.0109	0.2928	0.0037	3459	19	3506	41	3433	20
28.4965	1.0874	0.6970	0.0209	0.2965	0.0070	3436	37	3409	79	3452	37
27.2881	0.7968	0.6629	0.0159	0.2986	0.0050	3394	29	3278	62	3463	26
26.7901	0.8531	0.6768	0.0196	0.2871	0.0038	3376	31	3332	75	3402	21
26.6681	0.8246	0.6767	0.0193	0.2858	0.0034	3371	30	3332	74	3395	18
29.5610	1.2802	0.7129	0.0299	0.3007	0.0032	3472	43	3469	113	3474	17
28.9833	1.1938	0.7067	0.0279	0.2975	0.0035	3453	40	3446	105	3457	18
28.8491	1.3219	0.6974	0.0308	0.3000	0.0037	3448	45	3411	117	3470	19
30.1672	1.4056	0.7195	0.0319	0.3041	0.0043	3492	46	3494	120	3491	22
29.1795	1.1432	0.7029	0.0258	0.3011	0.0041	3460	38	3432	98	3476	21
28.7789	1.0166	0.7067	0.0235	0.2953	0.0035	3446	35	3446	89	3446	19
30.6424	1.8115	0.7045	0.0403	0.3155	0.0046	3508	58	3438	153	3548	23
30.0737	1.5520	0.7236	0.0358	0.3014	0.0044	3489	51	3509	134	3478	23
28.3457	1.2882	0.6905	0.0301	0.2977	0.0039	3431	45	3385	115	3458	20
29.2637	1.1750	0.7101	0.0266	0.2989	0.0043	3462	39	3459	100	3464	22
29.9516	2.2355	0.6997	0.0519	0.3104	0.0025	3485	73	3420	197	3523	12
29.0220	1.6037	0.6983	0.0371	0.3014	0.0045	3454	54	3414	141	3478	23
29.9299	1.6095	0.7273	0.0381	0.2985	0.0036	3485	53	3523	142	3462	19
29.2109	1.1374	0.6902	0.0257	0.3069	0.0034	3461	38	3383	98	3506	17
27.1830	0.8442	0.6686	0.0190	0.2949	0.0037	3390	30	3300	73	3444	19

Appendix C1. *(continued)*

ISOTOPIC RATIOS						CALCULATED AGES Ma					
$^{207}Pb/^{235}U$	± 1 sigma	$^{206}Pb/^{238}U$	± 1 sigma	$^{207}Pb/^{206}Pb$	± 1 sigma	$^{207}Pb/^{235}U$	± 1 sigma	$^{206}Pb/^{238}U$	± 1 sigma	$^{207}Pb/^{206}Pb$	± 1 sigma
Sample: KD2-62m											
34.3674	1.2864	0.7651	0.0175	0.3258	0.0096	3621	37	3663	64	3597	45
28.6938	1.2167	0.6994	0.0283	0.2976	0.0037	3443	42	3418	107	3458	19
30.2342	1.6286	0.7274	0.0382	0.3015	0.0037	3494	53	3524	142	3478	19
29.1932	2.2572	0.7034	0.0528	0.3010	0.0056	3460	76	3433	200	3476	29
29.7965	1.6554	0.7161	0.0384	0.3018	0.0044	3480	55	3481	144	3479	23
27.8887	1.9440	0.6793	0.0466	0.2977	0.0036	3415	68	3342	179	3459	19
29.7898	1.6243	0.7311	0.0378	0.2955	0.0052	3480	54	3537	141	3447	27
29.5359	1.7601	0.7175	0.0415	0.2985	0.0043	3471	59	3487	156	3463	22
27.4417	1.7602	0.6701	0.0420	0.2970	0.0041	3399	63	3306	162	3455	22
27.4059	1.1155	0.6792	0.0216	0.2926	0.0074	3398	40	3341	83	3432	39
29.4325	2.2625	0.7101	0.0533	0.3006	0.0049	3468	75	3459	201	3473	25
27.7204	1.5588	0.6876	0.0376	0.2924	0.0038	3409	55	3373	144	3430	20
24.4049	1.2913	0.6270	0.0324	0.2823	0.0033	3285	52	3138	128	3376	18
28.5689	2.1930	0.7128	0.0525	0.2907	0.0063	3439	75	3469	198	3421	34
28.9729	1.2209	0.6947	0.0268	0.3025	0.0051	3453	41	3401	102	3483	26
28.6646	1.9660	0.7067	0.0469	0.2942	0.0052	3442	67	3446	177	3440	27
26.9151	2.2485	0.6646	0.0548	0.2937	0.0040	3380	82	3285	212	3437	21
28.4428	2.4869	0.6969	0.0600	0.2960	0.0045	3434	86	3409	228	3450	23
28.8454	2.8391	0.7006	0.0682	0.2986	0.0042	3448	97	3423	259	3463	22
27.8327	1.9942	0.6851	0.0484	0.2946	0.0034	3413	70	3364	185	3442	18
27.3530	2.3643	0.6857	0.0584	0.2893	0.0042	3396	85	3366	223	3414	23
28.2418	1.9634	0.7016	0.0472	0.2919	0.0051	3428	68	3427	179	3428	27
28.3173	2.3985	0.7047	0.0592	0.2915	0.0032	3430	83	3438	224	3425	17
29.1712	1.5782	0.7117	0.0364	0.2973	0.0053	3459	53	3465	137	3456	28
28.8798	1.4655	0.7029	0.0331	0.2980	0.0056	3449	50	3431	125	3460	29
30.5345	2.0397	0.7176	0.0470	0.3086	0.0040	3504	66	3487	177	3514	20
23.8040	2.0988	0.6164	0.0538	0.2801	0.0036	3260	86	3096	214	3363	20
28.0383	1.2398	0.6985	0.0291	0.2911	0.0043	3420	43	3415	110	3424	23
27.2408	2.1720	0.6750	0.0530	0.2927	0.0040	3392	78	3325	204	3432	21
28.3572	2.1986	0.7099	0.0539	0.2897	0.0046	3432	76	3458	203	3416	25

Appendix C1. *(continued)*

ISOTOPIC RATIOS						CALCULATED AGES Ma					
$^{207}Pb/^{235}U$	± 1 sigma	$^{206}Pb/^{238}U$	± 1 sigma	$^{207}Pb/^{206}Pb$	± 1 sigma	$^{207}Pb/^{235}U$	± 1 sigma	$^{206}Pb/^{238}U$	± 1 sigma	$^{207}Pb/^{206}Pb$	± 1 sigma
Sample: KD2-62m											
28.0070	1.1924	0.6911	0.0272	0.2939	0.0047	3419	42	3387	104	3439	25
26.6796	1.2690	0.6705	0.0308	0.2886	0.0036	3372	47	3308	119	3410	19
27.3046	1.6869	0.6743	0.0408	0.2937	0.0037	3394	61	3322	157	3437	19
30.0279	2.2633	0.7200	0.0525	0.3025	0.0058	3488	74	3496	197	3483	30
28.3082	0.9867	0.6954	0.0230	0.2952	0.0033	3430	34	3403	87	3445	17
27.1423	2.0145	0.6552	0.0479	0.3005	0.0037	3389	73	3248	187	3473	19
26.1634	2.2455	0.6258	0.0526	0.3032	0.0054	3353	84	3133	208	3487	27
25.2276	3.2548	0.6271	0.0805	0.2918	0.0035	3317	126	3138	319	3427	19
27.4202	1.7866	0.6719	0.0431	0.2960	0.0033	3399	64	3313	166	3449	17
26.4553	1.1254	0.6653	0.0274	0.2884	0.0031	3364	42	3288	106	3409	17
28.4831	1.4293	0.6955	0.0333	0.2970	0.0045	3436	49	3404	126	3455	24
26.9728	2.8329	0.6616	0.0689	0.2957	0.0039	3382	103	3273	267	3448	21
26.8422	1.8371	0.6561	0.0442	0.2967	0.0035	3378	67	3252	172	3453	18
27.0507	2.4244	0.6546	0.0580	0.2997	0.0039	3385	88	3246	226	3469	20
29.0099	0.8101	0.7105	0.0169	0.2961	0.0044	3454	27	3460	64	3450	23
27.8333	1.9243	0.6858	0.0463	0.2943	0.0044	3413	68	3367	177	3441	23
28.0824	1.6343	0.6650	0.0375	0.3063	0.0043	3422	57	3287	145	3502	22

Appendix C1. *(continued)*

ISOTOPIC RATIOS						CALCULATED AGES Ma					
$^{207}Pb/^{235}U$	± 1 sigma	$^{206}Pb/^{238}U$	± 1 sigma	$^{207}Pb/^{206}Pb$	± 1 sigma	$^{207}Pb/^{235}U$	± 1 sigma	$^{206}Pb/^{238}U$	± 1 sigma	$^{207}Pb/^{206}Pb$	± 1 sigma
Sample: KD2-116m											
29.4560	1.5748	0.7293	0.0382	0.2929	0.0031	3469	53	3531	142	3433	16
29.4418	1.6158	0.7299	0.0385	0.2926	0.0045	3468	54	3533	143	3431	24
30.5688	1.8380	0.7567	0.0448	0.2930	0.0031	3505	59	3632	164	3434	17
25.8830	1.5683	0.6518	0.0377	0.2880	0.0052	3342	59	3235	147	3407	28
31.1729	1.7240	0.7753	0.0415	0.2916	0.0041	3525	54	3700	151	3426	22
29.6868	1.5070	0.7405	0.0370	0.2908	0.0026	3477	50	3572	137	3422	14
28.7243	1.9386	0.7179	0.0477	0.2902	0.0034	3444	66	3488	179	3419	18
26.4592	2.8384	0.6758	0.0694	0.2839	0.0088	3364	105	3328	267	3385	48
30.9185	1.7585	0.7369	0.0365	0.3043	0.0085	3516	56	3559	135	3492	43
28.5505	2.5940	0.7039	0.0629	0.2942	0.0048	3438	89	3436	238	3440	25
26.3747	1.3401	0.6498	0.0311	0.2944	0.0051	3361	50	3227	121	3441	27
27.8926	3.0208	0.7059	0.0760	0.2866	0.0033	3415	106	3443	287	3399	18
25.9686	2.1143	0.6601	0.0530	0.2853	0.0039	3345	80	3268	206	3392	22
29.5535	2.3639	0.7295	0.0577	0.2938	0.0036	3472	79	3532	215	3438	19
31.9907	3.2232	0.7555	0.0718	0.3071	0.0103	3550	99	3628	264	3507	52
29.5300	3.2186	0.7331	0.0782	0.2922	0.0066	3471	107	3545	291	3429	35
30.6987	1.8251	0.7150	0.0418	0.3114	0.0034	3509	58	3477	157	3528	17
28.9639	3.2466	0.7104	0.0788	0.2957	0.0047	3452	110	3460	297	3448	25
31.0150	1.8704	0.7171	0.0427	0.3137	0.0030	3520	59	3485	160	3539	15
28.7649	1.4083	0.7158	0.0335	0.2914	0.0042	3446	48	3480	126	3425	23
31.1861	1.6298	0.7381	0.0377	0.3064	0.0035	3525	51	3564	140	3503	18
27.7693	1.4748	0.6970	0.0344	0.2890	0.0056	3411	52	3409	131	3412	30
28.5394	2.3350	0.6998	0.0568	0.2958	0.0030	3438	80	3420	215	3448	16
26.1506	2.5627	0.6678	0.0636	0.2840	0.0066	3352	96	3297	246	3385	36
29.7591	1.4377	0.7394	0.0340	0.2919	0.0043	3479	47	3568	126	3428	23
26.6328	1.5030	0.6568	0.0363	0.2941	0.0034	3370	55	3255	141	3439	18
27.3948	1.1505	0.6767	0.0255	0.2936	0.0054	3398	41	3332	98	3437	29
28.0410	1.8144	0.6972	0.0445	0.2917	0.0030	3421	63	3410	169	3427	16
28.7209	2.3951	0.6954	0.0569	0.2996	0.0049	3444	82	3403	216	3468	25
29.7298	0.8964	0.7359	0.0213	0.2930	0.0025	3478	30	3556	79	3434	13

Appendix C1. *(continued)*

ISOTOPIC RATIOS						CALCULATED AGES Ma					
$^{207}Pb/^{235}U$	± 1 sigma	$^{206}Pb/^{238}U$	± 1 sigma	$^{207}Pb/^{206}Pb$	± 1 sigma	$^{207}Pb/^{235}U$	± 1 sigma	$^{206}Pb/^{238}U$	± 1 sigma	$^{207}Pb/^{206}Pb$	± 1 sigma
Sample: KD2-116m											
28.1970	1.6594	0.6928	0.0401	0.2952	0.0032	3426	58	3393	153	3445	17
31.0115	1.8796	0.7606	0.0449	0.2957	0.0041	3519	60	3646	164	3448	22
27.0146	4.0050	0.6656	0.0980	0.2944	0.0053	3384	145	3289	379	3441	28
26.9102	1.9990	0.6643	0.0490	0.2938	0.0027	3380	73	3284	190	3438	14
27.5072	3.0928	0.6854	0.0764	0.2911	0.0044	3402	110	3365	292	3423	23
29.9128	2.4718	0.7015	0.0577	0.3093	0.0023	3484	81	3426	219	3517	11
27.7999	1.8905	0.6901	0.0462	0.2921	0.0034	3412	67	3383	176	3429	18
28.6466	1.1196	0.7077	0.0265	0.2936	0.0033	3441	38	3450	100	3437	17
27.9920	1.1937	0.6819	0.0283	0.2977	0.0030	3419	42	3352	108	3458	15
25.6314	3.3533	0.6470	0.0844	0.2873	0.0030	3333	128	3216	330	3403	16
28.1360	3.1019	0.6958	0.0754	0.2933	0.0060	3424	108	3405	287	3435	32
29.9581	1.5047	0.7456	0.0356	0.2914	0.0045	3485	49	3591	132	3425	24
27.2995	2.0583	0.6789	0.0503	0.2917	0.0041	3394	74	3340	193	3426	22
34.8581	1.8662	0.8177	0.0425	0.3092	0.0040	3635	53	3852	151	3517	20
28.7304	2.4598	0.7070	0.0600	0.2947	0.0033	3444	84	3447	227	3443	18
26.4889	1.0230	0.6596	0.0232	0.2913	0.0047	3365	38	3266	90	3424	25
28.1857	1.3895	0.7124	0.0338	0.2870	0.0038	3426	48	3467	127	3401	21
27.4057	1.4448	0.6455	0.0282	0.3079	0.0091	3398	52	3211	110	3511	46
27.1044	1.7566	0.6362	0.0393	0.3090	0.0060	3387	63	3174	155	3516	30
28.2798	3.3612	0.6941	0.0817	0.2955	0.0049	3429	117	3398	311	3447	26
29.6718	1.2885	0.7304	0.0307	0.2946	0.0033	3476	43	3535	114	3442	17
27.6424	2.2414	0.6658	0.0533	0.3011	0.0038	3406	79	3290	206	3476	20
26.6336	1.4030	0.6642	0.0320	0.2908	0.0062	3370	52	3283	124	3422	33
27.6252	3.7707	0.6857	0.0930	0.2922	0.0044	3406	134	3366	356	3429	23
27.5410	1.9058	0.6836	0.0464	0.2922	0.0038	3403	68	3358	178	3429	20
28.3826	1.2939	0.6951	0.0309	0.2962	0.0030	3432	45	3402	117	3450	16
25.3986	1.5888	0.6423	0.0380	0.2868	0.0058	3324	61	3198	149	3400	32
25.5580	1.5846	0.6587	0.0392	0.2814	0.0049	3330	61	3262	152	3371	27
25.7035	1.1762	0.6477	0.0274	0.2878	0.0050	3335	45	3219	107	3406	27
24.5042	1.8404	0.6275	0.0450	0.2832	0.0064	3289	73	3140	178	3381	35

Appendix C1. *(continued)*

ISOTOPIC RATIOS						CALCULATED AGES Ma					
$^{207}Pb/^{235}U$	± 1 sigma	$^{206}Pb/^{238}U$	± 1 sigma	$^{207}Pb/^{206}Pb$	± 1 sigma	$^{207}Pb/^{235}U$	± 1 sigma	$^{206}Pb/^{238}U$	± 1 sigma	$^{207}Pb/^{206}Pb$	± 1 sigma
Sample: KD2-116m											
29.4750	0.6472	0.6754	0.0128	0.3165	0.0035	3469	22	3327	49	3553	17
27.6511	1.0392	0.6854	0.0250	0.2926	0.0026	3407	37	3365	96	3432	14
31.0225	1.0286	0.7354	0.0188	0.3060	0.0065	3520	33	3553	70	3501	33
26.2384	1.5795	0.6626	0.0389	0.2872	0.0037	3355	59	3277	151	3402	20
28.6194	1.5871	0.6997	0.0373	0.2966	0.0045	3441	54	3420	142	3453	24
29.2714	1.9798	0.7267	0.0456	0.2921	0.0074	3463	66	3521	170	3429	39
27.8044	0.7311	0.7001	0.0167	0.2881	0.0032	3412	26	3421	63	3407	17
32.1595	0.9596	0.7664	0.0177	0.3043	0.0058	3555	29	3668	65	3492	29
25.4563	1.7783	0.6404	0.0439	0.2883	0.0038	3326	68	3191	173	3408	21
34.4598	1.2784	0.7751	0.0237	0.3224	0.0068	3623	37	3699	86	3581	32
28.6807	1.6294	0.7152	0.0395	0.2908	0.0039	3443	56	3478	148	3422	21
27.1556	4.0492	0.6653	0.0981	0.2960	0.0064	3389	146	3288	380	3450	34
26.9900	0.9539	0.6865	0.0178	0.2851	0.0069	3383	35	3369	68	3391	38
26.5463	1.0932	0.6496	0.0230	0.2964	0.0062	3367	40	3227	90	3451	33
24.8144	1.3456	0.6191	0.0324	0.2907	0.0041	3301	53	3106	129	3421	22
28.2149	1.0021	0.7091	0.0222	0.2886	0.0049	3427	35	3455	84	3410	26
23.3984	1.7822	0.6100	0.0452	0.2782	0.0048	3244	74	3070	181	3353	27
27.7468	0.7070	0.6973	0.0159	0.2886	0.0033	3410	25	3411	60	3410	18
31.9276	0.9065	0.7546	0.0199	0.3069	0.0032	3548	28	3625	73	3505	16
27.6016	0.8152	0.6762	0.0182	0.2960	0.0036	3405	29	3330	70	3450	19
24.6963	3.5674	0.6340	0.0905	0.2825	0.0062	3296	141	3165	357	3377	34
32.0151	1.5890	0.7449	0.0361	0.3117	0.0033	3551	49	3589	133	3529	16

Appendix C1. *(continued)*

ISOTOPIC RATIOS						CALCULATED AGES Ma					
$^{207}Pb/^{235}U$	± 1 sigma	$^{206}Pb/^{238}U$	± 1 sigma	$^{207}Pb/^{206}Pb$	± 1 sigma	$^{207}Pb/^{235}U$	± 1 sigma	$^{206}Pb/^{238}U$	± 1 sigma	$^{207}Pb/^{206}Pb$	± 1 sigma
Sample: KD2-138.88m											
28.0215	1.3637	0.6453	0.0290	0.3149	0.0059	3420	48	3210	114	3545	29
27.6910	1.2258	0.6928	0.0294	0.2899	0.0036	3408	43	3393	112	3417	19
28.5137	1.2739	0.6679	0.0276	0.3096	0.0053	3437	44	3298	107	3519	26
28.3797	0.5272	0.7050	0.0100	0.2920	0.0035	3432	18	3439	38	3428	19
27.6630	1.5274	0.6777	0.0362	0.2960	0.0042	3407	54	3336	139	3450	22
29.5217	1.9015	0.6968	0.0420	0.3073	0.0070	3471	63	3409	160	3507	35
27.8057	1.4911	0.6840	0.0351	0.2948	0.0046	3412	53	3360	134	3443	24
26.1382	2.6964	0.6376	0.0637	0.2973	0.0077	3352	101	3180	251	3456	40
24.3521	1.5507	0.6234	0.0389	0.2833	0.0036	3283	62	3123	154	3381	20
25.1589	0.6920	0.6285	0.0157	0.2903	0.0034	3314	27	3144	62	3419	18
28.6655	1.4237	0.6670	0.0325	0.3117	0.0029	3442	49	3294	126	3529	15
29.7777	1.9310	0.6993	0.0440	0.3088	0.0048	3480	64	3418	167	3515	24
27.4347	2.7784	0.6667	0.0665	0.2985	0.0052	3399	99	3293	257	3462	27
27.6965	1.4432	0.6849	0.0339	0.2933	0.0047	3408	51	3363	130	3435	25
27.7680	1.4695	0.6865	0.0336	0.2934	0.0059	3411	52	3369	128	3435	31
26.6771	1.3316	0.6563	0.0317	0.2948	0.0037	3372	49	3253	123	3443	19
29.1110	1.7580	0.6971	0.0407	0.3029	0.0047	3457	59	3410	154	3485	24
28.6222	2.0329	0.6793	0.0466	0.3056	0.0056	3441	70	3342	179	3499	28
28.9751	1.6433	0.6915	0.0377	0.3039	0.0048	3453	56	3388	144	3490	24
29.1846	1.8022	0.6933	0.0414	0.3053	0.0048	3460	61	3395	158	3497	24
28.1315	2.0340	0.6682	0.0477	0.3053	0.0035	3424	71	3299	184	3497	18
26.9675	1.9575	0.6475	0.0458	0.3021	0.0050	3382	71	3218	179	3481	26
30.0469	0.8504	0.7040	0.0171	0.3095	0.0045	3488	28	3436	65	3519	22
25.8116	2.5099	0.6445	0.0597	0.2905	0.0086	3339	95	3207	234	3420	46
26.8192	1.0266	0.6796	0.0227	0.2862	0.0053	3377	37	3343	87	3397	29
27.3578	1.2160	0.6703	0.0274	0.2960	0.0051	3396	44	3307	106	3450	27
28.6577	2.1782	0.6711	0.0484	0.3097	0.0075	3442	75	3310	187	3520	37
26.6044	1.2032	0.6589	0.0257	0.2928	0.0067	3369	44	3263	100	3433	35
28.6287	3.1061	0.6712	0.0715	0.3094	0.0063	3441	106	3310	276	3518	32
25.5966	1.0291	0.6418	0.0249	0.2892	0.0031	3331	39	3196	98	3414	17

Appendix C1. *(continued)*

ISOTOPIC RATIOS						CALCULATED AGES Ma					
$^{207}Pb/^{235}U$	± 1 sigma	$^{206}Pb/^{238}U$	± 1 sigma	$^{207}Pb/^{206}Pb$	± 1 sigma	$^{207}Pb/^{235}U$	± 1 sigma	$^{206}Pb/^{238}U$	± 1 sigma	$^{207}Pb/^{206}Pb$	± 1 sigma
Sample: KD2-138.88m											
26.5386	2.2709	0.6466	0.0548	0.2977	0.0036	3367	84	3215	214	3458	19
27.2625	2.2721	0.6866	0.0533	0.2880	0.0088	3393	82	3370	204	3407	47
25.4373	0.8333	0.6352	0.0185	0.2904	0.0044	3325	32	3170	73	3420	23
26.2434	1.5744	0.6442	0.0341	0.2955	0.0083	3356	59	3205	134	3447	44
28.1216	1.3987	0.6757	0.0315	0.3018	0.0052	3423	49	3328	121	3480	27
28.6467	1.2723	0.6911	0.0287	0.3006	0.0048	3441	44	3387	109	3474	25
29.9100	2.0194	0.7142	0.0450	0.3037	0.0074	3484	66	3474	169	3489	38
29.9234	2.2754	0.7083	0.0520	0.3064	0.0060	3484	75	3452	196	3503	31
25.8513	1.6234	0.6377	0.0340	0.2940	0.0097	3341	61	3180	134	3439	51
28.6773	2.4163	0.6711	0.0552	0.3099	0.0058	3443	83	3310	213	3521	29
29.3004	1.3010	0.6925	0.0252	0.3069	0.0078	3464	44	3392	96	3505	39
27.4879	2.3309	0.6699	0.0549	0.2976	0.0065	3401	83	3305	212	3458	34
24.6341	3.9419	0.6189	0.0983	0.2887	0.0057	3294	156	3106	391	3410	31
26.1187	3.6334	0.6429	0.0867	0.2946	0.0101	3351	136	3200	340	3442	53
31.7822	2.8982	0.7545	0.0658	0.3055	0.0082	3544	90	3624	242	3498	41
24.8933	1.6517	0.6215	0.0396	0.2905	0.0053	3304	65	3116	158	3420	29
25.5164	2.0155	0.6216	0.0472	0.2977	0.0065	3328	77	3116	188	3458	34
30.6241	1.7678	0.7552	0.0413	0.2941	0.0054	3507	57	3627	152	3439	29
27.7812	1.2991	0.6866	0.0295	0.2935	0.0054	3411	46	3370	113	3436	29
28.5272	1.1780	0.7051	0.0244	0.2934	0.0066	3437	41	3440	92	3436	35
27.6430	1.4020	0.6818	0.0326	0.2941	0.0050	3407	50	3351	125	3439	26
29.5916	1.1934	0.6906	0.0237	0.3108	0.0066	3473	40	3385	90	3525	33
27.3232	2.7574	0.6716	0.0671	0.2951	0.0043	3395	99	3312	259	3445	22
29.0482	1.9021	0.7020	0.0426	0.3001	0.0074	3455	64	3428	161	3471	38
25.5264	2.0766	0.6379	0.0506	0.2902	0.0052	3329	79	3181	199	3419	28
27.8906	1.7618	0.6942	0.0422	0.2914	0.0050	3415	62	3399	160	3425	27
28.0897	1.6251	0.6822	0.0375	0.2986	0.0054	3422	57	3353	144	3463	28
24.3807	2.1806	0.6144	0.0541	0.2878	0.0045	3284	87	3088	216	3406	24
30.9531	1.4248	0.7210	0.0216	0.3114	0.0109	3518	45	3500	81	3528	54
30.5371	2.0193	0.7048	0.0455	0.3142	0.0045	3504	65	3439	172	3542	22

Appendix C1. *(continued)*

ISOTOPIC RATIOS						CALCULATED AGES Ma					
$^{207}Pb/^{235}U$	± 1 sigma	$^{206}Pb/^{238}U$	± 1 sigma	$^{207}Pb/^{206}Pb$	± 1 sigma	$^{207}Pb/^{235}U$	± 1 sigma	$^{206}Pb/^{238}U$	± 1 sigma	$^{207}Pb/^{206}Pb$	± 1 sigma
Sample: KD2-138.88m											
27.0899	1.9527	0.6679	0.0466	0.2942	0.0053	3387	71	3298	180	3440	28
24.6673	1.9011	0.6265	0.0466	0.2856	0.0058	3295	75	3136	185	3394	32
25.5535	1.5525	0.6667	0.0393	0.2780	0.0041	3330	59	3293	152	3352	23
28.2222	1.7936	0.7255	0.0448	0.2821	0.0043	3427	62	3517	167	3375	24
25.7748	1.9996	0.6669	0.0508	0.2803	0.0041	3338	76	3294	197	3365	23
30.5366	2.3623	0.7374	0.0552	0.3004	0.0058	3504	76	3561	205	3472	30
25.4905	5.3467	0.6335	0.1324	0.2918	0.0051	3327	205	3163	523	3427	27
25.7042	1.2638	0.6681	0.0313	0.2790	0.0041	3335	48	3299	121	3358	23
29.1989	1.1670	0.7000	0.0262	0.3025	0.0042	3460	39	3421	99	3483	22
26.0882	2.0982	0.6570	0.0519	0.2880	0.0045	3350	79	3256	202	3407	24
23.7205	3.2045	0.6103	0.0820	0.2819	0.0039	3257	132	3071	328	3373	22

Appendix C1. *(continued)*

ISOTOPIC RATIOS						CALCULATED AGES Ma					
$^{207}Pb/^{235}U$	± 1 sigma	$^{206}Pb/^{238}U$	± 1 sigma	$^{207}Pb/^{206}Pb$	± 1 sigma	$^{207}Pb/^{235}U$	± 1 sigma	$^{206}Pb/^{238}U$	± 1 sigma	$^{207}Pb/^{206}Pb$	± 1 sigma
Sample: KD2-176.08m											
27.9438	1.6644	0.6853	0.0400	0.2958	0.0036	3417	58	3364	153	3448	19
28.2666	1.3742	0.6685	0.0320	0.3067	0.0026	3428	48	3300	124	3504	13
29.0840	1.2037	0.7150	0.0285	0.2950	0.0033	3456	41	3477	107	3444	17
24.9870	1.9997	0.6302	0.0501	0.2876	0.0026	3308	78	3150	198	3404	14
28.4234	1.5805	0.6960	0.0380	0.2962	0.0032	3434	55	3406	144	3450	17
28.1156	1.5926	0.6976	0.0390	0.2923	0.0027	3423	56	3412	148	3430	14
27.5642	1.8780	0.6784	0.0455	0.2947	0.0035	3404	67	3338	175	3442	18
28.9321	1.5441	0.7170	0.0372	0.2927	0.0037	3451	52	3485	140	3432	20
28.7798	1.8141	0.6762	0.0423	0.3087	0.0024	3446	62	3330	163	3514	12
28.9292	1.7063	0.7126	0.0416	0.2944	0.0024	3451	58	3468	157	3441	13
26.9770	2.5571	0.6641	0.0625	0.2946	0.0032	3383	93	3283	242	3442	17
24.6991	2.0588	0.6209	0.0511	0.2885	0.0039	3296	81	3114	203	3410	21
27.3252	1.9136	0.6752	0.0467	0.2935	0.0033	3395	69	3326	180	3436	18
27.4683	1.0406	0.6787	0.0248	0.2935	0.0030	3400	37	3339	95	3436	16
27.0103	1.4687	0.6708	0.0356	0.2920	0.0035	3384	53	3309	137	3429	18
25.5296	1.7515	0.6378	0.0431	0.2903	0.0033	3329	67	3180	170	3419	18
25.9793	1.5035	0.6512	0.0368	0.2893	0.0035	3346	57	3233	144	3414	19
26.0901	1.4386	0.6406	0.0339	0.2954	0.0045	3350	54	3191	133	3446	24
27.1754	1.6101	0.6766	0.0395	0.2913	0.0029	3390	58	3331	152	3425	15
27.6118	1.4401	0.6753	0.0341	0.2966	0.0039	3405	51	3326	131	3452	20
27.4132	1.3207	0.6764	0.0319	0.2939	0.0030	3398	47	3331	123	3438	16
27.1520	0.8210	0.6802	0.0185	0.2895	0.0039	3389	30	3345	71	3415	21
27.3550	1.4316	0.6728	0.0344	0.2949	0.0032	3396	51	3317	133	3443	17
27.2641	1.2904	0.6766	0.0316	0.2923	0.0023	3393	46	3331	121	3430	12
27.3514	1.3242	0.6820	0.0309	0.2909	0.0049	3396	47	3352	119	3422	26
24.3958	1.5700	0.6173	0.0390	0.2866	0.0036	3284	63	3099	155	3399	20
26.4447	0.8060	0.6654	0.0181	0.2883	0.0039	3363	30	3288	70	3408	21
25.2282	0.9578	0.6394	0.0230	0.2861	0.0035	3317	37	3187	90	3397	19
25.9259	1.5163	0.6567	0.0379	0.2863	0.0027	3344	57	3254	148	3398	14
28.3754	1.3185	0.6803	0.0303	0.3025	0.0040	3432	46	3346	116	3483	20

Appendix C1. *(continued)*

ISOTOPIC RATIOS						CALCULATED AGES Ma					
$^{207}Pb/^{235}U$	± 1 sigma	$^{206}Pb/^{238}U$	± 1 sigma	$^{207}Pb/^{206}Pb$	± 1 sigma	$^{207}Pb/^{235}U$	± 1 sigma	$^{206}Pb/^{238}U$	± 1 sigma	$^{207}Pb/^{206}Pb$	± 1 sigma
Sample: KD2-176.08m											
25.9066	1.4816	0.6657	0.0373	0.2822	0.0033	3343	56	3289	144	3375	18
26.6418	1.5731	0.6872	0.0390	0.2812	0.0046	3370	58	3372	149	3369	26
27.7221	1.8560	0.6772	0.0445	0.2969	0.0038	3409	66	3334	171	3454	20
24.7815	2.1747	0.6421	0.0558	0.2799	0.0036	3300	86	3197	219	3362	20
27.4632	1.5028	0.6734	0.0357	0.2958	0.0039	3400	54	3319	138	3448	21
26.3542	1.9569	0.6825	0.0498	0.2801	0.0038	3360	73	3354	191	3363	21
27.0472	1.1959	0.6927	0.0293	0.2832	0.0037	3385	43	3393	112	3381	20
25.1292	2.3699	0.6519	0.0611	0.2796	0.0030	3313	92	3235	238	3361	17
25.5945	1.7668	0.6470	0.0437	0.2869	0.0040	3331	67	3216	171	3401	22
28.9457	1.3853	0.7021	0.0323	0.2990	0.0039	3452	47	3429	122	3465	20
26.5035	1.8789	0.6759	0.0475	0.2844	0.0027	3365	69	3329	183	3387	15
27.2388	0.8361	0.7012	0.0191	0.2817	0.0040	3392	30	3425	72	3373	22
25.6446	2.3187	0.6619	0.0594	0.2810	0.0031	3333	88	3274	230	3369	17
27.6287	2.0775	0.6776	0.0503	0.2957	0.0034	3406	74	3335	193	3448	18
30.5828	1.8987	0.7448	0.0450	0.2978	0.0043	3506	61	3588	166	3459	22
28.3069	1.3410	0.6939	0.0317	0.2959	0.0038	3430	46	3398	120	3449	20
27.8395	1.3355	0.6806	0.0316	0.2966	0.0035	3413	47	3347	121	3453	18
27.2783	0.9573	0.6720	0.0223	0.2944	0.0034	3394	34	3314	86	3441	18
29.2519	0.8189	0.6861	0.0154	0.3092	0.0051	3462	27	3368	59	3517	26
25.7469	3.2891	0.6296	0.0798	0.2966	0.0048	3337	125	3148	316	3453	25
26.9394	1.9132	0.6744	0.0452	0.2897	0.0068	3381	70	3323	174	3416	37
23.0999	0.8505	0.5773	0.0170	0.2902	0.0064	3231	36	2938	69	3419	35
28.0380	1.0648	0.6853	0.0248	0.2967	0.0035	3420	37	3365	95	3453	18
25.6885	2.0117	0.6350	0.0493	0.2934	0.0030	3335	77	3169	194	3436	16
27.5501	1.6805	0.6727	0.0407	0.2970	0.0023	3403	60	3316	157	3455	12
27.3432	1.6349	0.6728	0.0394	0.2947	0.0036	3396	59	3317	152	3443	19
27.3139	1.7822	0.6658	0.0427	0.2976	0.0035	3395	64	3289	165	3458	18
27.3016	1.5099	0.6724	0.0366	0.2945	0.0029	3394	54	3315	141	3441	15
27.4894	1.5761	0.6790	0.0382	0.2936	0.0033	3401	56	3341	147	3437	17
29.4807	1.6843	0.6844	0.0386	0.3124	0.0029	3470	56	3361	148	3533	14

Appendix C1. *(continued)*

ISOTOPIC RATIOS						CALCULATED AGES Ma					
$^{207}Pb/^{235}U$	± 1 sigma	$^{206}Pb/^{238}U$	± 1 sigma	$^{207}Pb/^{206}Pb$	± 1 sigma	$^{207}Pb/^{235}U$	± 1 sigma	$^{206}Pb/^{238}U$	± 1 sigma	$^{207}Pb/^{206}Pb$	± 1 sigma
Sample: KD2-176.08m											
26.3703	1.7051	0.6586	0.0418	0.2904	0.0035	3360	63	3262	163	3420	19
26.2660	1.4354	0.6554	0.0348	0.2907	0.0038	3356	53	3249	135	3421	20
26.9315	1.7307	0.6767	0.0429	0.2887	0.0029	3381	63	3332	165	3410	16
31.2412	1.1573	0.7696	0.0270	0.2944	0.0035	3527	36	3679	98	3441	18
27.4164	2.2528	0.6836	0.0555	0.2909	0.0037	3398	80	3358	213	3422	20
27.6801	1.8041	0.6816	0.0433	0.2945	0.0043	3408	64	3351	166	3442	23
27.6771	1.8472	0.6836	0.0445	0.2936	0.0044	3408	65	3358	170	3437	23
27.0348	2.3872	0.6713	0.0584	0.2921	0.0043	3385	86	3311	225	3429	23
27.1850	1.9021	0.6734	0.0466	0.2928	0.0030	3390	69	3319	180	3433	16
25.6073	1.3286	0.6580	0.0321	0.2822	0.0050	3332	51	3260	125	3375	28
30.9189	1.5854	0.7741	0.0377	0.2897	0.0047	3516	50	3696	137	3416	25
28.9643	3.3007	0.7257	0.0817	0.2895	0.0051	3452	112	3518	305	3415	28
30.0645	2.2450	0.7462	0.0548	0.2922	0.0040	3489	73	3593	202	3429	21
30.8235	2.5830	0.7728	0.0639	0.2893	0.0039	3513	82	3691	232	3414	21
27.1266	1.7577	0.6781	0.0435	0.2901	0.0027	3388	63	3337	167	3418	14
27.9572	2.6911	0.7001	0.0667	0.2896	0.0039	3418	94	3421	253	3416	21
27.2906	1.8685	0.6835	0.0464	0.2896	0.0025	3394	67	3358	178	3415	13
25.9340	2.4869	0.6356	0.0603	0.2959	0.0041	3344	94	3172	238	3449	21
27.5797	3.0361	0.6843	0.0749	0.2923	0.0034	3404	108	3361	287	3430	18
27.6845	1.7407	0.6874	0.0422	0.2921	0.0039	3408	62	3373	161	3429	21
29.7253	2.2605	0.7404	0.0550	0.2912	0.0047	3478	75	3572	204	3424	25
28.2302	2.4717	0.6945	0.0602	0.2948	0.0035	3427	86	3400	229	3443	19
28.5405	2.5138	0.7081	0.0619	0.2923	0.0030	3438	86	3451	234	3430	16
27.3060	2.1117	0.6793	0.0505	0.2915	0.0062	3395	76	3342	194	3426	33
27.4387	1.8557	0.6835	0.0433	0.2912	0.0069	3399	66	3358	166	3424	37

Appendix C2. U-Pb isotope data for detrital zircons in KD2 determined by laser abaltion multiple-collector ICP-MS analysis

	ISOTOPIC RATIOS						CALCULATED AGES Ma					
Analysis#	**$^{207}Pb/^{235}U$**	**± 1 sigma**	**$^{206}Pb/^{238}U$**	**± 1 sigma**	**$^{207}Pb/^{206}Pb$**	**± 1 sigma**	**$^{207}Pb/^{235}U$**	**± 1 sigma**	**$^{206}Pb/^{238}U$**	**± 1 sigma**	**$^{207}Pb/^{206}Pb$**	**± 1 sigma**
Sample KD-116.08m												
KD2-116-1	28.2728	0.3264	0.6927	0.0073	0.2968	0.0018	3429	11	3393	28	3453	5
KD2-116-2	26.7678	0.3239	0.6560	0.0073	0.2959	0.0018	3375	12	3252	28	3449	5
KD2-116-3	26.2880	0.2987	0.6406	0.0066	0.2986	0.0018	3357	11	3191	26	3463	5
KD2-116-4	27.0830	0.3111	0.6608	0.0069	0.2977	0.0018	3386	11	3270	27	3458	5
KD2-116-5	28.7974	0.3321	0.7007	0.0074	0.2978	0.0018	3447	11	3423	28	3459	5
KD2-116-6	28.3206	0.3261	0.6890	0.0073	0.2983	0.0018	3430	11	3379	28	3461	5
KD2-116-7	26.5399	0.3031	0.6526	0.0068	0.2949	0.0018	3367	11	3238	27	3444	5
KD2-116-8	25.1597	0.3128	0.6263	0.0069	0.2930	0.0018	3314	12	3135	28	3433	5
KD2-116-9	26.6296	0.3013	0.6509	0.0067	0.2979	0.0018	3370	11	3232	26	3459	5
KD2-116-10	27.8878	0.3215	0.6830	0.0073	0.2979	0.0018	3415	11	3356	28	3459	5
KD2-116-11	28.3712	0.3247	0.6599	0.0069	0.3118	0.0019	3432	11	3267	27	3530	5
KD2-116-12	28.6094	0.3258	0.6980	0.0073	0.2981	0.0018	3440	11	3413	28	3460	5
KD2-116-13	28.8225	0.3349	0.7047	0.0073	0.2962	0.0018	3447	11	3438	28	3450	5
KD2-116-14	28.1562	0.3236	0.6952	0.0073	0.2928	0.0018	3425	11	3402	28	3432	5
KD2-116-15	28.6167	0.3370	0.6946	0.0073	0.2976	0.0018	3440	12	3400	28	3458	5
KD2-116-16	29.2066	0.3319	0.7120	0.0074	0.2967	0.0018	3460	11	3466	28	3453	5
KD2-116-17	28.4525	0.3211	0.6908	0.0071	0.2991	0.0018	3435	11	3386	27	3466	5
KD2-116-18	31.6818	0.3643	0.7297	0.0076	0.3131	0.0019	3540	11	3532	28	3536	5
KD2-116-19	28.5127	0.3204	0.6941	0.0072	0.2992	0.0019	3437	11	3398	27	3466	5
KD2-116-20	31.2367	0.3562	0.7184	0.0075	0.3146	0.0019	3527	11	3490	28	3544	5
KD2-116-21	30.4869	0.4219	0.7130	0.0076	0.3122	0.0028	3503	14	3470	29	3532	7
KD2-116-22	29.0234	0.4006	0.6716	0.0071	0.3149	0.0028	3454	14	3312	27	3545	7
KD2-116-23	27.9878	0.3876	0.6683	0.0071	0.3067	0.0028	3419	14	3299	27	3504	7
KD2-116-24	29.7671	0.4102	0.7017	0.0075	0.3088	0.0028	3479	14	3427	29	3515	7
KD2-116-25	27.4163	0.3764	0.6740	0.0071	0.2961	0.0027	3398	14	3321	27	3450	7
KD2-116-26	30.6730	0.4259	0.7122	0.0076	0.3140	0.0028	3509	14	3467	29	3541	7
KD2-116-27	27.8073	0.3981	0.6586	0.0072	0.3079	0.0028	3412	14	3262	28	3511	7
KD2-116-28	27.9782	0.3957	0.6478	0.0070	0.3128	0.0028	3418	14	3220	28	3535	7
KD2-116-29	27.2236	0.3893	0.6693	0.0074	0.2973	0.0027	3392	14	3303	29	3456	7
KD2-116-30	30.1778	0.4215	0.6981	0.0075	0.3139	0.0028	3493	14	3413	28	3540	7

Appendix C2. *(Continued)*

	ISOTOPIC RATIOS						CALCULATED AGES Ma					
Analysis#	**$^{207}Pb/^{235}U$**	**± 1 sigma**	**$^{206}Pb/^{238}U$**	**± 1 sigma**	**$^{207}Pb/^{206}Pb$**	**± 1 sigma**	**$^{207}Pb/^{235}U$**	**± 1 sigma**	**$^{206}Pb/^{238}U$**	**± 1 sigma**	**$^{207}Pb/^{206}Pb$**	**± 1 sigma**
Sample KD-138.88m												
KD-138-1	27.8738	0.5196	0.6855	0.0110	0.2970	0.0015	3415	19	3366	43	3454	8
KD-138-2	27.8785	0.5132	0.6844	0.0109	0.2970	0.0015	3415	18	3361	42	3455	8
KD-138-3	29.6328	0.5509	0.7226	0.0116	0.2984	0.0015	3475	19	3506	44	3462	8
KD-138-4	27.8968	0.5106	0.6766	0.0106	0.2989	0.0015	3415	18	3331	41	3465	8
KD-138-5	30.4792	0.5613	0.7242	0.0115	0.3070	0.0015	3502	18	3512	43	3506	8
KD-138-6	31.2138	0.5754	0.7261	0.0115	0.3125	0.0016	3526	18	3519	43	3533	8
KD-138-7	31.2767	0.5789	0.7231	0.0115	0.3138	0.0016	3528	19	3508	43	3540	8
KD-138-8(1)	31.4958	0.5821	0.7229	0.0115	0.3145	0.0016	3535	19	3507	43	3543	8
KD-138-8(2)	31.2985	0.5745	0.7218	0.0114	0.3137	0.0016	3528	18	3503	43	3539	8
KD-138-8(3)	31.6626	0.5802	0.7320	0.0115	0.3150	0.0016	3540	18	3541	43	3545	8
KD-138-9	31.4897	0.5807	0.7236	0.0115	0.3165	0.0016	3534	18	3509	43	3553	8
KD-138-10	31.3793	0.3573	0.7259	0.0074	0.3173	0.0020	3531	11	3518	28	3557	5
KD-138-11	31.9365	0.3627	0.7404	0.0076	0.3141	0.0019	3548	11	3572	28	3541	5
KD-138-12	26.9286	0.3167	0.6641	0.0071	0.2940	0.0018	3381	12	3283	28	3439	5
KD-138-13	27.3368	0.3190	0.6707	0.0072	0.2967	0.0018	3396	11	3308	28	3453	5
KD-138-14	27.5524	0.3195	0.6697	0.0070	0.2993	0.0019	3403	11	3305	27	3467	5
KD-138-15	30.6838	0.3502	0.7027	0.0072	0.3168	0.0019	3509	11	3431	27	3554	5
KD-138-16	28.8695	0.3480	0.6693	0.0074	0.3136	0.0019	3449	12	3303	29	3539	5
KD-138-17	26.9890	0.3056	0.6574	0.0068	0.2971	0.0018	3383	11	3257	27	3455	5
KD-138-18	29.6663	0.3376	0.6823	0.0069	0.3153	0.0019	3476	11	3353	27	3547	5
KD-138-19	29.3450	0.3325	0.6765	0.0069	0.3149	0.0019	3465	11	3331	27	3545	5
KD-138-20	30.2323	0.3419	0.6953	0.0071	0.3161	0.0019	3494	11	3403	27	3551	5
KD-138-21	25.3887	0.3270	0.6235	0.0075	0.2946	0.0018	3323	13	3124	30	3442	5
KD-138-22	28.9061	0.3334	0.7065	0.0074	0.2962	0.0019	3450	11	3445	28	3451	5
KD-138-23	29.5052	0.3332	0.7189	0.0074	0.2989	0.0018	3470	11	3492	28	3465	5
KD-138-24	26.1067	0.3241	0.6345	0.0074	0.2972	0.0018	3351	12	3167	29	3456	5
KD-138-25	28.1314	0.3319	0.6899	0.0074	0.2961	0.0018	3424	12	3382	28	3450	5
KD-138-26	26.1615	0.3366	0.6422	0.0077	0.2964	0.0019	3353	13	3198	30	3451	5
KD-138-27	27.5530	0.3186	0.6830	0.0071	0.2951	0.0019	3403	11	3356	27	3445	5
KD-138-28	27.5571	0.3225	0.6785	0.0071	0.2962	0.0018	3403	12	3339	27	3451	5
KD-138-29	26.5849	0.3154	0.6449	0.0069	0.3001	0.0018	3368	12	3208	27	3471	5

Appendix C2. *(Continued)*

	ISOTOPIC RATIOS						CALCULATED AGES Ma					
Analysis#	**$^{207}Pb/^{235}U$**	**± 1 sigma**	**$^{206}Pb/^{238}U$**	**± 1 sigma**	**$^{207}Pb/^{206}Pb$**	**± 1 sigma**	**$^{207}Pb/^{235}U$**	**± 1 sigma**	**$^{206}Pb/^{238}U$**	**± 1 sigma**	**$^{207}Pb/^{206}Pb$**	**± 1 sigma**
					Sample KD-176.08m							
KD2-176-1	30.2449	0.6160	0.6997	0.0077	0.3113	0.0028	3495	20	3419	29	3527	7
KD2-176-2(1)	28.9994	0.5875	0.7026	0.0076	0.2970	0.0027	3453	20	3430	29	3455	7
KD2-176-2(2)	29.2432	0.6009	0.7169	0.0120	0.2960	0.0030	3462	20	3485	45	3450	8
KD2-176-3	28.3408	0.5811	0.6824	0.0075	0.2992	0.0027	3431	20	3354	29	3466	7
KD2-176-4	30.3864	0.6231	0.7333	0.0082	0.2980	0.0027	3499	20	3546	31	3460	7
KD2-176-5	28.5741	0.5787	0.6901	0.0075	0.2995	0.0027	3439	20	3383	29	3468	7
KD2-176-6	29.0090	0.5949	0.6771	0.0077	0.3097	0.0028	3454	20	3333	30	3519	7
KD2-176-7	29.6231	0.6000	0.7202	0.0077	0.2989	0.0027	3474	20	3497	29	3464	7
KD2-176-8	28.8729	0.5828	0.7079	0.0077	0.2962	0.0027	3449	20	3450	29	3450	7
KD2-176-9	28.0765	0.5701	0.6857	0.0074	0.2982	0.0027	3422	20	3366	28	3461	7
KD2-176-10	29.1686	0.5894	0.7148	0.0077	0.2969	0.0027	3459	20	3477	29	3454	7
KD2-176-11	28.2199	0.5736	0.6928	0.0075	0.2977	0.0027	3427	20	3393	28	3458	7
KD2-176-12	26.6412	0.5499	0.6629	0.0077	0.2936	0.0026	3370	20	3278	30	3437	7
KD2-176-13	27.1774	0.5553	0.6688	0.0074	0.2966	0.0027	3390	20	3301	29	3453	7
KD2-176-14	30.2462	0.6149	0.7091	0.0077	0.3118	0.0028	3495	20	3455	29	3530	7
KD2-176-15	28.6854	0.5790	0.7097	0.0076	0.2970	0.0027	3443	20	3457	29	3455	7
KD2-176-16	29.1685	0.5989	0.7046	0.0117	0.2999	0.0031	3459	20	3438	44	3470	8
KD2-176-17	28.9239	0.1756	0.7044	0.0027	0.2967	0.0016	3451	6	3437	10	3453	4
KD2-176-18	29.2089	0.1616	0.7126	0.0020	0.2969	0.0016	3461	5	3468	7	3454	4
KD2-176-19	26.3150	0.3060	0.6466	0.0067	0.2944	0.0018	3358	11	3215	26	3441	5
KD2-176-20	27.3563	0.3111	0.6616	0.0068	0.2988	0.0019	3396	11	3273	26	3464	5
KD2-176-21	26.8220	0.3106	0.6560	0.0070	0.2977	0.0018	3377	11	3252	27	3458	5
KD2-176-22	26.2116	0.3063	0.6382	0.0068	0.2979	0.0018	3354	11	3182	27	3459	5
KD2-176-23	27.8092	0.3136	0.6725	0.0069	0.2998	0.0018	3412	11	3316	27	3469	5
KD2-176-24	27.7387	0.3198	0.6740	0.0070	0.2976	0.0018	3410	11	3321	27	3458	5
KD2-176-25	26.7778	0.3052	0.6462	0.0067	0.2989	0.0018	3375	11	3213	26	3465	5
KD2-176-26	27.8103	0.3359	0.6753	0.0073	0.2970	0.0019	3412	12	3326	28	3454	5
KD2-176-27	26.9412	0.3041	0.6529	0.0067	0.2989	0.0018	3381	11	3239	26	3465	5
KD2-176-28	27.8770	0.3144	0.6752	0.0070	0.2987	0.0018	3415	11	3326	27	3463	5
KD2-176-29	27.9952	0.3196	0.6815	0.0070	0.2977	0.0018	3419	11	3350	27	3458	5
KD2-176-30	27.7848	0.3141	0.6710	0.0069	0.2996	0.0018	3412	11	3310	27	3468	5
KD2-176-31	28.4959	0.3242	0.6806	0.0071	0.3021	0.0018	3436	11	3346	27	3481	5

Appendix D1. All chlorite electron microprobe analyses and calculated chlorite temperature estimates

	T37chl4	T37chl6	T37chl5	T37chl8	T37chl10	T37chl12	T37chl13	T37chl14	T37chl15	T37chl16	T37chl22	T37chl24	T37chl25	T37chl27	T37chl21	T37chl1
SiO_2	27.29	26.97	27.51	27.01	27.80	27.17	27.39	27.18	27.29	27.17	26.87	26.59	26.21	26.89	26.33	27.55
TiO_2	0.07	0.04	0.02	0.18	0.07	0.08	0.06	0.05	0.02	0.02	0.15	0.21	0.07	0.05	0.13	0.05
Al_2O_3	20.10	19.96	20.27	19.75	20.12	20.53	20.54	21.16	20.74	19.82	19.84	19.64	19.31	20.42	20.05	21.41
FeO	24.58	24.66	24.06	24.41	24.05	25.20	24.69	25.11	24.50	24.43	24.41	24.28	24.93	24.68	24.79	25.11
MnO	0.21	0.20	0.21	0.20	0.18	0.24	0.24	0.19	0.15	0.16	0.17	0.22	0.18	0.16	0.22	0.17
MgO	16.90	16.73	17.44	16.58	17.60	17.21	16.91	16.59	16.94	17.04	17.21	17.49	16.67	16.78	16.86	17.14
CaO	0.02	0.02	0.02	0.07	0.00	0.04	0.00	0.12	0.04	0.02	0.06	0.04	0.05	0.02	0.06	0.03
Na_2O	0.00	0.02	0.03	0.05	0.02	0.03	0.04	0.01	0.05	0.00	0.03	0.04	0.05	0.04	0.03	0.02
K_2O	0.01	0.01	0.01	0.03	0.02	0.03	0.00	0.01	0.02	0.01	0.03	0.02	0.02	0.01	0.03	0.03
Cr_2O_3	1.52	1.85	0.71	2.57	0.36	0.20	0.92	0.20	1.06	1.39	1.85	1.78	2.34	1.71	1.91	0.01
Structural formula calculated on the basis of 14 O																
Si	2.73	2.72	2.73	2.73	2.74	2.70	2.72	2.70	2.72	2.73	2.71	2.69	2.70	2.71	2.69	2.70
Al^{iv}	1.27	1.28	1.27	1.27	1.26	1.30	1.28	1.30	1.28	1.27	1.29	1.31	1.30	1.29	1.31	1.30
Al^{vi}	1.11	1.10	1.11	1.09	1.09	1.11	1.14	1.19	1.15	1.08	1.08	1.06	1.05	1.14	1.11	1.18
Mg	2.52	2.52	2.58	2.50	2.59	2.55	2.51	2.46	2.52	2.55	2.59	2.64	2.56	2.52	2.57	2.51
Fe^{2+}	1.32	1.33	1.25	1.27	1.17	1.47	1.37	1.52	1.38	1.29	1.34	1.39	1.48	1.43	1.60	1.50
Fe^{3+}	0.74	0.75	0.75	0.79	0.81	0.62	0.69	0.57	0.66	0.77	0.71	0.67	0.67	0.64	0.52	0.56
Sum other elmts	0.02	0.02	0.02	0.03	0.02	0.03	0.02	0.03	0.02	0.02	0.03	0.03	0.03	0.02	0.03	0.02
Oct Sum	5.71	5.72	5.71	5.68	5.68	5.78	5.72	5.77	5.73	5.71	5.75	5.78	5.79	5.75	5.83	5.77
XMg	0.66	0.65	0.67	0.66	0.69	0.63	0.65	0.62	0.65	0.66	0.66	0.65	0.63	0.64	0.62	0.63
XFe^{3+}	36	36	37	39	41	30	34	27	32	37	35	32	31	31	25	27
T (^{o}C) Vidal (2006)	280	280	280	272	269	314	285	302	288	281	298	321	319	297	348	307
T(^{o}C) Inoue (2009)	281	290	282	271	270	322	286	305	292	287	305	329	334	307	354	313
T(°C) H&V (1992)	305	312	307	302	300	321	309	320	314	307	314	318	320	318	323	320

Appendix D1. (continued)

	T37chl2	T37chl3	T37chl8	T37chl9	T37chl10	T37chl11	T37chl17	T37chl18	T37chl19b	T37chl20b	T37chl23	T37chl26	T37chl28	T37chl29	T37chl30	T37Chl31
SiO_2	26.08	27.14	27.01	27.57	27.80	27.56	27.79	27.64	27.44	26.88	26.32	26.36	26.41	27.38	26.32	28.11
TiO_2	0.22	0.13	0.18	0.20	0.07	0.07	0.09	0.04	0.03	0.21	0.12	0.11	0.07	0.04	0.13	0.08
Al_2O_3	19.75	19.99	19.75	20.85	20.12	20.22	19.43	20.87	20.41	19.82	20.10	19.60	20.01	21.19	20.27	19.79
FeO	24.85	24.45	24.41	24.18	24.05	24.55	24.24	24.03	24.39	24.31	24.37	24.51	24.56	24.30	24.52	23.99
MnO	0.17	0.17	0.20	0.21	0.18	0.15	0.19	0.17	0.22	0.19	0.23	0.11	0.17	0.26	0.22	0.21
MgO	16.92	16.49	16.58	16.87	17.60	17.61	17.89	17.36	17.33	16.97	17.15	17.51	17.46	16.36	16.60	17.98
CaO	0.07	0.05	0.07	0.24	0.00	0.03	0.01	0.02	0.02	0.03	0.01	0.05	0.05	0.03	0.06	0.03
Na_2O	0.04	0.00	0.05	0.01	0.02	0.05	0.01	0.05	0.01	0.00	0.05	0.03	0.03	0.03	0.07	0.02
K_2O	0.04	0.01	0.03	0.03	0.02	0.02	0.02	0.02	0.02	0.01	0.01	0.02	0.01	0.03	0.03	0.02
Cr_2O_3	2.44	2.03	2.57	0.94	0.36	0.20	1.01	0.55	1.08	1.82	2.01	2.51	2.02	1.71	2.36	0.30
Structural formula calculated on the basis of 14 O																
Si	2.69	2.73	2.73	2.72	2.74	2.72	2.75	2.72	2.72	2.72	2.70	2.70	2.69	2.73	2.69	2.75
Al^{iv}	1.31	1.27	1.27	1.28	1.26	1.28	1.25	1.28	1.28	1.29	1.31	1.30	1.31	1.27	1.31	1.25
Al^{vi}	1.10	1.12	1.09	1.16	1.09	1.08	1.02	1.15	1.11	1.09	1.13	1.07	1.10	1.22	1.14	1.04
Mg	2.60	2.48	2.50	2.48	2.59	2.59	2.64	2.55	2.56	2.56	2.62	2.67	2.65	2.43	2.53	2.62
Fe^{2+}	1.69	1.27	1.27	1.28	1.17	1.30	1.13	1.27	1.30	1.31	1.64	1.60	1.66	1.40	1.55	1.08
Fe^{3+}	0.45	0.79	0.79	0.72	0.81	0.73	0.87	0.71	0.73	0.74	0.44	0.50	0.44	0.63	0.55	0.88
Sum other elmts	0.03	0.02	0.03	0.05	0.02	0.02	0.02	0.02	0.02	0.02	0.03	0.02	0.02	0.03	0.03	0.02
Oct Sum	5.87	5.67	5.68	5.69	5.68	5.73	5.68	5.70	5.72	5.72	5.86	5.86	5.88	5.71	5.81	5.66
XMg	0.61	0.66	0.66	0.66	0.69	0.67	0.70	0.67	0.66	0.66	0.61	0.63	0.62	0.63	0.62	0.71
XFe^{3+}	21	39	39	36	41	36	44	36	36	36	21	24	21	31	26	45
T (^{o}C) Vidal (2006)	393	264	272	269	269	291	278	273	282	288	384	387	398	275	327	266
T(^{o}C) Inoue (2009)	390	267	271	263	270	295	276	279	289	291	383	398	410	269	330	263
T(°C) H&V (1992)	321	302	302	305	300	309	297	310	312	308	321	320	324	307	323	294

Appendix D1. (continued)

	T37chl32	T37chl33	T37test	T37test2	T37test3	T37test4	T37chlx2	T37chlx3	T37chlx4	T37chlx5	T37chlx6	T37chlx7	T37chlx8	T37chlx9	T37chlx10	T37chlx11
SiO_2	26.96	28.21	25.91	26.08	25.91	26.20	26.62	26.65	26.51	25.73	25.98	26.04	25.47	25.94	25.43	25.59
TiO_2	0.10	0.07	0.04	0.22	0.14	0.05	0.02	0.05	0.06	0.04	0.04	0.07	0.52	0.15	0.07	0.12
Al_2O_3	20.31	20.34	16.90	17.15	17.54	18.09	17.48	17.51	18.29	17.39	18.85	17.22	17.07	17.37	17.37	17.34
FeO	24.54	24.37	24.60	24.96	25.27	25.53	25.21	25.19	26.01	24.93	25.47	23.94	25.30	24.53	24.96	25.61
MnO	0.21	0.19	0.21	0.23	0.19	0.22	0.18	0.12	0.18	0.15	0.22	0.20	0.15	0.24	0.23	0.16
MgO	16.87	16.79	15.70	16.03	15.66	15.64	16.15	15.91	15.39	15.81	15.52	16.50	15.44	16.33	16.22	15.68
CaO	0.75	0.03	0.47	0.17	0.08	0.13	0.05	0.12	0.02	0.06	0.01	0.02	0.12	0.07	0.06	0.07
Na_2O	0.01	0.04	0.05	0.10	0.03	0.02	0.06	0.04	0.01	0.02	0.01	0.01	0.10	0.06	0.04	0.04
K_2O	0.02	0.01	0.00	0.00	0.00	0.00	0.00	0.00	0.00	0.00	0.00	0.00	0.00	0.00	0.00	0.00
Cr_2O_3	1.36	1.28	1.10	2.50	2.44	0.69	0.61	1.20	1.30	1.99	1.18	1.87	2.48	2.50	2.63	2.20
Structural formula calculated on the basis of 14 O																
Si	2.70	2.77	2.77	2.75	2.74	2.74	2.77	2.78	2.75	2.75	2.72	2.76	2.72	2.74	2.72	2.73
Al^{iv}	1.30	1.23	1.23	1.25	1.26	1.26	1.23	1.22	1.25	1.25	1.28	1.24	1.28	1.26	1.28	1.27
Al^{vi}	1.11	1.13	0.90	0.90	0.94	0.97	0.92	0.94	1.00	0.94	1.06	0.92	0.92	0.91	0.91	0.92
Mg	2.52	2.46	2.50	2.52	2.47	2.44	2.51	2.48	2.38	2.52	2.43	2.61	2.46	2.57	2.58	2.49
Fe^{2+}	1.45	1.13	1.21	1.21	1.30	1.32	1.21	1.21	1.33	1.31	1.48	1.17	1.31	1.19	1.37	1.37
Fe^{3+}	0.61	0.87	0.99	0.99	0.94	0.92	0.99	0.99	0.93	0.91	0.75	0.96	0.95	0.97	0.86	0.91
Sum other elmts	0.10	0.02	0.08	0.05	0.03	0.04	0.03	0.03	0.02	0.02	0.02	0.02	0.04	0.04	0.03	0.03
Oct Sum	5.79	5.61	5.67	5.67	5.68	5.68	5.66	5.64	5.66	5.70	5.74	5.68	5.68	5.68	5.75	5.72
XMg	0.64	0.68			0.66	0.65			0.64	0.66	0.62		0.65	0.68	0.65	0.65
XFe^{3+}	30	44	45	45	42	41	45	45	41	41	34	45	42	45	39	40
T (°C) Vidal (2006)	318	242	304	305	285	278	296	292	269	292	293	295	296	293	313	297
T(°C) Inoue (2009)	291	238	265	275	283	280	269	260	270	293	302	281	285	287	327	306
T(°C) H&V (1992)	319	286	289	290	296	301	286	281	294	299	310	289	290	298	312	305

Appendix D1. (continued)

	T37chlx12	T37chlx13	T37chlx14	T37chlx15	T37chlx16	T37chlx17	T37chlx18	T37chlx19	T37chlx20	T37chlx21	T37chlx22	T37chlx23	T37chlx24	T37chlx25	T37chlx26	T37chlx27
SiO_2	25.92	25.92	25.96	26.32	25.91	25.77	24.92	25.17	26.07	26.47	25.11	25.46	25.39	25.34	25.57	26.29
TiO_2	0.05	0.12	0.06	0.06	0.29	0.19	0.05	0.18	0.15	0.09	0.05	0.05	0.14	0.48	0.08	0.07
Al_2O_3	17.93	17.44	17.38	17.54	18.05	17.89	17.67	17.65	18.95	18.68	18.92	18.46	18.13	17.97	17.98	18.84
FeO	25.10	25.02	25.33	24.70	25.29	25.41	25.07	25.04	24.83	24.80	24.36	25.29	24.57	25.77	24.74	25.38
MnO	0.18	0.22	0.20	0.14	0.18	0.22	0.16	0.19	0.14	0.19	0.18	0.21	0.17	0.18	0.18	0.21
MgO	16.06	15.48	15.79	14.72	16.23	16.17	15.58	16.23	15.17	15.72	15.85	15.98	16.21	15.89	16.43	16.16
CaO	0.05	0.05	0.05	0.13	0.06	0.01	0.11	0.08	0.06	0.07	0.18	0.09	0.06	0.06	0.05	0.04
Na_2O	0.02	0.01	0.01	0.07	0.02	0.02	0.06	0.04	0.06	0.05	0.04	0.03	0.01	0.04	0.02	0.02
K_2O	0.00	0.00	0.00	0.00	0.00	0.00	0.00	0.00	0.00	0.00	0.00	0.00	0.00	0.00	0.00	0.00
Cr_2O_3	2.28	2.71	1.93	1.59	2.33	2.36	1.76	2.09	2.11	1.85	1.24	2.02	2.48	2.31	2.03	1.03
Structural formula calculated on the basis of 14 O																
Si	2.73	2.76	2.75	2.81	2.71	2.71	2.70	2.70	2.74	2.75	2.70	2.70	2.70	2.68	2.71	2.72
Al^{iv}	1.27	1.24	1.25	1.19	1.29	1.29	1.30	1.30	1.26	1.25	1.30	1.30	1.30	1.32	1.29	1.28
Al^{vi}	0.96	0.96	0.93	1.01	0.96	0.95	0.97	0.94	1.09	1.04	1.10	1.01	0.99	0.95	0.96	1.02
Mg	2.52	2.46	2.49	2.34	2.53	2.54	2.52	2.59	2.37	2.43	2.54	2.53	2.57	2.50	2.59	2.49
Fe^{2+}	1.33	1.29	1.30	1.21	1.36	1.41	1.54	1.49	1.37	1.27	1.76	1.58	1.43	1.46	1.40	1.41
Fe^{3+}	0.88	0.94	0.94	0.99	0.85	0.83	0.74	0.75	0.81	0.88	0.43	0.67	0.76	0.82	0.79	0.79
Sum other elmts	0.02	0.03	0.02	0.03	0.02	0.02	0.03	0.03	0.03	0.03	0.04	0.03	0.02	0.03	0.02	0.02
Oct Sum	5.71	5.67	5.69	5.59	5.73	5.75	5.80	5.80	5.67	5.66	5.88	5.81	5.77	5.76	5.77	5.73
XMg	0.66	0.66	0.66		0.65	0.64	0.62	0.63	0.63	0.66	0.59	0.62	0.64	0.63	0.65	0.64
XFe^{3+}	40	42	42	45	39	37	32	34	37	41	20	30	35	36	36	36
T (°C) Vidal (2006)	290	283	291	270	300	308	328	336	266	265	403	335	314	310	315	293
T(°C) Inoue (2009)	301	273	288	231	309	320	346	355	267	264	391	352	332	331	334	304
T(°C) H&V (1992)	307	289	296	268	307	309	320	319	299	296	321	322	317	316	316	311

Appendix D1. (continued)

	T41-chl5	T41-chl6	T41ar2chl1	T41ar2chl5	T41cr2	T41cr3	T41a1	T41b5	T41b8	T41b10	T41a7	T41a8	T41-Y4	T41-Y5	T41-Y8	T41-Y10
SiO_2	28.18	28.59	27.95	28.01	28.02	27.75	26.79	27.43	28.78	28.89	28.08	27.06	27.83	27.42	28.35	29.19
TiO_2	0.24	0.09	0.05	0.22	0.05	0.03	0.09	0.03	0.02	0.05	0.04	0.16	0.02	0.03	0.04	0.07
Al_2O_3	18.93	19.09	18.40	18.52	19.04	19.58	18.04	19.47	20.10	19.43	19.03	18.52	18.72	19.51	19.66	19.96
FeO	23.99	24.14	23.86	23.67	23.56	23.99	24.37	24.44	24.12	23.18	24.83	24.02	23.76	23.62	23.89	22.96
MnO	0.21	0.18	0.20	0.20	0.20	0.13	0.18	0.16	0.13	0.25	0.21	0.22	0.23	0.20	0.16	0.19
MgO	18.05	18.45	19.37	18.21	18.71	18.26	18.36	17.44	17.93	18.39	18.05	16.83	18.53	18.11	18.82	18.79
CaO	0.04	0.03	0.05	0.04	0.08	0.07	0.05	0.04	0.03	0.21	0.05	0.06	0.04	0.09	0.03	0.05
Na_2O	0.02	0.05	0.02	0.03	0.02	0.03	0.02	0.06	0.04	0.04	0.03	0.02	0.02	0.00	0.04	0.03
K_2O	0.02	0.01	0.02	0.02	0.01	0.01	0.02	0.02	0.01	0.03	0.01	0.02	0.01	0.00	0.00	0.01
Cr_2O_3	1.56	1.82	2.65	2.08	0.04	0.41	1.69	0.54	0.58	0.03	1.49	1.57	0.78	0.66	0.13	0.03
Structural formula calculated on the basis of 14 O																
Si	2.77	2.78	2.75	2.78	2.76	2.74	2.72	2.74	2.78	2.80	2.76	2.76	2.76	2.73	2.75	2.79
Al^{iv}	1.23	1.22	1.25	1.22	1.24	1.26	1.28	1.26	1.22	1.20	1.24	1.24	1.24	1.27	1.25	1.21
Al^{vi}	0.98	0.97	0.89	0.96	0.97	1.02	0.89	1.03	1.07	1.02	0.96	1.00	0.95	1.03	1.00	1.05
Mg	2.65	2.67	2.84	2.69	2.74	2.69	2.78	2.60	2.58	2.66	2.64	2.56	2.74	2.69	2.72	2.68
Fe^{2+}	0.99	0.98	1.04	0.98	1.03	1.17	1.22	1.20	1.03	0.90	1.10	1.11	1.04	1.16	1.05	0.88
Fe^{3+}	0.99	0.98	0.92	0.98	0.91	0.81	0.85	0.84	0.92	0.98	0.94	0.94	0.93	0.81	0.89	0.96
Sum other elmts	0.02	0.02	0.03	0.03	0.03	0.02	0.02	0.02	0.02	0.05	0.03	0.03	0.03	0.03	0.02	0.02
Oct Sum	5.62	5.63	5.72	5.63	5.68	5.71	5.77	5.69	5.62	5.60	5.67	5.64	5.68	5.71	5.68	5.60
XMg	0.73	0.73	0.73	0.73	0.73	0.70	0.69	0.68	0.71	0.75	0.71	0.70	0.72	0.70	0.72	0.75
XFe^{3+}	50	50	47	50	47	41	41	41	47	52	46	46	47	41	46	52
T (^oC) Vidal (2006)	279	280	311	288	286	291	326	279	252	265	282	270	290	289	279	256
T(^oC) Inoue (2009)	253	255	304	257	276	290	337	282	244	232	275	258	280	291	278	234
T(°C) H&V (1992)	280	281	297	277	293	302	309	303	283	273	293	287	293	306	297	274

Appendix D1. (continued)

	T42-chl7	T45-chl16	T45-chl17	T42-chlmg	T42-chlmg3	T42-chlmg5	T42b1	T42b2	T43b3	T43mga1	T43mga2	T42test	T42test3	T42test4
SiO_2	28.11	28.78	28.74	28.77	27.75	28.52	28.28	27.64	27.33	28.34	28.54	28.76	28.80	28.22
TiO_2	0.05	0.04	0.04	0.06	0.00	0.05	0.04	0.05	0.02	0.05	0.03	0.00	0.05	0.06
Al_2O_3	17.59	18.96	19.14	21.28	20.26	21.05	19.02	18.89	18.90	18.90	18.84	18.72	19.35	19.27
FeO	21.82	22.15	21.97	21.63	21.58	22.04	22.03	21.88	21.85	21.70	22.45	22.25	22.19	22.14
MnO	0.17	0.21	0.16	0.21	0.22	0.16	0.21	0.19	0.22	0.20	0.22	0.19	0.28	0.15
MgO	20.01	19.08	19.63	19.59	19.31	19.40	19.70	20.00	19.83	20.39	20.36	20.27	19.87	19.92
CaO	0.08	0.12	0.14	0.03	0.03	0.01	0.05	0.11	0.15	0.03	0.09	0.01	0.02	0.12
Na_2O	0.02	0.03	0.03	0.01	0.05	0.01	0.01	0.05	0.05	0.00	0.04	0.00	0.04	0.05
K_2O	0.01	0.02	0.00	0.02	0.01	0.02	0.02	0.02	0.02	0.01	0.01	0.02	0.01	0.00
Cr_2O_3	2.68	1.46	1.71	0.42	0.66	0.59	1.13	1.07	0.67	0.40	0.33	1.16	0.79	0.93
Structural formula calculated on the basis of 14 O														
Si	2.80	2.81	2.79	2.74	2.73	2.74	2.77	2.73	2.72	2.76	2.76	2.78	2.77	2.75
Al^{iv}	1.20	1.19	1.21	1.26	1.27	1.26	1.23	1.27	1.28	1.24	1.24	1.22	1.23	1.25
Al^{vi}	0.86	0.99	0.98	1.14	1.08	1.13	0.96	0.94	0.95	0.93	0.91	0.92	0.97	0.96
Mg	2.97	2.77	2.84	2.78	2.83	2.78	2.87	2.95	2.95	2.96	2.94	2.92	2.85	2.89
Fe^{2+}	0.82	0.81	0.80	0.95	1.02	1.02	0.87	0.93	1.01	0.82	0.87	0.81	0.80	0.88
Fe^{3+}	1.00	0.99	0.98	0.77	0.75	0.75	0.94	0.88	0.81	0.95	0.94	0.99	0.98	0.92
Sum other elmts	0.03	0.03	0.03	0.02	0.03	0.02	0.02	0.03	0.04	0.02	0.03	0.02	0.03	0.03
Oct Sum	5.67	5.60	5.63	5.67	5.72	5.69	5.66	5.73	5.76	5.68	5.69	5.66	5.64	5.68
XMg	0.78	0.77	0.78	0.74	0.73	0.73	0.77	0.76	0.75	0.78	0.77	0.78	0.78	0.77
XFe^{3+}	55	55	55	45	42	42	52	49	45	54	52	55	55	51
T (^{o}C) Vidal (2006)	348	286	281	266	289	276	286	306	318	296	303	306	283	289
T(^{o}C) Inoue (2009)	274	237	250	262	287	273	270	304	317	282	286	271	258	281
T(°C) H&V (1992)	274	269	279	300	308	302	289	306	310	292	293	283	286	298

Appendix D1. (continued)

	T44chl1	T44chl3	T44chl5	T44chl10	T44chl12	T44chl13	T44chl16	T44chl17	T44chl18	T44chl20	T44ar2chl1	T44ar2chl2	T44ar2chl4	T44ar2chl6	T44ar2chl7	T44ar2chl8
SiO_2	27.88	27.39	28.49	27.29	27.13	27.29	27.62	27.93	27.40	27.72	27.54	27.89	27.68	27.47	27.67	28.04
TiO_2	0.13	0.21	0.08	0.06	0.04	0.05	0.06	0.02	0.11	0.02	0.07	0.04	0.07	0.04	0.09	0.00
Al_2O_3	22.28	20.88	20.99	21.51	22.15	21.35	20.85	21.07	21.27	21.20	21.72	21.28	21.53	21.30	20.66	20.91
FeO	19.44	19.60	19.38	20.29	19.48	19.93	20.26	20.45	20.26	19.28	20.24	20.13	20.48	19.97	20.23	19.70
MnO	0.19	0.14	0.14	0.16	0.15	0.20	0.15	0.13	0.11	0.18	0.19	0.18	0.11	0.18	0.14	0.12
MgO	19.39	19.03	20.83	19.75	19.79	18.11	20.24	19.98	19.95	20.43	20.39	20.13	19.83	20.47	20.82	20.15
CaO	0.20	1.24	0.14	0.16	0.17	0.12	0.11	0.14	0.13	0.10	0.12	0.14	0.12	0.12	0.13	0.08
Na_2O	0.03	0.07	0.03	0.04	0.03	0.05	0.06	0.06	0.05	0.03	0.04	0.06	0.05	0.05	0.04	0.03
K_2O	0.04	0.07	0.06	0.05	0.04	0.06	0.09	0.06	0.07	0.09	0.05	0.08	0.05	0.07	0.05	0.05
Cr_2O_3	0.21	0.73	0.42	1.04	0.76	0.84	0.78	0.86	0.97	0.65	0.45	0.32	0.53	0.41	0.32	0.36
Structural formula calculated on the basis of 14 O																
Si	2.72	2.71	2.74	2.70	2.70	2.74	2.71	2.72	2.70	2.72	2.70	2.71	2.70	2.71	2.70	2.74
Al^{iv}	1.28	1.29	1.26	1.30	1.30	1.26	1.29	1.28	1.30	1.28	1.30	1.29	1.30	1.29	1.30	1.26
Al^{vi}	1.28	1.16	1.12	1.22	1.30	1.27	1.12	1.14	1.17	1.17	1.21	1.16	1.19	1.18	1.09	1.14
Mg	2.82	2.81	2.98	2.92	2.93	2.71	2.96	2.90	2.93	2.98	2.98	2.92	2.89	3.01	3.03	2.93
Fe^{2+}	1.03	0.98	0.80	1.31	1.40	1.05	1.04	1.00	1.15	0.99	1.33	1.03	1.13	1.28	1.06	0.89
Fe^{3+}	0.55	0.64	0.76	0.38	0.22	0.62	0.62	0.66	0.52	0.59	0.33	0.61	0.54	0.37	0.60	0.72
Sum other elmts	0.04	0.15	0.03	0.04	0.04	0.04	0.04	0.03	0.03	0.03	0.04	0.04	0.03	0.04	0.03	0.02
Oct Sum	5.72	5.74	5.69	5.85	5.89	5.68	5.77	5.74	5.80	5.76	5.88	5.76	5.78	5.87	5.80	5.70
XMg	0.73	0.74	0.79	0.69	0.68	0.72	0.74	0.74	0.72	0.75	0.69	0.74	0.72	0.70	0.74	0.77
XFe^{3+}	35	40	49	22	14	37	37	40	31	37	20	37	32	22	36	45
T (^{o}C) Vidal (2006)	284	297	279	378	414	266	318	297	333	311	407	306	318	403	340	281
T(^{o}C) Inoue (2009)	267	252	269	351	379	252	311	291	324	300	381	295	311	374	335	275
T(°C) H&V (1992)	311	312	302	320	323	303	318	313	321	315	322	315	319	319	319	306

Appendix D1. (continued)

	T44ar2chl9	T44ar2chl10	T44ar2chl11	T44ar2chl13	T44ar2chl14	T44ar2chl19	T44ar2chl20	T44ar2chl21	T44ar2chl24	T44ar2chl27	T44chl7	T44chl13	T45A20	T46chlB8	T46chlB11	T46chlD16
SiO_2	27.94	27.57	28.25	27.86	27.77	27.82	27.38	27.65	27.31	27.24	27.25	28.80	27.58	28.98	28.61	27.68
TiO_2	0.03	0.01	0.02	0.01	0.02	0.03	0.02	0.04	0.04	0.04	0.09	0.06	0.06	0.07	0.05	0.08
Al_2O_3	21.15	20.83	20.87	21.07	21.00	20.90	20.78	20.74	20.57	21.01	21.16	20.35	17.89	19.84	19.96	18.31
FeO	20.26	20.19	20.02	20.22	19.99	20.49	20.05	20.06	20.08	20.63	20.16	20.34	19.93	20.20	20.29	20.26
MnO	0.13	0.14	0.15	0.15	0.17	0.15	0.17	0.17	0.21	0.19	0.12	0.15	0.12	0.13	0.14	0.08
MgO	20.92	20.45	20.81	20.70	20.27	20.29	20.32	19.86	20.35	20.01	19.44	19.46	22.09	21.36	20.92	21.38
CaO	0.11	0.10	0.12	0.17	0.14	0.17	0.21	0.26	0.48	0.23	0.10	0.09	0.09	0.03	0.03	0.04
Na_2O	0.03	0.03	0.04	0.06	0.04	0.05	0.05	0.03	0.08	0.04	0.07	0.06	0.01	0.04	0.00	0.03
K_2O	0.05	0.06	0.07	0.08	0.05	0.07	0.07	0.05	0.09	0.08	0.05	0.06	0.01	0.04	0.02	0.03
Cr_2O_3	0.34	0.40	0.40	0.38	0.34	0.40	0.39	0.38	0.32	0.55	0.89	1.07	1.82	0.27	0.22	2.27
Structural formula calculated on the basis of 14 O																
Si	2.71	2.71	2.73	2.71	2.72	2.71	2.70	2.72	2.71	2.70	2.71	2.79	2.73	2.77	2.75	2.74
Al^{iv}	1.29	1.29	1.27	1.29	1.28	1.29	1.30	1.28	1.29	1.30	1.29	1.21	1.27	1.24	1.25	1.26
Al^{vi}	1.12	1.12	1.10	1.12	1.14	1.12	1.12	1.13	1.11	1.16	1.19	1.11	0.83	1.00	1.02	0.88
Mg	3.02	3.00	2.99	3.00	2.96	2.95	2.99	2.91	3.01	2.96	2.88	2.81	3.26	3.04	3.00	3.15
Fe^{2+}	1.09	1.10	0.93	1.09	1.03	1.05	1.12	1.00	1.23	1.33	1.11	0.74	0.74	0.73	0.76	0.75
Fe^{3+}	0.55	0.56	0.68	0.55	0.61	0.62	0.53	0.66	0.43	0.38	0.56	0.91	0.91	0.89	0.87	0.92
Sum other elmts	0.03	0.03	0.03	0.04	0.04	0.04	0.05	0.05	0.08	0.05	0.03	0.03	0.02	0.02	0.02	0.02
Oct Sum	5.81	5.81	5.74	5.81	5.77	5.77	5.82	5.74	5.87	5.88	5.77	5.60	5.76	5.67	5.67	5.73
XMg	0.73	0.73	0.76	0.73	0.74	0.74	0.73	0.75	0.71	0.69	0.72	0.79	0.81	0.81	0.80	0.81
XFe^{3+}	34	34	42	34	37	37	32	40	26	22	34	55	55	55	54	55
T (^oC) Vidal (2006)	342	340	304	341	314	318	348	303	404	405	312	245	343	286	280	319
T(^oC) Inoue (2009)	338	333	295	328	303	309	332	287	343	371	304	230	344	269	273	317
T(°C) H&V (1992)	320	319	310	319	315	317	321	311	318	322	318	278	305	289	295	301

Appendix D1. (continued)

	T59-18	T59-20	T59-21	T59-27	T59-28	T59-29	T59-36	T59-37	T59-38	T59-39	T59-43	T59-44	T59-4	T59-6	T59-9	T59-23
SiO_2	28.82	28.59	28.75	28.51	27.91	28.23	28.45	28.59	28.98	29.25	28.14	28.27	28.05	28.92	28.73	28.57
TiO_2	0.06	0.02	0.04	0.02	0.00	0.01	0.00	0.02	0.02	0.03	0.09	0.04	0.08	0.04	0.66	0.03
Al_2O_3	22.26	22.00	21.96	20.83	21.70	22.61	22.10	22.64	23.15	22.99	20.57	23.25	22.71	21.63	21.81	22.93
FeO	16.79	17.70	16.77	16.46	17.16	17.41	19.26	17.21	16.79	16.42	16.92	17.27	17.48	17.02	16.64	17.13
MnO	0.23	0.20	0.21	0.17	0.21	0.20	0.19	0.15	0.24	0.15	0.20	0.19	0.17	0.22	0.12	0.19
MgO	22.80	22.98	23.25	23.52	22.80	22.23	21.09	22.60	22.51	22.20	23.03	22.26	22.27	22.96	21.98	21.95
CaO	0.08	0.09	0.38	0.07	0.01	0.04	0.09	0.12	0.11	0.04	0.09	0.08	0.03	0.03	0.03	0.13
Na_2O	0.04	0.00	0.04	0.00	0.04	0.03	0.04	0.06	0.09	0.07	0.05	0.05	0.02	0.04	0.02	0.03
K_2O	0.02	0.02	0.01	0.01	0.01	0.01	0.02	0.04	0.03	0.03	0.02	0.01	0.01	0.01	0.02	0.01
Cr_2O_3	0.06	0.00	0.04	0.01	0.02	0.07	0.01	0.03	0.00	0.01	0.11	0.10	0.14	0.17	0.15	0.12
Structural formula calculated on the basis of 14 O																
Si	2.72	2.71	2.71	2.72	2.70	2.71	2.71	2.71	2.71	2.74	2.72	2.70	2.70	2.73	2.72	2.71
Al^{iv}	1.28	1.29	1.29	1.28	1.30	1.29	1.29	1.29	1.29	1.26	1.28	1.30	1.30	1.27	1.28	1.29
Al^{vi}	1.19	1.17	1.15	1.07	1.18	1.27	1.20	1.23	1.27	1.28	1.06	1.32	1.27	1.14	1.21	1.28
Mg	3.20	3.25	3.27	3.35	3.29	3.18	3.00	3.19	3.14	3.10	3.31	3.17	3.19	3.23	3.11	3.11
Fe^{2+}	0.75	1.00	0.80	0.63	1.05	1.12	0.98	0.94	0.84	0.68	0.70	1.17	1.16	0.68	0.59	0.90
Fe^{3+}	0.58	0.40	0.53	0.69	0.34	0.28	0.55	0.42	0.47	0.61	0.66	0.20	0.24	0.67	0.73	0.46
Sum other elmts	0.03	0.03	0.06	0.02	0.02	0.02	0.03	0.03	0.04	0.02	0.03	0.03	0.02	0.03	0.02	0.03
Oct Sum	5.75	5.85	5.80	5.76	5.89	5.87	5.77	5.82	5.77	5.69	5.78	5.89	5.89	5.73	5.65	5.78
XMg	0.81	0.76	0.80	0.84	0.76	0.74	0.75	0.77	0.79	0.82	0.82	0.73	0.73	0.83	0.84	0.77
XFe^{3+}	44	29	40	52	25	20	36	31	36	47	49	15	17	50	55	34
T (^oC) Vidal (2006)	309	392	344	319	419	407	312	349	315	272	330	417	421	302	266	318
T(^oC) Inoue (2009)	292	367	310	310	406	378	301	327	290	256	316	385	400	288	250	297
T(°C) H&V (1992)	313	317	317	311	322	318	316	320	316	303	312	323	323	308	288	317

Appendix D1. (continued)

	T59-40	T59-41	T59-7	T59-11	T59-12
SiO_2	27.60	28.87	28.24	28.94	29.22
TiO_2	0.19	0.11	0.06	0.09	0.13
Al_2O_3	21.70	21.00	22.12	21.07	21.40
FeO	17.53	16.72	17.27	16.68	16.54
MnO	0.19	0.18	0.18	0.21	0.23
MgO	22.25	23.20	22.62	23.30	23.30
CaO	0.04	0.03	0.03	0.06	0.03
Na_2O	0.03	0.02	0.00	0.06	0.00
K_2O	0.02	0.01	0.01	0.02	0.01
Cr_2O_3	0.13	0.20	0.19	0.25	0.19
Structural formula calculated on the basis of 14 O					
Si	2.69	2.74	2.71	2.74	2.74
Al^{iv}	1.31	1.26	1.29	1.26	1.26
Al^{vi}	1.20	1.09	1.21	1.09	1.12
Mg	3.23	3.28	3.23	3.28	3.26
Fe^{2+}	1.09	0.60	0.99	0.59	0.58
Fe^{3+}	0.34	0.73	0.39	0.73	0.71
Sum other elmts	0.02	0.02	0.02	0.03	0.02
Oct Sum	5.88	5.72	5.84	5.72	5.71
XMg	0.75	0.85	0.76	0.85	0.85
XFe^{3+}	24	55	28	55	55
T (^oC) Vidal (2006)	415	300	381	302	296
T(^oC) Inoue (2009)	391	284	362	283	273
T(°C) H&V (1992)	322	301	318	302	297

Appendix D1. (continued)

	P2-166-2	P2-166-3	P2-166-4	P2-166-5	P2-166-8	P2-166-10	P2-166-11	P2-166-12	P2-166-15	P2-166-19	P2-166-21	P2-166-29	P2-166-32	P2-166-33	P2-166-35	P2-166-36
SiO_2	27.74	27.36	27.56	27.31	27.78	27.26	27.13	28.58	27.48	27.49	28.30	27.91	27.22	28.01	26.74	25.96
TiO_2	0.00	0.00	0.00	0.00	0.00	0.02	0.00	0.07	0.00	0.01	0.01	0.04	0.03	0.04	0.00	0.04
Al_2O_3	18.98	18.91	19.16	19.45	18.82	19.24	19.02	18.37	19.08	18.64	18.73	19.02	19.52	18.85	18.88	19.25
FeO	24.32	23.63	23.77	24.33	23.85	24.02	24.46	24.12	24.37	23.97	23.97	25.06	24.64	25.16	23.64	23.94
MnO	0.00	0.00	0.00	0.00	0.00	0.00	0.00	0.00	0.00	0.00	0.00	0.00	0.00	0.00	0.00	0.00
MgO	17.24	17.06	17.30	17.00	18.09	17.49	16.99	17.45	17.37	16.97	18.01	16.78	16.89	17.47	16.94	16.74
CaO	0.11	0.28	0.36	0.20	0.16	0.17	0.21	0.14	0.26	0.25	0.23	0.15	0.16	0.17	0.41	0.40
Na_2O	0.02	0.01	0.00	0.05	0.02	0.01	0.00	0.08	0.00	0.08	0.00	0.00	0.03	0.00	0.00	0.01
K_2O	0.01	0.01	0.03	0.02	0.01	0.01	0.00	0.05	0.00	0.02	0.00	0.00	0.03	0.01	0.02	0.03
Cr_2O_3	0.00	0.00	0.00	0.00	0.00	0.00	0.00	0.00	0.00	0.00	0.00	0.00	0.00	0.00	0.00	0.00
Structural formula calculated on the basis of 14 O																
Si	2.78	2.77	2.76	2.75	2.77	2.74	2.75	2.83	2.75	2.78	2.79	2.78	2.74	2.77	2.74	2.70
Al^{iv}	1.22	1.23	1.24	1.25	1.23	1.26	1.25	1.17	1.25	1.22	1.21	1.22	1.26	1.23	1.26	1.30
Al^{vi}	1.01	1.03	1.03	1.05	0.97	1.03	1.02	0.98	1.01	1.01	0.97	1.02	1.06	0.97	1.03	1.07
Mg	2.57	2.58	2.59	2.55	2.68	2.63	2.57	2.58	2.60	2.56	2.65	2.49	2.53	2.58	2.59	2.60
Fe^{2+}	1.10	1.08	1.08	1.21	1.05	1.19	1.22	1.00	1.15	1.08	0.99	1.13	1.24	1.12	1.20	1.47
Fe^{3+}	0.94	0.92	0.92	0.84	0.93	0.83	0.85	1.00	0.89	0.95	0.99	0.96	0.83	0.96	0.83	0.62
Sum other elmts	0.01	0.03	0.04	0.03	0.02	0.02	0.02	0.03	0.03	0.04	0.02	0.02	0.02	0.02	0.05	0.05
Oct Sum	5.64	5.64	5.65	5.68	5.66	5.70	5.69	5.59	5.67	5.63	5.62	5.62	5.69	5.65	5.70	5.80
XMg	0.70	0.70	0.71	0.68	0.72	0.69	0.68	0.72	0.69	0.70	0.73	0.69	0.67	0.70	0.68	0.64
XFe^{3+}	46	46	46	41	47	41	41	50	44	47	50	46	40	46	41	30
T (^oC) Vidal (2006)	266	264	264	272	279	283	279	336	276	266	284	263	272	279	282	330
T(^oC) Inoue (2009)	257	253	255	271	271	283	278	228	272	248	250	248	277	265	274	328
T(°C) H&V (1992)	286	288	292	300	291	300	298	254	296	283	277	281	303	287	301	320

Appendix D1. (continued)

	P2-166-37	P2-166-38	P2-166-39
SiO_2	26.34	26.16	27.02
TiO_2	0.02	0.00	0.03
Al_2O_3	18.90	19.14	18.56
FeO	24.42	24.15	24.66
MnO	0.00	0.00	0.00
MgO	16.91	16.90	16.55
CaO	0.18	0.21	0.20
Na_2O	0.03	0.07	0.59
K_2O	0.02	0.03	0.02
Cr_2O_3	0.00	0.00	0.00
Structural formula calculated on the basis of 14 O			
Si	2.72	2.71	2.75
Al^{iv}	1.28	1.29	1.25
Al^{vi}	1.02	1.05	0.98
Mg	2.60	2.61	2.51
Fe^{2+}	1.35	1.42	1.19
Fe^{3+}	0.76	0.68	0.91
Sum other elmts	0.02	0.03	0.08
Oct Sum	5.75	5.78	5.68
XMg	0.66	0.65	0.68
XFe^{3+}	36	32	44
T (^{o}C) Vidal (2006)	303	318	279
T(^{o}C) Inoue (2009)	315	327	260
T(°C) H&V (1992)	314	318	297

Appendix D1. (continued)

	P2-183-1	P2-183-2	P2-183-5	P2-183-6	P2-183-7	P2-183-8	P2-183-10	P2-183-11	P2-183-13	P2-183-14	P2-183-15	P2-183-16	P2-183-17	P2-183-18	P2-183-21	P2-183-22
SiO_2	26.42	26.68	25.64	26.14	25.77	26.18	26.09	26.65	25.93	25.70	26.20	26.15	25.96	26.11	26.37	25.88
TiO_2	0.02	0.07	0.04	0.07	0.02	0.02	0.03	0.01	0.05	0.00	0.08	0.01	0.10	0.00	0.00	0.01
Al_2O_3	18.57	18.50	19.11	18.62	18.60	18.25	18.76	18.21	18.50	18.24	18.46	18.78	18.45	18.17	17.65	18.75
FeO	28.29	28.36	28.63	29.10	28.85	28.33	28.35	28.49	28.29	28.33	28.59	28.83	28.20	27.49	27.71	28.95
MnO	0.00	0.00	0.00	0.00	0.00	0.00	0.00	0.00	0.00	0.00	0.00	0.00	0.00	0.00	0.00	0.00
MgO	14.03	14.01	13.90	13.87	13.91	14.46	14.31	14.05	14.34	13.66	14.22	13.56	14.01	14.38	13.49	13.59
CaO	0.10	0.57	0.12	0.15	0.14	0.14	0.46	0.42	0.11	0.14	0.10	0.08	0.14	0.73	0.68	0.15
Na_2O	0.07	0.03	0.00	0.04	0.00	0.11	0.00	0.00	0.10	0.00	0.00	0.12	0.00	0.00	0.00	0.09
K_2O	0.03	0.02	0.00	0.02	0.01	0.01	0.02	0.03	0.02	0.00	0.01	0.02	0.01	0.01	0.00	0.05
Cr_2O_3	0.00	0.00	0.00	0.00	0.00	0.00	0.00	0.00	0.00	0.00	0.00	0.00	0.00	0.00	0.00	0.00
Structural formula calculated on the basis of 14 O																
Si	2.75	2.75	2.70	2.72	2.71	2.73	2.71	2.76	2.72	2.73	2.73	2.73	2.73	2.73	2.78	2.72
Al^{iv}	1.25	1.25	1.30	1.28	1.29	1.27	1.29	1.24	1.28	1.27	1.27	1.27	1.27	1.27	1.22	1.28
Al^{vi}	1.02	1.00	1.07	1.01	1.01	0.97	1.02	0.98	1.01	1.01	1.00	1.05	1.02	0.98	0.98	1.03
Mg	2.17	2.15	2.18	2.15	2.18	2.25	2.22	2.17	2.24	2.16	2.21	2.11	2.19	2.24	2.12	2.13
Fe^{2+}	1.57	1.54	1.86	1.72	1.75	1.61	1.70	1.56	1.71	1.67	1.62	1.71	1.65	1.54	1.47	1.75
Fe^{3+}	0.89	0.90	0.66	0.81	0.79	0.86	0.76	0.91	0.77	0.84	0.87	0.81	0.83	0.87	0.98	0.79
Sum other elmts	0.02	0.07	0.01	0.02	0.02	0.03	0.05	0.05	0.02	0.02	0.01	0.02	0.02	0.08	0.08	0.03
Oct Sum	5.67	5.67	5.79	5.72	5.75	5.72	5.75	5.67	5.75	5.71	5.70	5.71	5.71	5.71	5.63	5.73
XMg	0.58	0.58	0.54	0.56	0.55	0.58	0.57	0.58	0.57	0.56	0.58	0.55	0.57	0.59	0.59	0.55
XFe^{3+}	36	37	26	32	31	35	31	37	31	34	35	32	34	36	40	31
T (^{o}C) Vidal (2006)	267	269	310	285	292	285	297	273	300	278	277	276	281	285	270	283
T(^{o}C) Inoue (2009)	275	259	340	301	320	300	305	265	316	296	297	287	294	277	240	302
T(°C) H&V (1992)	300	296	323	310	319	308	316	293	313	309	307	306	306	307	281	315

Appendix D1. (continued)

	P2-183-23	P2-183-24	P2-183-25	P2-183-26	P2-183-27	P2-183-28	P2-183-29	P2-183-30	P2-183-31	P2-183-32	P2-183-33	P2-183-34	P2-183-37	P2-183-38	P2-183-39	P2-183-40
SiO_2	26.37	26.42	26.12	26.03	26.06	26.22	26.14	26.20	25.55	25.48	25.67	26.17	25.90	25.52	27.18	25.86
TiO_2	0.01	0.00	0.09	0.07	0.01	0.01	0.07	0.01	0.00	0.04	0.02	0.00	0.02	0.01	0.07	0.00
Al_2O_3	18.51	18.70	18.40	18.45	18.37	18.30	18.56	18.73	18.66	18.56	18.98	18.46	18.66	18.83	18.39	18.05
FeO	28.37	28.60	28.47	27.97	28.47	28.08	27.97	28.62	28.14	28.15	28.39	28.51	28.18	28.74	28.74	28.88
MnO	0.00	0.00	0.00	0.00	0.00	0.00	0.00	0.00	0.00	0.00	0.00	0.00	0.00	0.00	0.00	0.00
MgO	14.37	13.77	14.30	14.63	14.15	13.72	13.92	13.68	14.22	13.81	14.07	13.72	13.69	14.15	13.85	13.34
CaO	0.14	0.26	0.16	0.27	0.19	0.34	0.19	0.22	0.12	0.13	0.15	0.32	0.27	0.09	0.50	0.15
Na_2O	0.00	0.00	0.00	0.00	0.07	0.01	0.08	0.00	0.00	0.00	0.00	0.16	0.00	0.11	0.00	0.08
K_2O	0.03	0.01	0.01	0.02	0.03	0.04	0.04	0.01	0.03	0.00	0.01	0.03	0.03	0.02	0.01	0.04
Cr_2O_3	0.00	0.00	0.00	0.00	0.00	0.00	0.00	0.00	0.00	0.00	0.00	0.00	0.00	0.00	0.00	0.00
Structural formula calculated on the basis of 14 O																
Si	2.74	2.74	2.73	2.72	2.73	2.75	2.74	2.74	2.70	2.71	2.70	2.74	2.73	2.69	2.78	2.74
Al^{iv}	1.26	1.26	1.28	1.28	1.27	1.25	1.26	1.27	1.30	1.29	1.30	1.27	1.27	1.31	1.22	1.26
Al^{vi}	1.00	1.03	0.99	0.99	0.99	1.02	1.03	1.04	1.03	1.03	1.06	1.01	1.05	1.04	1.00	0.99
Mg	2.22	2.13	2.22	2.28	2.21	2.15	2.17	2.13	2.24	2.19	2.21	2.14	2.15	2.23	2.11	2.11
Fe^{2+}	1.60	1.61	1.65	1.62	1.66	1.58	1.59	1.66	1.78	1.73	1.85	1.62	1.69	1.91	1.47	1.66
Fe^{3+}	0.86	0.87	0.83	0.82	0.83	0.89	0.86	0.84	0.71	0.78	0.65	0.87	0.79	0.63	0.98	0.90
Sum other elmts	0.02	0.03	0.02	0.03	0.03	0.04	0.03	0.03	0.02	0.02	0.02	0.05	0.03	0.02	0.06	0.03
Oct Sum	5.70	5.68	5.72	5.74	5.72	5.67	5.68	5.69	5.78	5.74	5.79	5.69	5.71	5.82	5.62	5.69
XMg	0.58	0.57	0.57	0.58	0.57	0.58	0.58	0.56	0.56	0.56	0.54	0.57	0.56	0.54	0.59	0.56
XFe^{3+}	35	35	34	34	34	36	35	34	29	31	26	35	32	25	40	35
T (^{o}C) Vidal (2006)	278	266	288	293	286	268	270	271	309	288	316	272	279	334	264	271
T(^{o}C) Inoue (2009)	292	273	303	308	299	266	276	282	339	315	340	276	288	368	242	282
T(°C) H&V (1992)	305	302	308	313	310	297	303	306	322	318	321	306	308	327	282	304

Appendix D1. (continued)

	P2-183-41	P2-183-42	P2-183-43	P2-183-44	P2-183-45	P2-183-48	P2-183-49	P2-183-51	P2-183-52	P2-183-54	P2-183-55	P2-183-56
SiO_2	25.96	25.76	26.56	26.08	25.23	26.09	26.25	26.88	27.25	26.87	27.85	27.40
TiO_2	0.00	0.03	0.01	0.00	0.05	0.01	0.04	0.00	0.06	0.03	0.00	0.00
Al_2O_3	18.61	18.54	18.22	18.70	18.85	18.22	18.12	17.87	18.70	18.79	18.66	18.56
FeO	28.72	28.55	28.68	28.61	28.30	28.62	27.53	23.77	28.64	28.79	29.45	28.74
MnO	0.00	0.00	0.00	0.00	0.00	0.00	0.00	0.00	0.00	0.00	0.00	0.00
MgO	13.86	14.09	13.71	14.06	13.76	13.79	13.93	17.13	13.98	14.21	13.30	14.25
CaO	0.15	0.17	0.22	0.22	0.18	0.22	0.46	1.15	0.41	0.26	0.33	0.45
Na_2O	0.12	0.15	0.00	0.04	0.00	0.00	0.00	0.00	0.00	0.00	0.00	0.00
K_2O	0.05	0.03	0.01	0.04	0.01	0.01	0.02	0.02	0.03	0.03	0.01	0.00
Cr_2O_3	0.00	0.00	0.00	0.00	0.00	0.00	0.00	0.00	0.00	0.00	0.00	0.00
Structural formula calculated on the basis of 14 O												
Si	2.72	2.71	2.77	2.72	2.69	2.74	2.76	2.76	2.77	2.75	2.82	2.78
Al^{iv}	1.28	1.29	1.23	1.28	1.31	1.26	1.24	1.24	1.23	1.25	1.18	1.22
Al^{vi}	1.02	1.00	1.00	1.02	1.07	1.00	1.01	0.91	1.02	1.01	1.04	0.99
Mg	2.17	2.21	2.13	2.19	2.19	2.16	2.18	2.62	2.12	2.17	2.01	2.15
Fe^{2+}	1.74	1.73	1.57	1.72	1.90	1.63	1.53	1.10	1.46	1.58	1.49	1.46
Fe^{3+}	0.78	0.78	0.92	0.77	0.62	0.88	0.90	0.94	0.97	0.89	1.00	0.97
Sum other elmts	0.03	0.04	0.03	0.03	0.02	0.03	0.05	0.13	0.05	0.03	0.04	0.05
Oct Sum	5.74	5.76	5.65	5.74	5.81	5.69	5.67	5.70	5.62	5.67	5.57	5.63
XMg	0.55	0.56	0.57	0.56	0.53	0.57	0.59	0.70	0.59	0.58	0.57	0.60
XFe^{3+}	31	31	37	31	25	35	37	46	40	36	40	40
T (^{o}C) Vidal (2006)	290	297	266	292	323	275	271	298	257	269	264	264
T(^{o}C) Inoue (2009)	304	317	263	305	351	285	259	261	244	272	222	248
T(°C) H&V (1992)	313	319	290	312	325	303	292	296	286	298	265	286

Appendix D1. (continued)

	P9-23-2	P9-23-3	P9-23-4	P9-23-5	P9-23-7	P9-23-8	P9-23-9	P9-23-10	P9-23-11	P9-23-13	P9-23-14	P9-23-15	P9-23-20	P9-23-21	P9-23-22	P9-23-26
SiO_2	27.05	27.88	27.72	26.90	27.14	27.21	27.28	26.75	29.10	27.44	27.18	27.58	27.39	28.01	27.53	28.13
TiO_2	0.00	0.09	0.02	0.01	0.00	0.02	0.02	0.01	0.00	0.01	0.02	0.02	0.03	0.00	0.00	0.03
Al_2O_3	21.11	19.27	21.11	21.47	19.80	21.16	21.13	18.76	19.89	19.82	20.88	20.98	21.45	21.87	20.00	20.89
FeO	25.41	25.16	25.23	25.91	25.09	25.40	25.16	25.59	25.01	25.49	25.93	24.82	25.20	25.03	25.65	25.05
MnO	0.46	0.46	0.42	0.43	0.39	0.49	0.44	0.42	0.39	0.47	0.45	0.42	0.45	0.40	0.46	0.45
MgO	17.02	16.58	17.05	16.30	16.52	16.68	17.07	17.20	17.21	16.84	16.85	16.82	16.46	15.73	16.69	15.77
CaO	0.04	0.33	0.06	0.02	0.38	0.13	0.05	0.12	0.80	0.13	0.08	0.30	0.11	0.19	0.07	0.36
Na_2O	0.03	0.02	0.03	0.01	0.00	0.02	0.00	0.02	0.05	0.05	0.02	0.03	0.02	0.02	0.05	0.01
K_2O	0.01	0.01	0.00	0.00	0.02	0.03	0.01	0.00	0.03	0.02	0.01	0.00	0.01	0.02	0.03	0.02
Cr_2O_3	0.00	0.00	0.00	0.00	0.00	0.00	0.00	0.00	0.00	0.00	0.00	0.00	0.00	0.00	0.00	0.00
Structural formula calculated on the basis of 14 O																
Si	2.70	2.76	2.71	2.70	2.73	2.70	2.70	2.71	2.79	2.73	2.70	2.72	2.71	2.74	2.73	2.76
Al^{iv}	1.30	1.24	1.29	1.30	1.27	1.30	1.30	1.29	1.21	1.27	1.30	1.28	1.29	1.26	1.27	1.24
Al^{vi}	1.19	1.02	1.15	1.24	1.07	1.17	1.17	0.95	1.03	1.05	1.14	1.16	1.21	1.27	1.07	1.18
Mg	2.53	2.45	2.49	2.44	2.47	2.47	2.52	2.60	2.46	2.50	2.49	2.47	2.43	2.30	2.47	2.31
Fe^{2+}	1.78	1.15	1.43	1.92	1.35	1.59	1.57	1.39	1.06	1.36	1.65	1.41	1.54	1.42	1.36	1.27
Fe^{3+}	0.34	0.94	0.64	0.26	0.76	0.52	0.51	0.78	0.94	0.76	0.51	0.63	0.54	0.64	0.77	0.79
Sum other elmts	0.05	0.08	0.04	0.04	0.08	0.06	0.04	0.05	0.12	0.06	0.05	0.07	0.05	0.06	0.05	0.08
Oct Sum	5.89	5.63	5.75	5.90	5.72	5.80	5.81	5.78	5.62	5.73	5.83	5.74	5.77	5.67	5.72	5.63
XMg	0.59	0.68	0.64	0.56	0.65	0.61	0.62	0.65	0.70	0.65	0.60	0.64	0.61	0.62	0.64	0.65
XFe^{3+}	16	45	31	12	36	25	25	36	47	36	24	31	26	31	36	39
T (^oC) Vidal (2006)	405	261	293	420	286	323	330	319	259	291	344	293	303	258	285	243
T(^oC) Inoue (2009)	383	243	291	397	276	314	325	325	223	283	339	278	293	242	279	228
T(°C) H&V (1992)	323	288	316	323	311	324	323	317	279	309	325	314	319	301	308	291

Appendix D1. (continued)

	P9-23-28	P9-23-29	P9-23-30	P9-23-31	P9-23-32	P9-23-33	P9-23-34	P9-23-35	P9-23-36	P9-23-37	P9-23-39	P9-23-41
SiO_2	25.72	26.49	27.15	26.93	27.20	27.65	26.46	27.03	27.54	27.96	27.06	27.61
TiO_2	0.00	0.03	0.02	0.02	0.04	0.02	0.04	0.01	0.00	0.01	0.03	0.00
Al_2O_3	18.53	18.54	20.91	21.09	20.99	19.30	19.09	20.59	19.92	21.28	21.50	20.46
FeO	25.44	24.83	24.74	25.58	25.40	25.43	25.94	25.53	24.80	25.14	24.58	24.48
MnO	0.51	0.43	0.48	0.41	0.45	0.43	0.44	0.44	0.49	0.43	0.44	0.44
MgO	16.03	17.13	17.27	16.86	17.04	16.95	16.62	16.31	16.87	16.15	16.74	16.92
CaO	0.10	0.27	0.08	0.05	0.08	0.33	0.08	0.07	0.27	0.34	0.06	0.63
Na_2O	0.02	0.00	0.01	0.00	0.00	0.04	0.03	0.00	0.03	0.03	0.00	0.00
K_2O	0.01	0.02	0.01	0.01	0.03	0.01	0.03	0.03	0.01	0.04	0.01	0.03
Cr_2O_3	0.00	0.00	0.00	0.00	0.00	0.00	0.00	0.00	0.00	0.00	0.00	0.00
Structural formula calculated on the basis of 14 O												
Si	2.71	2.72	2.70	2.70	2.70	2.74	2.70	2.71	2.74	2.74	2.70	2.73
Al^{iv}	1.29	1.28	1.30	1.30	1.30	1.26	1.30	1.29	1.26	1.26	1.30	1.27
Al^{vi}	1.00	0.96	1.15	1.19	1.15	1.00	1.00	1.14	1.07	1.20	1.23	1.11
Mg	2.51	2.62	2.56	2.52	2.52	2.51	2.53	2.44	2.50	2.36	2.49	2.49
Fe^{2+}	1.57	1.36	1.55	1.80	1.61	1.24	1.53	1.50	1.27	1.37	1.59	1.29
Fe^{3+}	0.66	0.77	0.51	0.34	0.50	0.87	0.69	0.63	0.79	0.69	0.46	0.73
Sum other elmts	0.06	0.07	0.05	0.04	0.05	0.08	0.05	0.05	0.07	0.08	0.04	0.11
Oct Sum	5.81	5.78	5.82	5.89	5.83	5.69	5.80	5.76	5.70	5.69	5.81	5.72
XMg	0.61	0.66	0.62	0.58	0.61	0.67	0.62	0.62	0.66	0.63	0.61	0.66
XFe^{3+}	30	36	25	16	24	41	31	30	39	34	22	36
T (^{o}C) Vidal (2006)	339	322	338	402	342	282	330	298	278	265	326	283
T(^{o}C) Inoue (2009)	337	314	329	390	334	268	335	299	266	249	317	262
T(°C) H&V (1992)	321	314	323	325	324	301	321	320	306	304	324	311

Appendix D1. (continued)

	P9-25-2	P9-25-3	P9-25-4	P9-25-5	P9-25-6	P9-25-7	P9-25-8	P9-25-9	P9-25-10	P9-25-11	P9-25-12	P9-25-13	P9-25-14	P9-25-15	P9-25-16	P9-25-17
SiO_2	25.47	25.82	26.15	25.75	25.96	25.61	25.89	25.64	25.84	25.63	25.94	25.48	25.22	25.18	25.85	25.59
TiO_2	0.04	0.00	0.02	0.04	0.06	0.07	0.00	0.04	0.03	0.00	0.00	0.09	0.04	0.02	0.00	0.00
Al_2O_3	19.89	19.70	19.98	20.09	19.88	19.88	19.89	19.74	19.94	19.89	19.95	19.91	19.50	19.97	19.86	19.70
FeO	28.89	28.75	29.18	29.12	28.95	28.95	29.05	28.73	29.12	29.32	29.20	29.37	28.90	28.96	29.18	29.03
MnO	0.00	0.00	0.00	0.00	0.00	0.00	0.00	0.00	0.00	0.00	0.00	0.00	0.00	0.00	0.00	0.00
MgO	12.59	12.60	12.83	12.91	13.04	12.84	12.93	12.86	13.43	12.97	12.82	13.04	12.35	12.81	12.74	12.94
CaO	0.08	0.09	0.06	0.07	0.06	0.06	0.06	0.14	0.08	0.06	0.04	0.06	0.06	0.06	0.08	0.07
Na_2O	0.00	0.04	0.00	0.00	0.06	0.05	0.00	0.06	0.01	0.07	0.04	0.12	0.00	0.00	0.08	0.05
K_2O	0.01	0.03	0.02	0.01	0.03	0.04	0.02	0.01	0.02	0.03	0.01	0.02	0.03	0.01	0.03	0.04
Cr_2O_3	0.00	0.00	0.00	0.00	0.00	0.00	0.00	0.00	0.00	0.00	0.00	0.00	0.00	0.00	0.00	0.00
Structural formula calculated on the basis of 14 O																
Si	2.70	2.73	2.72	2.70	2.71	2.70	2.71	2.70	2.70	2.70	2.71	2.68	2.71	2.70	2.71	2.70
Al^{iv}	1.30	1.27	1.28	1.30	1.29	1.30	1.29	1.30	1.30	1.30	1.29	1.32	1.29	1.31	1.29	1.30
Al^{vi}	1.19	1.18	1.18	1.18	1.16	1.18	1.16	1.16	1.15	1.17	1.17	1.16	1.18	1.22	1.16	1.15
Mg	1.99	1.98	1.99	2.02	2.03	2.02	2.02	2.02	2.09	2.04	2.00	2.05	1.98	2.04	1.99	2.04
Fe^{2+}	1.96	1.88	1.88	1.95	1.87	1.95	1.88	1.87	1.97	2.04	1.89	2.08	1.98	2.22	1.89	1.96
Fe^{3+}	0.60	0.66	0.66	0.60	0.66	0.60	0.66	0.66	0.57	0.54	0.66	0.51	0.61	0.37	0.67	0.60
Sum other elmts	0.01	0.02	0.01	0.01	0.01	0.01	0.01	0.02	0.01	0.02	0.01	0.02	0.01	0.01	0.02	0.02
Oct Sum	5.75	5.72	5.72	5.76	5.73	5.76	5.73	5.74	5.79	5.80	5.73	5.82	5.75	5.86	5.73	5.77
XMg	0.50	0.51	0.51	0.51	0.52	0.51	0.52	0.52	0.51	0.50	0.51	0.50	0.50	0.48	0.51	0.51
XFe^{3+}	24	26	26	24	26	24	26	26	22	21	26	20	24	14	26	24
T (^oC) Vidal (2006)	286	273	274	289	279	291	277	279	310	312	275	325	288	372	276	297
T(^oC) Inoue (2009)	308	283	287	314	296	311	300	298	337	336	297	350	309	410	295	320
T(°C) H&V (1992)	322	310	311	323	316	321	319	320	324	325	318	328	319	325	319	322

Appendix D1. (continued)

	P9-25-18	P9-25-19	P9-25-20	P9-25-21	P9-25-22	P9-25-23	P9-25-24	P9-25-25	P9-25-26	P9-25-27	P9-25-28	P9-25-29	P9-25-30	P9-25-31	P9-25-32	P9-25-34
SiO_2	25.58	25.70	26.40	25.54	25.47	26.01	26.22	26.33	25.29	25.58	26.20	25.90	25.94	26.09	25.74	26.79
TiO_2	0.01	0.07	0.06	0.00	0.04	0.01	0.00	0.04	0.01	0.08	0.07	0.00	0.00	0.09	0.03	0.00
Al_2O_3	19.32	18.78	18.76	19.37	19.37	19.10	18.67	18.65	19.22	19.00	19.18	18.79	18.76	19.41	19.09	18.48
FeO	28.90	27.97	28.17	28.38	28.30	28.42	28.23	27.87	28.52	28.82	28.47	28.13	28.38	28.59	28.46	27.87
MnO	0.00	0.00	0.00	0.00	0.00	0.00	0.00	0.00	0.00	0.00	0.00	0.00	0.00	0.00	0.00	0.00
MgO	12.88	13.43	13.40	13.89	13.52	13.40	13.58	13.38	13.32	12.98	13.19	13.67	13.31	12.98	13.45	13.12
CaO	0.11	0.09	0.09	0.05	0.10	0.27	0.52	0.82	0.12	0.15	0.15	0.09	0.29	0.15	0.18	0.76
Na_2O	0.00	0.00	0.00	0.07	0.00	0.02	0.06	0.07	0.04	0.00	0.03	0.03	0.00	0.01	0.00	0.06
K_2O	0.01	0.02	0.01	0.03	0.01	0.02	0.03	0.02	0.02	0.01	0.04	0.02	0.01	0.01	0.02	0.01
Cr_2O_3	0.00	0.00	0.00	0.00	0.00	0.00	0.00	0.00	0.00	0.00	0.00	0.00	0.00	0.00	0.00	0.00
Structural formula calculated on the basis of 14 O																
Si	2.71	2.73	2.76	2.70	2.70	2.73	2.74	2.75	2.70	2.71	2.74	2.73	2.74	2.73	2.72	2.79
Al^{iv}	1.29	1.27	1.24	1.30	1.30	1.27	1.26	1.25	1.30	1.29	1.26	1.27	1.26	1.27	1.29	1.21
Al^{vi}	1.13	1.08	1.08	1.11	1.12	1.09	1.04	1.05	1.11	1.10	1.11	1.07	1.07	1.13	1.09	1.05
Mg	2.04	2.13	2.09	2.19	2.14	2.09	2.11	2.08	2.12	2.05	2.06	2.15	2.09	2.03	2.11	2.03
Fe^{2+}	1.90	1.71	1.58	1.95	1.89	1.72	1.60	1.56	1.95	1.83	1.69	1.71	1.70	1.73	1.80	1.45
Fe^{3+}	0.67	0.77	0.89	0.56	0.62	0.77	0.86	0.88	0.60	0.73	0.80	0.77	0.80	0.78	0.72	0.97
Sum other elmts	0.01	0.01	0.01	0.01	0.01	0.03	0.07	0.10	0.02	0.02	0.02	0.01	0.03	0.02	0.02	0.09
Oct Sum	5.74	5.71	5.64	5.82	5.78	5.71	5.68	5.66	5.80	5.73	5.68	5.71	5.70	5.68	5.74	5.60
XMg	0.52	0.55	0.57	0.53	0.53	0.55	0.57	0.57	0.52	0.53	0.55	0.56	0.55	0.54	0.54	0.58
XFe^{3+}	26	31	36	22	25	31	35	36	24	29	32	31	32	31	29	40
T (^oC) Vidal (2006)	286	275	250	330	304	272	265	261	313	280	261	280	271	258	286	245
T(^oC) Inoue (2009)	305	287	256	358	330	281	265	246	339	297	267	292	277	269	302	224
T(°C) H&V (1992)	316	306	292	325	322	310	305	298	325	313	301	307	306	305	315	281

Appendix D1. (continued)

	P9-25-35	P9-25-36	P9-25-37	P9-25-39	P9-25-40	P9-25-41	P9-25-42	P9-25-43	P9-25-44	P9-25-45	P9-25-46	P9-25-47	P9-25-48	P9-25-49	P9-25-50	P9-25-51
SiO_2	25.66	26.28	25.81	25.91	25.25	25.60	25.48	24.97	25.50	25.10	25.24	25.65	26.19	25.61	26.23	25.55
TiO_2	0.05	0.02	0.05	0.00	0.00	0.02	0.03	0.05	0.12	0.00	0.03	0.01	0.00	0.02	0.03	0.02
Al_2O_3	19.39	19.08	19.11	19.27	19.52	19.71	19.55	19.81	19.84	19.85	19.96	19.49	19.73	19.74	20.00	19.83
FeO	28.45	28.14	28.61	28.95	29.11	28.52	28.66	28.77	28.75	28.86	28.59	28.87	28.82	28.85	29.02	28.95
MnO	0.00	0.00	0.00	0.00	0.00	0.00	0.00	0.00	0.00	0.00	0.00	0.00	0.00	0.00	0.00	0.00
MgO	13.22	13.26	13.09	13.19	13.18	12.67	12.58	12.94	12.99	12.95	13.05	12.95	12.93	12.75	12.87	12.73
CaO	0.06	0.23	0.11	0.05	0.03	0.08	0.16	0.09	0.07	0.06	0.04	0.05	0.07	0.10	0.08	0.09
Na_2O	0.03	0.00	0.02	0.00	0.00	0.03	0.01	0.00	0.06	0.00	0.00	0.02	0.10	0.00	0.02	0.09
K_2O	0.01	0.01	0.01	0.01	0.03	0.01	0.02	0.01	0.02	0.01	0.02	0.01	0.05	0.01	0.01	0.01
Cr_2O_3	0.00	0.00	0.00	0.00	0.00	0.00	0.00	0.00	0.00	0.00	0.00	0.00	0.00	0.00	0.00	0.00
Structural formula calculated on the basis of 14 O																
Si	2.71	2.75	2.72	2.72	2.70	2.71	2.71	2.69	2.69	2.70	2.70	2.71	2.73	2.71	2.73	2.70
Al^{iv}	1.29	1.25	1.28	1.28	1.30	1.29	1.29	1.31	1.31	1.30	1.30	1.29	1.27	1.29	1.27	1.30
Al^{vi}	1.14	1.10	1.10	1.11	1.15	1.18	1.16	1.22	1.17	1.21	1.22	1.14	1.16	1.16	1.18	1.17
Mg	2.08	2.07	2.06	2.07	2.10	2.00	2.00	2.08	2.04	2.08	2.08	2.04	2.01	2.01	1.99	2.01
Fe^{2+}	1.86	1.64	1.74	1.82	2.16	1.87	1.89	2.32	1.94	2.29	2.19	1.89	1.80	1.89	1.84	1.96
Fe^{3+}	0.65	0.82	0.78	0.72	0.44	0.66	0.66	0.28	0.60	0.31	0.36	0.66	0.72	0.66	0.68	0.60
Sum other elmts	0.01	0.03	0.02	0.01	0.01	0.01	0.02	0.01	0.02	0.01	0.01	0.01	0.02	0.01	0.01	0.02
Oct Sum	5.75	5.66	5.70	5.72	5.86	5.72	5.73	5.90	5.77	5.89	5.86	5.74	5.70	5.73	5.71	5.76
XMg	0.53	0.56	0.54	0.53	0.49	0.52	0.51	0.47	0.51	0.48	0.49	0.52	0.53	0.52	0.52	0.51
XFe^{3+}	26	34	31	29	17	26	26	11	24	12	14	26	29	26	27	24
T (^{o}C) Vidal (2006)	289	255	265	278	370	273	276	417	295	402	374	284	266	276	269	290
T(^{o}C) Inoue (2009)	306	259	284	298	418	291	293	457	317	449	408	306	275	300	280	310
T(°C) H&V (1992)	315	298	311	313	325	316	317	325	323	324	323	317	308	320	309	322

Appendix D1. (continued)

	P9-25-53	P9-25-54	P9-25-55	P9-25-56	P9-25-57	P9-25-58	P9-25-59	P9-25-60	P9-25-61	P9-25-62	P9-25-63	P9-25-64	P9-25-65	P9-25-66	P9-25-67	P9-25-68
SiO_2	25.20	25.46	25.97	25.10	25.73	25.75	25.47	25.84	25.62	25.06	25.49	25.10	25.77	25.88	25.38	25.60
TiO_2	0.04	0.04	0.02	0.00	0.06	0.00	0.01	0.06	0.01	0.04	0.00	0.02	0.00	0.01	0.01	0.00
Al_2O_3	19.91	20.04	20.01	20.11	19.89	20.16	19.96	19.94	20.18	20.17	19.74	19.83	19.91	19.90	19.87	19.90
FeO	28.91	29.06	29.27	29.13	29.02	29.11	29.12	29.01	28.98	29.06	28.93	28.74	29.06	28.90	28.95	28.74
MnO	0.00	0.00	0.00	0.00	0.00	0.00	0.00	0.00	0.00	0.00	0.00	0.00	0.00	0.00	0.00	0.00
MgO	12.94	13.00	12.83	12.97	13.09	12.92	12.90	12.90	12.81	13.00	12.80	12.66	13.00	13.15	13.07	13.32
CaO	0.09	0.05	0.08	0.07	0.06	0.06	0.05	0.08	0.05	0.06	0.07	0.06	0.07	0.07	0.08	0.07
Na_2O	0.00	0.02	0.13	0.04	0.00	0.12	0.00	0.00	0.00	0.05	0.09	0.00	0.03	0.01	0.03	0.00
K_2O	0.01	0.02	0.03	0.01	0.01	0.01	0.01	0.01	0.01	0.01	0.01	0.01	0.01	0.02	0.04	0.02
Cr_2O_3	0.00	0.00	0.00	0.00	0.00	0.00	0.00	0.00	0.00	0.00	0.00	0.00	0.00	0.00	0.00	0.00
Structural formula calculated on the basis of 14 O																
Si	2.69	2.69	2.71	2.68	2.70	2.70	2.69	2.70	2.70	2.68	2.70	2.69	2.70	2.70	2.69	2.70
Al^{iv}	1.31	1.31	1.29	1.32	1.30	1.30	1.31	1.30	1.30	1.32	1.30	1.31	1.30	1.30	1.31	1.30
Al^{vi}	1.20	1.19	1.16	1.21	1.16	1.19	1.18	1.17	1.21	1.22	1.16	1.20	1.17	1.16	1.17	1.17
Mg	2.06	2.05	1.99	2.07	2.05	2.02	2.03	2.01	2.01	2.07	2.02	2.02	2.03	2.05	2.06	2.09
Fe^{2+}	2.21	2.06	1.89	2.28	1.95	2.02	2.03	1.88	2.02	2.31	1.96	2.07	1.95	1.87	2.06	2.00
Fe^{3+}	0.37	0.50	0.66	0.32	0.60	0.54	0.54	0.66	0.54	0.29	0.60	0.51	0.60	0.66	0.50	0.53
Sum other elmts	0.01	0.01	0.02	0.01	0.01	0.02	0.01	0.01	0.01	0.01	0.02	0.01	0.01	0.01	0.01	0.01
Oct Sum	5.86	5.81	5.73	5.89	5.77	5.79	5.79	5.73	5.78	5.90	5.77	5.80	5.76	5.74	5.82	5.80
XMg	0.48	0.50	0.51	0.48	0.51	0.50	0.50	0.52	0.50	0.47	0.51	0.49	0.51	0.52	0.50	0.51
XFe^{3+}	15	20	26	12	24	21	21	26	21	11	24	20	24	26	20	21
T (^oC) Vidal (2006)	372	318	275	388	296	304	307	276	299	402	293	313	293	280	323	314
T(^oC) Inoue (2009)	404	348	294	439	320	322	340	299	324	452	316	344	316	306	353	343
T(°C) H&V (1992)	325	328	320	333	321	323	327	319	323	333	324	328	321	321	328	325

Appendix D1. (continued)

	P9-25-69	P9-25-70	P9-25-71	P9-25-72	P9-25-73	P9-25-74	P9-25-75	P9-25-76	P9-25-77	P9-25-78	P9-25-79	P9-25-80	P9-25-81	P9-25-82	P9-25-83	P9-25-84
SiO_2	25.94	25.18	25.60	25.52	25.54	25.58	25.88	25.31	25.21	25.65	24.98	25.36	25.60	25.77	25.87	25.70
TiO_2	0.01	0.00	0.05	0.00	0.05	0.00	0.00	0.02	0.01	0.06	0.02	0.01	0.01	0.00	0.00	0.00
Al_2O_3	19.99	19.97	20.06	19.99	19.98	19.70	19.50	19.72	19.83	19.98	19.77	19.84	20.05	19.70	19.46	19.89
FeO	28.86	28.86	28.79	28.82	28.84	28.68	28.82	28.75	28.68	28.90	28.67	28.94	28.99	28.92	28.81	28.86
MnO	0.00	0.00	0.00	0.00	0.00	0.00	0.00	0.00	0.00	0.00	0.00	0.00	0.00	0.00	0.00	0.00
MgO	13.09	13.25	13.06	13.23	13.16	13.03	13.09	12.46	13.22	13.22	13.15	13.20	13.01	12.81	13.50	12.95
CaO	0.04	0.07	0.07	0.07	0.10	0.09	0.04	0.08	0.06	0.04	0.07	0.08	0.04	0.06	0.03	0.06
Na_2O	0.00	0.00	0.00	0.00	0.08	0.00	0.00	0.00	0.00	0.10	0.00	0.03	0.01	0.09	0.00	0.05
K_2O	0.01	0.02	0.01	0.01	0.01	0.02	0.01	0.01	0.01	0.01	0.01	0.02	0.01	0.01	0.02	0.01
Cr_2O_3	0.00	0.00	0.00	0.00	0.00	0.00	0.00	0.00	0.00	0.00	0.00	0.00	0.00	0.00	0.00	0.00
Structural formula calculated on the basis of 14 O																
Si	2.71	2.69	2.70	2.69	2.69	2.71	2.72	2.70	2.70	2.69	2.69	2.69	2.70	2.71	2.71	2.71
Al^{iv}	1.29	1.31	1.30	1.31	1.31	1.29	1.28	1.30	1.30	1.31	1.31	1.31	1.30	1.29	1.29	1.29
Al^{vi}	1.17	1.20	1.19	1.18	1.17	1.16	1.14	1.19	1.21	1.17	1.20	1.18	1.19	1.16	1.12	1.17
Mg	2.04	2.11	2.05	2.08	2.07	2.06	2.05	1.98	2.11	2.07	2.11	2.09	2.04	2.01	2.11	2.03
Fe^{2+}	1.87	2.26	2.00	2.04	2.01	1.94	1.85	1.97	2.26	2.01	2.26	2.16	2.02	1.88	1.87	1.94
Fe^{3+}	0.66	0.32	0.53	0.50	0.53	0.60	0.68	0.60	0.31	0.53	0.32	0.42	0.54	0.66	0.66	0.60
Sum other elmts	0.01	0.01	0.01	0.01	0.02	0.01	0.01	0.01	0.01	0.02	0.01	0.01	0.01	0.02	0.00	0.01
Oct Sum	5.73	5.90	5.79	5.81	5.80	5.77	5.73	5.75	5.89	5.80	5.90	5.85	5.79	5.73	5.76	5.76
XMg	0.52	0.48	0.51	0.50	0.51	0.51	0.53	0.50	0.48	0.51	0.48	0.49	0.50	0.52	0.53	0.51
XFe^{3+}	26	12	21	20	21	24	27	24	12	21	12	16	21	26	26	24
T (^oC) Vidal (2006)	276	399	306	322	312	296	279	285	410	313	401	365	306	278	295	291
T(^oC) Inoue (2009)	301	454	330	353	335	317	298	308	454	334	454	397	335	296	319	312
T(°C) H&V (1992)	319	329	323	327	327	320	313	321	323	324	329	326	325	317	317	321

Appendix D1. (continued)

	P9-25-85	P9-25-86
SiO_2	25.46	25.26
TiO_2	0.00	0.06
Al_2O_3	19.94	19.83
FeO	28.89	28.71
MnO	0.00	0.00
MgO	13.30	12.88
CaO	0.07	0.08
Na_2O	0.04	0.01
K_2O	0.02	0.01
Cr_2O_3	0.00	0.00
Structural formula calculated on the basis of 14 O		
Si	2.70	2.69
Al^{iv}	1.30	1.31
Al^{vi}	1.19	1.18
Mg	2.10	2.04
Fe^{2+}	2.19	2.02
Fe^{3+}	0.37	0.54
Sum other elmts	0.01	0.01
Oct Sum	5.87	5.79
XMg	0.49	0.50
XFe^{3+}	15	21
T (^{o}C) Vidal (2006)	386	307
T(^{o}C) Inoue (2009)	418	336
T(°C) H&V (1992)	324	327

Appendix D1. (continued)

	P9-30-1	P9-30-2	P9-30-9	P9-30-14	P9-30-16	P9-30-18	P9-30-19	P9-30-20	P9-30-22	P9-30-23	P9-30-24	P9-30-25	P9-30-27	P9-30-31
SiO_2	25.73	26.35	26.40	26.07	25.74	26.84	25.99	25.84	25.94	25.61	25.67	25.97	25.77	26.64
TiO_2	0.03	0.00	0.05	0.03	0.01	0.03	0.00	0.04	0.01	0.05	0.04	0.02	0.02	0.03
Al_2O_3	19.83	18.31	19.00	19.07	18.95	19.26	18.90	18.74	19.06	18.49	18.99	19.13	18.85	19.16
FeO	33.14	33.06	33.53	33.47	33.83	32.07	33.35	33.34	33.28	33.57	33.44	33.57	33.94	32.44
MnO	0.42	0.43	0.46	0.51	0.46	0.46	0.42	0.51	0.46	0.44	0.46	0.47	0.45	0.38
MgO	11.25	11.87	11.83	11.37	12.07	11.52	11.45	11.74	12.32	12.27	11.95	11.62	11.65	12.76
CaO	0.24	0.10	0.05	0.07	0.07	0.43	0.06	0.07	0.05	0.03	0.03	0.04	0.06	0.18
Na_2O	0.02	0.01	0.01	0.02	0.01	0.21	0.03	0.00	0.00	0.01	0.00	0.03	0.03	0.03
K_2O	0.03	0.03	0.05	0.03	0.04	0.06	0.02	0.02	0.03	0.01	0.02	0.03	0.04	0.04
Cr_2O_3	0.00	0.00	0.00	0.00	0.00	0.00	0.00	0.00	0.00	0.00	0.00	0.00	0.00	0.00
Structural formula calculated on the basis of 14 O														
Si	2.69	2.73	2.71	2.70	2.68	2.74	2.71	2.69	2.70	2.69	2.69	2.69	2.69	2.71
Al^{iv}	1.31	1.27	1.29	1.30	1.32	1.26	1.29	1.31	1.30	1.31	1.31	1.31	1.31	1.29
Al^{vi}	1.14	0.96	1.01	1.04	1.01	1.06	1.03	1.00	1.03	0.98	1.04	1.03	1.01	1.00
Mg	1.76	1.83	1.81	1.76	1.88	1.75	1.78	1.82	1.91	1.92	1.87	1.80	1.81	1.93
Fe^{2+}	2.47	1.98	2.10	2.15	2.44	1.89	2.15	2.15	2.40	2.40	2.43	2.23	2.34	1.97
Fe^{3+}	0.43	0.89	0.78	0.75	0.51	0.85	0.76	0.76	0.50	0.55	0.50	0.68	0.62	0.79
Sum other elmts	0.07	0.05	0.05	0.06	0.05	0.11	0.05	0.05	0.05	0.04	0.05	0.05	0.05	0.06
Oct Sum	5.87	5.71	5.75	5.75	5.89	5.67	5.76	5.78	5.89	5.89	5.88	5.79	5.84	5.75
XMg	0.42	0.48	0.46	0.45	0.43	0.48	0.45	0.46	0.44	0.44	0.43	0.45	0.44	0.50
XFe^{3+}	15	31	27	26	17	31	26	26	17	19	17	24	21	29
T (^oC) Vidal (2006)	375	279	290	288	392	256	290	300	393	396	386	309	339	291
T(^oC) Inoue (2009)	358	290	306	304	417	246	310	326	406	426	405	331	363	306
T(°C) H&V (1992)	326	309	317	321	331	301	320	326	325	327	327	326	328	319

Appendix D1. (continued)

	P1-23-8	P1-23-9	P1-23-14	P1-23-26	P1-23-33	P1-23-39	P1-23-42	P1-23-50	P1-23-55	P1-23-56	P1-23-58	P1-23-59	P1-23-60	P1-23-64
SiO_2	26.39	26.02	26.37	26.49	26.04	25.22	26.67	26.04	25.92	25.33	25.69	25.93	25.96	26.82
TiO_2	0.07	0.02	0.04	0.12	0.10	0.12	0.01	0.05	0.02	0.13	0.00	0.01	0.03	0.11
Al_2O_3	18.13	19.01	17.83	18.67	18.52	19.82	17.56	18.83	19.04	19.17	18.70	18.42	19.05	18.02
FeO	28.33	29.02	27.93	28.85	28.81	28.95	28.28	28.64	28.80	29.07	28.84	28.87	28.62	28.34
MnO	0.00	0.00	0.00	0.00	0.00	0.00	0.00	0.00	0.00	0.00	0.00	0.00	0.00	0.00
MgO	13.58	12.36	13.45	12.71	12.91	12.83	13.55	12.83	12.95	12.43	13.09	13.00	12.98	12.74
CaO	0.40	0.22	0.07	0.15	0.12	0.07	0.09	0.06	0.16	0.66	0.07	0.10	0.14	0.44
Na_2O	0.10	0.11	0.04	0.04	0.00	0.00	0.01	0.01	0.00	0.07	0.02	0.00	0.12	0.00
K_2O	0.02	0.01	0.03	0.03	0.02	0.01	0.02	0.01	0.01	0.01	0.01	0.01	0.01	0.01
Cr_2O_3	0.00	0.00	0.00	0.00	0.00	0.00	0.00	0.00	0.00	0.00	0.00	0.00	0.00	0.00
Structural formula calculated on the basis of 14 O														
Si	2.76	2.75	2.79	2.77	2.75	2.69	2.81	2.75	2.73	2.70	2.73	2.74	2.73	2.81
Al^{iv}	1.24	1.25	1.21	1.23	1.25	1.31	1.19	1.25	1.27	1.30	1.27	1.26	1.27	1.19
Al^{vi}	1.00	1.11	1.01	1.08	1.06	1.18	0.98	1.10	1.10	1.11	1.07	1.04	1.10	1.05
Mg	2.12	1.95	2.12	1.98	2.03	2.04	2.12	2.02	2.03	1.97	2.07	2.05	2.04	1.99
Fe^{2+}	1.56	1.74	1.48	1.59	1.65	2.07	1.49	1.68	1.75	1.92	1.77	1.66	1.74	1.49
Fe^{3+}	0.92	0.82	0.99	0.93	0.89	0.51	1.00	0.85	0.79	0.67	0.79	0.89	0.78	0.99
Sum other elmts	0.06	0.04	0.01	0.02	0.02	0.01	0.01	0.01	0.02	0.08	0.01	0.01	0.03	0.05
Oct Sum	5.66	5.66	5.61	5.60	5.65	5.81	5.61	5.65	5.69	5.75	5.71	5.66	5.69	5.57
XMg	0.58	0.53	0.59	0.55	0.55	0.50	0.59	0.55	0.54	0.51	0.54	0.55	0.54	0.57
XFe^{3+}	37	32	40	37	35	20	40	34	31	26	31	35	31	40
T (^{o}C) Vidal (2006)	268	251	263	241	254	318	283	253	265	289	272	256	265	259
T(^{o}C) Inoue (2009)	256	256	246	241	263	346	244	263	278	287	293	272	273	219
T(°C) H&V (1992)	290	299	279	284	296	326	271	297	307	320	310	301	305	264

Appendix D1. (continued)

	P1-152-4	P1-152-6	P1-152-8	P1-152-9	P1-152-11	P1-152-14	P1-152-15	P1-152-17	P1-152-18	P1-152-19	P1-152-20	P1-152-23	P1-152-26	P1-152-27	P1-152-28	P1-152-29
SiO_2	27.94	27.88	28.66	28.65	28.18	28.40	27.74	28.72	28.75	28.70	28.59	28.37	29.32	29.24	29.00	28.60
TiO_2	0.05	0.00	0.04	0.00	0.04	0.02	0.02	0.02	0.02	0.02	0.02	0.00	0.01	0.03	0.00	0.01
Al_2O_3	18.67	19.03	19.83	19.52	19.69	20.14	18.79	19.52	19.67	19.88	19.49	20.18	20.32	20.02	20.43	19.95
FeO	28.06	28.02	28.31	28.35	29.01	28.69	27.98	28.76	28.85	29.17	28.29	28.33	28.21	27.12	27.35	26.98
MnO	0.55	0.42	0.47	0.49	0.49	0.50	0.49	0.48	0.48	0.46	0.52	0.48	0.44	0.47	0.49	0.48
MgO	15.18	13.65	14.14	14.21	13.74	14.91	15.46	13.89	14.91	14.61	13.82	13.65	14.40	15.39	15.17	15.58
CaO	0.20	0.07	0.24	0.06	0.09	0.06	0.03	0.05	0.06	0.06	0.24	0.11	0.08	0.09	0.09	0.23
Na_2O	0.05	0.04	0.01	0.00	0.00	0.02	0.02	0.04	0.03	0.03	0.01	0.00	0.02	0.03	0.01	0.00
K_2O	0.00	0.01	0.01	0.00	0.01	0.02	0.01	0.02	0.01	0.00	0.02	0.03	0.01	0.03	0.03	0.00
Cr_2O_3	0.00	0.00	0.00	0.00	0.00	0.00	0.00	0.00	0.00	0.00	0.00	0.00	0.00	0.00	0.00	0.00
Structural formula calculated on the basis of 14 O																
Si	2.78	2.82	2.81	2.82	2.79	2.77	2.77	2.83	2.79	2.79	2.83	2.80	2.83	2.82	2.80	2.79
Al^{iv}	1.22	1.18	1.19	1.18	1.21	1.23	1.23	1.17	1.21	1.21	1.17	1.20	1.17	1.18	1.20	1.21
Al^{vi}	0.97	1.08	1.10	1.09	1.09	1.08	0.97	1.09	1.04	1.07	1.10	1.15	1.14	1.10	1.13	1.08
Mg	2.25	2.06	2.07	2.09	2.03	2.17	2.30	2.04	2.16	2.12	2.04	2.01	2.07	2.21	2.18	2.26
Fe^{2+}	1.35	1.37	1.35	1.35	1.44	1.47	1.38	1.37	1.36	1.42	1.36	1.40	1.32	1.20	1.28	1.28
Fe^{3+}	0.98	0.99	0.97	0.98	0.96	0.87	0.96	0.99	0.98	0.95	0.98	0.94	0.96	0.98	0.93	0.92
Sum other elmts	0.07	0.05	0.07	0.05	0.05	0.05	0.05	0.05	0.05	0.05	0.07	0.05	0.05	0.05	0.05	0.06
Oct Sum	5.63	5.55	5.56	5.56	5.58	5.64	5.65	5.54	5.59	5.60	5.55	5.56	5.54	5.55	5.57	5.60
XMg	0.62	0.60	0.61	0.61	0.58	0.60	0.63	0.60	0.61	0.60	0.60	0.59	0.61	0.65	0.63	0.64
XFe^{3+}	42	42	42	42	40	37	41	42	42	40	42	40	42	45	42	42
T (^{o}C) Vidal (2006)	273	245	231	239	232	255	273	244	251	244	236	217	223	237	229	245
T(^{o}C) Inoue (2009)	243	213	210	212	222	243	259	208	230	231	204	210	202	209	216	228
T(°C) H&V (1992)	282	265	268	263	277	289	290	260	278	279	260	273	259	263	273	280

Appendix D1. (continued)

	P1-152-30	P1-152-38	P1-152-39	P1-152-40
SiO_2	29.78	27.34	26.39	27.65
TiO_2	0.00	0.03	0.05	0.00
Al_2O_3	20.70	21.32	20.72	21.92
FeO	27.16	28.79	27.97	27.86
MnO	0.44	0.46	0.47	0.45
MgO	15.06	14.66	14.35	13.82
CaO	0.23	0.13	0.15	0.05
Na_2O	0.01	0.01	0.03	0.03
K_2O	0.02	0.02	0.01	0.03
Cr_2O_3	0.00	0.00	0.00	0.00
Structural formula calculated on the basis of 14 O				
Si	2.83	2.70	2.69	2.74
Al^{iv}	1.17	1.30	1.31	1.26
Al^{vi}	1.16	1.18	1.18	1.29
Mg	2.14	2.16	2.18	2.04
Fe^{2+}	1.19	1.82	1.88	1.71
Fe^{3+}	0.97	0.56	0.50	0.60
Sum other elmts	0.06	0.05	0.06	0.05
Oct Sum	5.52	5.78	5.81	5.69
XMg	0.64	0.54	0.54	0.54
XFe^{3+}	45	24	21	26
T (^{o}C) Vidal (2006)	215	302	321	258
T(^{o}C) Inoue (2009)	194	300	317	248
T(°C) H&V (1992)	256	322	326	305

Appendix D1. (continued)

	P1-155-1	P1-155-2	P1-155-3	P1-155-4	P1-155-5	P1-155-6	P1-155-7	P1-155-8	P1-155-9	P1-155-10	P1-155-11	P1-155-12	P1-155-13	P1-155-14	P1-155-16	P1-155-17
SiO_2	25.51	25.75	25.86	25.98	26.42	25.63	26.14	26.21	25.93	26.14	26.23	25.88	25.60	25.79	26.26	26.33
TiO_2	0.04	0.06	0.03	0.03	0.05	0.00	0.00	0.04	0.03	0.06	0.03	0.04	0.07	0.00	0.08	0.06
Al_2O_3	19.35	19.07	19.58	19.40	19.10	19.60	19.26	19.47	19.82	19.45	19.25	19.48	19.04	19.53	19.52	19.63
FeO	30.17	29.84	30.27	30.30	30.07	29.97	29.57	30.06	30.13	30.26	29.89	30.05	28.91	29.74	30.07	29.52
MnO	0.00	0.00	0.00	0.00	0.00	0.00	0.00	0.00	0.00	0.00	0.00	0.00	0.00	0.00	0.00	0.00
MgO	12.50	12.04	12.51	12.17	11.94	12.50	12.18	12.44	12.60	12.39	12.29	12.58	12.45	12.46	12.49	12.25
CaO	0.05	0.09	0.05	0.10	0.09	0.16	0.09	0.07	0.07	0.04	0.09	0.07	0.11	0.11	0.12	0.12
Na_2O	0.03	0.00	0.05	0.00	0.02	0.02	0.00	0.00	0.03	0.05	0.06	0.07	0.00	0.05	0.01	0.00
K_2O	0.01	0.01	0.01	0.02	0.01	0.00	0.01	0.02	0.01	0.02	0.02	0.02	0.00	0.03	0.03	0.01
Cr_2O_3	0.00	0.00	0.00	0.00	0.00	0.00	0.00	0.00	0.00	0.00	0.00	0.00	0.00	0.00	0.00	0.00
Structural formula calculated on the basis of 14 O																
Si	2.70	2.73	2.71	2.73	2.77	2.70	2.75	2.73	2.71	2.73	2.74	2.71	2.73	2.72	2.73	2.74
Al^{iv}	1.30	1.27	1.29	1.27	1.24	1.30	1.25	1.27	1.29	1.27	1.26	1.29	1.27	1.28	1.27	1.26
Al^{vi}	1.12	1.12	1.12	1.13	1.12	1.14	1.14	1.12	1.14	1.12	1.12	1.12	1.12	1.14	1.12	1.16
Mg	1.97	1.90	1.95	1.91	1.86	1.97	1.91	1.93	1.96	1.93	1.92	1.97	1.98	1.96	1.93	1.90
Fe^{2+}	2.04	1.85	1.96	1.94	1.79	2.02	1.79	1.83	1.97	1.89	1.80	1.95	1.80	1.94	1.83	1.78
Fe^{3+}	0.63	0.79	0.69	0.72	0.84	0.62	0.81	0.79	0.66	0.75	0.81	0.68	0.77	0.68	0.78	0.80
Sum other elmts	0.01	0.01	0.01	0.01	0.01	0.02	0.01	0.01	0.01	0.01	0.02	0.02	0.01	0.02	0.02	0.01
Oct Sum	5.77	5.68	5.74	5.71	5.63	5.77	5.66	5.68	5.75	5.70	5.66	5.74	5.69	5.73	5.68	5.65
XMg	0.49	0.51	0.50	0.50	0.51	0.49	0.52	0.51	0.50	0.51	0.52	0.50	0.52	0.50	0.51	0.52
XFe^{3+}	24	30	26	27	32	24	31	30	25	29	31	26	30	26	30	31
T (^oC) Vidal (2006)	300	256	280	271	244	295	248	257	283	266	253	283	261	279	258	244
T(^oC) Inoue (2009)	328	274	306	285	248	317	260	276	308	282	264	302	277	296	274	255
T(°C) H&V (1992)	321	306	319	308	289	322	299	307	320	308	301	316	307	316	307	300

Appendix D1. (continued)

	P1-155-18	P1-155-19	P1-155-20	P1-155-21	P1-155-22	P1-155-23	P1-155-25	P1-155-26	P1-155-27	P1-155-28	P1-155-29	P1-155-30	P1-155-31	P1-155-33	P1-155-35	P1-155-36
SiO_2	25.51	26.13	25.94	26.00	25.64	26.14	26.21	26.20	26.12	25.99	26.03	25.89	25.88	25.50	25.76	25.25
TiO_2	0.00	0.06	0.02	0.04	0.01	0.03	0.14	0.05	0.11	0.00	0.03	0.04	0.06	0.00	0.05	0.01
Al_2O_3	18.97	19.55	19.06	19.22	19.20	19.27	19.42	19.27	19.33	19.33	19.32	19.80	19.53	19.60	19.70	19.60
FeO	28.59	29.92	29.36	29.78	28.78	29.65	29.82	29.62	29.85	29.96	29.87	30.16	29.64	29.85	29.46	29.57
MnO	0.00	0.00	0.00	0.00	0.00	0.00	0.00	0.00	0.00	0.00	0.00	0.00	0.00	0.00	0.00	0.00
MgO	11.90	12.36	12.27	12.49	12.30	12.01	12.40	12.42	12.36	12.42	12.32	12.41	12.59	12.50	12.50	12.49
CaO	0.12	0.09	0.08	0.09	0.09	0.12	0.14	0.12	0.12	0.09	0.10	0.09	0.12	0.08	0.17	0.11
Na_2O	0.00	0.00	0.00	0.08	0.00	0.00	0.00	0.03	0.00	0.00	0.02	0.00	0.09	0.00	0.00	0.05
K_2O	0.02	0.02	0.01	0.01	0.01	0.01	0.03	0.01	0.02	0.02	0.03	0.01	0.03	0.02	0.02	0.00
Cr_2O_3	0.00	0.00	0.00	0.00	0.00	0.00	0.00	0.00	0.00	0.00	0.00	0.00	0.00	0.00	0.00	0.00
Structural formula calculated on the basis of 14 O																
Si	2.75	2.73	2.74	2.73	2.73	2.75	2.73	2.74	2.73	2.73	2.73	2.71	2.72	2.70	2.71	2.69
Al^{iv}	1.25	1.27	1.26	1.27	1.27	1.25	1.27	1.26	1.27	1.27	1.27	1.29	1.28	1.30	1.29	1.31
Al^{vi}	1.15	1.14	1.12	1.11	1.15	1.14	1.12	1.12	1.12	1.12	1.12	1.15	1.14	1.14	1.16	1.16
Mg	1.91	1.92	1.93	1.95	1.95	1.88	1.93	1.94	1.93	1.94	1.93	1.93	1.97	1.97	1.96	1.99
Fe^{2+}	1.78	1.87	1.79	1.83	1.80	1.80	1.79	1.79	1.80	1.88	1.83	1.95	1.93	2.02	1.92	2.08
Fe^{3+}	0.80	0.74	0.81	0.78	0.77	0.81	0.81	0.80	0.81	0.75	0.79	0.69	0.68	0.62	0.67	0.55
Sum other elmts	0.02	0.01	0.01	0.02	0.01	0.01	0.02	0.02	0.01	0.01	0.02	0.01	0.02	0.01	0.02	0.02
Oct Sum	5.65	5.69	5.66	5.69	5.68	5.65	5.66	5.67	5.67	5.70	5.68	5.73	5.73	5.77	5.73	5.80
XMg	0.52	0.51	0.52	0.52	0.52	0.51	0.52	0.52	0.52	0.51	0.51	0.50	0.51	0.49	0.51	0.49
XFe^{3+}	31	29	31	30	30	31	31	31	31	29	30	26	26	24	26	21
T (^{o}C) Vidal (2006)	245	262	253	262	255	246	252	254	252	267	257	274	281	293	275	310
T(^{o}C) Inoue (2009)	257	276	265	278	271	255	266	264	269	285	274	300	292	324	293	338
T(°C) H&V (1992)	301	307	301	308	307	297	303	301	305	310	308	319	313	324	317	327

Appendix D1. (continued)

	P1-155-37	P1-155-38	P1-155-39	P1-155-40	P1-155-41	P1-155-42	P1-155-43	P1-155-44	P1-155-45	P1-155-46	P1-155-47	P1-155-48	P1-155-49	P1-155-50	P1-155-51	P1-155-52
SiO_2	25.69	26.02	25.88	25.76	26.24	26.04	26.18	26.03	26.09	25.91	25.55	25.66	25.98	25.84	25.58	25.96
TiO_2	0.00	0.00	0.00	0.00	0.00	0.07	0.01	0.02	0.00	0.00	0.07	0.00	0.00	0.01	0.00	0.00
Al_2O_3	19.47	19.49	19.49	19.47	19.56	19.40	19.57	19.83	19.40	19.74	19.22	19.38	19.59	19.58	19.44	19.63
FeO	30.01	29.98	30.04	30.08	29.99	29.94	30.04	30.04	29.89	29.69	28.93	29.90	30.15	30.21	30.07	30.01
MnO	0.00	0.00	0.00	0.00	0.00	0.00	0.00	0.00	0.00	0.00	0.00	0.00	0.00	0.00	0.00	0.00
MgO	12.27	12.86	12.36	12.24	12.29	12.60	12.35	12.41	12.70	12.62	12.12	12.06	12.42	12.73	12.37	12.32
CaO	0.11	0.13	0.06	0.08	0.07	0.06	0.13	0.07	0.07	0.05	0.10	0.07	0.08	0.07	0.05	0.05
Na_2O	0.01	0.01	0.09	0.01	0.04	0.00	0.02	0.01	0.00	0.06	0.00	0.01	0.10	0.04	0.05	0.02
K_2O	0.02	0.01	0.01	0.01	0.02	0.01	0.03	0.01	0.02	0.00	0.01	0.02	0.02	0.01	0.00	0.02
Cr_2O_3	0.00	0.00	0.00	0.00	0.00	0.00	0.00	0.00	0.00	0.00	0.00	0.00	0.00	0.00	0.00	0.00
Structural formula calculated on the basis of 14 O																
Si	2.71	2.72	2.72	2.72	2.73	2.72	2.73	2.72	2.72	2.71	2.73	2.72	2.72	2.70	2.71	2.72
Al^{iv}	1.29	1.28	1.28	1.28	1.27	1.28	1.27	1.28	1.28	1.29	1.27	1.28	1.28	1.30	1.29	1.28
Al^{vi}	1.14	1.11	1.13	1.14	1.14	1.12	1.14	1.16	1.11	1.15	1.16	1.15	1.13	1.12	1.13	1.15
Mg	1.93	2.00	1.94	1.92	1.91	1.96	1.92	1.93	1.98	1.97	1.93	1.91	1.94	1.99	1.95	1.93
Fe^{2+}	1.96	1.94	1.95	1.96	1.83	1.87	1.87	1.94	1.87	1.92	1.85	1.96	1.95	1.98	1.99	1.95
Fe^{3+}	0.69	0.68	0.69	0.69	0.78	0.75	0.75	0.68	0.74	0.68	0.74	0.69	0.69	0.66	0.67	0.68
Sum other elmts	0.02	0.02	0.02	0.01	0.01	0.01	0.02	0.01	0.01	0.01	0.01	0.01	0.02	0.01	0.01	0.01
Oct Sum	5.73	5.75	5.73	5.73	5.67	5.70	5.69	5.72	5.71	5.73	5.69	5.72	5.73	5.76	5.75	5.72
XMg	0.50	0.51	0.50	0.50	0.51	0.51	0.51	0.50	0.51	0.51	0.51	0.49	0.50	0.50	0.49	0.50
XFe^{3+}	26	26	26	26	30	29	29	26	29	26	29	26	26	25	25	26
T (^{o}C) Vidal (2006)	277	288	278	276	252	269	263	272	271	277	260	273	279	291	285	273
T(^{o}C) Inoue (2009)	299	306	294	297	269	288	276	292	290	298	272	290	294	318	313	291
T(°C) H&V (1992)	317	316	313	315	306	310	308	314	311	317	306	312	314	322	321	312

Appendix D1. (continued)

	P1-155-53	P1-155-56	P1-155-57	P1-155-58
SiO_2	26.11	25.81	26.18	25.76
TiO_2	0.02	0.03	0.02	0.04
Al_2O_3	19.30	19.73	19.43	19.40
FeO	29.85	30.08	30.02	30.13
MnO	0.00	0.00	0.00	0.00
MgO	12.37	12.20	12.49	12.44
CaO	0.07	0.06	0.10	0.07
Na_2O	0.00	0.01	0.02	0.00
K_2O	0.00	0.01	0.01	0.01
Cr_2O_3	0.00	0.00	0.00	0.00
Structural formula calculated on the basis of 14 O				
Si	2.74	2.71	2.73	2.71
Al^{iv}	1.26	1.29	1.27	1.29
Al^{vi}	1.12	1.16	1.12	1.12
Mg	1.93	1.91	1.94	1.95
Fe^{2+}	1.83	1.96	1.83	1.96
Fe^{3+}	0.78	0.69	0.78	0.69
Sum other elmts	0.01	0.01	0.01	0.01
Oct Sum	5.68	5.72	5.69	5.74
XMg	0.51	0.49	0.51	0.50
XFe^{3+}	30	26	30	26
T (^{o}C) Vidal (2006)	257	271	258	281
T(^{o}C) Inoue (2009)	273	294	277	304
T(°C) H&V (1992)	305	316	309	316

Appendix D1. (continued)

	P1-161-4	P1-161-5	P1-161-6	P1-161-7	P1-161-10	P1-161-11	P1-161-27	P1-161-28	P1-161-29	P1-161-30	P1-161-31	P1-161-34	P1-161-35	P1-161-39	P1-161-40	P1-161-41
SiO_2	29.13	28.57	28.87	28.25	29.46	28.45	29.96	28.90	29.30	29.16	33.55	28.90	29.68	29.10	28.52	27.94
TiO_2	0.02	0.00	0.00	0.02	0.01	0.00	0.05	0.00	0.02	0.02	0.03	0.02	0.00	0.03	0.00	0.02
Al_2O_3	17.88	16.92	17.34	16.59	17.21	16.50	18.35	17.60	17.88	17.70	16.36	17.26	17.73	17.84	17.45	16.95
FeO	29.69	29.47	29.67	29.40	28.96	28.83	29.01	29.81	29.43	29.59	27.82	28.62	28.51	29.06	28.84	29.38
MnO	0.36	0.35	0.36	0.34	0.35	0.38	0.31	0.30	0.41	0.36	0.31	0.29	0.30	0.31	0.31	0.35
MgO	14.00	15.06	13.69	13.74	14.25	14.41	13.80	14.26	13.68	14.08	11.76	14.20	12.34	13.70	14.56	14.48
CaO	0.05	0.28	0.13	0.16	0.14	0.16	0.15	0.07	0.01	0.12	0.26	0.24	0.33	0.08	0.03	0.05
Na_2O	0.01	0.00	0.01	0.03	0.01	0.01	0.00	0.00	0.01	0.02	0.03	0.02	0.00	0.02	0.02	0.00
K_2O	0.05	0.01	0.02	0.02	0.00	0.01	0.05	0.02	0.01	0.01	0.02	0.01	0.01	0.07	0.02	0.00
Cr_2O_3	0.00	0.00	0.00	0.00	0.00	0.00	0.00	0.00	0.00	0.00	0.00	0.00	0.00	0.00	0.00	0.00
Structural formula calculated on the basis of 14 O																
Si	2.92	2.90	2.86	2.91	2.93	2.94	2.91	2.94	2.88	2.92	2.90	2.90	2.91	2.87	2.92	2.88
Al^{iv}	1.08	1.10	1.14	1.09	1.07	1.06	1.09	1.06	1.12	1.08	1.10	1.10	1.09	1.13	1.08	1.12
Al^{vi}	0.96	0.99	0.86	0.97	0.97	0.97	0.96	1.06	0.95	1.02	0.98	1.03	0.97	0.91	1.03	0.95
Mg	2.11	2.08	2.25	2.06	2.01	2.12	2.12	2.02	2.12	2.03	2.09	2.09	2.13	2.16	2.05	2.19
Fe^{2+}	1.47	1.52	1.48	1.51	1.58	1.43	1.45	1.38	1.52	1.50	1.52	1.47	1.42	1.55	1.49	1.46
Fe^{3+}	0.98	0.95	0.99	0.99	0.97	0.99	0.99	1.00	0.97	0.96	0.95	0.94	0.99	0.97	0.95	0.97
Sum other elmts	0.05	0.04	0.06	0.05	0.05	0.05	0.05	0.04	0.03	0.04	0.05	0.04	0.05	0.04	0.04	0.03
Oct Sum	5.57	5.58	5.64	5.57	5.57	5.55	5.57	5.50	5.60	5.55	5.58	5.56	5.57	5.63	5.55	5.60
XMg	0.59	0.58	0.60	0.58	0.56	0.60	0.59	0.59	0.58	0.58	0.58	0.59	0.60	0.58	0.58	0.60
XFe^{3+}	40	39	40	40	38	41	41	42	39	39	39	39	41	39	39	40
T (^oC) Vidal (2006)	143	149	209	176	113	122	166	153	175	124	142	140	153	185	131	187
T(^oC) Inoue (2009)	202	206	237	203	197	193	203	178	218	193	205	199	200	232	194	222
T(°C) H&V (1992)	215	225	242	220	207	203	218	203	232	212	221	222	216	238	214	236

Appendix D1. (continued)

	P1-161-42	P1-161-43	P1-161-44
SiO_2	27.96	28.67	29.14
TiO_2	0.03	0.04	0.00
Al_2O_3	17.17	17.79	17.10
FeO	29.40	29.36	28.72
MnO	0.34	0.37	0.33
MgO	13.54	13.30	12.26
CaO	0.07	0.07	0.10
Na_2O	0.01	0.03	0.01
K_2O	0.04	0.02	0.03
Cr_2O_3	0.00	0.00	0.00
Structural formula calculated on the basis of 14 O			
Si	2.85	2.87	2.90
Al^{iv}	1.15	1.13	1.10
Al^{vi}	0.89	0.96	1.03
Mg	2.20	2.08	2.01
Fe^{2+}	1.54	1.57	1.55
Fe^{3+}	0.97	0.96	0.94
Sum other elmts	0.04	0.04	0.04
Oct Sum	5.64	5.60	5.56
XMg	0.59	0.57	0.56
XFe^{3+}	39	38	38
T (^{o}C) Vidal (2006)	200	173	141
T(^{o}C) Inoue (2009)	243	219	199
T(°C) H&V (1992)	246	235	221

Appendix D2. All electron microprobe mica analyses for selected listvenite surface samples in the KSM

	KP21-m1	KP21-m2	KP21-m3	KP21-m4	KP21-m5	KP21-m6	KP21-m7	KP21-m8	KP21-m9	KP21-m10	KP21-m11	KP21-m12	KP21-m13	KP21-m14
SiO_2	48.26	47.82	47.70	48.02	48.27	47.99	48.16	47.27	47.36	48.25	47.83	47.89	48.86	48.39
TiO_2	0.22	0.32	0.15	0.16	0.20	0.18	0.16	0.18	0.28	0.23	0.28	0.25	0.14	0.23
Al_2O_3	36.13	35.34	36.28	35.68	35.75	35.65	36.19	35.45	35.47	35.97	35.13	35.47	35.95	35.25
Cr_2O_3	1.31	1.27	1.15	1.40	1.47	1.45	1.17	1.27	1.36	1.43	1.46	1.42	1.58	1.61
FeO	0.76	0.87	0.63	0.69	0.75	0.73	0.62	0.65	0.82	0.69	0.80	0.84	0.81	0.69
Fe_2O_3	n.d.	n.d.	n.d.	n.d.	n.d.	n.d.	n.d.	n.d.	n.d.	n.d.	n.d.	n.d.	n.d.	n.d.
MnO	0.04	0.06	0.08	0.04	0.06	0.06	0.03	0.05	0.00	0.02	0.00	0.04	0.02	0.03
MgO	0.90	1.15	0.90	0.97	0.93	0.89	0.83	0.95	0.95	0.96	0.99	1.02	0.99	1.10
CaO	0.00	0.00	0.00	0.00	0.00	0.00	0.00	0.02	0.32	0.00	0.14	0.00	0.02	0.00
Na_2O	0.39	0.35	0.43	0.50	0.51	0.35	0.48	0.44	0.35	0.32	0.37	0.38	0.42	0.28
K_2O	10.48	10.77	10.54	10.21	10.46	10.66	10.43	10.48	10.31	10.68	10.55	10.64	10.49	10.65
F	0.02	0.05	0.08	0.16	0.06	0.08	0.00	0.11	0.00	0.10	0.21	0.22	0.14	0.19
Cl	0.04	0.09	0.08	0.08	0.08	0.05	0.04	0.10	0.07	0.03	0.06	0.08	0.03	0.05
Total	98.53	98.09	98.01	97.91	98.54	98.08	98.11	96.97	97.29	98.67	97.81	98.25	99.45	98.47
Si	3.10	3.10	3.08	3.11	3.10	3.10	3.10	3.09	3.09	3.10	3.11	3.10	3.11	3.12
Ti	0.01	0.02	0.01	0.01	0.01	0.01	0.01	0.01	0.01	0.01	0.01	0.01	0.01	0.01
Al(iv)	0.90	0.90	0.92	0.89	0.90	0.90	0.90	0.91	0.91	0.90	0.89	0.90	0.89	0.88
Al(vi)	1.83	1.80	1.85	1.83	1.81	1.82	1.85	1.83	1.81	1.82	1.80	1.81	1.81	1.80
Cr	0.07	0.07	0.06	0.07	0.07	0.07	0.06	0.07	0.07	0.07	0.07	0.07	0.08	0.08
$*Fe^{2+}$	0.04	0.05	0.03	0.04	0.04	0.04	0.03	0.04	0.04	0.04	0.04	0.05	0.04	0.04
Mn	0.00	0.00	0.00	0.00	0.00	0.00	0.00	0.00	0.00	0.00	0.00	0.00	0.00	0.00
Mg	0.09	0.11	0.09	0.09	0.09	0.09	0.08	0.09	0.09	0.09	0.10	0.10	0.09	0.11
Ca	0.00	0.00	0.00	0.00	0.00	0.00	0.00	0.00	0.02	0.00	0.01	0.00	0.00	0.00
Na	0.05	0.04	0.05	0.06	0.06	0.04	0.06	0.06	0.04	0.04	0.05	0.05	0.05	0.04
K	0.86	0.89	0.87	0.84	0.86	0.88	0.86	0.87	0.86	0.88	0.87	0.88	0.85	0.88
Xprl	0.09	0.07	0.08	0.09	0.08	0.08	0.08	0.07	0.08	0.08	0.07	0.07	0.09	0.09
Xms	0.86	0.89	0.87	0.84	0.86	0.88	0.86	0.87	0.86	0.88	0.87	0.88	0.85	0.88
Xpg	0.05	0.04	0.05	0.06	0.06	0.04	0.06	0.06	0.04	0.04	0.05	0.05	0.05	0.04
T0 (^oC)	295	298	306	292	291	289	298	301	296	292	285	296	288	290
T2kbar (^oC)	334	338	347	330	328	327	337	341	335	331	322	335	325	323
T3kbar (^oC)	353	357	368	349	347	346	356	361	354	350	340	355	343	339

*All Fe reported as Fe^{2+}. n.d = not determined Xprl = pyrophyllite (mol%), Xms = muscovite (mol%), Xpg = paragonite (mol%)

T (^oC) calculated after the method of Dubaq et al. (2009)

Appendix D2. *(Continued)*

	KP21-m15	KP21-m16	KP21-m17	KP21-m18	KP21-m19	KP21-m20	KP21-m21
SiO_2	46.58	48.09	47.60	47.85	47.87	47.78	47.77
TiO_2	0.21	0.20	0.18	0.20	0.18	0.17	0.17
Al_2O_3	35.05	35.20	35.77	34.78	35.92	36.18	35.80
Cr_2O_3	1.61	1.62	1.41	1.68	1.19	1.31	1.37
FeO	1.54	0.86	0.68	0.91	0.65	0.61	0.85
Fe_2O_3	n.d.	n.d.	n.d.	n.d.	n.d.	n.d.	n.d.
MnO	0.07	0.04	0.03	0.06	0.02	0.01	0.00
MgO	1.33	1.12	0.91	1.09	0.90	0.86	1.04
CaO	0.26	0.00	0.01	0.00	0.01	0.01	0.01
Na_2O	0.34	0.34	0.39	0.37	0.41	0.48	0.48
K2O	10.24	10.60	10.50	10.66	10.46	10.40	10.54
F	0.19	0.27	0.13	0.08	0.00	0.22	0.19
Cl	0.09	0.07	0.03	0.06	0.07	0.04	0.07
Total	97.50	98.41	97.64	97.76	97.68	98.08	98.29
Si	3.05	3.11	3.09	3.11	3.10	3.09	3.09
Ti	0.01	0.01	0.01	0.01	0.01	0.01	0.01
Al(iv)	0.95	0.89	0.91	0.89	0.90	0.91	0.91
Al(vi)	1.76	1.79	1.83	1.78	1.84	1.84	1.82
Cr	0.08	0.08	0.07	0.09	0.06	0.07	0.07
*Fe^{2+}	0.08	0.05	0.04	0.05	0.04	0.03	0.05
Mn	0.00	0.00	0.00	0.00	0.00	0.00	0.00
Mg	0.13	0.11	0.09	0.11	0.09	0.08	0.10
Ca	0.02	0.00	0.00	0.00	0.00	0.00	0.00
Na	0.04	0.04	0.05	0.05	0.05	0.06	0.06
K	0.86	0.87	0.87	0.88	0.86	0.86	0.87
Xprl	0.08	0.08	0.08	0.07	0.08	0.08	0.07
Xms	0.86	0.87	0.87	0.88	0.86	0.86	0.87
Xpg	0.04	0.04	0.05	0.05	0.05	0.06	0.06
T0 (^oC)	305	288	301	283	302	305	304
T2kbar (^oC)	347	325	340	320	340	345	346
T3kbar (^oC)	368	344	360	339	359	366	367

*All Fe reported as Fe^{2+}. n.d = not determined Xprl = pyrophyllite (mol%), Xms = muscovite (mol%), Xpg = paragonite (mol%)

T (^oC) calculated after the method of Dubaq et al. (2009)

Appendix D2. *(Continued)*

	KA17-m1	KA17-m2	KA17-m3	KA17-m4	KA17-m5	KA17-m6	KA17-m7	KA17-m8	KA17-m9	KA17-m10	KA17-m11	KA17-m12	KA17-m13	KA17-m14
SiO_2	48.78	47.65	46.71	47.82	47.18	46.48	47.58	47.40	47.77	47.40	47.28	47.46	49.02	47.61
TiO_2	0.19	0.16	0.31	0.11	0.32	0.13	0.19	0.24	0.22	0.20	0.27	0.25	0.09	0.14
Al_2O_3	35.92	34.55	33.22	34.57	33.09	35.28	36.03	34.29	34.71	35.06	34.73	36.34	34.21	35.94
Cr_2O_3	1.17	1.92	2.04	1.56	2.57	1.16	1.74	1.95	1.87	2.20	1.95	2.88	0.93	1.63
FeO	0.59	0.83	1.17	0.74	1.58	1.26	0.52	0.80	0.74	0.99	0.80	1.60	0.72	0.44
Fe_2O_3	n.d.	n.d.	n.d.	n.d.	n.d.	n.d.	n.d.	n.d.	n.d.	n.d.	n.d.	n.d.	n.d.	n.d.
MnO	0.02	0.06	0.06	0.01	0.04	0.06	0.04	0.04	0.00	0.08	0.05	0.10	0.02	0.00
MgO	0.97	1.23	1.16	0.95	1.57	0.82	0.82	1.15	1.14	1.10	1.01	0.66	1.25	0.76
CaO	0.00	0.02	0.02	0.02	0.02	0.00	0.00	0.01	0.00	0.02	0.02	0.03	0.02	0.00
Na_2O	0.56	0.47	0.45	0.56	0.34	0.38	0.53	0.48	0.44	0.48	0.47	0.35	0.37	0.42
K2O	10.45	10.54	10.58	10.00	10.37	10.32	10.17	10.15	10.37	10.35	10.36	10.08	9.77	10.22
F	0.29	0.38	0.21	0.06	0.21	0.09	0.31	0.01	0.27	0.25	0.18	0.00	0.26	0.13
Cl	0.06	0.06	0.10	0.10	0.08	0.06	0.04	0.05	0.08	0.06	0.07	0.11	0.28	0.01
Total	99.00	97.87	96.02	96.50	97.37	96.04	97.97	96.57	97.62	98.19	97.19	99.86	96.94	97.29
Si	3.12	3.11	3.11	3.14	3.11	3.08	3.08	3.11	3.11	3.08	3.10	3.03	3.19	3.09
Ti	0.01	0.01	0.02	0.01	0.02	0.01	0.01	0.01	0.01	0.01	0.01	0.01	0.00	0.01
Al(iv)	0.88	0.89	0.89	0.86	0.89	0.92	0.92	0.89	0.89	0.92	0.90	0.97	0.81	0.91
Al(vi)	1.83	1.76	1.72	1.81	1.67	1.83	1.83	1.77	1.78	1.76	1.78	1.77	1.82	1.85
Cr	0.06	0.10	0.11	0.08	0.13	0.06	0.09	0.10	0.10	0.11	0.10	0.15	0.05	0.08
*Fe^{2+}	0.03	0.05	0.07	0.04	0.09	0.07	0.03	0.04	0.04	0.05	0.04	0.09	0.04	0.02
Mn	0.00	0.00	0.00	0.00	0.00	0.00	0.00	0.00	0.00	0.00	0.00	0.01	0.00	0.00
Mg	0.09	0.12	0.12	0.09	0.15	0.08	0.08	0.11	0.11	0.11	0.10	0.06	0.12	0.07
Ca	0.00	0.00	0.00	0.00	0.00	0.00	0.00	0.00	0.00	0.00	0.00	0.00	0.00	0.00
Na	0.07	0.06	0.06	0.07	0.04	0.05	0.07	0.06	0.06	0.06	0.06	0.04	0.05	0.05
K	0.85	0.88	0.90	0.84	0.87	0.87	0.84	0.85	0.86	0.86	0.87	0.82	0.81	0.85
Xprl	0.08	0.06	0.04	0.09	0.08	0.08	0.09	0.09	0.08	0.08	0.07	0.13	0.14	0.10
Xms	0.85	0.88	0.90	0.84	0.87	0.87	0.84	0.85	0.86	0.86	0.87	0.82	0.81	0.85
Xpg	0.07	0.06	0.06	0.07	0.04	0.05	0.07	0.06	0.06	0.06	0.06	0.04	0.05	0.05
T0 (^oC)	296	288	290	286	284	312	303	290	290	294	287	311	261	297
T2kbar (^oC)	329	326	323	317	319	354	342	323	325	334	325	351	292	335
T3kbar (^oC)	346	345	339	333	337	375	361	340	342	354	344	372	308	354

*All Fe reported as Fe^{2+}. n.d = not determined Xprl = pyrophyllite (mol%), Xms = muscovite (mol%), Xpg = paragonite (mol%)

T (^oC) calculated after the method of Dubaq et al. (2009)

Appendix D2. *(Continued)*

	KA17-m15	KA17-m16	KA17-m17	KA17-m18	KA17-m19	KA17-m20	KA17-m21	KA17-m22	KA17-m23	KA17-m24	KA17-m25
SiO_2	47.42	48.78	47.52	47.65	46.40	48.07	47.53	47.37	48.19	47.61	47.66
TiO_2	0.21	0.28	0.28	0.12	0.95	0.10	0.11	0.04	0.11	0.07	0.12
Al_2O_3	35.13	34.71	36.04	35.54	34.92	35.70	36.39	35.21	35.71	35.74	35.87
Cr_2O_3	1.79	2.01	1.66	1.69	1.77	1.28	1.66	1.65	1.11	1.56	1.49
FeO	0.97	0.97	0.56	0.90	0.75	0.59	0.59	0.63	0.42	0.66	0.56
Fe_2O_3	n.d.	n.d.	n.d.	n.d.	n.d.	n.d.	n.d.	n.d.	n.d.	n.d.	n.d.
MnO	0.06	0.04	0.03	0.02	0.00	0.04	0.01	0.05	0.03	0.04	0.01
MgO	1.04	1.28	0.86	1.07	1.02	0.96	0.84	0.95	0.93	0.94	0.89
CaO	0.08	0.02	0.00	0.04	0.02	0.02	0.03	0.01	0.01	0.04	0.00
Na_2O	0.40	0.33	0.51	0.51	0.48	0.50	0.48	0.42	0.47	0.54	0.50
K2O	10.13	9.87	10.36	9.94	10.35	10.03	10.29	10.28	9.99	10.15	10.30
F	0.09	0.20	0.13	0.35	0.28	0.07	0.12	0.04	0.04	0.29	0.24
Cl	0.06	0.08	0.02	0.12	0.04	0.05	0.05	0.07	0.02	0.07	0.05
Total	97.36	98.57	97.98	97.95	96.98	97.41	98.10	96.72	97.03	97.72	97.68
Si	3.09	3.14	3.07	3.09	3.05	3.11	3.07	3.10	3.13	3.09	3.09
Ti	0.01	0.01	0.01	0.01	0.05	0.00	0.01	0.00	0.01	0.00	0.01
Al(iv)	0.91	0.86	0.93	0.91	0.95	0.89	0.93	0.90	0.87	0.91	0.91
Al(vi)	1.79	1.77	1.82	1.81	1.76	1.84	1.84	1.82	1.86	1.83	1.84
Cr	0.09	0.10	0.08	0.09	0.09	0.07	0.08	0.09	0.06	0.08	0.08
*Fe^{2+}	0.05	0.05	0.03	0.05	0.04	0.03	0.03	0.03	0.02	0.04	0.03
Mn	0.00	0.00	0.00	0.00	0.00	0.00	0.00	0.00	0.00	0.00	0.00
Mg	0.10	0.12	0.08	0.10	0.10	0.09	0.08	0.09	0.09	0.09	0.09
Ca	0.01	0.00	0.00	0.00	0.00	0.00	0.00	0.00	0.00	0.00	0.00
Na	0.05	0.04	0.06	0.06	0.06	0.06	0.06	0.05	0.06	0.07	0.06
K	0.84	0.81	0.86	0.82	0.87	0.83	0.85	0.86	0.83	0.84	0.85
Xprl	0.10	0.15	0.08	0.11	0.07	0.11	0.09	0.09	0.11	0.09	0.08
Xms	0.84	0.81	0.86	0.82	0.87	0.83	0.85	0.86	0.83	0.84	0.85
Xpg	0.05	0.04	0.06	0.06	0.06	0.06	0.06	0.05	0.06	0.07	0.06
T0 (^oC)	292	268	305	296	306	293	312	292	297	304	300
T2kbar (^oC)	330	302	346	334	347	329	354	330	330	342	340
T3kbar (^oC)	349	319	366	354	367	348	374	349	346	361	359

*All Fe reported as Fe^{2+}. n.d = not determined Xprl = pyrophyllite (mol%), Xms = muscovite (mol%), Xpg = paragonite (mol%)

T (^oC) calculated after the method of Dubaq et al. (2009)

Appendix D2. *(Continued)*

	KP1-2m1	KP1-2m2	KP1-2m3	KP1-2m4	KP1-2m5	KP1-2m6	KP1-2m7	KP1-2m8	KP1-2m9	KP1-2m10	KP1-2m11	KP1-2m12	KP1-2m13	KP1-2m14
SiO_2	46.40	46.56	47.79	46.50	46.20	46.17	48.02	47.93	46.90	45.29	48.35	48.14	47.37	48.01
TiO_2	0.15	0.20	0.16	0.24	0.16	0.22	0.19	0.12	0.16	0.04	0.27	0.13	0.18	0.16
Al_2O_3	35.91	35.39	36.55	32.18	33.44	35.38	36.04	35.12	35.74	36.31	35.80	37.47	35.78	36.67
Cr_2O_3	1.12	1.20	1.07	0.62	2.01	1.35	1.16	0.59	1.29	0.39	1.61	1.40	1.74	1.41
FeO	0.66	0.64	0.68	1.51	1.09	0.63	0.71	1.16	0.91	0	1.23	0.59	0.84	0.77
Fe_2O_3	n.d.	n.d.	n.d.	n.d.	n.d.	n.d.	n.d.	n.d.	n.d.	n.d.	n.d.	n.d.	n.d.	n.d.
MnO	0.00	0.05	0.03	0.06	0.07	0.00	0.06	0.04	0.06	0.04	0.07	0.03	0.03	0.06
MgO	0.89	1.02	1.00	1.74	1.24	0.90	0.94	1.27	0.97	0.68	1.04	0.72	0.82	0.83
CaO	0.16	0.20	0.07	0.04	0.02	0.12	0.07	0.03	0.01	0.03	0.13	0.04	0.08	0.07
Na_2O	0.70	0.64	0.56	0.21	0.32	0.66	0.54	0.28	0.38	0.31	0.56	0.86	0.67	0.63
K2O	10.28	10.42	10.49	10.75	10.72	10.37	10.47	10.62	10.51	10.37	10.11	9.93	10.11	10.21
F	0.11	0.28	0.05	0.12	0.05	0.03	0.23	0.09	0.25	0	0.11	0.00	0.08	0.17
Cl	0.13	0.15	0.07	0.05	0.03	0.12	0.09	0.02	0.03	0.00	0.11	0.13	0.14	0.10
Total	96.51	96.77	98.52	94.02	95.36	95.96	98.52	97.27	97.21	93.46	99.39	99.45	97.84	99.09
Si	3.05	3.07	3.07	3.16	3.10	3.06	3.09	3.12	3.07	3.05	3.09	3.06	3.07	3.07
Ti	0.01	0.01	0.01	0.01	0.01	0.01	0.01	0.01	0.01	0.00	0.01	0.01	0.01	0.01
Al(iv)	0.95	0.93	0.93	0.84	0.90	0.94	0.91	0.88	0.93	0.95	0.91	0.94	0.93	0.93
Al(vi)	1.84	1.81	1.84	1.73	1.74	1.82	1.83	1.82	1.83	1.93	1.79	1.86	1.81	1.84
Cr	0.06	0.06	0.05	0.03	0.11	0.07	0.06	0.03	0.07	0.02	0.08	0.07	0.09	0.07
*Fe^{2+}	0.04	0.04	0.04	0.09	0.06	0.03	0.04	0.06	0.05	0.00	0.07	0.03	0.05	0.04
Mn	0.00	0.00	0.00	0.00	0.00	0.00	0.00	0.00	0.00	0.00	0.00	0.00	0.00	0.00
Mg	0.09	0.10	0.10	0.18	0.12	0.09	0.09	0.12	0.09	0.07	0.10	0.07	0.08	0.08
Ca	0.01	0.01	0.00	0.00	0.00	0.01	0.00	0.00	0.00	0.00	0.01	0.00	0.01	0.00
Na	0.09	0.08	0.07	0.03	0.04	0.09	0.07	0.04	0.05	0.04	0.07	0.11	0.08	0.08
K	0.86	0.88	0.86	0.93	0.92	0.88	0.86	0.88	0.88	0.89	0.82	0.80	0.84	0.83
Xprl	0.04	0.03	0.06	0.04	0.04	0.03	0.07	0.08	0.07	0.07	0.10	0.09	0.07	0.08
Xms	0.86	0.88	0.86	0.93	0.92	0.88	0.86	0.88	0.88	0.89	0.82	0.80	0.84	0.83
Xpg	0.09	0.08	0.07	0.03	0.04	0.09	0.07	0.04	0.05	0.04	0.07	0.11	0.08	0.08
T0 (^oC)	342	334	318	281	304	343	301	290	310	342	295	326	311	314
T2kbar (^oC)	392	382	361	323	348	393	341	329	354	392	334	369	351	355
T3kbar (^oC)	417	406	383	345	370	417	361	348	376	417	353	390	371	375

*All Fe reported as Fe^{2+}. n.d = not determined Xprl = pyrophyllite (mol%), Xms = muscovite (mol%), Xpg = paragonite (mol%)

T (^oC) calculated after the method of Dubaq et al. (2009)

Appendix D2. *(Continued)*

	KP1-2m15	KP1-2m16	KP1-2m17	KP1-2m18	KP1-2m19	KP1-2m20	KP1-2m21	KP1-2m22	KP1-2m23	KP1-2m24	KP1-2m25	KP1-2m26	KP1-2m27	KP1-2m28
SiO_2	46.39	47.91	47.23	46.86	46.97	48.71	46.65	46.94	47.52	47.17	46.85	47.52	47.03	47.62
TiO_2	0.19	0.17	0.12	0.18	1.09	0.32	0.20	0.15	0.04	0.20	0.16	0.12	0.09	0.16
Al_2O_3	36.56	36.58	36.69	35.48	36.13	37.34	36.02	36.08	36.73	35.56	35.26	36.19	35.62	36.35
Cr_2O_3	1.18	1.52	1.26	1.54	1.19	1.36	1.29	1.06	1.04	1.38	1.33	1.33	0.98	1.06
FeO	0.60	0.73	0.60	2.34	0.78	0.66	0.63	1.12	0.93	0.63	0.65	0.66	0.55	0.62
Fe_2O_3	n.d.	n.d.	n.d.	n.d.	n.d.	n.d.	n.d.	n.d.	n.d.	n.d.	n.d.	n.d.	n.d.	n.d.
MnO	0.01	0.08	0.04	0.03	0.06	0.05	0.05	0.01	0.04	0.04	0.01	0.04	0.03	0.05
MgO	0.67	0.84	0.69	1.68	0.70	0.84	0.80	1.12	0.57	0.94	0.91	0.93	0.88	0.88
CaO	0.08	0.10	0.13	0.09	0.07	0.03	0.05	0.06	0.22	0.16	0.25	0.09	0.21	0.02
Na_2O	0.69	0.60	1.26	0.63	0.94	0.62	0.93	0.75	0.84	0.59	0.80	0.67	1.39	0.85
K2O	10.24	10.44	9.33	9.52	9.60	10.23	10.05	10.01	9.34	10.37	9.78	10.39	9.27	9.96
F	0.06	0.00	0.00	0.09	0.06	0.00	0.16	0.03	0.03	0.08	0.19	0.16	0.00	0.11
Cl	0.13	0.12	0.14	0.13	0.12	0.08	0.12	0.10	0.06	0.11	0.15	0.14	0.23	0.10
Total	96.80	99.08	97.50	98.58	97.70	100.24	96.94	97.43	97.35	97.22	96.35	98.24	96.29	97.79
Si	3.04	3.07	3.06	3.04	3.04	3.07	3.06	3.06	3.08	3.08	3.08	3.07	3.09	3.08
Ti	0.01	0.01	0.01	0.01	0.05	0.02	0.01	0.01	0.00	0.01	0.01	0.01	0.00	0.01
Al(iv)	0.96	0.93	0.94	0.96	0.96	0.93	0.94	0.94	0.92	0.92	0.92	0.93	0.91	0.92
Al(vi)	1.86	1.83	1.86	1.74	1.80	1.84	1.84	1.83	1.88	1.82	1.82	1.83	1.84	1.85
Cr	0.06	0.08	0.06	0.08	0.06	0.07	0.07	0.05	0.05	0.07	0.07	0.07	0.05	0.05
$*Fe^{2+}$	0.03	0.04	0.03	0.13	0.04	0.03	0.03	0.06	0.05	0.03	0.04	0.04	0.03	0.03
Mn	0.00	0.00	0.00	0.00	0.00	0.00	0.00	0.00	0.00	0.00	0.00	0.00	0.00	0.00
Mg	0.07	0.08	0.07	0.16	0.07	0.08	0.08	0.11	0.05	0.09	0.09	0.09	0.09	0.08
Ca	0.01	0.01	0.01	0.01	0.00	0.00	0.00	0.00	0.02	0.01	0.02	0.01	0.02	0.00
Na	0.09	0.07	0.16	0.08	0.12	0.08	0.12	0.09	0.11	0.08	0.10	0.08	0.18	0.11
K	0.86	0.85	0.77	0.79	0.79	0.82	0.84	0.83	0.77	0.86	0.82	0.86	0.78	0.82
Xprl	0.05	0.07	0.06	0.13	0.08	0.10	0.04	0.07	0.11	0.05	0.06	0.05	0.03	0.07
Xms	0.86	0.85	0.77	0.79	0.79	0.82	0.84	0.83	0.77	0.86	0.82	0.86	0.78	0.82
Xpg	0.09	0.07	0.16	0.08	0.12	0.08	0.12	0.09	0.11	0.08	0.10	0.08	0.18	0.11
T0 (^oC)	342	311	331	302	317	311	337	323	322	308	303	317	312	313
T2kbar (^oC)	392	354	374	338	356	352	385	368	363	348	342	361	346	355
T3kbar (^oC)	417	375	395	356	376	372	409	391	383	368	362	383	364	377

*All Fe reported as Fe^{2+}. n.d = not determined Xprl = pyrophyllite (mol%), Xms = muscovite (mol%), Xpg = paragonite (mol%)

T (^oC) calculated after the method of Dubaq et al. (2009)

Appendix E1. Major and trace element data determined by XRF across the KSM

Sample	KD1-T1	KD1-T2	KD1-T4	KD1-T3	KD1-T5	KD1-T6	KD1-T7	KD1-T8	KD1-T9	KD1-T10	KD1-T11	KD1-T12	KD1-T13	KD1-T14
SiO_2	87.85	91.07	83.42	25.96	42.74	55.10	64.37	72.37	86.59	52.25	45.04	54.06	55.96	54.95
TiO_2	0.07	0.07	0.07	0.78	1.00	1.50	0.95	1.20	0.10	0.77	0.63	0.29	0.89	0.88
Al_2O_3	1.16	1.14	1.33	7.30	10.22	14.60	9.04	11.07	1.73	12.67	10.51	5.09	16.06	15.09
Fe_2O_3	2.45	2.12	2.32	12.42	7.59	8.04	8.30	5.57	2.38	8.94	9.23	9.06	8.90	7.90
MnO	0.08	0.08	0.13	0.46	0.44	0.18	0.15	0.05	0.12	0.29	0.53	0.31	0.12	0.17
MgO	1.54	0.98	2.15	9.57	6.22	3.96	4.49	2.79	1.47	5.23	6.32	4.66	4.92	5.17
CaO	2.21	1.20	4.08	16.49	11.22	4.66	3.60	0.53	2.30	5.43	9.73	5.43	2.35	3.43
Na_2O	0.11	0.19	0.13	0.02	0.66	1.09	1.24	0.27	0.13	0.14	0.06	0.09	1.34	1.15
K_2O	0.16	0.11	0.30	1.18	2.31	2.84	0.67	2.12	0.35	2.97	2.33	0.14	2.59	2.87
P_2O_5	0.02	0.01	0.01	0.07	0.15	0.18	0.08	0.10	0.02	0.12	0.13	0.02	0.14	0.18
SO_3	0.20	0.06	0.10	0.47	1.42	0.12	0.26	0.21	0.23	0.10	0.12	0.26	0.43	0.47
Cr_2O_3	0.02	0.02	0.02	0.04	0.01	0.01	0.06	0.17	0.02	0.22	0.21	0.08	0.33	0.30
NiO	0.02	0.01	0.02	0.02	0.01	0.01	0.03	0.02	0.02	0.07	0.07	0.05	0.15	0.11
H2O-	0.03	0.10	0.03	0.14	0.08	0.06	0.03	0.20	0.06	0.01	0.04	0.06	0.06	0.00
LOI	3.67	2.06	6.01	25.01	15.91	7.65	6.65	2.97	3.84	10.18	14.87	19.84	5.20	6.80
Total	99.58	99.25	100.11	99.95	100.01	100.03	99.90	99.63	99.36	99.40	99.83	99.44	99.45	99.49
Mo	2.7	3.0	1.7	1.9	b.d.l	b.d.l	b.d.l	b.d.l	b.d.l	b.d.l	1.2	10.3	b.d.l	b.d.l
Nb	3.2	3.7	6.1	3.6	6.5	8.8	5.5	6.3	3.4	4.5	4.2	4.1	4.5	4.4
Zr	3.3	3.4	44.9	3.2	65.0	102.6	48.0	62.7	7.0	41.2	32.8	18.6	46.2	43.3
Y	5.2	1.0	16.1	3.5	18.4	23.9	9.0	10.6	3.2	15.9	18.2	11.1	15.3	17.2
Sr	5.6	3.4	31.9	7.2	19.2	22.7	12.5	4.6	4.4	13.8	16.8	8.3	13.6	13.1
U	b.d.l	b.d.l	b.d.l	b.d.l	b.d.l	b.d.l	b.d.l	b.d.l	b.d.l	b.d.l	b.d.l	b.d.l	b.d.l	b.d.l
Th	b.d.l	b.d.l	b.d.l	b.d.l	b.d.l	b.d.l	b.d.l	b.d.l	b.d.l	b.d.l	b.d.l	b.d.l	b.d.l	b.d.l
Rb	4.3	3.4	32.5	8.4	64.9	80.7	19.7	63.2	9.5	88.4	71.2	3.8	78.2	85.4
Pb	b.d.l	b.d.l	b.d.l	b.d.l	b.d.l	b.d.l	b.d.l	b.d.l	b.d.l	b.d.l	b.d.l	b.d.l	b.d.l	b.d.l
Zn	11.2	11.6	79.9	7.6	40.6	68.9	79.1	62.3	25.2	216.5	183.0	112.5	118.0	107.4
Cu	10.8	0.8	28.6	6.9	73.3	96.9	268.0	349.5	14.8	88.3	72.7	49.4	78.5	84.7
Ni	135.2	103.2	143.6	101.6	82.7	70.0	151.7	161.2	138.4	457.7	440.7	431.1	945.3	721.0
Co	20.1	6.6	57.4	4.2	52.5	33.8	46.7	40.8	14.1	68.4	68.4	59.1	146.0	127.5
Mn	743.1	742.9	2993.2	744.3	1824.8	1818.9	760.1	757.5	743.8	1822.0	1826.7	2180.1	1817.8	1819.0
Cr	97.5	102.1	b.d.l	94.1	b.d.l	b.d.l	349.9	1227.0	117.8	1615.6	1469.3	589.1	2639.0	2228.8
V	14.9	12.5	194.0	12.6	186.0	307.5	383.6	441.3	16.1	334.4	272.4	152.3	470.9	432.0
Ba	4.1	0.8	12.5	2.0	23.8	35.5	7.2	28.2	4.1	32.9	27.8	b.d.l	52.2	62.2
Sc	4.3	2.3	30.7	4.3	20.1	30.2	57.7	69.6	4.8	51.1	41.7	31.5	58.4	62.1

Appendix E1. *(Continued)*

Sample	KD1-T15	KD1-T16	KD1-T17	KD1-T18	KD1-T19	KD1-T20	KD1-T21	KD1-T22	KD1-T23	KD1-T24	KD1-T25	KD1-T26	KD1-T27	KD1-T28
SiO_2	55.76	42.34	40.28	44.07	43.14	50.42	42.52	42.53	44.61	51.01	50.51	48.95	46.55	49.04
TiO_2	0.86	0.76	0.61	0.60	0.58	0.90	0.69	0.71	0.83	0.80	0.80	0.80	0.76	0.89
Al_2O_3	14.64	9.93	9.74	9.32	9.34	12.77	10.91	12.46	13.88	12.94	11.84	13.61	12.45	14.59
Fe_2O_3	6.36	7.67	10.75	10.34	9.84	12.48	9.53	8.86	17.25	8.97	9.35	10.42	9.90	7.58
MnO	0.16	0.34	0.20	0.22	0.24	0.14	0.22	0.24	0.19	0.27	0.34	0.29	0.29	0.24
MgO	4.38	7.13	7.40	7.51	7.60	8.72	5.93	3.55	8.96	3.53	3.35	0.15	2.74	2.66
CaO	4.89	11.78	14.06	12.94	15.86	4.84	13.83	14.09	4.81	8.50	9.98	10.61	12.13	10.40
Na_2O	1.05	0.86	0.66	0.28	0.29	0.90	1.28	2.02	0.64	2.61	2.07	3.71	2.98	3.62
K_2O	3.14	1.75	0.20	0.04	0.05	0.15	0.42	1.28	0.01	1.25	1.04	0.64	0.61	1.27
P_2O_5	0.10	0.08	0.05	0.05	0.05	0.08	0.06	0.06	0.07	0.07	0.07	0.06	0.07	0.08
SO_3	0.29	0.42	0.51	0.48	0.07	0.06	0.20	0.70	0.04	0.23	0.24	0.38	0.23	0.20
Cr_2O_3	0.21	0.08	0.10	0.08	0.05	0.06	0.03	0.03	0.02	0.03	0.02	0.03	0.02	0.03
NiO	0.06	0.03	0.02	0.02	0.02	0.02	0.02	0.02	0.01	0.03	0.02	0.02	0.01	0.01
H2O-	0.04	0.05	0.04	0.05	0.06	0.06	0.01	0.02	0.01	0.02	0.01	0.02	0.01	0.02
LOI	7.48	16.85	15.17	13.42	12.66	7.82	13.85	13.09	8.71	9.07	10.20	9.79	11.36	9.57
Total	99.44	100.07	99.80	99.42	99.84	99.41	99.49	99.67	100.05	99.32	99.82	99.46	100.11	100.20
Mo	b.d.l	b.d.l	b.d.l	b.d.l	b.d.l	b.d.l	b.d.l	b.d.l	b.d.l	b.d.l	b.d.l	b.d.l	b.d.l	b.d.l
Nb	4.4	4.5	4.3	4.3	3.9	4.6	4.9	4.4	4.5	4.7	4.4	5.0	4.8	5.0
Zr	46.0	41.7	31.8	31.6	28.4	50.5	41.9	41.2	46.3	40.2	46.5	43.0	45.9	47.7
Y	17.0	17.2	13.0	13.8	14.2	15.7	14.8	16.8	15.8	16.9	18.6	17.7	20.8	18.3
Sr	20.3	29.2	62.6	60.2	58.8	31.5	62.6	63.8	18.6	37.0	38.5	45.7	45.7	46.2
U	b.d.l	b.d.l	b.d.l	b.d.l	b.d.l	b.d.l	b.d.l	b.d.l	b.d.l	b.d.l	b.d.l	b.d.l	b.d.l	b.d.l
Th	b.d.l	b.d.l	b.d.l	b.d.l	b.d.l	b.d.l	b.d.l	b.d.l	b.d.l	b.d.l	b.d.l	b.d.l	b.d.l	b.d.l
Rb	94.1	52.6	6.6	b.d.l	b.d.l	4.6	15.0	44.8	b.d.l	39.3	32.8	18.5	19.0	38.7
Pb	b.d.l	b.d.l	b.d.l	b.d.l	b.d.l	b.d.l	b.d.l	b.d.l	b.d.l	b.d.l	b.d.l	b.d.l	b.d.l	b.d.l
Zn	75.4	58.4	130.5	115.4	106.7	144.9	113.9	84.9	182.2	104.6	103.3	97.9	95.9	93.8
Cu	78.8	114.2	74.7	103.2	43.6	60.5	51.0	52.7	43.3	41.3	33.3	27.2	47.0	59.6
Ni	387.4	179.5	130.8	127.4	86.2	98.9	81.3	66.9	67.3	154.6	111.7	56.6	52.7	68.0
Co	56.2	37.6	46.4	48.4	35.8	51.6	41.2	41.2	63.2	70.0	36.3	24.8	37.3	53.1
Mn	1818.5	1822.7	1819.5	1819.8	1819.9	1818.3	1819.8	1820.1	1819.4	1821.1	1822.3	1820.9	1821.2	1820.2
Cr	1511.0	468.6	541.6	501.9	219.1	291.7	125.8	51.6	24.2	55.8	13.1	58.3	14.0	24.8
V	363.7	236.4	242.2	247.7	199.4	332.6	232.7	249.2	350.0	291.0	251.3	291.9	252.9	303.4
Ba	82.4	44.6	0.4	b.d.l	b.d.l	b.d.l	3.0	18.5	<1.8	20.3	14.8	4.8	6.6	17.0
Sc	56.7	36.3	37.0	36.4	30.1	45.7	33.2	33.6	46.5	33.9	35.7	39.8	37.5	40.4

Appendix E1. *(Continued)*

Sample	KD1-T29	KD1-T30	KD1-T31	KD1-T32	KD1-T33	KD1-T34	KD1-T35	KD1-T36	KD1-T37	KD1-T38	KD1-T39	KD1-T40	KD1-T41	KD1-T42
SiO_2	51.14	62.13	48.48	58.07	63.38	58.26	59.94	23.90	19.14	51.10	46.58	41.55	31.61	26.47
TiO_2	0.89	0.85	1.28	1.21	0.91	0.85	0.77	0.15	0.19	0.47	0.41	0.16	0.20	0.24
Al_2O_3	14.68	14.75	16.25	15.12	15.72	16.55	16.93	1.83	2.53	7.00	6.12	2.79	2.67	3.46
Fe_2O_3	10.35	4.95	10.32	6.80	5.75	5.85	7.22	8.24	8.65	8.58	7.47	8.31	8.60	8.87
MnO	0.20	0.11	0.19	0.14	0.08	0.12	0.08	0.96	0.97	0.26	0.29	0.77	0.85	0.87
MgO	4.84	2.27	4.16	3.30	3.34	3.37	4.36	7.26	7.98	8.31	10.17	7.38	7.92	8.83
CaO	6.26	4.12	5.99	4.51	1.39	3.31	1.08	25.93	27.62	10.19	12.01	16.55	21.05	22.50
Na_2O	2.64	2.63	3.85	3.60	3.29	3.79	3.86	0.11	0.18	0.02	0.07	0.08	0.01	0.00
K_2O	1.13	2.63	1.27	1.61	2.07	2.20	1.83	0.03	0.03	0.02	0.01	0.02	0.03	0.01
P_2O_5	0.07	0.10	0.13	0.12	0.10	0.09	0.06	0.05	0.06	0.03	0.03	0.04	0.05	0.05
SO_3	0.05	0.09	0.05	0.07	0.05	0.04	0.05	0.39	0.34	0.09	0.05	0.45	0.07	0.05
Cr_2O_3	0.02	0.02	0.01	0.01	0.03	0.03	0.04	0.16	0.19	0.38	0.27	0.20	0.20	0.30
NiO	0.02	0.02	0.02	0.02	0.02	0.01	0.02	0.04	0.04	0.05	0.05	0.07	0.05	0.07
H2O-	0.02	0.02	0.03	0.07	0.12	0.08	0.08	0.07	0.08	0.09	0.08	0.05	0.10	0.09
LOI	7.67	5.07	7.31	5.64	3.35	4.88	3.62	30.20	31.41	13.26	16.09	21.23	26.13	27.61
Total	99.97	99.79	99.33	100.29	99.60	99.44	99.93	99.31	99.38	99.85	99.71	99.66	99.54	99.41
Mo	b.d.l	b.d.l	b.d.l	b.d.l	b.d.l	b.d.l	b.d.l	b.d.l	b.d.l	b.d.l	b.d.l	b.d.l	1.9	b.d.l
Nb	5.1	5.1	5.2	5.4	4.3	4.0	4.1	3.5	3.7	4.1	3.8	3.1	4.0	3.4
Zr	45.0	63.1	74.8	68.1	45.9	44.8	37.7	4.6	7.0	20.2	15.8	3.7	7.3	9.2
Y	16.2	20.9	27.0	21.5	18.5	17.7	15.4	4.9	4.8	9.2	8.1	10.2	6.1	6.0
Sr	26.1	24.2	34.9	29.8	18.7	25.9	19.7	48.3	56.7	49.3	43.7	29.1	40.5	44.9
U	b.d.l	b.d.l	b.d.l	b.d.l	b.d.l	b.d.l	b.d.l	b.d.l	b.d.l	b.d.l	b.d.l	b.d.l	b.d.l	b.d.l
Th	b.d.l	b.d.l	b.d.l	b.d.l	b.d.l	b.d.l	b.d.l	b.d.l	b.d.l	b.d.l	b.d.l	b.d.l	b.d.l	b.d.l
Rb	36.3	84.3	42.9	53.4	68.8	75.4	60.7	1.7	b.d.l	b.d.l	b.d.l	b.d.l	b.d.l	b.d.l
Pb	b.d.l	b.d.l	b.d.l	b.d.l	b.d.l	b.d.l	b.d.l	b.d.l	b.d.l	b.d.l	b.d.l	b.d.l	b.d.l	b.d.l
Zn	166.2	104.2	180.1	112.6	92.5	83.7	111.7	67.5	82.4	130.1	141.5	104.4	118.6	120.7
Cu	64.6	60.1	49.0	76.9	87.6	64.5	68.7	18.3	16.4	172.4	90.2	11.0	14.3	23.1
Ni	85.5	89.5	112.7	108.8	112.2	90.5	127.2	215.4	275.2	392.3	445.6	448.0	384.5	518.5
Co	75.5	40.9	73.4	54.8	41.8	48.9	57.1	33.8	42.1	41.2	60.8	33.6	44.1	59.3
Mn	1819.5	759.4	1819.4	1818.3	758.4	1817.6	1817.0	3003.6	3003.3	1821.1	2177.5	2188.7	3002.6	3002.6
Cr	25.3	26.6	b.d.l	b.d.l	21.2	55.2	151.2	1024.8	1262.3	3025.6	1896.2	1267.0	1293.7	2175.5
V	347.5	299.2	402.9	376.1	377.0	369.6	384.0	49.3	70.8	309.2	270.0	67.0	85.3	103.6
Ba	18.9	44.1	22.7	33.1	46.1	51.4	45.3	b.d.l	b.d.l	b.d.l	b.d.l	b.d.l	b.d.l	b.d.l
Sc	47.0	44.9	51.2	50.9	49.5	59.6	64.0	8.9	10.9	64.0	59.9	12.7	17.1	17.0

Appendix E1. *(Continued)*

Sample	KD1-T43	KD1-T44	KD1-T45	KD1-T46	KD1-T47	KD1-T48	KD1-T49	KD1-T50	KD1-T51	KD1-T52	KD1-T53	KD1-T54	KD1-T55	KD1-T56
SiO_2	26.54	26.06	19.91	18.97	38.21	31.11	39.21	37.90	54.62	36.43	33.51	39.71	34.30	56.28
TiO_2	0.23	2.58	2.83	2.86	5.61	3.61	4.61	3.98	4.25	3.87	6.00	12.07	6.23	9.39
Al_2O_3	3.47	0.18	0.19	0.19	0.47	0.20	0.29	0.32	0.29	0.22	0.34	0.71	0.35	0.59
Fe_2O_3	8.42	7.89	8.38	8.33	11.56	8.38	8.66	7.63	7.52	8.26	9.01	13.15	11.67	6.72
MnO	0.83	0.77	0.75	0.75	0.15	0.27	0.29	0.35	0.26	0.37	0.36	0.14	0.47	0.37
MgO	8.70	9.31	10.63	14.31	21.41	14.93	12.40	12.20	9.48	11.97	13.51	11.84	18.14	6.95
CaO	23.13	22.76	24.15	21.01	6.50	15.22	12.28	14.02	8.64	14.53	11.26	0.61	19.80	7.28
Na_2O	0.18	0.06	0.06	0.07	0.16	0.14	0.13	0.06	0.09	0.07	0.06	0.11	0.11	0.82
K_2O	0.01	0.01	0.00	0.01	0.00	0.01	0.01	0.01	0.01	0.01	0.01	0.04	0.01	0.92
P_2O_5	0.06	0.03	0.03	0.02	0.05	0.01	0.03	0.03	0.02	0.02	0.03	0.05	0.03	0.08
SO_3	0.03	0.04	0.05	0.18	0.09	0.12	0.23	0.05	0.03	0.10	0.14	0.02	0.21	0.05
Cr_2O_3	0.33	0.33	0.42	0.35	0.76	0.27	0.44	0.28	0.20	0.29	0.45	0.37	0.48	0.18
NiO	0.05	0.05	0.07	0.08	0.21	0.11	0.13	0.09	0.06	0.09	0.14	0.07	0.16	0.08
H2O-	0.11	0.05	0.09	0.08	0.12	0.08	0.09	0.07	0.05	0.08	0.09	0.07	0.14	0.04
LOI	27.71	29.03	31.75	32.32	14.11	24.96	20.61	22.46	14.75	23.09	25.23	20.49	7.40	10.23
Total	99.81	99.15	99.30	99.53	99.44	99.42	99.42	99.47	100.27	99.40	100.16	99.47	99.49	99.98
Mo	b.d.l	b.d.l	b.d.l	b.d.l	b.d.l	b.d.l	b.d.l	b.d.l	b.d.l	b.d.l	b.d.l	b.d.l	b.d.l	b.d.l
Nb	3.2	3.2	3.2	3.2	4.3	3.9	3.8	3.2	3.8	2.7	3.7	3.1	4.2	3.9
Zr	7.3	6.0	6.6	4.2	23.9	6.0	11.3	12.4	13.3	8.6	11.3	14.2	36.7	26.3
Y	6.0	2.2	8.3	4.6	6.7	9.7	5.8	6.1	4.8	6.0	6.3	4.6	12.1	17.6
Sr	55.4	72.9	54.6	22.8	30.6	47.9	37.2	28.2	23.2	57.4	53.8	46.6	4.0	40.5
U	b.d.l	b.d.l	b.d.l	b.d.l	b.d.l	b.d.l	b.d.l	b.d.l	b.d.l	b.d.l	b.d.l	b.d.l	b.d.l	b.d.l
Th	b.d.l	b.d.l	b.d.l	b.d.l	b.d.l	b.d.l	b.d.l	b.d.l	b.d.l	b.d.l	b.d.l	b.d.l	b.d.l	b.d.l
Rb	b.d.l	b.d.l	b.d.l	b.d.l	b.d.l	b.d.l	b.d.l	b.d.l	b.d.l	b.d.l	b.d.l	b.d.l	2.1	36.1
Pb	b.d.l	b.d.l	b.d.l	b.d.l	b.d.l	b.d.l	b.d.l	b.d.l	b.d.l	b.d.l	b.d.l	b.d.l	b.d.l	b.d.l
Zn	82.6	88.6	101.2	97.0	210.7	122.1	126.3	93.6	100.2	154.3	166.3	209.1	366.5	174.6
Cu	14.8	14.5	8.0	4.3	64.2	21.4	55.1	0.5	22.1	13.8	33.1	61.6	2.1	43.8
Ni	418.3	381.4	543.4	548.3	1824.3	845.7	967.3	748.2	494.4	691.9	935.2	1111.0	625.5	640.0
Co	68.7	55.0	73.7	54.8	161.3	75.5	92.5	62.9	42.9	68.2	89.7	121.2	142.7	115.3
Mn	3001.5	2999.9	2999.7	3000.6	2985.3	2988.6	2989.2	2991.0	2177.0	2991.5	2991.6	2991.9	2986.5	2180.0
Cr	2331.2	2192.9	2780.9	2942.6	8113.9	2489.2	4297.1	2550.0	1737.0	2523.2	3593.2	4801.8	4836.8	1301.9
V	101.5	77.1	83.8	91.8	230.3	115.0	164.2	143.5	133.6	126.7	163.4	215.9	574.5	277.4
Ba	b.d.l	b.d.l	b.d.l	b.d.l	b.d.l	b.d.l	b.d.l	b.d.l	b.d.l	b.d.l	b.d.l	b.d.l	b.d.l	21.8
Sc	16.3	13.1	15.2	15.0	29.8	19.6	25.5	23.2	17.0	21.5	25.9	31.1	82.0	45.8

Appendix E1. *(Continued)*

Sample	KD1-T57	KD1-T58	KD1-T59	KD1-T60	KD1-T61	KD1-T61A	KD1-T62	KD1-T63	KD1-T64	KD1-T65	KD1-T66	KD1-T67	KD1-T68	KD1-T69
SiO_2	44.06	32.19	36.16	29.06	34.18	28.22	33.54	31.32	34.22	33.46	24.25	36.19	91.28	29.85
TiO_2	7.98	7.33	5.07	5.54	4.49	5.23	4.70	5.63	8.75	5.66	5.26	7.23	1.43	5.25
Al_2O_3	0.48	0.43	0.31	0.34	0.26	0.33	0.32	0.41	0.64	0.34	0.32	0.44	0.09	0.54
Fe_2O_3	9.20	8.63	6.56	8.07	8.56	10.54	8.85	10.14	14.51	9.23	7.04	10.12	1.44	8.24
MnO	0.51	0.64	0.56	0.22	0.23	0.24	0.24	0.27	0.18	0.28	0.39	0.22	0.05	0.38
MgO	9.57	8.23	7.37	7.29	9.87	12.11	9.73	10.38	14.45	8.30	5.82	8.28	0.63	5.10
CaO	12.34	21.16	21.70	25.46	19.12	17.74	20.11	20.97	11.83	22.24	33.64	18.96	2.52	29.92
Na_2O	0.12	0.24	0.04	0.08	0.11	0.08	0.00	0.06	0.09	0.05	0.04	0.10	0.01	0.01
K_2O	0.05	0.06	0.03	0.01	0.01	0.01	0.01	0.01	0.03	0.02	0.02	0.01	0.10	0.01
P_2O_5	0.08	0.05	0.03	0.03	0.02	0.03	0.02	0.04	0.05	0.02	0.03	0.03	0.02	0.18
SO_3	0.13	0.09	0.06	0.28	0.43	0.26	0.27	0.35	0.35	0.25	0.06	0.13	0.08	0.13
Cr_2O_3	0.67	0.47	0.43	0.52	0.42	0.52	0.43	0.45	0.54	0.36	0.33	0.35	0.02	0.30
NiO	0.20	0.15	0.11	0.23	0.14	0.17	0.14	0.15	0.19	0.11	0.09	0.11	0.03	0.10
H2O-	0.05	0.03	0.04	0.04	0.03	0.07	0.04	0.05	0.10	0.05	0.07	0.03	0.00	0.04
LOI	14.93	19.96	20.96	22.51	22.08	24.36	21.20	19.48	14.01	19.29	22.59	17.00	2.17	19.89
Total	100.38	99.66	99.41	99.67	99.96	99.89	99.59	99.70	99.93	99.67	99.95	99.21	99.87	99.93
Mo	b.d.l	b.d.l	b.d.l	b.d.l	b.d.l	3.2	b.d.l	b.d.l	b.d.l	b.d.l	b.d.l	b.d.l	2.0	b.d.l
Nb	2.7	3.0	3.4	3.5	3.6	14.0	3.4	3.4	4.5	3.7	3.9	4.1	3.8	4.4
Zr	20.0	21.6	16.9	15.5	11.0	6.9	14.6	18.8	33.2	16.1	15.2	22.6	7.0	31.5
Y	9.8	13.0	6.1	4.8	6.4	81.3	5.8	6.9	9.5	7.6	7.0	8.4	2.2	15.1
Sr	74.0	154.7	161.1	117.0	84.4	<1.6	101.4	109.4	69.1	116.6	139.0	134.3	15.0	148.5
U	b.d.l	b.d.l	b.d.l	b.d.l	b.d.l	b.d.l	b.d.l	b.d.l	b.d.l	b.d.l	b.d.l	b.d.l	b.d.l	b.d.l
Th	b.d.l	b.d.l	b.d.l	b.d.l	b.d.l	b.d.l	b.d.l	b.d.l	b.d.l	b.d.l	b.d.l	b.d.l	b.d.l	b.d.l
Rb	b.d.l	b.d.l	b.d.l	b.d.l	b.d.l	b.d.l	b.d.l	b.d.l	2.7	b.d.l	b.d.l	b.d.l	3.9	b.d.l
Pb	b.d.l	b.d.l	b.d.l	b.d.l	b.d.l	b.d.l	b.d.l	b.d.l	b.d.l	b.d.l	b.d.l	b.d.l	b.d.l	b.d.l
Zn	211.8	99.7	80.9	126.0	127.6	141.7	116.1	130.3	191.1	128.4	95.1	129.1	21.0	139.0
Cu	38.8	29.2	30.9	19.6	18.6	24.8	23.5	30.6	31.7	33.3	14.4	30.0	28.6	30.6
Ni	1565.5	1214.2	900.3	1419.9	996.5	1254.9	1000.4	1000.6	1306.1	795.8	653.0	795.1	225.9	671.4
Co	142.2	92.2	124.7	83.1	84.3	106.8	81.0	97.0	139.9	75.3	65.1	84.5	18.9	66.6
Mn	2182.5	2996.4	2994.2	2986.2	2986.7	2987.1	2986.9	2987.2	2985.8	2987.7	2988.9	2986.6	742.4	2989.2
Cr	5526.5	3756.0	3167.3	4016.5	3601.7	4785.5	3567.2	3827.2	4996.0	2895.8	1944.2	2696.0	124.6	1954.0
V	235.4	210.5	145.1	158.2	140.0	182.2	152.5	184.9	312.2	172.4	115.9	220.0	14.0	162.9
Ba	b.d.l	b.d.l	b.d.l	b.d.l	b.d.l	b.d.l	b.d.l	b.d.l	b.d.l	b.d.l	b.d.l	b.d.l	b.d.l	b.d.l
Sc	37.8	31.1	23.2	23.7	21.9	29.5	24.5	29.2	41.1	27.4	17.9	34.4	2.6	24.0

Appendix E1. *(Continued)*

Sample	KD1-T70	KD1-T71	KD1-T72	KD1-T73	KD1-T74	KD1-T75	KD1-T76	KD1-T77	KD1-T78	KD1-T79	KD1-T80	KD1-T81	KD1-T82	KD1-T83
SiO_2	22.03	25.58	41.52	43.50	37.26	44.79	39.52	34.90	35.69	83.77	52.57	44.06	46.28	46.19
TiO_2	4.53	1.92	7.58	5.45	6.55	5.98	5.52	5.11	5.11	2.24	13.80	10.16	11.08	6.68
Al_2O_3	0.49	0.20	0.79	0.69	0.69	0.61	0.59	0.51	0.54	0.27	0.85	0.61	0.66	0.47
Fe_2O_3	7.85	4.41	14.31	10.10	11.88	13.23	12.37	11.97	12.13	1.40	9.74	12.29	12.11	6.80
MnO	0.46	0.32	0.16	0.25	0.21	0.13	0.20	0.23	0.21	0.11	0.24	0.22	0.23	0.28
MgO	6.50	5.17	16.24	11.44	14.81	20.89	18.37	14.86	14.66	0.65	3.81	8.47	9.50	5.41
CaO	34.77	42.40	9.19	15.94	13.37	3.97	10.09	15.71	14.95	6.09	6.92	10.59	8.28	17.31
Na_2O	0.06	0.02	0.12	0.12	0.09	0.14	0.09	0.08	0.08	0.42	4.45	0.66	0.76	0.29
K_2O	0.01	0.01	0.01	0.01	0.01	0.01	0.01	0.02	0.06	0.20	0.16	0.38	0.03	0.56
P_2O_5	0.05	0.01	0.06	0.05	0.04	0.05	0.05	0.03	0.04	0.06	0.09	0.05	0.05	0.03
SO_3	0.10	0.04	0.16	0.24	0.22	0.04	0.13	0.41	0.22	0.09	0.44	0.24	0.08	0.56
Cr_2O_3	0.18	0.10	0.39	0.30	0.39	0.47	0.37	0.40	0.37	0.16	0.24	0.23	0.22	0.15
NiO	0.06	0.05	0.13	0.09	0.14	0.18	0.15	0.16	0.15	0.04	0.09	0.06	0.06	0.12
H2O-	0.04	0.02	0.05	0.02	0.01	0.04	0.01	0.03	0.23	0.00	0.01	0.05	0.05	0.03
LOI	22.36	19.03	8.91	11.11	14.04	8.87	11.96	15.48	14.75	4.76	6.64	11.51	10.58	15.12
Total	99.50	99.29	99.63	99.33	99.72	99.42	99.43	99.91	99.18	100.26	100.06	99.59	99.98	99.98
Mo	b.d.l	b.d.l	b.d.l	b.d.l	b.d.l	b.d.l	b.d.l	b.d.l	b.d.l	b.d.l	b.d.l	b.d.l	b.d.l	b.d.l
Nb	4.7	3.7	5.0	5.1	5.2	4.7	4.6	3.7	4.2	3.4	3.9	3.8	4.3	3.8
Zr	28.4	13.6	41.4	35.7	37.1	28.9	29.0	23.2	26.0	9.0	44.4	33.0	33.3	24.0
Y	10.7	6.1	11.3	10.5	9.4	7.8	9.1	7.9	8.7	5.6	19.4	12.2	13.9	9.2
Sr	161.8	231.6	70.7	72.8	104.0	26.8	67.3	75.8	78.6	25.0	69.1	96.7	68.2	93.0
U	b.d.l	b.d.l	b.d.l	b.d.l	b.d.l	b.d.l	b.d.l	b.d.l	b.d.l	b.d.l	b.d.l	b.d.l	b.d.l	b.d.l
Th	b.d.l	b.d.l	b.d.l	b.d.l	b.d.l	b.d.l	b.d.l	b.d.l	b.d.l	b.d.l	b.d.l	b.d.l	b.d.l	b.d.l
Rb	b.d.l	b.d.l	b.d.l	2.2	b.d.l	b.d.l	b.d.l	1.9	4.7	6.4	4.0	41.5	2.7	13.3
Pb	b.d.l	b.d.l	b.d.l	b.d.l	b.d.l	b.d.l	b.d.l	b.d.l	b.d.l	b.d.l	b.d.l	b.d.l	b.d.l	12.3
Zn	90.6	57.8	194.7	141.3	159.4	182.5	161.9	148.7	144.5	43.3	112.9	153.1	169.2	133.2
Cu	38.5	17.9	79.1	65.1	47.5	44.6	53.3	43.0	46.7	30.2	75.1	47.1	68.1	8.8
Ni	487.0	337.2	950.5	663.1	1040.9	1454.8	1226.2	1171.2	1124.7	239.8	568.5	389.1	418.2	686.9
Co	52.3	27.1	111.4	72.8	113.8	138.7	120.3	109.9	104.5	30.1	100.9	83.3	92.3	61.3
Mn	2990.5	2987.4	2174.5	2176.1	2986.8	2174.0	2986.4	2986.8	2986.7	743.7	2176.7	2176.0	2176.7	2176.7
Cr	965.1	333.8	3263.4	2439.9	3585.8	4569.7	3429.8	3626.8	3242.3	1106.1	1787.1	1581.5	1587.7	855.2
V	136.1	49.5	261.9	182.1	253.5	220.1	222.1	193.9	191.2	74.3	385.5	280.5	322.8	185.0
Ba	b.d.l	b.d.l	b.d.l	b.d.l	b.d.l	b.d.l	b.d.l	b.d.l	b.d.l	3.8	3.8	b.d.l	b.d.l	27.0
Sc	19.2	5.5	39.6	26.9	35.1	32.1	30.4	26.6	24.7	12.7	50.7	39.8	46.5	26.1

Appendix E1. *(Continued)*

Sample	KD1-T84	KD1-T85	KD1-T86	KD1-T87	KD1-T88	KD1-T89	KD1-T90	KD1-T91	KD1-T92	KD1-T93
SiO_2	44.88	44.69	46.09	44.66	42.71	41.11	36.72	42.13	22.73	34.83
TiO_2	11.29	9.01	10.33	8.68	9.37	9.75	7.70	8.70	2.99	5.55
Al_2O_3	0.62	0.61	0.62	0.59	0.56	0.58	0.78	0.83	0.32	0.54
Fe_2O_3	12.93	11.87	13.79	13.23	14.32	14.06	13.79	14.72	3.80	11.21
MnO	0.23	0.22	0.23	0.23	0.21	0.22	0.28	0.24	0.43	0.25
MgO	11.03	11.67	13.30	14.94	16.89	14.93	14.39	14.47	2.36	11.04
CaO	8.06	10.23	6.13	8.29	5.54	8.15	14.42	9.25	38.82	18.21
Na_2O	0.76	0.05	0.08	0.07	0.04	0.03	0.08	0.10	0.24	0.09
K_2O	0.24	0.04	0.05	0.04	0.04	0.04	0.03	0.02	0.05	0.21
P_2O_5	0.05	0.05	0.05	0.04	0.05	0.05	0.06	0.07	0.03	0.04
SO_3	0.05	0.03	0.03	0.19	0.24	0.37	0.06	0.15	0.06	0.81
Cr_2O_3	0.21	0.20	0.20	0.45	0.43	0.46	0.41	0.41	0.20	0.46
NiO	0.05	0.04	0.04	0.11	0.13	0.14	0.09	0.12	0.04	0.16
H2O-	0.05	0.12	0.03	0.11	0.14	0.15	0.10	0.12	0.00	0.04
LOI	9.39	10.95	8.31	8.24	8.47	9.74	10.64	8.45	27.54	15.66
Total	99.83	99.78	99.28	99.88	99.15	99.78	99.55	99.77	99.61	99.10
Mo	b.d.l	b.d.l	b.d.l	b.d.l	b.d.l	b.d.l	b.d.l	b.d.l	b.d.l	b.d.l
Nb	4.2	4.2	3.8	4.6	4.1	3.8	7.4	6.5	4.5	5.4
Zr	32.4	31.9	30.0	28.5	27.3	27.9	44.2	44.3	19.1	29.6
Y	15.7	12.5	14.2	12.7	12.0	11.5	10.2	9.9	10.3	8.7
Sr	69.8	79.7	38.0	36.3	31.6	53.5	78.0	42.8	166.6	123.6
U	b.d.l	b.d.l	b.d.l	b.d.l	b.d.l	b.d.l	b.d.l	b.d.l	b.d.l	b.d.l
Th	b.d.l	b.d.l	b.d.l	b.d.l	b.d.l	b.d.l	b.d.l	b.d.l	b.d.l	b.d.l
Rb	23.9	3.8	6.5	4.9	5.0	6.1	3.0	2.5	b.d.l	17.4
Pb	b.d.l	b.d.l	b.d.l	b.d.l	b.d.l	b.d.l	b.d.l	b.d.l	b.d.l	b.d.l
Zn	153.6	151.7	171.4	166.8	184.0	186.0	174.6	175.2	61.7	156.1
Cu	56.4	31.6	29.8	28.1	32.2	30.5	46.8	102.0	16.8	70.8
Ni	381.8	278.7	354.6	776.8	833.7	910.1	700.9	822.1	296.2	977.7
Co	92.9	72.4	87.3	96.6	112.8	109.9	101.2	100.6	46.8	93.7
Mn	2176.3	2176.0	2176.6	2176.2	2176.1	2176.2	2988.4	2176.5	2989.8	2987.5
Cr	1495.2	1450.6	1655.2	3987.2	4055.3	4163.2	3296.9	3426.7	1077.5	3903.1
V	296.4	271.3	313.7	311.8	291.8	320.6	260.7	269.9	83.9	182.4
Ba	b.d.l	b.d.l	b.d.l	b.d.l	b.d.l	b.d.l	b.d.l	b.d.l	b.d.l	31.0
Sc	40.9	41.3	42.9	42.8	33.5	42.4	36.3	37.5	9.6	21.6

Appendix E2. REE concentrations (ppm) for selected samples across the KSM

	T12	T15	T17	T19	T21	T23	T26	T31	T33	T37	T41	T43	T45	T47	T49
La	2.28	2.19	1.64	1.75	1.98	1.55	2.66	2.29	2.32	1.12	1.15	1.15	1.45	0.81	1.30
Ce	4.88	5.19	3.80	4.26	4.79	3.90	6.03	5.32	5.56	2.22	2.01	2.25	2.69	2.04	2.45
Pr	0.56	0.69	0.62	0.68	0.77	0.62	0.89	0.81	0.76	0.21	0.18	0.23	0.27	0.21	0.24
Nd	2.96	3.90	3.20	3.49	3.74	3.11	4.52	3.96	4.19	1.54	1.44	1.65	1.82	1.67	1.70
Sm	0.88	1.42	1.30	1.31	1.39	1.17	1.59	1.43	1.43	0.60	0.53	0.61	0.72	0.71	0.65
Eu	0.31	0.41	0.55	0.52	0.56	0.35	0.67	0.44	0.35	0.59	0.27	0.23	0.26	0.23	0.37
Gd	1.18	1.64	1.55	1.61	1.82	1.37	1.88	1.72	1.63	0.97	0.92	1.05	1.29	0.96	0.98
Tb	0.13	0.18	0.25	0.26	0.30	0.23	0.30	0.28	0.18	0.09	0.09	0.11	0.15	0.10	0.11
Dy	1.48	1.59	1.56	1.56	1.85	1.41	1.79	1.72	1.47	1.27	1.26	1.38	1.72	1.14	1.25
Ho	0.32	0.30	0.27	0.29	0.34	0.27	0.35	0.35	0.28	0.26	0.28	0.29	0.39	0.22	0.26
Er	0.98	0.81	0.79	0.80	0.97	0.79	0.98	0.89	0.76	0.73	0.82	0.87	1.11	0.62	0.69
Tm	0.17	0.13	0.11	0.11	0.14	0.12	0.14	0.13	0.11	0.13	0.14	0.14	0.18	0.11	0.12
Yb	0.98	0.70	0.78	0.77	0.93	0.84	0.97	0.90	0.77	0.64	0.83	0.78	1.01	0.54	0.61
Lu	0.16	0.12	0.11	0.12	0.14	0.11	0.15	0.13	0.10	0.11	0.14	0.14	0.17	0.09	0.10

	T51	T53	T55	T57	T59	T61-A	T64	T68	T71	T73	T75	T77	T79	T85
La	0.76	1.32	1.34	1.00	0.98	0.82	0.67	1.35	3.61	3.70	1.65	2.21	1.15	1.22
Ce	1.83	3.06	3.13	2.16	2.14	1.95	1.56	3.13	7.62	8.05	4.50	5.09	2.65	3.06
Pr	0.29	0.35	0.36	0.23	0.22	0.19	0.29	0.33	0.99	1.11	0.74	0.77	0.29	0.51
Nd	1.39	2.22	2.22	1.64	1.61	1.53	1.33	1.79	4.38	5.22	3.58	3.72	2.06	2.61
Sm	0.50	0.86	0.89	0.75	0.76	0.75	0.62	0.48	1.04	1.60	1.23	1.18	0.75	1.13
Eu	0.24	0.55	0.17	0.22	0.25	0.38	0.28	0.09	0.41	0.70	0.46	0.44	0.33	0.47
Gd	0.77	1.35	0.99	1.16	1.30	1.33	1.16	0.44	1.22	2.04	1.60	1.52	1.05	1.95
Tb	0.14	0.18	0.08	0.13	0.16	0.19	0.20	b.d.l	0.18	0.35	0.28	0.27	0.102	0.37
Dy	1.00	1.68	0.97	1.33	1.61	1.81	1.52	0.47	1.16	2.19	1.81	1.77	1.16	2.66
Ho	0.20	0.34	0.18	0.25	0.33	0.40	0.33	0.09	0.24	0.46	0.36	0.35	0.22	0.57
Er	0.59	0.90	0.48	0.72	0.93	1.06	0.94	0.25	0.75	1.28	0.96	0.97	0.52	1.62
Tm	0.09	0.15	0.09	0.13	0.15	0.17	0.14	0.05	0.10	0.17	0.14	0.13	0.08	0.23
Yb	0.56	0.79	0.47	0.69	0.83	0.92	0.92	0.19	0.71	1.08	0.84	0.84	0.38	1.49
Lu	0.08	0.13	0.09	0.13	0.14	0.16	0.14	0.04	0.10	0.16	0.12	0.12	0.06	0.23

Appendix E3: ***Multiple sulphur isotopes by Secondary Ion Microprobe (IMS 1280)***

Multiple sulfur isotopes (^{32}S, ^{33}S and ^{34}S) were analysed using the Cameca IMS1280 of the NordSIM facility at the Swedish Natural History Museum, utilizing a multi-collection method similar to that described by Whitehouse et al. (2005). Analyses were conducted on 30 μm and 100 μm thick standard polished thin-sections cut into ~25 mm diameter discs, from which a sector was cut to enable mounting with 3 sulfide standards embedded in epoxy resin, and together these were placed in a 25 mm diameter Cameca sample holder. The five samples containing pyrites were first mapped in reflected light and these images were used to locate the pyrite grains when the sample was placed in the IMS 1280. The sample was coated with a ca. 30 nm gold coat to provide conductivity at high voltage.

Instrument parameters were broadly similar to those described by Whitehouse et al. (2005), and Kamber and Whitehouse (2007). Briefly, a +10 kV, ~ 2.5 nA Cs^+ primary beam was operated in critical focusing (Gaussian) mode and homogenized using a 5 x 5 μm raster to analyse a ca. 10 μm diameter region on the sample. Although the sulfide targets are conductors, the normal incidence electron flooding gun was utilised for charge compensation in the event that the primary ion beam overlapped onto insulating matrix minerals. All analyses were performed in automated chain sequences (using the Cameca CIPS, version 5.061) with a 90 second pre-sputter over a 25 x 25 μm area to remove the gold coating, during which the detector backgrounds were measured for 30 seconds, followed by re-centering of the secondary beam in the field aperture to accommodate minor misalignments resulting from small variations in surface relief. Magnetic field stability was maintained using NMR regulation, obviating the need for regular mass re-centering and permitting a wider entrance slit (and hence transmission) than utilised in earlier studies at this facility (110 μm cf. 60 μm). The -10 kV secondary sulfur beam was measured in three Faraday detectors at an effective mass resolution of ~ 4500 on the ^{33}S channel, sufficient to resolve ^{33}S from $^{32}S^1H$. Data were collected in 16 cycles with 4 second integrations. The detector amplifiers were housed in an evacuated chamber heated slightly above ambient. Long (several hours) background measurements showed noise on the background of the critical ^{33}S channel of ca. 2000 cps (1 standard deviation) which

results in a limiting external precision of 0.07 ‰ (1 standard deviation) on $^{33}S/^{32}S$ ratios at typical ^{32}S count rates of 10^9 cps. Raw $^{33}S/^{32}S$ and $^{34}S/^{32}S$ ratios (IMS 1280 data Table) were corrected for instrumental and matrix related mass bias using two reference Sulphides of appropriate composition, described and analysed by Crowe and Vaughan (1996). These were the Ruttan pyrite ($\delta^{34}S_{CDT}$ = + 1.2‰; $\delta^{i}S_{CDT}$ = [1000 x ($^{i}S/^{32}S$sample)/($^{i}S/^{32}S_{CDT}$) – 1] where i refers to a particular isotope of S, CDT refers to the accepted composition of Canyon Diablo Troilite), and the Balmat pyrite ($\delta^{34}S_{CDT}$ = + 15.1‰) both of which lie on the MDF trend (i.e. $\Delta^{33}S$ = 0‰; $\Delta^{33}S$ is the deviation from the mass-dependent fractionation (MDF) line between $\delta^{33}S_{CDT}$ and $\delta^{34}S_{CDT}$ defined by $\Delta^{33}S = \delta^{33}S - 1000 \times [(1 + \delta^{34}S/1000)\ 0.515 - 1])$. In addition, a $+\Delta^{33}S$ pyrite from an early Archean (ca. 3,700 Ma) BIF in the Isua Greenstone Belt which previously yielded $\delta^{34}S_{CDT}$ = + 1.99 ± 0.36‰ and $\Delta^{33}S$ of + 3.31 ± 0.19‰ (95% confidence interval (CI)) by conventional S-isotope analysis (Baublys et al., 2004), and $\Delta^{33}S$ of +3.27 ± 0.07‰ (95% CI) by SIMS (Whitehouse et al., 2005) was analysed as a monitor during this study. Replicate analyses of the two MDF standards in the NordSIM laboratory over several years suggest that the $\delta^{34}S$ value for Balmat (at least the grains used in Stockholm) is slightly higher than the quoted -15.1‰ value (Crowe and Vaughan, 1996). For this reason, only the Ruttan pyrite was used as a reference for $\delta^{34}S$, yielding a value for the Isua pyrite of ca. 2‰, in accord with the conventional determination. Since both the Ruttan and Balmat pyrites are MDF, both were utilised to estimate the external precision on $\Delta^{33}S$.

Data were obtained in 10 separate analytical sessions (see IMS 1280 Data Table). External precision on $\Delta^{33}S$ was between 0.08 and 0.09 ‰ (1σ) over all sessions and these were propagated together with internal errors to yield an overall uncertainty <0.15‰ for analyses where the secondary ion signal of ^{32}S was ca. 10^9 cps. These errors are close to the expected errors based on signal/background ratio and amplifier noise and are comparable to those reported in previous multicollector SIMS studies of S isotopes (e.g. Mojzsis et al., 2003; Whitehouse et al., 2005). Analyses where the ^{32}S cps were <10% of the average for the standards were rejected.

Appendix E4 - *KD1 Multiple sulphur isotope analyses - IMS 1280 Data Tables*

Sample ID	^{32}S cps (x1 e6)	$^{34}S/^{32}S$	±1σ (%)	$^{33}S/^{32}S$	±1σ (%)	$\delta^{34}S$	±1σ	±2σ	$\delta^{33}S$	±1σ	$\Delta^{33}S$	±1σ	±2σ
Rut_5A_091213@2	939	0.044397	0.01	0.0079060	0.01	0.96	0.18	0.37	0.74	0.16	0.24	0.16	0.31
Rut_5A_091213@3	916	0.044411	0.01	0.0079044	0.01	1.29	0.19	0.37	0.54	0.16	-0.12	0.16	0.32
Rut_5A_091213@4	899	0.044409	0.01	0.0079048	0.01	1.24	0.17	0.35	0.59	0.16	-0.05	0.16	0.31
Rut_5A_091213@5	881	0.044412	0.01	0.0079045	0.01	1.31	0.17	0.35	0.55	0.16	-0.12	0.16	0.31
Bal_5A_091213@1	940	0.045069	0.01	0.0079632	0.01	16.11	0.17	0.34	8.17	0.16	-0.12	0.16	0.32
Bal_5A_091213@2	922	0.045067	0.01	0.0079653	0.01	16.08	0.17	0.34	8.44	0.16	0.16	0.16	0.31
Bal_5A_091213@3	892	0.045062	0.01	0.0079636	0.01	15.97	0.17	0.34	8.23	0.17	0.00	0.17	0.33
Bal_5A_091213@4	891	0.045070	0.01	0.0079644	0.01	16.15	0.17	0.34	8.33	0.16	0.01	0.16	0.32
KD1-83.11-A1	759	0.044335	0.01	0.0079028	0.01	-0.44	0.17	0.34	0.31	0.16	0.54	0.16	0.32
KD1-83.11-A2	717	0.044332	0.01	0.0079034	0.01	-0.50	0.19	0.39	0.39	0.19	0.65	0.19	0.37
KD1-83.11-A3	886	0.044320	0.01	0.0079041	0.01	-0.77	0.18	0.36	0.47	0.15	0.87	0.15	0.31
KD1-83.11-A4	496	0.044337	0.01	0.0079035	0.01	-0.39	0.17	0.34	0.40	0.18	0.60	0.18	0.37
KD1-83.11-A5	810	0.044315	0.01	0.0079027	0.01	-0.87	0.18	0.35	0.30	0.17	0.75	0.17	0.34
KD1-83.11-A6	857	0.044260	0.01	0.0078948	0.00	-2.12	0.19	0.38	-0.72	0.15	0.37	0.15	0.29
KD1-83.11-A7	503	0.044284	0.01	0.0078946	0.02	-1.59	0.18	0.35	-0.74	0.22	0.07	0.22	0.43
KD1-83.11-A8	838	0.044282	0.01	0.0079000	0.01	-1.62	0.18	0.37	-0.06	0.17	0.78	0.17	0.34
KD1-83.11-A9	790	0.044302	0.01	0.0078983	0.01	-1.17	0.19	0.38	-0.26	0.16	0.34	0.16	0.33
KD1-83.11-A10	595	0.044323	0.01	0.0079020	0.01	-0.69	0.18	0.35	0.20	0.17	0.56	0.17	0.34
KD1-83.11-A11	831	0.044349	0.01	0.0079042	0.01	-0.11	0.19	0.37	0.49	0.15	0.54	0.15	0.31
KD1-83.11-A12	782	0.044263	0.01	0.0078951	0.01	-2.06	0.18	0.37	-0.69	0.17	0.37	0.17	0.34
KD1-83.11-A13	764	0.044297	0.01	0.0079011	0.01	-1.29	0.21	0.41	0.09	0.18	0.75	0.18	0.36
KD1-83.11-A14	814	0.044311	0.01	0.0079016	0.01	-0.98	0.17	0.34	0.15	0.15	0.66	0.15	0.31
KD1-83.11-A15	492	0.044265	0.01	0.0078946	0.02	-2.00	0.18	0.37	-0.74	0.21	0.29	0.21	0.41
KD1-83.11-A16	679	0.044339	0.01	0.0079026	0.01	-0.34	0.19	0.37	0.28	0.15	0.46	0.15	0.30
Is_5A_091213@1	909	0.044474	0.01	0.0079345	0.01	2.71	0.18	0.36	4.37	0.17	2.98	0.17	0.33
Is_5A_091213@2	910	0.044434	0.01	0.0079328	0.00	1.81	0.17	0.34	4.14	0.15	3.21	0.15	0.29
Is_5A_091213@3	875	0.044459	0.01	0.0079340	0.01	2.38	0.17	0.35	4.30	0.15	3.08	0.15	0.30

Appendix E4 - *IMS 1280 Data Tables (continued)*

Sample ID	^{32}S cps (x1 e6)	^{34}S/^{32}S	±1σ (%)	^{33}S/^{32}S	±1σ (%)	δ^{34}S	±1σ	±2σ	δ33S	±1σ	Δ33S	±1σ	±2σ
Rut_5A_091210@1	760	0.044442	0.02	0.0079074	0.01	1.02	0.26	0.51	0.47	0.15	-0.05	0.15	0.31
Rut_5A_091210@2	756	0.044453	0.02	0.0079068	0.01	1.27	0.26	0.52	0.40	0.16	-0.26	0.16	0.32
Rut_5A_091210@3	761	0.044457	0.02	0.0079106	0.01	1.36	0.24	0.49	0.87	0.16	0.18	0.16	0.32
Rut_5A_091210@4	755	0.044441	0.02	0.0079075	0.01	1.00	0.23	0.47	0.49	0.17	-0.02	0.17	0.33
Rut_5A_091210@5	752	0.044457	0.02	0.0079102	0.01	1.35	0.25	0.49	0.83	0.16	0.13	0.16	0.32
Bal_5A_0912010@1	907	0.045072	0.02	0.0079655	0.01	15.21	0.25	0.49	7.92	0.14	0.09	0.14	0.29
Bal_5A_0912010@2	922	0.045066	0.01	0.0079640	0.01	15.07	0.23	0.45	7.73	0.17	-0.03	0.17	0.34
Bal_5A_0912010@3	917	0.045047	0.01	0.0079626	0.01	14.64	0.22	0.44	7.55	0.16	0.01	0.16	0.33
Bal_5A_0912010@4	931	0.045028	0.01	0.0079606	0.01	14.21	0.22	0.45	7.30	0.16	-0.02	0.16	0.32
Bal_5A_091210@5	838	0.045102	0.01	0.0079673	0.01	15.88	0.22	0.45	8.15	0.15	-0.03	0.15	0.29
KD1-83.11-B1	909	0.044222	0.02	0.0078974	0.01	-3.94	0.27	0.55	-0.82	0.19	1.21	0.19	0.37
KD1-83.11-B2	861	0.044285	0.01	0.0078961	0.01	-2.51	0.23	0.45	-0.98	0.13	0.32	0.13	0.27
KD1-83.11-B3	804	0.044103	0.03	0.0078936	0.02	-6.63	0.37	0.73	-1.33	0.23	2.09	0.23	0.46
KD1-83.11-B4	765	0.044258	0.01	0.0079054	0.01	-3.13	0.22	0.44	0.19	0.15	1.80	0.15	0.31
KD1-83.11-B5	745	0.044329	0.01	0.0079088	0.01	-1.53	0.20	0.40	0.63	0.16	1.42	0.16	0.32
KD1-83.11-B6	739	0.044327	0.01	0.0078993	0.01	-1.58	0.21	0.43	-0.56	0.15	0.25	0.15	0.31
KD1-83.11-B7	798	0.044249	0.02	0.0078963	0.01	-3.33	0.24	0.48	-0.95	0.17	0.76	0.17	0.35
KD1-83.11-B8	771	0.044309	0.02	0.0079100	0.01	-1.97	0.24	0.49	0.79	0.18	1.81	0.18	0.37
KD1-83.11-B9	436	0.044216	0.01	0.0078874	0.02	-4.07	0.22	0.45	-2.09	0.22	0.00	0.22	0.44
KD1-83.11-B10	389	0.044185	0.02	0.0078887	0.03	-4.76	0.30	0.60	-1.93	0.29	0.52	0.29	0.58
KD1-83.11-B11	555	0.044307	0.02	0.0079043	0.01	-2.02	0.25	0.49	0.06	0.18	1.10	0.18	0.36
KD1-83.11-B12	698	0.044335	0.01	0.0079013	0.01	-1.40	0.21	0.42	-0.32	0.17	0.40	0.17	0.35
KD1-83.11-B13	891	0.044265	0.01	0.0078932	0.01	-2.98	0.23	0.46	-1.35	0.15	0.18	0.15	0.31
KD1-83.11-B14	745	0.044193	0.03	0.0078896	0.02	-4.58	0.31	0.61	-1.81	0.20	0.55	0.20	0.40
Is_5A_091210@1	758	0.044478	0.02	0.0079350	0.01	1.83	0.27	0.53	3.98	0.16	3.04	0.16	0.32
Is_5A_091210@2	791	0.044479	0.02	0.0079347	0.01	1.84	0.24	0.47	3.94	0.17	2.99	0.17	0.34
Is_5A_091210@3	736	0.044510	0.02	0.0079399	0.01	2.54	0.25	0.49	4.61	0.16	3.30	0.16	0.32

Appendix E4 - *IMS 1280 Data Tables (continued)*

Sample ID	^{32}S cps (x1 e6)	^{34}S/^{32}S	±1σ (%)	^{33}S/^{32}S	±1σ (%)	δ^{34}S	±1σ	±2σ	δ^{33}S	±1σ	Δ^{33}S	±1σ	±2σ
Rut_5A_091213@6	856	0.044440	0.01	0.0079072	0.01	1.09	0.17	0.34	0.57	0.17	0.01	0.17	0.33
Rut_5A_091213@8	847	0.044442	0.01	0.0079073	0.01	1.14	0.18	0.35	0.58	0.15	-0.01	0.15	0.30
Rut_5A_091213@9	842	0.044452	0.01	0.0079089	0.01	1.37	0.17	0.34	0.79	0.13	0.08	0.13	0.26
Bal_5A_091213@6	890	0.045087	0.01	0.0079664	0.01	15.68	0.16	0.33	8.09	0.13	0.01	0.13	0.27
Bal_5A_091213@7	889	0.045094	0.01	0.0079681	0.01	15.82	0.16	0.32	8.30	0.13	0.15	0.13	0.26
Bal_5A_091213@8	884	0.045098	0.01	0.0079658	0.01	15.91	0.16	0.32	8.02	0.13	-0.18	0.13	0.25
Bal_5A_091213@9	866	0.045103	0.01	0.0079678	0.01	16.03	0.16	0.32	8.27	0.13	0.02	0.13	0.25
KD1-83.11-C1	836	0.044312	0.01	0.0079007	0.01	-1.78	0.16	0.32	-0.26	0.12	0.66	0.12	0.25
KD1-83.11-C2	832	0.044292	0.01	0.0078997	0.01	-2.25	0.17	0.33	-0.38	0.12	0.78	0.12	0.24
KD1-83.11-C3	807	0.044361	0.01	0.0079189	0.01	-0.69	0.17	0.34	2.06	0.16	2.41	0.16	0.32
KD1-83.11-C4	865	0.044311	0.00	0.0079007	0.01	-1.82	0.16	0.31	-0.26	0.11	0.68	0.11	0.22
KD1-83.11-C5	795	0.044175	0.01	0.0078893	0.01	-4.87	0.20	0.40	-1.71	0.13	0.80	0.13	0.25
KD1-83.11-C6	842	0.044349	0.00	0.0079043	0.01	-0.97	0.16	0.31	0.20	0.13	0.70	0.13	0.25
KD1-83.11-C7	864	0.044322	0.00	0.0079027	0.01	-1.56	0.16	0.32	-0.01	0.12	0.79	0.12	0.25
KD1-83.11-C8	858	0.044281	0.01	0.0079043	0.01	-2.49	0.17	0.34	0.20	0.12	1.48	0.12	0.24
KD1-83.11-C9	792	0.044280	0.01	0.0079018	0.01	-2.51	0.17	0.33	-0.12	0.14	1.17	0.14	0.27
KD1-83.11-C10	614	0.044273	0.01	0.0079031	0.01	-2.67	0.16	0.32	0.05	0.15	1.43	0.15	0.29
KD1-83.11-C11	810	0.044347	0.00	0.0079048	0.01	-0.99	0.15	0.31	0.26	0.13	0.77	0.13	0.27
Is_5A_091213@4	844	0.044487	0.01	0.0079368	0.01	2.14	0.17	0.34	4.33	0.12	3.22	0.12	0.24
Is_5A_091213@5	869	0.044459	0.01	0.0079346	0.01	1.51	0.16	0.33	4.05	0.14	3.27	0.14	0.28
Is_5A_091213@6	837	0.044490	0.00	0.0079371	0.01	2.21	0.16	0.31	4.36	0.13	3.22	0.13	0.27

Appendix E4 - *IMS 1280 Data Tables (continued)*

Sample ID	^{32}S cps (x1 e6)	^{34}S/^{32}S	±1σ (%)	^{33}S/^{32}S	±1σ (%)	δ^{34}S	±1σ	±2σ	δ^{33}S	±1σ	Δ^{33}S	±1σ	±2σ
Rut_5A_110525@10	837	0.044183	0.03	0.0078815	0.02	1.48	0.34	0.68	0.70	0.18	-0.06	0.18	0.37
Rut_5A_110525@11	840	0.044180	0.02	0.0078822	0.01	1.39	0.33	0.66	0.79	0.15	0.07	0.15	0.30
Rut_5A_110525@12	901	0.044164	0.02	0.0078799	0.01	1.05	0.33	0.66	0.49	0.16	-0.05	0.16	0.32
Rut_5A_110525@13	944	0.044167	0.03	0.0078817	0.01	1.11	0.35	0.69	0.72	0.16	0.15	0.16	0.33
Rut_5A_110525@14	942	0.044161	0.03	0.0078790	0.01	0.97	0.34	0.68	0.38	0.17	-0.12	0.17	0.34
Bal_5A_110525@8	798	0.044853	0.03	0.0079432	0.02	16.65	0.35	0.70	8.60	0.19	0.02	0.19	0.39
Bal_5A_110525@9	821	0.044851	0.02	0.0079424	0.01	16.62	0.32	0.65	8.49	0.16	-0.07	0.16	0.33
Bal_5A_110525@10	906	0.044846	0.03	0.0079429	0.02	16.50	0.35	0.69	8.56	0.18	0.06	0.18	0.37
KD1-178.48-1	854	0.044089	0.02	0.0078781	0.01	-0.66	0.30	0.61	0.25	0.16	0.59	0.16	0.33
KD1-178.48-2	833	0.044125	0.02	0.0078797	0.01	0.16	0.32	0.64	0.46	0.15	0.38	0.15	0.31
KD1-178.48-3	817	0.044076	0.03	0.0078742	0.02	-0.94	0.35	0.71	-0.24	0.19	0.24	0.19	0.38
KD1-178.48-4	836	0.044116	0.02	0.0078795	0.01	-0.04	0.31	0.62	0.44	0.14	0.46	0.14	0.28
KD1-178.48-5	896	0.044128	0.02	0.0078820	0.01	0.23	0.33	0.66	0.75	0.17	0.64	0.17	0.34
KD1-178.48-6	908	0.044104	0.03	0.0078780	0.02	-0.32	0.34	0.68	0.24	0.19	0.41	0.19	0.37
KD1-178.48-7	927	0.044099	0.02	0.0078775	0.01	-0.43	0.30	0.59	0.18	0.16	0.40	0.16	0.33
KD1-178.48-8	860	0.044076	0.02	0.0078756	0.01	-0.95	0.30	0.60	-0.06	0.17	0.43	0.17	0.34
Is_5A_110525@5	924	0.044227	0.03	0.0079112	0.01	2.47	0.34	0.68	4.47	0.17	3.20	0.17	0.35
Is_5A_110525@6	914	0.044228	0.02	0.0079118	0.01	2.49	0.33	0.66	4.55	0.15	3.27	0.15	0.30

Appendix E4 - *IMS 1280 Data Tables (continued)*

Sample ID	^{32}S cps (x1 e6)	^{34}S/^{32}S	±1σ (%)	^{33}S/^{32}S	±1σ (%)	δ^{34}S	±1σ	±2σ	δ^{33}S	±1σ	Δ^{33}S	±1σ	±2σ
Rut_5A_110525@5	1020	0.044160	0.03	0.0078804	0.02	0.97	0.35	0.71	0.58	0.22	0.08	0.22	0.44
Rut_5A_110525@6	1013	0.044167	0.03	0.0078805	0.02	1.12	0.34	0.68	0.60	0.23	0.02	0.23	0.46
Rut_5A_110525@7	997	0.044172	0.03	0.0078793	0.02	1.23	0.37	0.74	0.45	0.22	-0.19	0.22	0.44
Rut_5A_110525@9	947	0.044180	0.03	0.0078818	0.02	1.43	0.33	0.65	0.76	0.22	0.02	0.22	0.43
Rut_5A_110525@8	945	0.044173	0.03	0.0078811	0.02	1.25	0.34	0.69	0.67	0.24	0.02	0.24	0.49
Bal_5A_110525@4	759	0.044840	0.02	0.0079394	0.01	16.38	0.28	0.57	8.18	0.18	-0.26	0.18	0.36
Bal_5A_110525@5	960	0.044833	0.03	0.0079421	0.02	16.23	0.33	0.66	8.52	0.23	0.16	0.23	0.46
Bal_5A_110525@6	942	0.044845	0.03	0.0079426	0.02	16.49	0.31	0.62	8.58	0.22	0.09	0.22	0.44
Bal_5A_110525@7	950	0.044839	0.03	0.0079417	0.02	16.35	0.32	0.64	8.47	0.23	0.05	0.23	0.45
KD1-195.58-1	941	0.044143	0.03	0.0078785	0.02	0.58	0.34	0.67	0.34	0.24	0.04	0.24	0.48
KD1-195.58-2	923	0.044132	0.03	0.0078764	0.02	0.33	0.33	0.65	0.07	0.22	-0.11	0.22	0.45
KD1-195.58-3	1010	0.043778	0.04	0.0078436	0.02	-7.69	0.40	0.80	-4.14	0.27	-0.18	0.27	0.54
KD1-195.58-4	938	0.044156	0.03	0.0078790	0.02	0.87	0.31	0.63	0.41	0.22	-0.04	0.22	0.43
KD1-195.58-5	942	0.044138	0.03	0.0078788	0.02	0.47	0.31	0.62	0.37	0.21	0.13	0.21	0.42
KD1-195.58-6	910	0.044105	0.02	0.0078744	0.01	-0.28	0.30	0.59	-0.19	0.20	-0.05	0.20	0.40
KD1-195.58-7	917	0.044079	0.03	0.0078730	0.02	-0.88	0.31	0.62	-0.37	0.22	0.08	0.22	0.43
KD1-195.58-8	743	0.044145	0.02	0.0078731	0.01	0.62	0.27	0.55	-0.35	0.19	-0.67	0.19	0.38
KD1-195.58-9	826	0.044080	0.03	0.0078722	0.02	-0.85	0.38	0.75	-0.47	0.23	-0.03	0.23	0.46
KD1-195.58-10	694	0.044169	0.02	0.0078789	0.02	1.17	0.28	0.55	0.39	0.21	-0.21	0.21	0.43
KD1-195.58-11	772	0.044116	0.03	0.0078753	0.02	-0.04	0.31	0.62	-0.08	0.25	-0.06	0.25	0.50
KD1-195.58-12	881	0.044179	0.02	0.0078825	0.02	1.39	0.29	0.58	0.86	0.21	0.14	0.21	0.41
KD1-195.58-13	905	0.044078	0.03	0.0078723	0.02	-0.90	0.35	0.71	-0.46	0.26	0.00	0.26	0.51
KD1-195.58-14	890	0.044178	0.03	0.0078817	0.02	1.37	0.31	0.62	0.75	0.21	0.04	0.21	0.42
KD1-195.58-15	890	0.044162	0.03	0.0078801	0.02	1.02	0.32	0.64	0.54	0.22	0.01	0.22	0.45
KD1-195.58-16	870	0.044104	0.03	0.0078754	0.02	-0.31	0.32	0.63	-0.06	0.23	0.10	0.23	0.46
Is_5A_110525@3	977	0.044225	0.03	0.0079092	0.02	2.45	0.33	0.66	4.24	0.22	2.98	0.22	0.44
Is_5A_110525@4	948	0.044240	0.03	0.0079130	0.02	2.77	0.32	0.63	4.73	0.21	3.30	0.21	0.43

Appendix E4 - *IMS 1280 Data Tables (continued)*

Sample ID	^{32}S cps (x1 e6)	^{34}S/^{32}S	±1σ (%)	^{33}S/^{32}S	±1σ (%)	δ^{34}S	±1σ	±2σ	δ^{33}S	±1σ	Δ^{33}S	±1σ	±2σ
Rut_5B_110525@5	962	0.044177	0.02	0.0078811	0.02	1.20	0.25	0.50	0.60	0.19	-0.01	0.19	0.38
Rut_5B_110525@6	949	0.044176	0.03	0.0078804	0.01	1.16	0.26	0.53	0.52	0.17	-0.08	0.17	0.33
Rut_5B_110525@7	934	0.044178	0.02	0.0078823	0.01	1.22	0.25	0.50	0.75	0.17	0.12	0.17	0.33
Rut_5B_110525@8	930	0.044178	0.02	0.0078809	0.01	1.21	0.23	0.45	0.58	0.17	-0.05	0.17	0.35
Bal_5B_110525@5	939	0.044844	0.03	0.0079423	0.02	16.32	0.26	0.51	8.40	0.18	-0.01	0.18	0.37
Bal_5B_110525@6	901	0.044837	0.03	0.0079407	0.01	16.16	0.25	0.51	8.19	0.17	-0.13	0.17	0.35
Bal_5B_110525@7	893	0.044846	0.03	0.0079436	0.02	16.35	0.26	0.52	8.57	0.18	0.15	0.18	0.36
KD1-212.58-1	827	0.044153	0.02	0.0078781	0.01	0.64	0.23	0.46	0.23	0.17	-0.10	0.17	0.34
KD1-212.58-2	808	0.044116	0.02	0.0078753	0.02	-0.18	0.23	0.45	-0.13	0.19	-0.04	0.19	0.38
KD1-212.58-3	847	0.044148	0.02	0.0078787	0.02	0.53	0.23	0.46	0.30	0.19	0.03	0.19	0.39
KD1-212.58-4	860	0.044180	0.03	0.0078826	0.01	1.27	0.25	0.51	0.80	0.15	0.14	0.15	0.29
KD1-212.58-5	880	0.044110	0.03	0.0078764	0.02	-0.32	0.25	0.51	0.01	0.19	0.17	0.19	0.39
KD1-212.58-6	880	0.044122	0.02	0.0078772	0.01	-0.05	0.25	0.50	0.10	0.16	0.13	0.16	0.31
KD1-212.58-7	866	0.044158	0.03	0.0078816	0.01	0.76	0.27	0.54	0.67	0.17	0.28	0.17	0.35
KD1-212.58-8	877	0.044115	0.02	0.0078752	0.02	-0.22	0.24	0.48	-0.15	0.19	-0.03	0.19	0.37
Is_5A_091213@4	844	0.044487	0.01	0.0079368	0.01	2.14	0.17	0.34	4.33	0.12	3.22	0.12	0.24

Appendix E4 - *IMS 1280 Data Tables (continued)*

Sample ID	^{32}S cps (x1 e6)	^{34}S/^{32}S	±1σ (%)	^{33}S/^{32}S	±1σ (%)	δ^{34}S	±1σ	±2σ	δ^{33}S	±1σ	Δ^{33}S	±1σ	±2σ
Rut_5B_110526@1	1175	0.04417459	0.03	0.0078814	0.02	1.17	0.31	0.62	0.63	0.19	0.02	0.19	0.38
Rut_5B_110526@3	1161	0.04417633	0.03	0.0078817	0.01	1.21	0.33	0.67	0.67	0.17	0.04	0.17	0.35
Rut_5B_110526@2	1179	0.04416695	0.03	0.0078803	0.02	1.00	0.33	0.66	0.49	0.20	-0.03	0.20	0.41
Rut_5B_110526@4	1164	0.04418492	0.03	0.0078818	0.01	1.41	0.32	0.64	0.68	0.16	-0.05	0.16	0.32
Bal_5B_110526@2	1189	0.04484902	0.03	0.0079430	0.02	16.46	0.34	0.68	8.42	0.19	-0.06	0.19	0.39
Bal_5B_110526@1	1181	0.04484288	0.03	0.0079419	0.02	16.32	0.37	0.74	8.29	0.22	-0.12	0.22	0.43
Bal_5B_110526@3	1162	0.04484782	0.03	0.0079448	0.02	16.43	0.35	0.71	8.65	0.18	0.19	0.18	0.37
KD1-187.30-1	750	0.04419223	0.03	0.0078815	0.02	1.57	0.31	0.61	0.64	0.20	-0.17	0.20	0.40
KD1-187.30-2	918	0.04410258	0.03	0.0078770	0.02	-0.46	0.32	0.65	0.07	0.22	0.31	0.22	0.43
KD1-187.30-3	723	0.04417701	0.02	0.0078822	0.01	1.23	0.29	0.58	0.72	0.17	0.09	0.17	0.34
Is_5A_091213@2	910	0.044434	0.01	0.0079328	0.00	1.81	0.17	0.34	4.14	0.15	3.21	0.15	0.29

References

Abu-Alam, T and Stüwe, K., (2009). MBC(1.7): A visual basic code to calculate bulk composition of rocks from chemistry and volume proportions of the phases. Geological Society of America Abstracts with Programs, **41(7)**, 500.

Alt, J.C. and Honnorez, J., (1984). Alteration of the upper oceanic crust, DSDP site 417: mineralogy and chemistry. *Contributions to Mineralogy and Petrology*, **87**, 149-169.

Agard P., Vidal O. and Goffé B., (2001). Interlayer and Si content of phengite in HP-LT carpholite-bearing metapelites. *Journal of Metamorphic Geology, **19**, 477-493.*

Anhaeusser, C.R., (1969). The stratigraphy, structure, and gold mineralization of the Jamestown and Sheba Hills areas of the Barberton Mountain Land. *University of Witwatersrand, Johannesburg*, 332 p.

Anhaeusser, C.R., (1972). The geology of the Jamestown hills area of the Barberton Mountain Land, South Africa. *Geological Society of South Africa Transactions*, **75**, 225-263.

Anhaeusser, C.R., (1973). The evolution of the early Precambrian Crust of southern Africa. *Royal Society of London Philosophical Transactions, series A* **273**, 359-388.

Anhaeusser, C.R., (1983). Contributions to the Geology of the Barberton Mountain Land, *Special Publication Geological Society South Africa*, **9**, 223 pp.

Anhaeusser, C.R. and Robb, L.J., (1983). Geological and geochemical characteristics of the Heerenveen and Mpuluzi batholiths south of the Barberton greenstone belt and preliminary thoughts on their petrogenesis. In: *Contributions to the Geology of the Barberton Mountain Land*. Anhaeusser, C. R. (ed), *Special Publication of the Geological Society of South Africa* **9**, 131-152.

Anhaeusser, C.R., (2010). Magmatic and structural characteristics of the ca. 3440 Ma Theespruit pluton, Barberton Mountain Land, South Africa. *American Journal of Science*, **310**, 1136-1167; doi:10.2475/09.2010.14.

Armstrong, R.A., Compston, W., de Wit, M.J. and William I.S., (1990). The stratigraphy of the 3.5-3.2 Ga Barberton Greenstone Belt revisited: a single zircon ion microprobe study: *Earth* and *Planetary Science Letters*, **101**, 90-106.

Arndt, N., (1983). Role of a thin, komatiite-rich oceanic crust in the Archean plate-tectonic process. *Geology*, **11**, 372-375.

Ash, C.H., (2001). Relationship between ophiolites and gold–quartz veins in the North American Cordillera. *Department of Energy, Mines and Petroleum Resources, Mineral. Div. Geol. Surv. Branch, Bull.* **108**.

Auclair, M., Gauthier, M., Trottier, J., Jébrak, M. and Chartrand, F., (1993). Mineralogy, geochemistry, and paragenesis of the Eastern Metals serpentinite-associated Ni–Cu–Zn deposit, Quebec Appalachians. *Economic Geology*, **88**, 123-138.

Augier, R., Agard, P., Monie, P., Jolivet, L., Robin, C. and Booth-Rea, G., (2005). Exhumation, doming and slab retreat in the Betic Cordillera (SE Spain): in-situ $^{40}Ar/^{39}Ar$ ages and P–T-d-t paths for the Nevado-Filabride complex. *Journal of Metamorphic Geology*, **23**, 357–381.

Bach, W., Alt, J. C., Niu, Yaoling, Humphris, S.E., Erzinger, J. and Dick, H.J.B., (2001). The geochemical consequences of late-stage low-grade alteration of lower ocean crust at the

SW Indian Ridge: results from ODP Hole 735B (Leg 176). *Geochimica et Cosmochimica Acta* **65**, 3267-3287.

Bailey, S.W., (1988). In: S.W. Bailey (ed.), Chlorites: structures and crystal chemistry in Hydrous Phyllosilicates (exclusive of micas). *Rev. Mineral.* **19**, 347-403.

Banno, S., (1998). Pumpellyite-actinolite facies of the Sanbagawa metamorphism. *Journal of Metamorphic Geology*, **16**, 117–128.

Barnes , S.J., and Roeder, P.L., (2001). The range of spinel compositions in terrestrial mafic and ultramafic rocks. Journal of Petrology, **42**, 279-302.

Battaglia, S., (2004). Variations in the chemical composition of illite from five geothermal fields: a possible geothermometer. *Clay Minerals*, **39**, 501-510.

Baublys, K.A., Golding, S.D., Young, E., and Kamber, B.S., (2004). Simultaneous determination of ^{33}SV-CDT and ^{34}SV-CDT using masses 48, 49 and 50 on a continuous flow isotope ratio mass spectrometer. *Rapid Communications in Mass Spectrometry*, **18**, 2765–2769.

Bekker, A., Barley, M.E., Fiorentini, M.L., Rouxel, O.J., Rumble, D. and Beresford, S.W., (2009). Atmospheric Sulfur in Archean Komatiite-Hosted Nickel Deposits**.** *Science*, **326**, 1086-1089.

Belcher, R.W. and Kisters, A.F.M., (2006). Progressive adjustments of ascent and emplacement controls during incremental construction of the 3.1 Ga Heerenveen batholith, South Africa. *Journal of Structural Geology* **28**, 1406-1421.

Berman, R.G., (1991). Thermobarometry using multiequilibrium calculations: a new technique with petrologic applications. *Canadian Mineralogist*, **29**, 833–855.

Béziat, D., Bourges, F., Debat, P., Lompo, M., Tollon, F. and Zonou, S., (1998). Albitite et "listvenite": sites de concentration aurifère inédits dans les ceintures de roches vertes birimiennes fortement hydrothermalisées du Burkina Faso. *Bull. Soc. Géol. France*, **169**, 563-571.

Biggin, A.J, de Wit, M.J, Langereis, C.G, Zegers, T.E., Voûte, S, Dekkers, M.J. and Drost, K., (2011). Palaeomagnetism of Archaean rocks of the Onverwacht Group, Barberton Greenstone Belt (southern Africa): Evidence for a stable and potentially reversing geomagnetic field at ca. 3.5 Ga. *Earth Planetary Science Letters*, **302**, 314-328.

Bishop, B.P., and Bird, D.K., (1987). Variation in sericite compositions from fracture zones within the Coso Hot Springs geothermal system. *Geochim. Cosmochim. Acta*, **51**, 1245-1256.

Bohlen, S.R., Montana, A. and Kerrick, D.M., (1991). Precise determinations of the equilibria kyanite = sillimanite and kyanite = andalusite and a revised triple point for Al_2SiO_5 polymorphs. *American Mineralogist*, **76**, 677-680.

Borthwick, J., and Harmon, R.S., (1982). A note regarding ClF_3 as an alternative to BrF5 for oxygen isotope analysis. *Geochimica et Cosmochimica Acta*, **46**, 1665–1668.

Brandl, G., Cloete, M., and Anhaeusser, C.R., (2006). Archaean greenstone belts. In: Johnson M.R., Anhaeusser, C.R. and Thomas, R.J. (Eds.), *The Geology of South Africa*. Geological Society of South Africa, Johannesburg/Council for Geoscience, Pretoria, 9-51.

Brukeraxs, (2005). DIFFRACplus Evaluation Package Release 2005. BrukerAXS, Karlsruhe, Germany.

Bucher, K. and Frey, M., (1994). *Petrogenesis of Metamorphic Rocks*. Springer-Verlag. Berlin. 318pp.

Byerly, G.R., Kröner, A., Lowe, D.R., and Walsh, M.M., (1993). Sequential magmatic evolution of the early Archean Onverwacht Group: evidence from the upper formations: *Eos* (Transactions, American Geophysical Union), **74**, 660.

Byerly, G.R., Kröner, A., Lowe, D.R., Todt, W., and Walsh, M.M., (1996). Prolonged magmatism and time constraints for sediment deposition in the early Archean Barberton greenstone belt: Evidence from the Upper Onverwacht and Fig Tree groups, Precambrian Res., **78**, 125 – 138.

Byerly, G.R., (1999). Komatiites of the Mendon Formation: Late-stage ultramafic volcanism in the Barberton Greenstone Belt. *Geological Society of America Special Paper, Special Paper,* **329,** 189-211.

Carson, C.J., Powell, R., Wilson, C.J.L., and Dirks, P.H.G.M., (1997). Partial melting during tectonic exhumation of a granulite terrane: an example from the Larsemann Hills, East Antarctica. *J. Metamorphic Geol*ogy, **15**, 105–126.

Cathelineau, M., (1988). Cation site occupancy in chlorites and illites as a function of temperature. *Clay Minerals,* **23**, 471-485.

Cathelineau, M. and Nieva, D., (1985). A chlorite solid solution geothermometer. The Los Azufres geothermal system (Mexico). *Contributions to Mineralogy and Petrology*, **91**, 235-244.

Chadwick, B and Crewe, M.A., (1986). Chromite in the early Archean Akilia association (ca. 3800 m.y.) Ivisartoq region, inner Gothabsfjord, southern Greenland. *Economic Geology* **81**, 184-191.

Chatterjee, N.D., (1976). Margarite stability and compatibility relations in the system CaO-Al_2O_3-SiO_2-H_2O as a pressure-temperature indicator. *American Mineralogist,* **61**, 699-709.

Chavagnac, V., 2004. A geochemical and Nd isotopic study of the Barberton komatiites (South Africa): implications for the Archean mantle. Lithos 75, 253–281, doi:10.1016/j.lithos.2004.03.001.

Cho, M., Maruyama, S. and Liou, J.G., (1986). Transition from the zeolite to prehnite-pumpellyite facies in the Karmutsen metabasites, Vancouver Island, B.C. *Journal of Petrology,* **27**, 467-494.

Clayton, R.N., and Mayeda, T.K., (1963). The use of brominepentafluoride in the extraction of oxygen from oxides and silicates for isotopic analysis. *Geochimica et Cosmochimica Acta*, **27**, 43–52.

Cloete, M., (1991). An overview of metamorphism in the Barberton greenstone belt, In: *Two Cratons and an Orogen* - Excursion Guidebook and Review Articles for a Field Workshop through Selected Archean Terranes of Swaziland, South Africa and Zimbabwe: Johannesburg, Ashwal L. D. (ed.), *IGCP project 280, Dept. of Geology, Univ. Witwatersrand,* 84-98

Cloete, M., (1999). Aspects of volcanism and metamorphism of the Onverwacht Group lava in the Southwestern portion of the Barberton Greenstone Belt, *Memoirs of the Geological Survey of South Africa.*, **84**, 232 pp.

Cotterill, P., (1969). The chromite deposits of Selukwe, Rhodesia. *Economic Geology Monograph*, **4**, 154-186.

Compston, W., Kröner, A., (1988). Multiple zircon growth within early Archean tonalitic gneiss from the Ancient Gneiss Complex, Swaziland. *Earth Planetary Science Lett*ers, **87**, 13 – 28.

Condie, K.C and Hunter, D.R., (1976). Trace element geochemistry of Archean granitic rocks from the Barberton region, South Africa. *Earth Planetary Science Lett*ers, **29**, 389-400.

Coplen, T.B., (1994). Reporting of stable hydrogen, carbon, and oxygen isotopic abundances. *Pure and Applied Chemistry*, **66**, 273–276.

Coplen, T.B., Brand, W.A., Gehre, M., Gröning, M., Meijer, H.A.J., Toman, B., and Verkouteren, R.M., (2006). New guidelines for $\delta^{13}C$ measurements. *Analytical Chemistry*, **78**, 2439–2441.

Crawford, A.J., (1989). Boninites, Unwin Hyman, London, 149pp.

Crowe, D.E., and Vaughan, R.G., (1996). Characterization and use of isotopically homogeneous standards for in situ laser microprobe analysis of $^{34}S/^{32}S$ ratios. *American Mineralogist*, **81**, 187–193.

Dann, J.C., (2000). The 3.5 Ga Komati Formation, Barberton Greenstone Belt, South Africa, Part I: New maps and magmatic architecture. *South African Journal of Geol*ogy, **103**, 47-68.

Dann, J.C., Grove, T.L., (2007). Volcanology of the Barberton greenstone Belt, South Africa: inflation and evolution of flow fields. In: van Kranendonk, M.J., Smithies, R.H., Bennett, V.C. (Eds.), *Earth's Oldest Rocks*. Developments in Precambrian Geology, **15**. Elsevier, Amsterdam, 527-570.

de Caritat, P., Hutcheon, I. and Walshe, J.L., (1993). Chlorite geothermometry: a review. *Clays and Clay minerals*, **41**, 219-239.

de Ronde, C.E.J., Kamo, S., Davis, D.W., de Wit, M.J. and Spooner, E.T.C., (1991). Field, geochemical and U-Pb isotopic constraints from hypabyssal felsic intrusions within the Barberton greenstone belt, South Africa: Implications for tectonics and the timing of gold mineralization. *Precambrian Research* **1991**, 261-280.

de Ronde, C.E.J., and de Wit, M.J., (1994). Tectonic history of the Barberton Greenstone Belt, South Africa: 490 million years of Archean crustal evolution. *Tectonics*, **13**, 983-1005.

de Ronde, C.E.J., and Kamo, S., (2000). An Archean arc-arc collisional event: a short-lived (ca. 3 Myr) episode, Weltevreden area, Barberton greenstone belt, South Africa. *Journal of African Earth Sciences*, **30**, 219-248.

de Vries, S.T., Nijman, W., and de Boer, P.L., (2010). Sedimentary geology of the Palaeoarchean Buck Ridge (South Africa) and Kittys Gap (Western Australia) volcano-sedimentary complexes. *Precambrian Research*, **183**, 749-769.

de Vries, S.T., Nijman, W., and Armstrong, R.A., (2006). Growth-fault structure and stratigraphic architecture of the Buck Ridge volcano-sedimentary complex, upper Hooggenoeg Formation, Barberton Greenstone Belt, South Africa. *Precambrian Res*earch, **149**, 77–98.

de Wit, M.J., (1982a). Gliding and overthrust nappe tectonics in the Barberton greenstone belt. *Journal of Structural Geology*, **4**, 117-136.

de Wit, M.J., (1982b). Archean abiogenic and probable biogenic structures associated with mineralized hydrothermal vent systems and regional metasomatism, with implications for greenstone belt studies. *Economic Geology*, **77**, 1783 - 1802.

de Wit, M.J., Fripp, R.E.P. and Stanistreet, I.G., (1983). Tectonic and stratigraphic implications of new field observations along the southern part of the Barberton greenstone belt. *Spec. Publ. Geological Society* of *South Africa*, **9**, 21-29.

de Wit, M.J., (1983). Notes on a preliminary 1:25,000 geological map of the southern part of the Barberton Greenstone Belt. In: C.R. Anhaeusser (Ed), Contributions to the Geology of the Barberton Mountain Land. *Spec. Publ. Geol. Soc. South Africa*, 85-187.

de Wit, M.J., (1986a). Extensional tectonics during the igneous emplacement of the mafic-ultramafic rocks of the Barberton greenstone belt (abstract). *Tech. Rep. Lunar Planet. Inst*, **86-10**, 84-85.

de Wit, M.J., (1986b). A Mid-Archean Ophiolite Complex (abstract). *Tech. Rep. Lunar Planet. Inst*, **86-10**, 86-87.

de Wit, M.J., Armstrong, R.A., Hart, R.J., and Wilson, A.H., (1987a). Felsic igneous rocks within the 3.3 – 3.5 Ga Barberton greenstone belt: High crustal level equivalents of the surrounding tonalite-trondhjemite terrain, emplaced during thrusting. *Tectonics*, **6**, 529–549.

de Wit, M.J., Hart, R.A., and Hart, R.J., (1987b). The Jamestown ophiolite complex, Barberton mountain belt; a section through 3.5 Ga oceanic crust. *Journal African Earth Science*, **6**, 681 – 730.

de Wit, M.J., (1991). Archean greenstone belt tectonism and basin development: Some insights from the Barberton and Pietersburg greenstone belts, Kaapvaal Craton, South Africa. *Journal of African Earth Sciences*, **13**, 45-63.

de Wit, M.J., Roering, C., Hart, R.J.R., Armstrong, A., de Ronde, C.E., Green, W.E., Tredoux, M., Peberdy, E. and Hart, R.A., (1992). Formation of an Archean continent. *Nature*, **357**, 553-562.

de Wit, M.J., (1998). On Archean granites, greenstones, cratons and tectonics: does the evidence demand a verdict? *Precambrian Research*, **91**, 181–226.

de Wit, M.J., Furnes, H., and Robins, B., (2011). Geology and Tectonostratigraphy of the Onverwacht Suite, Barberton Greenstone Belt, South Africa. *Precambrian Research*, **186,** 1-27.

Dick, H.J.B. and Bullen, T., (1984). Chromian spinel as a petrogenetic indicator in abyssal and alpine-type peridotites and spatially associated lavas. *Contributions to Mineralogy and Petrology*, **86**, 54-76.

Dick, H.J.B., Schouten, H., Meyer, P.S., Gallo, D.G., Bergh , H., Tyce, R., Patri at, P., Johnson, K.T.M., Snow, J. and Fisher, A., (1991). Tectonic evolution of the Atlantis II fracture zone. *Proc. ODP, Sci. Results*, **118**, 359-398.

Diener, J.F.A., Stevens, G., Kisters, A.F.M. and Poujol, M., (2005). Metamorphism and exhumation of the basal parts of the Barberton greenstone belt, South Africa: Constraining the rates of Mesoarchean tectonism. *Precambrian Research*, **143**, 87-112.

Diener, J.F.A., Powell, R. White, R.W. and Holland, T.J.B., (2007). A new thermodynamic model for clino- and orthoamphiboles in the system Na_2O–CaO–FeO–MgO–Al_2O_3–SiO_2–H_2O–O. *Journal of Metamorphic Geology*, **25**, 631–656.

Drits V.A., and McCarty, D.K., (2007). The nature of structure-bonded H2O in illite and leucophyllite from dehydration and dehydroxylation experiments. *Clay Clay Minerals,* **55,** 45–58.

Dubacq, B. Vidal., O and de Andrade, V., (2010). Dehydration of dioctahedral aluminous phyllosilicates: thermodynamic modelling and implications for thermobarometric estimates. *Contribution to Mineralogy and Petrology,* **159**, 159–174.

Dubacq, B., Vidal, O., and Lewin, E., (2011). Atomistic investigation of the pyrophyllitic substitution and implications on clays stability. *American Mineralogist,* **96**, 241–249.

Duchac, K.C., and Hanor, J.S., (1987). Origin and timing of metasomatic silicification of an early Archean komatiite sequence, Barberton Mountain Land, South Africa. *Precambrian Research,* **37**, 125–146.

Dunstan L.P., Gramch, J.W., Barnes, I.L., and Purdy, W.C., (1980). The absolute abundance and the atomic weight of a reference sample of thallium. *Journal of Research of the National Bureau of Standards,* **85**, 1-10.

Dziggel, A., Stevens, G., Poujol, M., Anhaeusser, C.R. and Armstrong, R.A., (2002). Metamorphism of the granite-greenstone terrane south of the Barberton Greenstone Belt, South Africa: an insight into the tectono-thermal evolution of the 'lower' portions of the Onverwacht Group. *Precambrian Research,* **114**, 221-247.

Faure, G., (1986). Principles of Isotope Geology. New York: John Wiley and Sons.

Farquhar, J., Bao, H., and Thiemens, M., (2000). Atmospheric influence of Earth's earliest sulfur cycle. *Science*, **289**, 756–758.

Farquhar, J. and Wing, B.A., (2003). Multiple sulphur isotopes and the evolution of the atmosphere. *Earth and Planetary Science Letters*, **213,** 1-13.

Fliegel, D.J., Kosler, J., Simonetti, A., McLoughlin, N., de Wit, M.J., Wirth D. and Furnes, H., (2010). In-situ dating of the Earth's oldest trace fossil in volcanic glass at 3.34 Ga. *Earth Planetary Science Letters, **299**, 290-298.*

Frey, M., de Capitani, C. and Liou, J.G., (1991). A new petrogenetic grid for low-grade metabasites. *Journal of Metamorphic Geology,* **9**, 497-509.

Fripp, R.E.P., Van Nierop, D.A., Callow, M.J., Lilly, P.A. and de Plessis, L.U., (1980). Deformation in part of the Archaean Kaapvaal Craton, South Africa. *Precambrian Research,* **13**, 241-251.

Furnes, H, Banerjee, N.R., Muehlenbachs, K., Staudigel, H., and de Wit, M.J., (2004). Early life recorded in Archean pillow lavas. *Science,* **304**, 578-581.

Furnes, H., McLoughlin, N., Muehlenbachs, K., Banerjee, N.R., Staudigel, H., Dilek, Y., de Wit, M., Van Kranendonk, M., and Schiffmann, P., (2008). Oceanic pillow lavas and hyaloclastites as habitats for microbial life through time—A review, in *Links Between Geological Processes, Microbial Activities, and Evolution of Life.* Modern Approaches Solid Earth Science Series, **4**, (Eds) Y. Dilek, H. Furnes, and K. Muehlenbachs, Springer, New York, 1–68.

Furnes, H., de Wit, M.J., Robins, B., and Sandståd, N.R., (2011). Volcanic evolution of the upper Onverwacht Suite, Barberton Greenstone Belt, South Africa. *Precambrian Research*, **186**, 28-50.

Furnes, H., de Wit, M.J., Staudigel, H., Rosing, M., and Muehlenbachs, K., (2007). A vestige of Earth's oldest ophiolite. *Science,* **315**, 1704-1707.

Green, E.C.R., Holland, T.J.B. and Powell, R., (2007). An order-disorder model for omphacitic pyroxenes in the system jadeite-diopside-hedenbergite-acmite, with applications to eclogitic rocks. *American Mineralogist,* **92**, 1181-1189.

Gregory, R.J. and Taylor, H.P., (1981). An oxygen isotope profile in a section of Cretaceous oceanic crust: Samail Ophiolite, Oman: Evidence of $\delta^{18}O$ buffering of the oceans by deep (5 km) seawater hydrothermal circulation at mid-ocean ridges. *Journal of geophysical Research*, **86**, 2737-2755.

Grosch, E.G., McLoughlin, N., de Wit, M.J. and Furnes, H., (2009a). Drilling for the Archean Roots of Life and Tectonic Earth in the Barberton Mountains. *Scientific Drilling*, **8**, 24-28.

Grosch, E.G., McLoughlin, N., de Wit, M.J. and Furnes, H., (2009b). Deciphering Earth's Deep History: Drilling in Africa's Oldest Greenstone Belt. *Eos*, **90**, 350-351.

Guidotti C.V., (1984). Micas in metamorphic rocks. In: S.W. Bailey (ed.), Micas. *Reviews in Mineralogy*, Minerological Society of America, **13**, 357-468.

Halls, C. and Zhao, R., (1995). Listvenite and related rocks: perspectives on terminology and mineralogy with reference to an occurrence at Cregganbaun, Co. Mayo, Republic of Ireland. *Mineral Deposita,* **30**, 303-313.

Hanor, J.S. and Duchac, K.C., (1990). Isovolumetric silicification of early Archean komatiites: geochemical mass balances and constraints on origin. *Journal of Geology,* **98**, 863–877.

Hamilton, W.B., (1998). Archean magmatism and deformation were not the products of plate tectonics. *Precambrian Research,* **91**, 143-180.

Harmon, R.S. and Hoefs, J., (1995) Oxygen isotope heterogeneity of the mantle deduced from global ^{18}O systematics of basalts from different geotectonic settings. *Contributions to Mineralogy and Petrology*, **120**, 95-114.

Heubeck, C., and Lowe, D.R., (1994a). Depositional and tectonic setting of the Archean Moodies Group, Barberton Greenstone Belt, South Africa. *Precambrian Research*, **68**, 257 – 290.

Heubeck, C., and Lowe, D.R., (1994b). Late syndepositional deformation and detachment tectonics in the Barberton Greenstone Belt, South Africa. *Tectonics*, **13**, 1514 – 1536.

Hillier, S. and Velde, B., (1992). Octahedral occupancy and the chemical composition of diagenetic (low-temperature) chlorites. *Clay Minerals,* **26**, 146–168.

Hoefs, J., (1987). Stable Isotope Geochemistry. Springer-Verlag, 241p.

Hoffman, A., (2011). Archean hydrothermal systems in the Barberton Greenstone Belt and their significance as a Habitat for Early Life. (eds) S.D. Golding and M.Glikson. Earliest Life on Earth: Habitats, Environments and Methods of Detection, 51-77.

Hoffman, A and Harris, C., (2008). Stratiform alteration zones in Barberton Greenstone belt: a window into subseafloor processes 3.5-3.3 Ga ago. *Chemical Geology*, **257**, 224-242.

Holland, T.J.B. and Powell, R., (1998). An internally-consistent thermodynamic dataset for phases of petrological interest. *Journal of Metamorphic Geology,* **16**, 309-344.

Holland, T.J.B. and Powell, R., (2003). Activity–composition relations for phases in petrological calculations: an asymmetric multicomponent formulation. *Contributions to Mineralogy and Petrology,* **145**, 492–501.

Holland, T.J.B., Baker, J.M. and Powell, R., (1998). Mixing properties and activity–composition relationships of chlorites in the system $MgO–FeO–Al_2O_3–SiO_2–H_2O$. *European Journal of Mineralogy*, **10**, 395–406.

Horn, I., Rudnick, R.L., and McDonough, W.F., (2000). Precise elemental and isotope ratio measurement by simultaneous solution nebulisation and laser ablation-ICP-MS: application to U-Pb geochronology. *Chemical Geology*, **164**, 281-301.

Hunter, D.R., (1968). The Precambrian terrain in Swaziland with particular reference to the granitic rocks. PhD Thesis, University of Witwatersrand, Johannesburg (unpublished).

Hunter, D.R., (1973a). The Ancient Gneiss Complex in Swaziland. *Transactions Geological Society of South Africa*, **73**, 107-150.

Hunter, D.R., (1974). Crustal development in the Kaapvaal craton, I. The Archaean: *Precambrian Research*, **1**, 259-294.

Inoue, A., Meunier, A., Patrier-Mas, P., Rigault, C., Beaufort, D., and Viellard., P., (2009). Application of chemical geothermometry to low-temperature trioctahedral chlorites. *Clays and Clay Minerals*, **57**, 371–382.

Irvine, T.N., (1965). Chromian spinel as a petrogenetic indicator: Part 1, Theory. *Canadian Journal of Earth Science*, **2**, 648-671.

Jackson, M.P.A., Eriksson, K.A., and Harris, C.W., (1987). Early Archean foredeep sedimentation related to crustal shortening: A reinterpretation of the Barberton Sequence, southern Africa, *Tectonophysics*, **136**, 197 – 221.

Jackson, S.E., Pearson, N.J., Griffin, W.L., and Belousova, E., A., (2004). The application of laser ablation-inductively coupled plasma-mass spectrometry to in situ U-Pb zircon geochronology. *Chemical Geology*, **211**, 47-69.

Jamieson, R.A., (1980). Formation of metamorphic aureoles beneath ophiolites – Evidence from the St. Anthony Complex, Newfoundland. *Geology*, **8**, 150-154.

Jamieson, R.A., (1986). P-T paths from high temperature shear zone beneath ophiolites. *Journal of Metamorphic Geology*, **4**, 3-22.

Jiang, W.T., Peacor, D.R. and Buseck, P.R., (1994). Chlorite geothermometry-contamination and apparent octahedral vacancies. *Clays and Clay Minerals*, **42**, 593-605.

Johannes, W., (1978). Loss of iron to the platinum-container in melting experiments with basalts and a method to reduce it. *Contributions to mineralogy and petrology*, **67**, 221-225.

Johnson, P.R., Kattan, F.H., and Al-Saleh, A.M., (2004). Neoproterozoic ophiolites in the Arabian Shield: Field relations and structure. In: Kusky, T.M. (Ed.), *Precambrian Ophiolites and Related Rocks*. In: Developments in Precambrian Geology, **13**. Elsevier, Amsterdam, 129–162.

Jones, D.L., Howell, D.G., Coney, P.J., and Monger, J.W.H., (1983). Recognition character and analysis of tectonostratigraphic terranes in western North America. In: *Advances in Earth and Planetary Sciences*, ed. M. Hashimoto, S. Uyeda, Tokyo: Terra Sci. Publ. Co, 21-35.

Kamber, B.S., and Whitehouse, M.J., (2007). Micro-scale sulphur isotope evidence for sulphur cycling in the late Archean shallow ocean. *Geobiology*, **5**, 5–17.

Kamo, S. and Davis, D.W., (1994). Reassessment of Archean crustal development in the Barberton Mountain Land, South Africa, based on U-Pb dating. *Tectonics,* **13**, 167-192.

Karson, J.A. and Lawrence, R.M., (1997). Tectonic window into gabbroic rocks of the middle oceanic crust in the MARK area near Sites 921-924. *Proc. ODP, Sci. Results,* **153**, 61-76.

Karson, J.A., Früh-Green, G.L., Kelley, D.S., Williams, E.A., Yoerger, D.R. and Jakuba, M., (2006). Detachment shear zone of the Atlantis Massif core complex, Mid-Atlantic Ridge, 30°N. *Geochemistry Geophysics Geosystems* **7**(6), doi:10.1029/2005GC001109.

Kelley, D.S., Karson, J.A., Blackman, D.K., Früh-Green, G.L., Butterfield, D.A., Lilley, M.D., Olson, E.J., Schrenk, M.O., Roe, K.K., Lebon, G.T., Rivizzigno, P. and the AT3-60 Shipboard Party., (2001). An off-axis hydrothermal vent field near the Mid-Atlantic Ridge at 30^{o}N. *Nature,* **412**, 145–149.

Kishida, A. and Kerrich, R., (1987). Hydrothermal alteration zoning and gold concentration at the Kerr–Addison Archean lode gold deposit, Kirkland Lake, Ontario. *Economic Geology*, **82**, 649-690.

Kosler, J., Fonneland, H., Sylvester, P., Tubrett, M., and Pedersen, R.B., (2002). U-Pb dating of detrital zircons for sediment provenance studies – a comparison of laser ablation ICPMS and SIMS techniques. *Chemical Geology*, **182**, 605-618.

Kosler, J., and Sylvester, P., (2003). Present trends and the future of zircon in geochronology: laser ablation ICPMS. *Reviews in Mineralogy and Geochemistry*, **53**, 243-275.

Kretz, R., (1983). Symbols for rock-forming minerals. *American Mineralogist* **68**, 277-279.

Kröner, A., Compston, W., and William, I.S., (1989). Growth of early Archean crust in the Ancient Gneiss Complex of Swaziland as revealed by single zircon dating. *Tectonophysics*, **161**, 271–298.

Kröner, A., and Tegtmeyer, A., (1994). Gneiss-greenstone relationships in the Ancient Gneiss Complex of southwestern Swaziland, southern Africa and implications for crustal evolution. *Precambrian Research*, **67**, 109-139.

Kröner, A., Todt, W., (1988). Single zircon dating constraining the maximum age of the Barberton greenstone belt, southern Africa. *Journal of Geophysical Research*, **93**, 329–337.

Kröner, A., Byerly, G.R. and Lowe, D.R., (1991). Chronology of early Archaean granite-greenstone evolution in the Barberton Mountainland, South Africa, based on precise dating of single zircon evaporation. *Earth and Planetary Science Letters,* **103**, 41-54.

Kröner, A., Hegner, E., Byerly, G.R., and Lowe, D.R., (1992). Possible terrane identification in the early Archean Barberton Greenstone Belt. South Africa, using single zircon geochronology: Eos (Transactions, American Geophysical Union), **73**, 616.

Kröner, A., Hegner, E., Wendt, J.I., and Byerly, G.R., (1996). The oldest part of the Barberton granitoid greenstone terrain, South Africa: Evidence for crust formation between 3.5 and 3.7 Ga. *Precambrian Research*, **78**, 105 – 124.

Kusky, T.M. and Jianghai, L., (2010). Origin and Emplacement of Archean Ophiolites of the Central Orogenic Belt, North China Craton. *Journal of Earth Science*, **21**, 744–781.

Kyser, T.K., O'Neil, J.R., and Carmichael, I.S.E., (1981). Oxygen isotope thermometry of basic lavas and mantle nodules. *Contributions to Mineralogy and Petrology,* **77**, 11-23.

Kyser, T.K., O'Neil, J.R., and Carmichael, I.S.E., (1982). Genetic relations among basic lavas and ultramafic nodules: evidence from oxygen isotope compositions. *Contributions to Mineralogy and Petrology*, **81**, 88-102.

Kyser, T.K., (1986). Stable isotope variations in the mantle. In Valley, J.W., Taylor, H.P., and O'Neil, J.R., eds., *Stable isotopes in high temperature geological processes*. Chelsea, Michigan. *Reviews in Mineralogy*, **16**, 141-164.

Lamb, S.H., (1984). Structures on the eastern margin of the Archaean Barberton Greenstone Belt, northwest Swaziland. In: Kröner, A., and Greiling, A., eds. *Precambrian tectonics illustrated*: Stuttgart, E. Schweizerbart'sche Verlagsbuchhandlung, 19-39.

Le Hebel, F., Vidal, O., Kienast J.R., and Gapais, D., (2002). Evidence for HP-LT Hercynian metamorphism within the 'Porphyroides' of South Brittany (France). *Comptes Rendus Geoscience*, **334**, 205-211.

Le Maitre, R.W., (1976). The chemical variability of some common igneous rocks. *Journal of Petrology*, **17**, 589-637.

le Roex, A.P., (1985). Geochemistry, mineralogy and magmatic evolution of the basaltic and trachytic lavas from Gough Island, South Atlantic. *Journal of Petrology* **26**, 149-186.

le Roex, A., Späth, A., and Zartman, L.R.E., (2001). Lithospheric thickness beneath the southern Kenya Rift: implications from basalt geochemistry. *Contributions to Mineralogy and Petrology*, **142**, 89–106.

Liou, J.G., Seki, Y., Guillemette, R. and Sakai, H., (1985). Compositions and paragenesis of secondary minerals in the Onikobe geothermal system, Japan. *Chemical Geology*, **49**, 1-20.

Lopez-Martinez, M., York, D., and Hanes, J.A., (1992). A $^{40}Ar/^{39}Ar$ geochronological study of komatiites and komatiitic basalts from the Lower Onverwacht Volcanics: Barberton Mountain Land, South Africa. *Precambrian Research* **57**, 91-119.

Loucks, R.R., (1991). The bound interlayer H_2O content of potassic white micas: muscovite - hydromuscovite -hydropyrophyllite solutions. *American Mineralogist*, **76**, 1563-1579.

Lowe, D.R., and Knauth, L.P., (1977). Sedimentology of the Onverwacht Group (3.4 billion years), Transvaal, South Africa and its bearing on the characteristics and evolution of the early Earth. *Journal of Geology*, **85**, 699-723.

Lowe, D.R. and Byerly, G.R., (1986). Archean flow-top alteration zones formed initially in a low temperature sulphate-rich environment environment. *Nature*, **324**, 245-248.

Lowe, D.R., (1994). Accretionary history of the Archean Barberton greenstone belt (3.55–3.22 Ga) southern Africa. *Geology*, **22**, 1099–1102.

Lowe, D.R. and Byerly, G.R., (1999a). Geologic evolution of the Barberton Greenstone Belt, South Africa. *Geological Society of America Special Paper*, *Special Paper* **329**.

Lowe, D.R. and Byerly, G.R., (1999b). Stratigraphy of the west-central part of the Barberton Greenstone Belt, South Africa, In: *Geologic evolution of the Barberton Greenstone Belt, South Africa*. Lowe, D. R. and Byerly, G. R. (eds). *Geological Society of America Special Paper*, **329**, 1-36.

Lowe, D.R., Byerly, G.R. and Heubeck, C., (1999). Structural divisions and development of the west-central part of the Barberton Greenstone Belt. In: *Geologic evolution of the Barberton Greenstone Belt, South Africa.* Lowe, D. R. and Byerly, G. R. (eds). *Geological Society of America Special Paper*, **329**, 37-82.

Lowe, D.R., and Byerly, G.R., (2007). An overview of the geology of the Barberton greenstone belt and vicinity: implications for early crustal development. In: Van Kranendonk, M.J., Smithies, R.H., Bennett, V.C. (Eds.) *Earth's Oldest Rocks*. Developments in Precambrian Geology, **15**, 481–526. Elsevier, Amsterdam.

Ludwig, K.R., (1999). IsoplotEx v. 2.6. Berkeley Geochronological Center Special Publication no. 1a.

Mahar, E.M., Baker, J.M., Powell, R., Holland, T.J.B. and Howell, N., (1997). The effect of Mn on mineral stability in metapelites. *Journal of Metamorphic Geology,* **15**, 223–238.

Malpas, J.G., (1979). The dynamothermal aureole of the Bay of Islands ophiolite suite. Canadian *Journal of Earth Sciences*, **16**, 2086-2101.

Maruyama, S., Suzuki, K. and Liou, J.G., (1983). Greenschist-amphibolite transition equilibria at low pressures. *Journal of Petrology,* **24**, 583-604.

Massonne, H.J. and Schreyer, W., (1987). Phengite geobarometry based on the limiting assemblage with K-felspar, phlogopite, and quartz. *Contributions to Mineralogy and Petrology*, **96**, 212–224.

Massonne, H.J. and Szpurka, Z., (1997). Thermodynamic properties of white micas on the basis of high-pressure experiments in the systems K_2O-MgO-Al_2O_3-SiO_2-H_2O and K_2O-FeO-Al_2O_3-SiO_2-H_2O. *Lithos*, **41**, 229–250.

Mattey, D.P., Lowry, D., and MacPherson, C., (1994). Oxygen isotope composition of mantle peridotites. *Earth and Planetary Science Letters,* **128**, 231-241.

Matveev, S and Balhaus, C., (2002). Role of water in the origin of podiform chromite deposits. *Earth and Planetary Science Letters*, **203**, 235-243.

McCaig, A.M., Wayne, D.M., Marshall, J.D., Banks, D., and Henderson, I., (1995). Isotopic and fluid inclusion studies of fluid movement along the Garvanie Thrust, Central Pyrenees: reaction fronts in carbonate mylonites. *American Journal of Science*, **295**, 309-343.

McLoughlin, N., Staudigel, H., Furnes, H., Eickmann, B. and Ivarsson, M., (2010). Mechanisms of microtunneling in rock substrates - Distinguishing endolithic biosignatures from abiotic microtunnels. *Geobiology*, **8**, 245-255.

Miyashiro, A., Shido, F. and Ewing, M., (1971). Metamorphism in the mid-Atlantic ridge near 24^o and 30^{o}N. *Philosophical Transactions of the Royal Society*, **A268**, 589-603.

Miller, J.A., Viola, G., and Mancktelow, N.S., (2008). Oxygen, carbon and strontium isotope constraints on the mechanisms of nappe emplacement and fluid–rock interaction along the subhorizontal Naukluft Thrust, central Namibia. *Journal of the Geological Society, London*, **165**, 739–753.

Moyen, J.F., Stevens, G., and Kisters, A.F.M., (2006). Record of mid-Archaean subduction from metamorphism in the Barberton terrain, South Africa. *Nature,* **44**, 559-662.

Mojzsis, S.J., Coath, C.D., Greenwood, J.P., McKeegan, K.D., and Harrison, T.M., (2003). Mass independent isotope effects in Archean (2.5 to 3.8 Ga) sedimentary sulfides determined by ion microprobe analysis. *Geochimica et Cosmochimica Acta*, **67**, 1635–1658.

Muehlenbachs, K., and Clayton, R.N., (1972a). Oxygen isotope studies of fresh and weathered submarine basalts. *Canadian Journal of Earth Sci*ences, **9**, 172-184.

Muehlenbachs, K., and Clayton, R.N., (1972b). Oxygen isotope geochemistry of submarine Greenstones. *Canadian Journal of Earth Sci*ences, **9**, 471-478.

Muehlenbachs, K., and Clayton, R.N., (1976). Oxygen isotope composition of the oceanic crust and its bearing on seawater. *Journal of Geophysical Res*earch, **81**, 4365-4369.

Munoz, M., de Andrade, V., Vidal, O., Lewin, E., Pascarelli, S. and Susisi, J., (2006). X-ray absorption micro-mapping of iron redox and speciation in chlorite. *G-cube*, **7**, Q11020, 10PP, doi: 10. 1029/2006GC001381.

Nasir, S., Al Sayigha, A.R., Al Harthya, A., Al-Khirbasha, S., Al-Jaaidia, O., Musllamb, A., Al-Mishwat, A., and Al-Bu'saidi, S. (2007). Mineralogical and geochemical characterization of listwaenite from the Semail Ophiolite, Oman. *Chemie der Erde*, **67,** (2007) 213–228.

Norrish, K., and Hutton, J.T., (1969). An accurate X-ray spectrographic method for the analysis of a wide range of geological samples. *Geochimica et Cosmichimica Acta*, **33**, 431-453.

Ohmoto H., (1986). Stable isotope geochemistry of ore deposits. *Reviews in Mineralogy*, **16**, 491-559.

Ono, S.B., Wing, B., Johnston, D., Farquhar, J., and Rumble, D., (2006). Mass-dependent fractionation of quadruple stable sulfur isotope system as a new tracer of sulfur biogeochemical cycles, *Geochimica et Cosmichimica Acta, **70**, 2238-2252.*

Paris, I., Stanistreet, I.G., and Hughes, M.J., (1985). Cherts of the Barberton greenstone belt interpreted as products of submarine exhalative activity. *Journal of Geology* **93**,111–129.

Parman, S.W. and Grove, T.L., (2004). Petrology and Geochemistry of Barberton Komatiites and basaltic Komatiites: evidence of Archean Fore-arc Magmatism. In Kusky, T.M. (ed) *Precambrian Ophiolites and Related Rocks*. Developments in Precambrian Geology, **13**, 539-566.

Parra, T., Vidal, O. and Agard, P., (2002a). A thermodynamic model for Fe–Mg dioctahedral K white micas using data from phase-equilibrium experiments and natural pelitic assemblages. Contributions to *Mineralogy* and *Petrology*, **143**, 706-732.

Parra, T., Vidal, O. and Jolivet, L., (2002b). Relation between the intensity of deformation and retrogression in blueschist metapelites of Tinos Island (Greece) evidenced by chlorite-mica local equilibria. *Lithos*, **63**, 41–66.

Patrier, P., Beaufort, D., Meunier, A., Eymery, J.P. and Petit, S., (1991). Determination of the nonequilibrium ordering state in epidote from the ancient geothermal field of Saint Martin: Application of Mössbauer spectroscopy. *American Mineralogist*, **76**, 602-610.

Pattison, D.R.M., (2003). Petrogenetic significance of orthopyroxene-free garnet + clinopyroxene + plagioclase ± quartz-bearing metabasites with respect to the amphibolite and granulite facies. *Journal of Metamorphic Geology*, **21**, 21-34.

Pearce, J.A., (2003). Supra-Subduction Zone ophiolites: the search for modern analogues. *Geological Society of America Special Pape*, **373**, 269-293.

Pederson, R.B., Furnes, H., Dunning, G., (1991). A U/Pb age for the Sulitjelma Gabbro, Northern Norway: further evidence for the development of a Caledonian marginal basin in Ashgill-Llandovery time. *Geological Magazine*, **128** (2), 141-153.

Pedersen, R.B., Rapp, H. T., Thorseth, I.H., Lilley, M.D., Barriga, F. J. A. S., Baumberger, T., Flesland, K., Fonseca, R., Früh-Green, G. L., and Jorgensen, S. L., (2010). Discovery of a

black smoker vent field and vent fauna at the Arctic Mid-Ocean Ridge. *Nature Communications*. 1:126 doi: 10.1038/ncomms1124 (2010).

Piwinskii, A.J., (1968). Experimental studies of igneous rock series, central Sierra Nevada Batholith, California. *Journal of Geology,* **76**, 548 – 570.

Plissart, G., Féménias, O., Mãruntiu, M., Diot, H. and Demaiffe, D., (2009). Mineralogy and geothermometry of gabbro-derived listvenites in the Tisovita-Iuti ophiolite, Southwestern Romania. *The Canadian Mineralogist,* **47**, 81-105.

Philippot, P., van Zuilen, M.A., Lepot, K., Thomazo, C., Farquhar, J., and Van Kranendonk, M.J., (2007). Early Archaean micro-organisms preferred elemental sulfur, not sulfate. S*cience,* **317**, 1534–1537.

Powell, R. and Holland, T.J.B., (1988). An internally consistent thermodynamic dataset with uncertainties and correlations: 3. Application, methods, work examples and a computer program. *Journal of Metamorphic Geology,* **6**, 173-204.

Poujol, M., Robb, L. J., Anhaeusser, C. R., and Gericke, B., (2003). A review of the geochronological constraints on the evolution of the Kaapvaal Craton, South Africa. Precambrian Research, **127 (1)**, 181-213, doi:10.1016/S0301-9268(03)00187-6.

Rimmelé, G., Parra, T., Goffe, B., Oberhänsli, R., Jolivet, L. and Candan, O., (2005). Exhumation paths of high pressure-low temperature rocks from the Lycian Nappes and the Menderes Massif (SW Turkey): a multi-equilibrium approach. *Journal of Petrology*, **46**, 641–669.

Robb, L.J., Anhaeusser, C.R. and Van Nierop, D.A., (1983). The recognition of the Nelspruit batholith north of the Barberton greenstone belt and its significance in terms of Archaean crustal evolution. In: *Contributions to the Geology of the Barberton Mountain Land*. Anhaeusser, C. R. (ed.). *Special Publication Geological Society* of *South Africa* **9**, 117-130.

Schandal, E.S., and Naldrett, A.J., (1992). CO_2 metasomatism of serpentinites, south of Timmins, Ontario. *Canadian Mineralogist*, **30**, 93-108.

Schidlowski, M., Hayes, J.M., Kaplan I.R., (1983). Isotopic inferences of ancient biochemistries: carbon, sulfur, hydrogen and nitrogen. In: Schopf, J.W. (ed). Earth's earliest biosphere: its origin and evolution. Princeton University Press, Princeton, pp 149-186.

Schoene, B., de Wit, M.J. and Bowring, S., (2008). Mesoarchean assembly and stabilization of the eastern Kaapvaal craton: A structural-thermochronological perspective. *Tectonics*, **27**, TC5010, doi:10.1029/2008TC002267.

Schoene, B., Dundas, F.O.L., Bowring, S.A., de Wit., M.J., (2009). Sm-Nd isotopic mapping of lithospheric growth and stabilization in the eastern Kaapvaal craton, *Terra Nova*, **21**, 219–228.

Searle, M.P., (2007). Structural geometry, style and timing of deformation in the Hawasina Window, Al Jabal al Akhdar and Saih Hatat culminations, Oman Mountains. *GeoArabia*, **12**, 99-130.

Sharhan, A. and Nasir, S., (1996). Sedimentological and geochemical interpretation of a transgrissive sequence: the Late Cretaceous Qahla Formation in the western Oman Mountains, United Arab Emirates. *Sedimentary Geology*, **101**, 227-242.

Slama, J., Kosler, J., Condon, D.J., Crowley, J.L., Gerdes, A., Hanchar, J.M., Horstwood, M., Morris, G.A., Nasdala, L., Norbert, N., Schaltegger, U., Schoene, B., Tubrett, M.N., Whitehouse, M.J., (2008). Plešovice zircon – a new natural reference material for U-Pb and Hf isotopic microanalysis. *Chemical Geology*, **249**, 1-35.

Sibson, R.H., (1990). Conditions of fault-valve behaviour. In: Knipe, R.J. and Rutter, E.H. (eds), Deformation mechanisms, Rheology and Tectonics. *Geological Society of London, Special Publication*, **54**, 15-28.

Smith. H.S., O'Neil, J.R. and Erlank, A.J., (1984). Oxygen Isotope Compositions of minerals and rocks and chemical alteration patterns in pillow lavas from the Barberton Greenstone Belt, South Africa. In: Archaean Geochemistry (Edited by Kröner, A., Hanson, G. N. and Goodwin, A. M.), pp. 113-137. Springer, Berlin.

Spear, F., (1993). Metamorphic phase equilibria and pressure-temperature-time paths. *Mineralogical Society of America Monograph, BookCrafters, Washington*, 799pp.

Spridonow, E.M., (1991). Listwaenites and zodites. *Inter. Geol. Rev*., 397-407.

Stanger, G., (1985). Silicified serpentinite in the Semail nappe of Oman. *Lithos*, **18**, 13–22.

Stern, R.J., Johnson., P.R., Kröner., A and Yibas, B., (2004). Neoproterozoic ophiolites of the Arabian-Nubian Shield. In: Kusky, T.M. (Ed.), *Precambrian Ophiolites and Related Rocks*. Developments in Precambrian Geology, **13**. Elsevier, Amsterdam, 95-128.

Stevens, G., Droop, G.T.R., Armstrong, R.A., and Anhaeusser, C.R., (2002). Amphibolite facies metamorphism in the Schapenburg schist belt: A record of the mid-crustal response to ~3.23 Ga terrane accretion in the Barberton greenstone belt: South African. *Journal of Geology*, **105**, 271-284.

Stowe, C.W., (1994). Compositions and tectonic setting of deposits through time. *Economic Geology*, **89**, 528-546.

Tarantola, A., Mullis, J., Guillaume, D., Dubessy, J., de Capitani, C., and Abdelmoula, M., (2009). Oxidation of CH_4 to CO_2 and H_2O by chloritization of detrital biotite at 270±5 °C in the external part of the Central Alps, Switzerland. *Lithos*, **112**, 497–510.

Taylor, H.P., Jr., (1968). The oxygen isotope geochemistry of igneous rocks. *Contributions to Mineralogy and Petrology*, **19**, 1-71.

Taylor, B.E., (1986). Magmatic volatiles: Isotopic variation of C, H and S. *Reviews in Mineralogy*, **16**, 185-225.

Tegtmeyer, A. and Kröner, A., (1987). U-Pb zircon ages bearing on the nature of early Archaean greenstone belt evolution, Barberton Mountainland, South Africa. *Precambrian R*esearch, **36**, 1–20.

Tice, M.M., Bostick, B.C. and Lowe, D.R., (2004). Thermal history of the 3.5-3.2 Ga Onverwacht and Fig Tree Groups, Barberton greenstone belt, South Africa, inferred by Raman microspectroscopy of carbonaceous material. *Geology*, **32**, 37-40.

Trotet, F., Jolivet, L. and Vidal, O., (2001a). Tectono-metamorphic evolution of Syros and Sifnos Islands (Cyclades, Greece). *Tectonophysics*, **2**, 179–206.

Trotet, F., Vidal, O. and Jolivet, L., (2001b). Exhumation of Syros and Sifnos metamorphic rocks (Cyclades, Greece). New constraints on the P–T paths. *European Journal of Mineralogy*, **13**, 901–920.

Tsikouras, B., Karipi, S., Gramatikopoulos, T. and Hatzipanagiotou, K. (2006). Listwaenite evolution in the ophiolite mélange of Iti Mountain (continental central Greece). *European Journal of Mineralogy*, **18**, 243-255.

Ucurum A., (2000). Listwaenites in Turkey: Perspectives on the formation and precious metal concentration with reference to the occurrences in East-Central Anatolia. *Ofioliti*, **25**, 15-29.

Van Kranendonk, M.J., Kröner, A., Hegner, E., Connelly, J., (2009). Age, lithology and structural evolution of the c. 3.53 Ga Theespruit Formation in the Tjakastad area, southwestern Barberton Greenstone Belt, South Africa, with implications for Archaean tectonics. *Chemical Geology*, **261**, 115–139.

Van Kranendonk, M.J., (2011). Cool greenstone drips and the role of partial convective overturn in the Barberton greenstone belt evolution. *Journal of African Earth Sciences*, **60**, 346-352.

Van Zuilen M. A., Chaussidon M., Rollion-Bard C., and Marty B., (2007). Carbonaceous cherts of the Barberton Greenstone Belt, South Africa; isotopic, chemical, and structural characteristics of individual microstructures. *Geochimica et Cosmochimica Acta*, **71**, 655-669.

Veizer, J. and Hoefs, J., (1976). The nature of $^{18}O/^{16}O$ and $^{13}C/^{12}C$ secular trends in sedimentary carbonate rocks. *Geochim Cosmochim Acta*, **44**, 579-587.

Veizer, J., Hoefs, J., Ridler, R.H., Jensen, S.L. and Lowe, D.R., (1989a). Geochemistry of Precambrian carbonates: I. Archean hydrothermal systems. *Geochimmica et Cosmochimica Acta.*, **53**, 845-857.

Veizer, J., Hoefs, J., Ridler, R.H., Lowe, D.R., and Thurston, P.C., (1989b). Geochemistry of Precambrian carbonates: II. Archean greenstone belts and Archean seawater. *Geochimmica et Cosmochimica Acta*. **53**, 859-871.

Velde, B., (1965). Phengitic micas: synthesis, stability, and natural occurrence. *American Journal of Science*, **263**, 886–913.

Velde, B., (1967). Si^{4+} content of natural phengites. *Contributions to Mineralogy* and *Petrology*, **14**, 250-258.

Vidal, O. and Parra, T., (2000). Exhumation paths of high-pressure metapelites obtained from local equilibria for chlorite-phengite assemblages. *Geological Journal*, **35**, 139–161.

Vidal, O., Parra, T. and Trotet, F., (2001). A thermodynamic model for Fe-Mg aluminous chlorite using data from phase equilibrium experiments and natural pelitic assemblages in the 100-600 ^{o}C, 1–25 kbar P–T range. *American Journal of Science*, **301**, 557–592.

Vidal, O., Parra, T. and Vieillard, P., (2005). Experimental data on the Tschermak solid solution in Fe-chlorites: application to natural examples and possible role of oxidation. *American Mineralogist*, **90**, 359–370.

Vidal, O., de Andrade, V., Lewin, E., Munoz, M., Parra, T. and Pascarelli, S., (2006). P–T-deformation-Fe^{3+}/Fe^{2+} mapping at the thin section scale and comparison with XANES mapping: application to a garnet-bearing metapelite from the Sambagawa metamorphic belt (Japan). *Journal of Metamorphic Geology*, **24**, 669–683.

Vidal, O. and Dubacq, B., (2009). Thermodynamic modelling of clay dehydration, stability and compositional evolution with temperature, pressure and aH_2O. *Geochimica et Cosmochimica Acta*, **73**, 6544–6564.

Vidal, O., Dubacq, B., Lanari, P., (2010). Comment on "The Role of H_3O^+ in the Crystal Structure of Illite" by F. Niéto, M. Melini, and I. Abad. *Clays and Clay Minerals,* **58**, 717-720.

Viljoen, M.J. and Viljoen, R.P., (1969a). An introduction to the geology of the Barberton, granite-greenstone terrain. *Special Publication Geological Society* of *South Africa,* **9**, 1-20.

Viljoen, M.J. and Viljoen, R.P., (1969b). The geology and geochemistry of the lower ultramafic unit of the Onverwacht Group and a proposed new class of igneous rocks. *Geological Society of South Africa Special Publication,* **2**, 55-86.

Viljoen, M.J., Viljoen, R.P., (1969c). The geological and geochemical significance of the upper formations of the Onverwacht Group. *Geological Society of South Africa Special Publication,* **2**, 113-152.

Wacey, D., McLoughlin, N., Whitehouse, M.J. and Kilburn, M.R., (2010). Two co-existing sulfur metabolisms in a ca. 3,400 Ma sandstone. *Geology,* **38**, 1115-1118.

Walsh, M.M., (1992). Microfossils and possible microfossils from the Early Archean Onverwacht Group, Barberton Mountain Land, South Africa. *Precambrian Res*earch, **54**, 271-293.

Westraat, J.D., Kisters, A.F.M., Poujol, M., and Stevens, G., (2005). Transcurrent shearing, granite sheeting and the incremental construction of the tabular 3.1 Ga Mpuluzi batholith, Barberton granite-greenstone terrane, South Africa. *Journal of the Geological Society, London,* **162**, 373-388.

White, R.W., Powell, R. and Clarke, G.L., (2002). The interpretation of reaction textures in Fe-rich metapelitic granulites of the Musgrave Block, central Australia: Constraints from mineral equilibria calculations in the system K_2O–FeO–MgO– Al_2O_3–SiO_2–H_2O–TiO_2–Fe_2O_3. *Journal of Metamorphic Geology*, **20**, 41–55.

Whitehouse, M.J., Kamber, B.S., Fedo, C.M., and Lepland, A., (2005). Integrated Pb- and S-isotope investigation of sulphide minerals from the early Archaean of southwest Greenland. *Chemical Geology,* **222**, 112–131

Wiedenbeck, M., Alle, P., Corfu, F., Griffin, W.L., Meier, M., Oberli, F., von Quadt, A., Roddick, J.C., Spiegel, W., (1995). Three natural zircon standards for U-Th-Pb, Lu-Hf, trace element and REE analyses. *Geostandards Newsletter,* **19**, 1-23.

Williams, H. and Smyth, W.R., (1973). Metamorphic aureoles beneath ophiolite suites and Alpine peridotites: Tectonic implications with west Newfoundland examples. *American Journal of Science,* **273**, 594-621.

Willner, A.P., (2005). Pressure-temperature evolution of a Late Palaeozoic paired metamorphic belt in North-Central Chile (34^o–$35^o30'$S). *Journal of Petrology,* **46**, 1805–1833.

Wyllie, P.J. and Wolf, M.B., (1993). Amphibolite dehydration-melting: sorting out the solidus. In: *Magmatic Processes and Plate Tectonics*. Prichard, H. M., Alabaster, T., Harris, N. B. W. and Neary, C.R. (eds). *Special publication Geological Society, London,* **76**, 405-416.

Xie, X., Byerly, G.R., and Ferrell, R.E., (1997). IIb trioctehedral chlorite from the Barberton greenstone belt; crystal structure and rock composition constraints with implications to geothermometry. *Contributions to Mineralogy and Petrology*, **126**, 275-291.

Yamato P, Agard P, Goffé B., De Andrade, V., Vidal., O. and Jolivet, L., (2007). New, high-precision P-T estimates for Oman blueschists: implications for obduction, nappe stacking and exhumation processes. *Journal of Metamorphic Geology*, **25,** 657-682.